Three dimensional estimation of vegetation moisture content using dual-wavelength terrestrial laser scanning

Ahmed Elsherif

Thesis submitted for the degree of Doctor of Philosophy

School of Engineering

Newcastle University

February 2020

Abstract

Leaf Equivalent Water Thickness (EWT) is a water status metric widely used in vegetation health monitoring. Optical Remote Sensing (RS) data, spaceborne and airborne, can be used to estimate canopy EWT at landscape level, but cannot provide information about EWT vertical heterogeneity, or estimate EWT predawn. Dual-wavelength Terrestrial Laser Scanning (TLS) can overcome these limitations, as TLS intensity data, following radiometric corrections, can be used to estimate EWT in three dimensions (3D). In this study, a Normalized Difference Index (NDI) of 808 nm wavelength, utilized in the Leica P20 TLS instrument, and 1550 nm wavelength, employed in the Leica P40 and P50 TLS systems, was used to produce 3D EWT estimates at canopy level. Intensity correction models were developed, and NDI was found to be able to minimize the incidence angle and leaf internal structure effects.

Multiple data collection campaigns were carried out. An indoors dry-down experiment revealed a strong correlation between NDI and EWT at leaf level. At canopy level, 3D EWT estimates were generated with a relative error of 3 %. The method was transferred to a mixed-species broadleaf forest plot and 3D EWT estimates were generated with relative errors < 7 % across four different species. Next, EWT was estimated in six short-rotation willow plots during leaf senescence with relative errors < 8 %. Furthermore, a broadleaf mixed-species urban tree plot was scanned during and two months after a heatwave, and EWT temporal changes were successfully detected. Relative error in EWT estimates was 6 % across four tree species. The last step in this research was to study the effects of EWT vertical heterogeneity on forest plot reflectance. Two virtual forest plots were reconstructed in the Discrete Anisotropic Radiative Transfer (DART) model. 3D EWT estimates from TLS were utilized in the model and Sentinel-2A bands were simulated. The simulations revealed that the top four to five metres of canopy dominated the plot reflectance. The satellite sensor was not able to detect severe water stress that started in the lower canopy layers.

This study showed the potential of using dual-wavelength TLS to provide important insights into the EWT distribution within the canopy, by mapping the EWT at canopy level in 3D. EWT was found to vary vertically within the canopy, with EWT and Leaf Mass per Area (LMA) being highly correlated, suggesting that sun leaves were able to hold more moisture than shade leaves. The EWT vertical profiles varied between species, and trees reacted in different ways during drought conditions, losing moisture from different canopy layers. The proposed method can provide time series of the change in EWT at very high spatial and temporal resolutions, as TLS instruments are active sensors, independent of the solar illumination. It also has the potential to provide EWT estimates at the landscape level, if coupled with automatic tree

segmentation and leaf-wood separation techniques, and thus filling the gaps in the time series produced from satellite data. In addition, the technique can potentially allow the characterisation of whole-tree leaf water status and total water content, by combining the EWT estimates with Leaf Area Index (LAI) measurements, providing new insights into forest health and tree physiology.

Acknowledgements

I would like to express my sincere gratitude to my supervisors Dr Rachel Gaulton and Prof. Jon Mills for their support, encouragement, advice and assistance throughout the years of my PhD. Thank you for having faith in me. This thesis would not have been possible without your help and support.

My appreciation is due to the Egyptian Ministry of Higher Education for funding my PhD research, and for the Egyptian Cultural and Educational Bureau in London for supporting me during the years of my PhD.

I would like to thank Leica Geosystems UK for loan of the P40 and P50 instruments used in this research. I also would like to thank the Natural Environment Research Council (NERC) for providing the Spectralon panels used in the calibration experiments. I am also very grateful to Prof. Mark Danson for hosting the dry-down experiment at Salford University, Manchester, UK, and for my friend Fadal Sasse for his help during the experiment. Many thanks to Prof. Yadvinder Malhi, Dr Alexander Shenkin, Mr Nigel Fisher, and of course my friend and colleague Zheng Wang for their help and support at Wytham Woods. In addition, Prof. Yadvinder Malhi and Dr Alexander Shenkin have contributed to the results interpretation presented in Sections 5.5.1 and 5.5.4. Many thanks to Mr Martin Robertson for actually teaching me how to use a TLS instrument.

I would like to thank the entire Geospatial Engineering group at Newcastle University for making me feel at home here in Newcastle. Special thanks to my best friends Elias Berra, Maria Peppa, Magdalena Śmigaj, Kzr Moreri, David Walker, Marcos Baluja, Nurten Akgun, Katarina Vardic, and Marine Roger for all the good time we had, and for the special moments that have become memories that will live forever.

Lastly, I would like to thank my entire family, especially my mother, and my friends and colleagues in Egypt for their unconditional support throughout my study. I also would like to thank Prof. Hafez Afify for helping me become the researcher I am today.

Related publications

The following publications contain work related to or derived from this thesis:

Elsherif, A., Gaulton, R. and Mills, J. (2019) 'Four dimensional mapping of vegetation moisture content using dual-wavelength terrestrial laser scanning', *Remote Sensing*, 11, 2311.

Elsherif, A., Gaulton, R., Shenkin, A., Malhi, Y. and Mills, J. (2019) 'Three dimensional mapping of forest canopy equivalent water thickness using dual-wavelength terrestrial laser scanning', *Agricultural and Forest Meteorology*, 276, 107627.

Elsherif, A., Gaulton, R. and Mills, J. (2018) 'Estimation of vegetation water content at leaf and canopy level using dual-wavelength commercial terrestrial laser scanners', *Interface Focus*, 8(2), 59-69.

Elsherif, A., Gaulton, R., and Mills, J. P. (2019) 'The potential of dual-wavelength terrestrial laser scanning in 3D canopy fuel moisture content mapping', *International Archives of the Photogrammetry, Remote Sensing and Spatial Information Sciences*, XLII-2/W13, 975-979.

Elsherif, A., Gaulton, R., and Mills, J. P. (2019) 'Measuring leaf equivalent water thickness of short-rotation coppice willow canopy using terrestrial laser scanning', *IEEE International Geoscience and Remote Sensing Symposium (IGARSS)*, Yokohama, Japan, 28 July – 2 August.

Table of Contents

List of Figures

List of Tables

List of Abbreviations

3D	Three Dimensions
ASTER	Advanced Spaceborne Thermal Emission and Reflection Radiometer
AVIRIS	Airborne Visible/Infrared Imaging Spectrometer
BOA	Bottom Of Atmosphere
BRDF	Bidirectional Reflectance Distribution Function
C_{ab}	Chlorophyll a and b content
C_{ar}	Carotenoid content
C_b	Brown pigment content
CESBIO	CEntre for the Study of the BIOsphere from space
C_m	Leaf dry matter content
C_w	Leaf water content
CWC	Canopy Water Content
DART	Discrete Anisotropic Radiative Transfer
DW	Dry Weight
DWEL	Dual Wavelength Echidna LiDAR
E (%)	Relative error
EWT	Equivalent Water Thickness
FaNNI	Foliage and Needles Naïve Insertion
FLIGHT	Three-dimensional Forest Light Interaction
FLIM	Forest Light Interaction Model
FMC	Fuel Moisture Content
FRT	Forest Reflectance and Transmittance
FW	Fresh Weight
GVMI	Global Vegetation Moisture Index
HA	High Atmosphere
INFORM	INvertible FOrest Reflectance Model
LA	Lower Atmosphere
LAI	Leaf Area Index
LIBERTY	Leaf Incorporating Biochemistry Exhibiting Reflectance and Transmittance Yields
LMA	Leaf Mass per Area
LOPEX93	Leaf Optical Properties Experiment 1993
LUT	Look-Up Table

MA	Mid Atmosphere
MIVIS	Multispectral Infrared and Visible Imaging Spectrometer
MODIS	Moderate-Resolution Imaging Spectroradiometer
MODTRAN	MODerate resolution atmospheric TRANsmission
MSI	Moisture Stress Index
N	Leaf structure coefficient
NDI	Normalized Difference Index
NDII	Normalized Difference Infrared Index
NDVI	Normalized Difference Vegetation Index
NDWI	Normalized Difference Water Index
NIR	Near InfraRed
QSM	Quantitative Structure Model
RAMI	RAdiation transfer Model Intercomparison
RMSE	Root Mean Squared Error
RS	Remote Sensing
RTM	Radiative Transfer Model
RWC	Relative Water Content
SA	Surface Area
SAIL	Scattering by Arbitrarily Inclined Leaves
SALCA	Salford Advanced Laser Canopy Analyser
SLA	Specific Leaf Area
SPOT	Satellite for observation of Earth (*Satellite Pour l'Observation de la Terre*)
SPRINT	Spreading of Photons for Radiation Interaction
SWIR	ShortWave InfraRed
TLS	Terrestrial Laser Scanning
TOA	Top Of Atmosphere
UAV	Unmanned Aerial Vehicle
VWC	Vegetation Water Content
WI	Water Index

Chapter 1. Introduction

1.1 Research context

Climate change has been linked to the recent increase in frequency and intensity of heatwaves, with climate models predicting more heatwaves to occur in the future (Schär *et al.*, 2004). Heatwaves, when accompanied by lack of rainfall, can trigger severe drought conditions with catastrophic effects on the agricultural and forestry sectors, reducing crop yields and increasing rates of forest fires and tree mortality (Allen *et al.*, 2015). For instance, the record-breaking 2003 European heatwave caused a fall in arable crop production by more than 10% (23 million tons, the highest recorded drop in a century) in comparison to the previous year (García-Herrera *et al.*, 2010). In addition, more than 25,000 forest fires were reported across Europe, destroying approximately 730,000 hectares of forests (García-Herrera *et al.*, 2010). A total estimated loss of approximately 13 billion Euros was reported, including losses in agricultural and livestock sectors (García-Herrera *et al.*, 2010). Stott *et al.* (2004) estimated that the risk of occurrence of the 2003 European heatwave was doubled because of the increase in greenhouse gases concentrations in the atmosphere caused by human activities. Similarly, Vogel *et al.* (2019) rendered human-caused climate change as a factor that increased the magnitude of the 2018 European heatwave. Recently, the heatwave that hit Europe in June and July 2019 broke the highest temperature records set by the 2003 heatwave (Mitchell *et al.*, 2019).

During drought, plants use different survival mechanisms, one of which is closing leaf stomata (pores on the underside of leaves) to minimize water loss, thus allowing less water evaporation from leaves and reducing plant transpiration rate (Carter, 1993; Peñuelas *et al.*, 1994; Ceccato *et al.*, 2001). Transpiration refers to water movement through a plant from roots to leaves, to distribute water and nutrients needed for photosynthesis, before water gets evaporated through leaf stomata (Jarvis and McNaughton, 1986). Stomatal closure further affects plant photosynthetic rate by limiting carbon dioxide intake and exchange of gases with the atmosphere (Farquhar and Sharkey, 1982; Chaves *et al.*, 2003; Zivcak *et al.*, 2013). The drop in rates of transpiration, photosynthesis, and carbon gain cause a decline in the plant growth rate and productivity (Lawlor and Cornic, 2002; McDowell *et al.*, 2008; Mendiguren *et al.*, 2015), and it also becomes more prone to burning (Bartlett *et al.*, 2016). If drought conditions are prolonged, the plant may suffer from carbon starvation or hydraulic failure, eventually leading to its death (McDowell *et al.*, 2013; Sevanto *et al.*, 2014). Continuous monitoring of

vegetation water status can lead to early detection of vegetation stress, which can help in improving decision making during droughts, regarding crop irrigation and harvest scheduling (Sepulcre-Cantó *et al.*, 2006), and preventing and fighting forest fires (Yebra *et al.*, 2008). Furthermore, monitoring vegetation water status can help in the early detection of symptoms of disease and signs of pest infestations in forests and agricultural crops (Carter, 1993; Ferretti, 1997; Jones and Tardieu, 1998; Datt, 1999; Meentemeyer *et al.*, 2008; Trumbore *et al.*, 2015; Große-Stoltenberg *et al.*, 2016).

A widely-used approach to determine vegetation water status and detect vegetation water stress is measuring the water potential (Ψ) of leaf or stem, typically predawn, expressed in bar or megapascal (Jarvis, 1976; Chone *et al.*, 2001). Water potential is a direct measurement that can be conducted on a plant in the field using a pressure chamber (Scholander *et al.*, 1965). It is directly linked to water movement through a plant from soil to foliage, and a drop in water potential can indicate a water deficit, as it indicates that loss of water in transpiration exceeds absorption of water via the roots (Jarvis, 1976; McCutchan and Shackel, 1992). However, measuring the water potential with the pressure chamber is a slow process that can be impractical if the aim is to determine the water status of a large number of plants (Vila *et al.*, 2011). Alternatively, thermal imagery can be used to estimate the water potential, as it can detect the increase in canopy temperature caused by leaf stomatal closure during water stress, which is inversely proportional to leaf water potential (Ehrler *et al.*, 1978; Idso *et al.*, 1981; Vila *et al.*, 2011).

Another approach to quantify water in vegetation is using vegetation water status metrics, including leaf Equivalent Water Thickness (EWT), Fuel Moisture Content (FMC), Canopy Water Content (CWC), Vegetation Water Content (VWC), and Relative Water Content (RWC). EWT (g cm^{-2}) is the amount of liquid water in a given leaf area (Danson *et al.*, 1992), and is widely adopted in vegetation health monitoring as it can reflect the physiological status of vegetation and is related to the leaf tolerance to dehydration (Wright *et al.*, 2004; Yilmaz *et al.*, 2008; Gaulton *et al.*, 2013; Féret *et al.*, 2018). FMC (%) is defined as the amount of liquid water in a leaf divided by leaf dry weight (Burgan, 1996). It is a key metric in forest fire modelling and is widely utilized in the early detection of wildfire risk (Danson and Bowyer, 2004; Aponte *et al.*, 2016; Zhu *et al.*, 2017). CWC (kg m^{-2}) is the mass of water in a canopy per unit ground area (Clevers *et al.*, 2010), and is a parameter of interest in studying the water cycle and its role in global climate change (Clevers *et al.*, 2010; Mendiguren *et al.*, 2015). VWC (kg m^{-2}) is the total mass of water in leaves, branches, and stems, per unit ground area. VWC is used in

retrieving soil moisture content under vegetation canopies from active and passive microwave remote sensing (Njoku and Entekhabi, 1996; Yilmaz *et al.*, 2008). RWC (%) is the ratio between liquid water volume in a leaf to maximum water volume when the same leaf is fully saturated with water (Hunt Jr *et al.*, 1987). RWC can reflect how a plant responds to water stress, but is difficult to measure as it requires the measurement of leaf weight when the leaf is fully saturated with water, which is hard to obtain in the field (Maki *et al.*, 2004).

This research focuses mainly on EWT because it not only serves as a vegetation stress indicator, but can also be used to retrieve other key vegetation water status metrics. EWT, when coupled with canopy Leaf Area Index (LAI) measurements, the one-sided green leaf area per unit ground surface area (Jonckheere *et al.*, 2004), can be used to estimate CWC, expressed as EWT multiplied by LAI (Clevers *et al.*, 2010; Mendiguren *et al.*, 2015). In the same manner, EWT can be linked to FMC, expressed as EWT divided by Leaf Mass per Area (LMA) (Danson and Bowyer, 2004). LMA (g cm^{-2}) is the ratio of leaf dry weight to its surface area, and is an important trait in plant growth rate (Gutschick and Wiegel, 1988; Poorter *et al.*, 2009). Furthermore, EWT can be used to estimate VWC using allometric relationships (Yilmaz *et al.*, 2008). Another important characteristic of EWT is that it is linked to water depth in the leaf, thus can be estimated directly from reflectance in the optical domain, allowing the use of optical Remote Sensing (RS) data in obtaining EWT estimates over large spatial scales (Ceccato *et al.*, 2002; Colombo *et al.*, 2008).

Methods that utilize spaceborne and airborne optical RS data, both multispectral and hyperspectral, to estimate EWT are considered a more efficient alternative to *in-situ* approaches (destructive methods and field spectroscopy), which are time and effort consuming and impractical for large areas (Pu *et al.*, 2003; Dash *et al.*, 2017). Such methods can not only provide estimates of canopy EWT at a landscape level, but are also useful for producing time series of data to monitor the change in vegetation moisture content (Foley *et al.*, 1998; Colombo *et al.*, 2008; Clevers *et al.*, 2010). EWT estimation from optical RS data is primarily based on the interaction of radiation with foliage, with reflectance in the ShortWave InfraRed (SWIR) region in leaf spectra being dominated by absorption by water (Knipling, 1970; Zarco-Tejada *et al.*, 2003). The two most common approaches to estimate EWT are using vegetation indices or inversion of physical Radiative Transfer Models (RTMs) (Serrano *et al.*, 2000; Mirzaie *et al.*, 2014). Vegetation indices combine the reflectance measured by the sensor in two or more spectral bands (wavelengths) in a simple ratio or a Normalized Difference Index (NDI) and link it to EWT using different types of regression analysis (Bannari *et al.*, 1995; Jones and Vaughan,

2010). RTMs, on the other hand, simulate vegetation spectra at the leaf level, such as the PROSPECT model (Jacquemoud and Baret, 1990), or at canopy level, such as the SAIL model (Scattering by Arbitrarily Inclined Leaves) (Verhoef, 1984). By inverting these models, EWT and other canopy biochemical characteristics can be estimated (Ceccato *et al.*, 2002; Zarco-Tejada *et al.*, 2003; Mendiguren *et al.*, 2015).

Estimating EWT from spaceborne and airborne optical RS data, despite its advantages over *in-situ* approaches, has some limitations. Firstly, EWT can only be estimated at midday as the sensors are dependent on the solar illumination (Eitel *et al.*, 2010). Detecting the vegetation water status at midday can be an unreliable indicator of water stress since leaves lose water during photosynthesis, and it is therefore better to conduct the measurements predawn when there is no transpiration (Améglio *et al.*, 1999; Williams and Araujo, 2002). In addition, EWT estimation from optical remote sensing data is affected by canopy structure, understory vegetation and background soil reflectance, atmosphere, and shadows, as these factors affect the canopy reflectance and the signal received by the sensor (Baret and Guyot, 1991; Zarco-Tejada *et al.*, 2003; Ali *et al.*, 2016). Furthermore, the vertical heterogeneity in the canopy biophysical and biochemical traits affects the light penetration and scattering within a canopy, and thus plays a role in the canopy reflectance; a role that is often ignored because such heterogeneity is difficult to measure and thus still needs to be investigated further (Valentinuz and Tollenaar, 2004; Ciganda *et al.*, 2008; Wang and Li, 2013; Liu *et al.*, 2015). There is a unique opportunity to address the aforementioned limitations using Terrestrial Laser Scanning (TLS).

TLS instruments provide dense point clouds that include high-resolution information about the structure of the scanned objects. As a result, TLS instruments have been widely utilized in measuring vegetation canopy biophysical attributes, especially in forests, including but not limited to: tree height, diameter at breast height, forest biomass, and canopy LAI (Takeda *et al.*, 2008; Ramirez *et al.*, 2013; Calders *et al.*, 2015). Furthermore, TLS point clouds include intensity data in which the backscattered energy for each point is recorded, which can be linked to scanned target reflectance (Penasa *et al.*, 2014). However, radiometric correction is needed for numerous factors that affect the TLS intensity data, including the instrumental effects, the effects of the target distance, and the effects of the incidence angle of the laser beam: the angle between the incident laser beam and the object's surface normal (Kaasalainen *et al.*, 2011; Krooks *et al.*, 2013; Tan and Cheng, 2016). Such effects have been highlighted in numerous studies, and methods to calibrate the intensity to apparent reflectance have been successfully

developed for various TLS instruments (Höfle and Pfeifer, 2007; Jutzi and Gross, 2009; Kaasalainen *et al.*, 2011; Krooks *et al.*, 2013; Blaskow and Schneider, 2014; Anttila *et al.*, 2016; Tan and Cheng, 2016; Zhu *et al.*, 2017; Tan *et al.*, 2018; Bolkas, 2019). The calibrated intensity data can then be used to provide estimates of vegetation biochemical characteristics in three dimensions (3D), if the TLS instrument operates at a suitable wavelength, such as the SWIR if estimating EWT (Eitel *et al.*, 2010; Gaulton *et al.*, 2013; Magney *et al.*, 2014).

One advantage of using TLS to estimate EWT is that the estimation can be carried out both at midday and predawn, as TLS instruments are active sensors that are independent of the solar illumination and cloud coverage. Another advantage is that the understory vegetation and soil can easily be separated from the canopy in the point cloud, using the spatial positioning information, thus removing their effect on the EWT estimation (Höfle, 2014). Furthermore, 3D estimates of EWT enable the vertical heterogeneity in EWT within canopy to be studied, including how it varies between species. In addition, more complex 3D RTMs that allow representation of the heterogeneity in tree structure have been developed and validated, e.g., DART (Discrete Anisotropic Radiative Transfer) (Gastellu-Etchegorry *et al.*, 1996; Demarez and Gastellu-Etchegorry, 2000), SPRINT (Spreading of Photons for Radiation Interaction) (Goel and Thompson, 2000), FLIM (Forest Light Interaction Model) (Rosema *et al.*, 1992), and FLIGHT (Three-dimensional Forest Light Interaction) (North, 1996), among others. Including the 3D EWT estimates in RTMs can lead to a better understanding of how the EWT heterogeneity affects canopy reflectance and received satellite signal.

There have been a few successful attempts in recent years to utilize TLS intensity data in the estimation of EWT, using a single SWIR wavelength (Zhu *et al.*, 2015; Zhu *et al.*, 2017), or NDI of two laser wavelengths (Gaulton *et al.*, 2013; Junttila *et al.*, 2016; Junttila *et al.*, 2018; Junttila *et al.*, 2019). One advantage of using NDI over using a single SWIR wavelength is that it does not require radiometric correction for the incidence angle effects, if the two wavelengths involved in NDI were similarly affected (Eitel *et al.*, 2014b; Hancock *et al.*, 2017). Another advantage is that NDI can be insensitive to leaf internal structure effects (leaf thickness and LMA), while such effects can be significant when a single SWIR wavelength is used (Ceccato *et al.*, 2001). Although the aforementioned studies showed the potential of using TLS intensity data in retrieving EWT, they investigated the relationship between TLS data and EWT at leaf level only, or at leaf and canopy level for small individual trees in a controlled environment. Only Junttila *et al.* (2019) recently used TLS to estimate EWT in a field campaign, but no 3D EWT estimates were generated. There remains a gap regarding the use of TLS to retrieve 3D

EWT estimates in complex vegetation environments such as forests. In addition, methods to model the EWT vertical heterogeneity in 3D RTMs are needed, as these models typically do not account for the heterogeneity in vegetation biochemical traits within the canopy.

1.2 Research aim

The main aim of this research is to estimate EWT at leaf and canopy level in 3D using the NDI of 808 nm Near InfraRed (NIR) wavelength (as utilized in Leica P20 commercial TLS instruments) and 1550 nm SWIR wavelength (as utilized in Leica P40 and P50 commercial TLS instruments), both in a laboratory setting and in multiple field campaigns (forest plot, willow crop site, and urban tree plot). This necessitates the development of methods to calibrate the intensity data from the different instruments used in the research to apparent reflectance, and also the investigation into the ability of NDI to minimize the incidence angle and leaf internal structure effects. Additional aims include: (1) investigating the potential of this EWT estimation approach for detecting temporal changes in EWT, and (2) utilising the 3D EWT estimates in the DART model to investigate how the vertical heterogeneity of EWT affects forest plot reflectance and received satellite signal.

1.2.1 Research questions

Key research questions include:

1. Can intensity data from commercial dual-wavelength TLS be used to retrieve 3D estimates of EWT at leaf and canopy level in complex vegetation environments?
2. Can the NDI of 808 nm and 1550 nm wavelengths minimize the incidence angle and leaf internal structure effects without the need for further radiometric corrections?
3. How significant is the vertical heterogeneity of EWT within canopy and how does such heterogeneity vary between species?
4. Can TLS detect temporal changes in EWT, and thus provide 4D EWT estimates?
5. Can the 3D EWT estimates be utilised in 3D RTMs to study how such heterogeneity affects forest plot reflectance and received satellite signal?

1.2.2 Research objectives

The main research objectives are to:

1. Develop robust methods to calibrate the intensity data from commercially-available TLS instruments to apparent reflectance.

2. Investigate the ability of NDI to minimize the effects of incidence angle and leaf internal structure without the need for further radiometric corrections.

3. Examine the relationship between NDI and EWT at leaf level across a range of species.

4. Use NDI to generate 3D EWT estimates at canopy level in a controlled laboratory experiment, as well as in field campaigns.

5. Study EWT vertical heterogeneity within canopy and determine how it varies across different species and also between individual trees within each species.

6. Investigate the potential of using TLS to detect temporal changes in EWT due to drought conditions.

7. Develop methods to utilise the 3D EWT estimates in the DART model and simulate the effects of EWT vertical heterogeneity on satellite signal.

1.3 Thesis structure

This thesis consists of this introductory chapter and seven additional chapters. Chapter 2 reviews relevant literature in the field of estimating EWT using optical RS and TLS data, discussing the advantages and limitations of such methods. Chapter 3 describes the different TLS instruments utilized in this research, the research method, the intensity correction models, and the incidence angle and leaf internal structure effects on NDI. Chapter 4 describes a dry-down experiment conducted in a laboratory setting using four small trees from two different species to investigate the ability of NDI to estimate EWT at leaf and canopy level in a controlled environment. Chapter 5 describes the main data collection campaign conducted in a mixed-species deciduous forest plot, aiming at estimating EWT in 3D in a real forest environment, and addressing the issues associated with the process. Chapter 6 describes two additional data sets, a willow crop plot and a mixed-species urban tree plot, with the first data set aiming at testing the transferability of the presented method to a different site, and the second focusing mainly on using TLS data to detect temporal changes in EWT. Chapter 7 describes methods to utilize the 3D EWT estimates in DART, aiming at studying the effects of EWT vertical heterogeneity, woody materials, and understory effects on forest plot reflectance. Finally, Chapter 8 presents a general discussion and conclusion, and highlights the key findings of the research.

Chapter 2. Remote sensing of leaf equivalent water thickness

2.1 Introduction

This chapter reviews previous literature related to estimating EWT from optical RS data, using vegetation indices and RTMs. Also, factors that affect the accuracy of the EWT estimation from optical RS data are discussed, including the effects of the canopy biochemical and biophysical traits vertical heterogeneity on canopy reflectance. Furthermore, the few previous studies that have looked into the use of TLS in estimating EWT and other vegetation biochemical traits are examined.

2.2 Measuring EWT

EWT can be measured on a small scale using *in-situ* approaches: destructive methods and field spectroscopy. In destructive methods, leaf samples are collected and their Fresh Weight (FW), Dry Weight (DW), and Surface Area (SA) are measured. EWT can then be expressed as follows (Danson *et al.*, 1992):

$$EWT\ (g\ cm^{-2}) = \frac{FW\ -\ DW}{SA} \tag{2.1}$$

Field spectroscopy, using portable spectroradiometers, measures leaf reflectance and transmittance and links them to leaf biochemical traits, such as EWT (Fourty and Baret, 1998). This is based on the interaction of radiation with leaves being dependant on the biochemical and biophysical characteristics of leaves (Jacquemoud and Baret, 1990) (Figure 2-1). Leaf spectra in the visible region of the electromagnetic spectrum (350 – 700 nm), characterized by low reflectance and transmittance, is mainly dominated by the influence of leaf pigments, including carotenoids, chlorophyll, and brown pigments (Gausman, 1977; Jacquemoud and Baret, 1990). Leaf internal structure dominates the spectra in the NIR region (700 – 1300 nm), where leaf spectral response is characterized by high reflectance and transmittance (Gausman, 1977). In the SWIR region (1300 – 2500 nm), leaf water content is the main parameter that influences the leaf spectral response (Tucker, 1980).

Measuring EWT using *in-situ* approaches is known to be time and effort consuming, in addition to being impractical for large areas (Peñuelas *et al.*, 1993; Pu *et al.*, 2003; Dash *et al.*, 2017). An alternative approach to determine leaf EWT indirectly is by measuring leaf temperature, assuming that the difference between air and leaf surface temperatures is caused by transpiration, and thus can be linked to leaf water content (Chuvieco *et al.*, 1999; Qi *et al.*,

2005). However, using such an approach at the canopy level has limitations, as canopy temperature is not only affected by transpiration, but also by various metrological and environmental conditions, such as wind speed, air temperature, and humidity (Leinonen *et al.*, 2006; Zhao *et al.*, 2016). As a result of the limitations of the aforementioned approaches, methods utilizing optical RS multispectral and hyperspectral data, airborne and spaceborne, have been widely adopted in EWT estimation. Such methods are more efficient, cost-effective, non-destructive, and can provide estimates of canopy EWT at a landscape level (Colombo *et al.*, 2008; Clevers *et al.*, 2010; Wangab *et al.*, 2015; Dash *et al.*, 2017). It is worth mentioning that radar remote sensing (wavelengths between 0.1 and 100 cm in the electromagnetic spectrum) can also be used as a non-destructive approach to estimate vegetation moisture content by measuring the leaf dielectric constant (leaf permittivity), which is directly proportional to its moisture content (Moghaddam and Saatchi, 1999). However, this is outside the scope of this research.

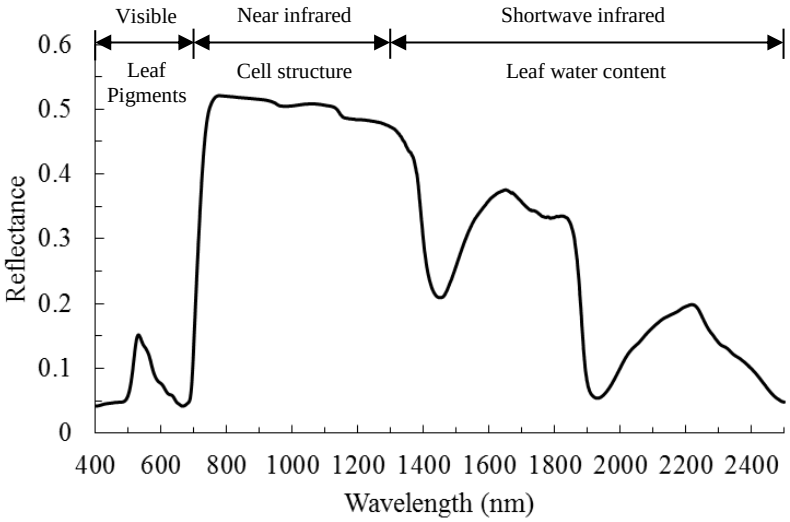

Figure 2-1. Typical leaf spectra in the visible, NIR, and SWIR regions of the electromagnetic spectrum.

2.3 Estimating EWT from optical RS data

Optical RS sensors have a number of wavelength bands that record reflected energy in specific sections in the electromagnetic spectrum, between 350 to 2500 nm, covering visible, NIR, and SWIR regions. Multispectral sensors usually have three to 10 spectral bands, while hyperspectral sensors can have dozens to hundreds of wavelength bands (Thenkabail *et al.*, 2015). Satellite sensors can provide EWT estimates at a landscape level and are very useful for producing time series of comparable data (Foley *et al.*, 1998). In addition, free access is

available to data from a number of the earth observation satellite sensors, such as Landsat, MODIS (Moderate-Resolution Imaging Spectroradiometer), Hyperion and Sentinel-2, reducing the cost needed for continuous monitoring of vegetation health. Figure 2-2 shows a time series of the change in CWC for natural vegetated areas in the USA generated from MODIS data.

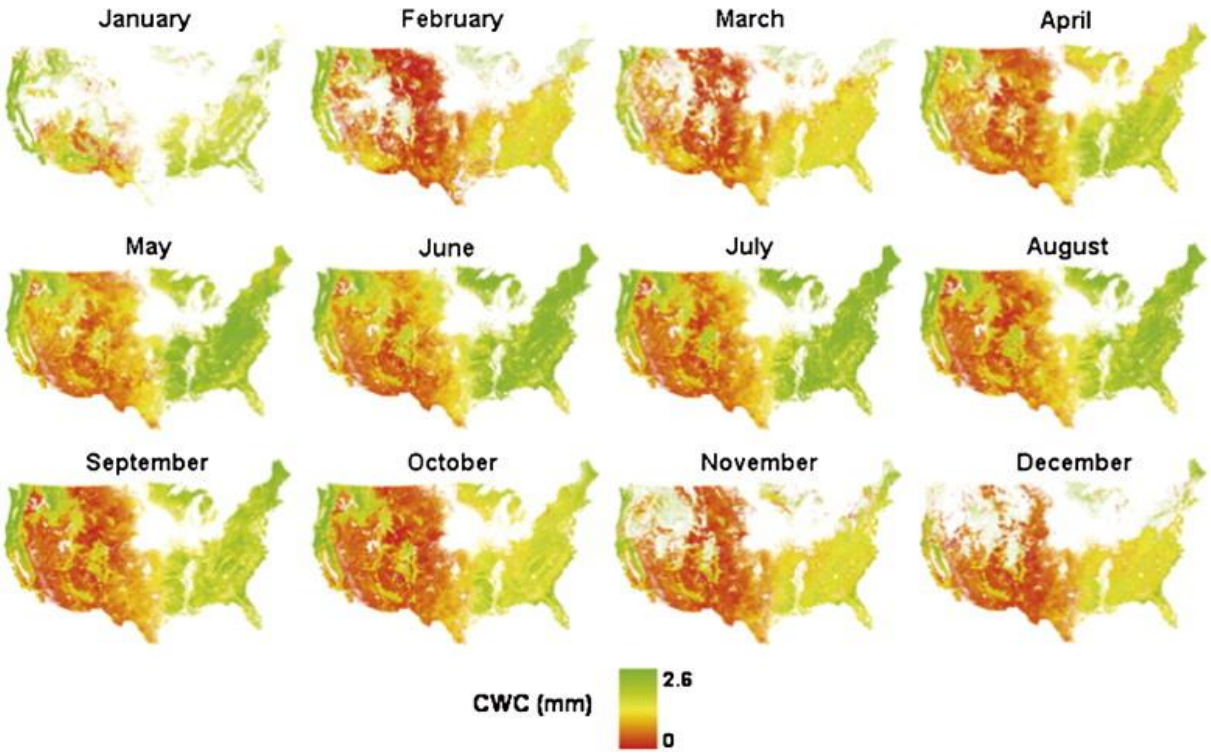

Figure 2-2. Multi-temporal change in CWC for 2005 for natural vegetated areas in the USA generated from MODIS data. Figure was adapted from Trombetti *et al.* (2008).

Similar to field spectroscopy approaches, estimating EWT from optical RS data is primarily based on the interaction of radiation with foliage in the SWIR wavelengths, being dominated by absorption by water, where reflected energy is negatively related to leaf water content (Knipling, 1970; Tucker, 1980; Faurtyot and Baret, 1997; Datt, 1999; Zarco-Tejada *et al.*, 2003; Féret *et al.*, 2018). Figure 2-3 shows how the change in EWT mainly affects the leaf spectra in the SWIR region, while having less effect on the NIR and no effect on the visible wavelengths. However, SWIR reflectance alone is insufficient to accurately retrieve EWT, as leaf internal structure and LMA also affect the SWIR reflectance (Ceccato *et al.*, 2001) (See Section 3.6 for more about the leaf internal structure effects). Combining NIR and SWIR reflectance in vegetation indices can minimize the leaf internal structure effects and thus lead to a more accurate estimation of EWT (Hunt and Rock, 1989; Ceccato *et al.*, 2001; Ceccato *et al.*, 2002).

In addition to vegetation indices, EWT can be estimated using inversion of physical RTMs (Serrano *et al.*, 2000; Yebra *et al.*, 2013; Mirzaie *et al.*, 2014).

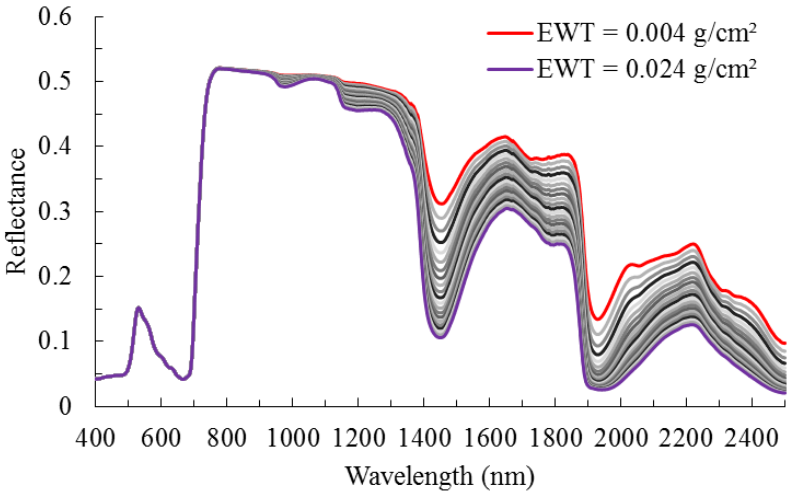

Figure 2-3. The effects of changing EWT on leaf spectra. Water absorption bands can be seen, centred around 970, 1200, 1470, 1940, and 2500 nm.

2.3.1 Vegetation indices

Vegetation indices link the reflectance measured by the sensor in two or more spectral bands (wavelengths) to a specific vegetation biochemical trait, such as EWT, using different types of regression analysis (Bannari *et al.*, 1995; Jones and Vaughan, 2010). Table 2-1 shows the widely used vegetation moisture content indices.

Table 2-1. The widely used vegetation moisture content estimation indices.

Index	Formula	Reference
Normalised Difference Vegetation Index (NDVI)	$NDVI = (P_{858} - P_{648}) / (P_{858} + P_{648})$	(Rouse Jr *et al.*, 1974)
Normalized Difference Infrared Index (NDII)	$NDII = (P_{820} - P_{1650}) / (P_{820} + P_{1650})$	(Hardisky *et al.*, 1983)
Normalised Difference Water Index (NDWI)	$NDWI = (P_{860} - P_{1240}) / (P_{860} + P_{1240})$	(Gao, 1996)
Water Index (WI)	$WI = (P_{900}) / (P_{970})$	(Peñuelas *et al.*, 1993)
Moisture Stress Index (MSI)	$MSI = (P_{1600}) / (P_{820})$	(Hunt and Rock, 1989)

The Normalized Difference Vegetation Index (NDVI) (Rouse Jr *et al.*, 1974), derived from the reflectance in NIR and red wavelengths, mainly measures the vegetation greenness and

chlorophyll content, as red is a strong chlorophyll absorption region (Rouse Jr *et al.*, 1974; Tucker, 1979; Gao, 1996; Pettorelli *et al.*, 2005). Based on the assumption that the change in chlorophyll content is proportional to the leaf rate of drying and the change in leaf moisture content (Paltridge and Barber, 1988; Illera *et al.*, 1996), NDVI has been linked to vegetation water status metrics, including FMC, EWT, and VWC (Peñuelas *et al.*, 1994; Illera *et al.*, 1996; Sims and Gamon, 2003; Jackson, 2004; Hunt *et al.*, 2017). However, this assumption cannot be generalized to all species, limiting the use of NDVI in measuring vegetation moisture content (Ceccato *et al.*, 2001; Sims and Gamon, 2003; Chen *et al.*, 2005). Combining NDVI with leaf surface temperature measurements, derived from thermal imagery, was reported to lead to a more accurate estimation of leaf moisture content than using NDVI alone (Alonso *et al.*, 1996; Chuvieco *et al.*, 1999; Chuvieco *et al.*, 2004b).

Hardisky *et al.* (1983) introduced the Normalized Difference Infrared Index (NDII), which is a variation of NDVI that utilized SWIR reflectance instead of red, aiming at EWT retrieval from Landsat data. Gao (1996) introduced a similar index, the Normalized Difference Water Index (NDWI), which used a SWIR band centred at 1240 nm instead of 1650 nm as in NDII, as it has atmospheric transmittance similar to the NIR band used in the index. Both indices have been reported to be highly correlated to EWT (Maki *et al.*, 2004; Cheng *et al.*, 2008b; Colombo *et al.*, 2008; De Jong *et al.*, 2014; Yi *et al.*, 2014; Hunt Jr *et al.*, 2016), and numerous variations have been developed using different band combinations, e.g., (Ceccato *et al.*, 2002; Fensholt and Sandholt, 2003; Van Niel *et al.*, 2003; Chen *et al.*, 2005; Rodríguez-Pérez *et al.*, 2007). Hunt and Rock (1989) introduced the Moisture Stress Index (MSI), a simple ratio of reflectance at 1600 nm and 820 nm, while Peñuelas *et al.* (1993) proposed the Water Index (WI), a simple ratio of reflectance at 900 nm and 970 nm wavelengths. Both indices have also been successfully used to retrieve EWT (Colombo *et al.*, 2008; De Jong *et al.*, 2014; Yi *et al.*, 2014; Liu *et al.*, 2016; Neto *et al.*, 2016).

Vegetation indices can easily be parameterized and applied, thus have been widely utilized in estimating EWT at leaf and canopy levels. Ceccato *et al.* (2001) used the data of the Leaf Optical Properties Experiment 1993 (LOPEX93) (Hosgood *et al.*, 1995), in which leaf samples from 50 species were collected in the area of Ispra, Italy, and their spectra and water content, in addition to other biochemical traits, were measured, to study the relationship between MSI and EWT, reporting high correlation ($R^2 = 0.92$). Rodríguez-Pérez *et al.* (2007) reported a high correlation ($R^2 > 0.91$) between WI, calculated from *in-situ* spectroradiometer data, and EWT of grapevines in commercial vineyards. De Jong *et al.* (2014) investigated the possibility of

estimating EWT for semi-natural vegetation and agricultural crops, including vineyards and pasture, in the Peyne catchment in Mediterranean southern France, using WI and NDWI derived from field spectroradiometer data. Good correlation was reported between EWT and the tested vegetation indices ($R^2 > 0.7$). Yi *et al.* (2014) reported high correlation between EWT and NDII, NDWI, and WI ($R^2 > 0.9$) in cotton plants during the growing season. Neto *et al.* (2016) studied the relationship between WI and EWT of sunflower plants during a controlled dry-down experiment for a duration of 12 days, reporting very high correlation ($R^2 > 0.94$). Liu *et al.* (2016) used destructive sampling and field spectroradiometer data to examine the relationship between NDWI, NDII, WI, MSI, and EWT of winter wheat during the growing season, reporting high correlation for all indices ($R^2 > 0.8$). Hunt Jr *et al.* (2016) tested different WorldView-3 NIR and SWIR band combinations and reported that the NDWI of 832 nm and 2165 nm wavelengths was highly correlated to EWT of leaf samples from various species. Zhang *et al.* (2019) used the data of LOPEX93 to modify NDWI, and introduced a new vegetation index constructed with 1725 and 2200 nm wavelengths, reporting that it was more correlated to EWT than the original NDWI.

At the landscape level, Cheng *et al.* (2008b) used NDVI, NDWI, and NDII to retrieve canopy EWT in sixteen plots of seven vegetation communities in south-eastern Arizona (grasslands, shrublands, riparian grasslands, riparian cottonwood, riparian mesquite, oak woodlands, and agriculture) from MODIS data. Due to the large pixel size of MODIS imagery (500 m × 500 m), it was not possible to directly link the data to the EWT measured from leaf sampling in the sixteen plots (40 m × 40 m). Thus, AVIRIS (Airborne Visible/Infrared Imaging Spectrometer) data (20 m spatial resolution) was first linked to the ground truth data and EWT maps were generated and validated with high accuracy ($R^2 = 0.9$). For this, the leaf samples had to be collected from canopy top layers. The AVIRIS EWT map was then degraded to MODIS 500 m spatial resolution and used to retrieve and validate EWT from MODIS data. R^2 ranged between 0.45 and 0.8 (R^2 between 0.6 and 0.87 in the woodland plots). Colombo *et al.* (2008) estimated EWT in 12 poplar plantation stands located on the floodplain of the Ticino River in Northern Italy using numerous vegetation indices, including NDWI, NDII, and MSI, derived from MIVIS (airborne Multispectral Infrared and Visible Imaging Spectrometer) data. Leaf sampling was conducted on three trees from each stand, with the leaf samples being collected from the upper canopy, and the total number of leaf samples being 144 leaves. The relative error in the canopy EWT estimates was 20%.

Yilmaz *et al.* (2008) used NDII derived from Landsat-5 data to estimate canopy EWT in sites of corn, soybean, and deciduous woodlands in Iowa, USA, reporting high correlation between NDII and EWT ($R^2 = 0.85$), and using the EWT estimates to retrieve the VWC. Landsat spatial resolution allowed direct validation of the estimated EWT and VWC using destructive sampling in 20 m × 20 m plots. However, the challenge of collecting leaf samples from the canopy top in the woodland plots was highlighted. Zhao *et al.* (2016) used NDWI derived from MODIS data to estimate canopy EWT in four 1 km^2 winter wheat plots in Ningxia Plain, China. To build the estimation model and validate the estimations, leaf samples were collected from upper canopy layers from five locations in each 1 km^2 plot, with each location consisting of ten trees. The total number of leaf samples from each location was 100 leaves. EWT was measured and the average EWT in each sampling location was considered the average of EWT of the leaf samples collected. Good agreement was reported between estimated and measured EWT ($R^2 = 0.7$). This study highlighted that using destructive sampling to fit EWT estimation models, and to validate the estimation, for MODIS data can be very challenging, as it would require collecting a large number of leaf samples from sampling plots, which have to be large enough to match the MODIS pixel size.

Vegetation indices are sensor specific and dependant on site and sampling conditions, meaning that an index developed using a specific data set may not be transferable to other sites or applicable to different species (Tucker, 1980; Riaño *et al.*, 2005; Yebra *et al.*, 2008; Chuvieco *et al.*, 2009; Al-Moustafa *et al.*, 2012; Yebra *et al.*, 2013). At the landscape level, the performance of vegetation indices is also influenced by canopy structure, understory vegetation, soil moisture content, non-photosynthetic components, atmospheric conditions, solar illumination and sensor viewing angles (Baret and Guyot, 1991; Serrano *et al.*, 2000; Zarco-Tejada *et al.*, 2003; Eitel *et al.*, 2010; Ali *et al.*, 2016). Another limitation is that the indices not only depend on the vegetation moisture content but also on other vegetation parameters (Serrano *et al.*, 2000). Zarco-Tejada *et al.* (2003) reported that NDWI was influenced, to an extent, by leaf thickness, LMA and canopy LAI. Yi *et al.* (2014) and Zhang and Zhou (2015) also reported that NDII, NDWI, and WI were affected by the canopy LAI. De Jong *et al.* (2014) further highlighted that the accuracy of EWT estimation using vegetation indices was heavily affected by canopy LAI.

Furthermore, at the landscape level, it is possible to directly link the vegetation indices calculated from airborne and spaceborne optical RS data with high spatial resolution to canopy EWT measured from leaf sampling conducted in sampling plots. However, leaves have to be

collected from the upper canopy layers, which can be challenging in forest plots. For spaceborne sensors with low spatial resolution (large pixel size), such as MODIS, airborne imagery and/or extensive destructive sampling is needed to scale the EWT estimates from plot level to landscape level, and vegetation indices derived from the satellite imagery cannot be directly linked to ground truth data.

2.3.2 Radiative transfer models

RTMs simulate vegetation spectra using the radiative transfer equation (Ross, 1981; Ross, 2012) and take the characteristics of leaf biophysical and biochemical traits, canopy structure, and background soil into consideration. By inverting these models, EWT and other canopy characteristics can be estimated (Jacquemoud *et al.*, 1995; Ustin *et al.*, 1998; Ceccato *et al.*, 2002; Zarco-Tejada *et al.*, 2003; Kötz *et al.*, 2004; Mendiguren *et al.*, 2015). Another advantage of RTMs over vegetation indices is that they are not site-dependant as they are based on a physical principle, which means they can be applied at different locations and obtain good results, as long as they accurately represent the vegetation canopy (Yebra *et al.*, 2008; Yebra *et al.*, 2013; Quan *et al.*, 2017).

Among the existing RTMs, the SAIL (Verhoef, 1984), PROSPECT (Jacquemoud and Baret, 1990; Jacquemoud *et al.*, 2009), LIBERTY (Leaf Incorporating Biochemistry Exhibiting Reflectance and Transmittance Yields) (Dawson *et al.*, 1998), PROSAIL (Baret *et al.*, 1992), and GeoSail (Huemmrich, 2001) models are the most popular in retrieving biochemical and biophysical characteristics of vegetation from optical RS data (Yebra *et al.*, 2008; Zhang and Zhou, 2015; Quan *et al.*, 2017). PROSPECT simulates leaf optical properties for broadleaf species at leaf level by parametrizing a number of leaf traits, including EWT, LMA, and chlorophyll content, and modelling a leaf as a number of layers (plates), based on the plate model introduced by Allen *et al.* (1969) (Jacquemoud and Baret, 1990). For more about parameterizing PROSPECT, see Section 3.6. LIBERTY, on the other hand, was designed for conifer needles and simulates needles' spectra by modelling them as spherical cells separated by airspace (Dawson *et al.*, 1998). SAIL approximates the canopy as a turbid medium (a set of infinitely small flat surfaces), assuming a homogenous and continuous canopy, then simulates the canopy reflectance using canopy structural parameters, including LAI, leaf angle distribution, and relative leaf size (Verhoef, 1984). PROSAIL links PROSPECT and SAIL to describe the canopy reflectance as a function of leaf biochemistry and canopy structure parameters (Baret *et al.*, 1992). GeoSAIL combines SAIL with the Jasinski geometric model (Jasinski and Eagleson, 1989), defining a vegetation plot as a number of trees modelled as

cylinders or cones distributed over a plane. GeoSAIL splits any scene into three components: illuminated canopy, shadowed background, and illuminated background, aiming at simulating canopy reflectance for discontinuous canopies (Huemmrich, 2001).

RTMs can be used to select suitable wavelengths for vegetation biochemistry estimation and for developing and testing vegetation indices. For instance, Faurtyot and Baret (1997) used the PROSPECT and SAIL models to determine which wavelengths were suitable for estimating EWT, LMA, and LAI at canopy level from satellite data (900, 1100, 1190, 2040, and 2260 nm for canopy EWT). Ceccato *et al.* (2002) used PROSPECT simulations to develop the Global Vegetation Moisture Index (GVMI), a vegetation index optimized specifically to retrieve EWT at canopy level from the SPOT-VEGETATION sensor (SPOT: Satellite for observation of Earth, *Satellite Pour l'Observation de la Terre*). Sun *et al.* (2019) used PROSPECT simulations and the LOPEX93 dataset to determine the suitable wavelengths to be utilized in multispectral Lidar systems for EWT and chlorophyll content estimation, recommending the use of 680 nm and 716 nm wavelengths for chlorophyll estimation and 1882 nm and 1920 nm wavelengths for EWT.

Furthermore, RTMs were widely adopted in estimating canopy EWT at the landscape level from optical RS data. Zarco-Tejada *et al.* (2003) found a high correlation ($R^2 > 0.7$) between EWT estimated from MODIS data, by inversion of the PROSPECT and SAIL models, and actual EWT measured by destructive sampling in ten study sites of chaparral vegetation in California, USA. The study also highlighted that NDWI was influenced by leaf LMA and canopy LAI, and that inversion of RTMs, utilizing all MODIS bands, can minimize such effects, making this method suitable for generating time series of canopy EWT, independent of seasonal changes of LAI. Riaño *et al.* (2005) used the LOPEX93 dataset and inversion of PROSPECT to estimate EWT and LMA, then to investigate the accuracy of estimating FMC from EWT and LMA at leaf level, validating the estimates using destructive sampling of three trees (gall oak, rosemary, and rock rose) in a laboratory experiment. EWT was estimated with high accuracy ($R^2 = 0.94$), while LMA was poorly estimated ($R^2 = 0.38$), which affected the accuracy of FMC estimation as a result ($R^2 = 0.33$). PROSPECT was then linked to the Lillesaeter infinitive reflectance canopy model (Lillesaeter, 1982) to estimate EWT and FMC at canopy level, reporting that canopy EWT can be retrieved more accurately than canopy FMC ($R^2 = 0.75$ and 0.62 respectively). This study further showed that inversion of RTMs can retrieve canopy EWT, insensitive to leaf and canopy structure effects. Colombo *et al.* (2008) estimated canopy EWT for 12 poplar plantation stands from MIVIS data by inversion of the PROSPECT and SAIL

models, validating the estimation using destructive sampling, and reporting a relative error of 27% in the estimation. This study highlighted that the successful estimation of canopy EWT at landscape level using inversion of RTM requires prior knowledge of the model variables to improve the performance of the model.

Trombetti *et al.* (2008) estimated canopy EWT in four sites in continental USA covering three major vegetation types: woodlands, shrublands, and grasslands, from MODIS data by inverting the PROSAIL model. Canopy EWT retrieved from AVIRIS data was used to calibrate the model and validate the estimates, and good correlation was reported between canopy EWT estimated from MODIS and AVIRIS data (R^2 ranging between 0.57 and 0.71). The canopy EWT estimated from MODIS was not validated directly using destructive sampling, as it was considered extremely difficult and costly to collect a sufficient number of leaf samples in a large number of sampling plots to directly scale the EWT measurements to 500 m MODIS pixels.

Jurdao *et al.* (2013) inverted PROSPECT and GeoSAIL models to estimate canopy FMC from canopy EWT using MODIS data in evergreen broadleaf, deciduous broadleaf, and coniferous woodlands in Eurosiberian (energy-limited environment) and Mediterranean (water-limited environment) regions in Spain. Leaf samples were collected from 19 sampling plots, 500 × 500 m to be representative of a MODIS pixel, and used in parametrizing the RTMs and in validating the FMC estimates. Relative RMSE was reported to be < 30 %. Once again, the challenge of collecting a sufficient number of leaf samples to represent EWT/FMC in large sampling plots that matched MODIS pixel size was highlighted, and a total of 154 field measurements, each consisting of 80 to 100 g of randomly-selected leaves, were used in this study. Also, it was reported that collecting leaf samples from the canopy top was not always possible, as not all trees were accessible.

Quan *et al.* (2017) showed that coupling different RTMs to invert Landsat 8 data to estimate FMC from EWT and LMA, by using PROSAIL to simulate understory spectra, and GeoSAIL to simulate canopy spectra, instead of using GeoSAIL alone, improved the accuracy of the estimation (R^2 = 0.86 and 0.74 respectively), in four study areas in Sichuan province, China. The study areas consisted of evergreen broadleaf, deciduous broadleaf, and coniferous forests. A total of 572 leaves samples were collected from the upper canopy in 41 plots, 40 m × 40 m to be as close as possible to the pixel size of Landsat 8 (30 m × 30 m). FMC and EWT were overestimated, and this was explained as a result of the number of leaf samples collected to

calibrate and validate the models being insufficient to represent all canopy properties in the samples plots. This further highlighted the challenges associated with scaling up field measurements to the landscape level. Zhu *et al.* (2019) inverted the INvertible FOrest Reflectance Model (INFORM) to estimate canopy EWT in the southern part of the Bavarian Forest National Park in Germany from airborne hyperspectral data, using canopy structural parameters derived from airborne LiDAR data (Riegl LMS-Q 680i sensor) to parametrize the model. Leaf samples were collected from the canopy top in 26 forest plots to calibrate and validate the model. It was reported that using LiDAR data to parametrize the model improved the canopy EWT estimation accuracy (R^2 = 0.87 and 0.82 respectively).

One downside of using RTMs is the ill-posed nature of model inversion, that is, different combinations of inputs can produce almost identical spectra (Combal *et al.*, 2003; Baret *et al.*, 2007; Yebra and Chuvieco, 2009; Li and Wang, 2011). Solutions to this issue include the use of *a priori* information about canopy characteristics to optimize the accuracy of RTMs inversion, using look-up table based approaches (Weiss *et al.*, 2000; Combal *et al.*, 2003; Darvishzadeh *et al.*, 2008) or artificial neural network approaches (Baret *et al.*, 1995; Atzberger, 2004). In addition, RTMs assume a homogenous canopy, using mean values of canopy biophysical and biochemical traits to parametrize the model, which can lead to errors in the simulated canopy reflectance in sites that exhibit large vertical and/or horizontal heterogeneity, such as forests (Kuusk, 2001; Wang and Li, 2013). To overcome this limitation, Kuusk (2001) developed a two-layer RTM that represents a vegetation plot as two different layers (a canopy layer and an understory layer), allowing biochemical and biophysical traits to be assigned to each layer separately, thus introducing some heterogeneity. However, the model did not account for the horizontal heterogeneity, or for the vertical heterogeneity within the canopy.

More complex 3D RTMs have been developed, such as the DART (Gastellu-Etchegorry *et al.*, 1996; Demarez and Gastellu-Etchegorry, 2000), SPRINT (Goel and Thompson, 2000), FLIM (Rosema *et al.*, 1992), and FLIGHT models (North, 1996), among others. 3D RTMs, despite being demanding in terms of computational time and the number of parameters that need to be accurately defined, allow 3D realistic representation of vegetation canopies and account for the horizontal and vertical heterogeneity in canopy structure. However, the models do not take the vertical heterogeneity in canopy biochemical traits in consideration.

Overall, estimating EWT from spaceborne and airborne optical RS data, despite its advantages over *in-situ* approaches, has some limitations. The temporal resolution (revisit time) of

spaceborne sensors may not be suitable for monitoring rapid changes in vegetation water status (e.g. 16 days for Landsat, and 10 days for Sentinel-2 with one satellite, five days with two satellites). Cloud coverage can also further reduce the temporal resolution, preventing usable data collection on overcast days, and creating gaps in time series (White *et al.*, 2014; Xue and Su, 2017). The spatial resolution can also be a limiting factor in some applications, such as precision agriculture and heterogeneous canopy areas where a single pixel may integrate spectral response of numerous species and land cover types with different characteristics (Eastman *et al.*, 2013). Using data from very high resolution commercial sensors such as WorldView-2 and WorldView-3 is not cost effective. On the other hand, optical and thermal sensors mounted on Unmanned Aerial Vehicles (UAVs) can acquire data at very high temporal and spatial resolutions, overcoming some of the limitations associated with spaceborne sensors (Honkavaara *et al.*, 2013; Ballesteros *et al.*, 2015). However, some limitations associated with UAVs include their limited coverage, short flying time, and payload and airspace law constraints (Berni *et al.*, 2009; Anderson and Gaston, 2013).

Estimating canopy EWT from optical RS data is also limited by the effects of canopy structure, especially canopy LAI, and to reduce such effects, canopy EWT at landscape level is considered the product of EWT and LAI. Calibrating and validating the EWT estimation models, whether vegetation indices or RTMs are used in the estimation, requires collecting a large number of leaf samples from the upper canopy layers in sampling plots that match the pixel size of the spaceborne sensor. This is a challenging process, as the canopy top layers are not always accessible, and the leaf samples collected from a sampling plot do not necessarily represent the actual EWT in the whole plot. MODIS data is very popular in vegetation water status monitoring because of the large coverage and high temporal resolution of MODIS. However, scaling up the EWT measurements retrieved from destructive sampling to the landscape level is even more challenging with MODIS data because of its large pixel size. The studies reviewed in Section 2.3 showed that there is a need for a fast, non-destructive EWT estimation method that can retrieve canopy EWT in large sampling plots and can be used in calibrating and validating the EWT estimation models from spaceborne optical RS data. TLS can serve as such a tool because of the high speed and long range of the commercially-available modern instruments, making them suitable for collecting data at plot level. Also, TLS can easily provide information about the canopy top layers, even if these layers are not accessible from the ground, and EWT in such layers is crucial for calibrating and validating the EWT estimation models. Furthermore, TLS can fill the gap in the time series of canopy EWT estimates derived from

satellite data, because TLS instruments are active sensors. In addition, TLS can provide information about the vertical heterogeneity in canopy structure and biochemistry, which is covered in Section 2.3.3.

2.3.3 Vertical heterogeneity in canopy biochemical traits

Leaves at different heights within a canopy contribute differently to the total canopy photosynthesis, resulting in vertical heterogeneity in canopy biophysical and biochemical traits, which can be linked to the canopy foliage-height profile (Aber, 1979; Ellsworth and Reich, 1993; Parker *et al.*, 2001; Weerasinghe *et al.*, 2014). Well-illuminated leaves in the canopy top, known as sun leaves, usually have a higher photosynthetic rate than shaded leaves in the canopy bottom, and plants tend to dedicate more nutrients and water to sun leaves to optimize photosynthesis (Hirose and Werger, 1987; Hikosaka, 2004; Coble *et al.*, 2016). The canopy vertical heterogeneity affects the light penetration and scattering within the canopy, and thus affects the canopy reflectance (Valentinuz and Tollenaar, 2004; Ciganda *et al.*, 2008; Tang *et al.*, 2012; Wang and Li, 2013; Liu *et al.*, 2015; He *et al.*, 2016; Gara *et al.*, 2018). Such vertical heterogeneity has been recognized and highlighted in a number of studies.

Keating and Wafula (1992) found that a maize canopy has bell-shaped vertical distribution of LAI, while for the same canopy type, Ciganda *et al.* (2008) reported that it also has bell-shaped vertical distribution of chlorophyll content and leaf nitrogen content. Valentinuz and Tollenaar (2004) reported that during senescence, which changes leaf internal structure (Jacquemoud and Baret, 1990), leaves in the top and bottom canopy were the first to senesce, while leaves in the middle canopy were the last. Koetz *et al.* (2008) reported that the vertical heterogeneity of CWC can play a role in wildfire propagation. Tang *et al.* (2012) showed that canopy LAI varies vertically, with LAI in the top of canopy being higher than that in the bottom of the canopy, in a tropical rain forest. Liu *et al.* (2015) analysed the vertical distribution of EWT in winter wheat and reported it to be a near bell-shaped curve with the highest values in the middle canopy layers.

Zhu *et al.* (2017) reported that EWT varied vertically in 20 small trees from five different species: *Schefflera arboricola compacta* (dwarf schefflera), *Ficus benjamina twilight* (weeping fig), *Ficus microcarpa* (Chinese banyan), *Ficus benjamina Danielle* (ficus), and *Zamioculcas zamiifolia* (Zanzibar gem), with EWT being higher in the top part of the canopy than the rest of the canopy. This was explained as a result of new leaves at the top of the canopy having higher water than older leaves (Mooney *et al.*, 1977). Arellano *et al.* (2017) showed that canopy

biochemical and biophysical traits, including chlorophyll, EWT, and leaf thickness, varied vertically within the canopy in three plots in the Amazon forest of Ecuador, with EWT and leaf thickness being higher in canopy top layers, and chlorophyll being higher in middle canopy layers. A possible explanation for the observations was the top layers of canopy receiving the majority of irradiance (Chazdon and Fetcher, 1984). Ma and Upadhyaya (2018) reported vertical heterogeneity in chlorophyll content and LMA in a tomato crop, showing that such heterogeneity affected leaf spectra at different canopy heights. Gara *et al.* (2018) reported that nitrogen, carbon, chlorophyll, EWT, and LMA were higher in the canopy top than in the canopy bottom in four small trees (*Camellia japonica*, *Ficus benjamina*, *Chamaedorea elegans*, and *Fatshedera lizei*).

Vegetation indices do not take into consideration the effects that vertical heterogeneity has on canopy reflectance, which can influence their EWT estimation accuracy (Liu *et al.*, 2015; Zhu *et al.*, 2017). RTMs assume that the canopy is vertically homogeneous in terms of the canopy biochemical and biophysical properties, including LAI, chlorophyll and EWT, using an average value to define each parameter in the model. The more complex 3D RTMs account for the vertical heterogeneity in the canopy structure, but do not consider the vertical heterogeneity in the biochemical characteristics, which can affect their canopy reflectance simulation accuracy (Wang and Li, 2013). Such heterogeneity cannot be measured using optical RS spaceborne and airborne data, as the reflectance measured by these sensors is dominated by the canopy top (Li *et al.*, 2014; Liu *et al.*, 2015). Destructive sampling and field spectroscopy can provide some information about the vertical distribution of canopy biochemical traits, by splitting the canopy into multiple layers, typically upper, middle, and bottom canopy, and taking measurements in each layer (Arellano *et al.*, 2017; Gara *et al.*, 2018). However, this is an impractical approach for large areas and also cannot provide detailed vertical profiles of canopy biochemical traits, which requires taking measurements in each canopy layer. TLS, being able to provide high-resolution 3D information, can be a useful tool to measure such heterogeneity.

2.4 Terrestrial laser scanning

TLS instruments have the ability to determine the relative location of points in the surrounding environment quickly and accurately. They record the backscattered laser beam energy and measure the 3D coordinates of points on surfaces that reflected the laser signal. The 3D coordinates are stored in dense point clouds that represent the 3D structure of the scanned objects. In addition to the 3D coordinates of surrounding points, a point cloud includes an intensity image in which the magnitude of the recorded backscattered energy for each point is

recorded. Available TLS instruments can be divided into three categories: time-of-flight discrete pulse systems, continuous wave phase-shift systems, and time-of-flight full waveform systems.

A time-of-flight discrete pulse scanner measures the time a pulse of light needs to travel to a surface, interact with it and reflect back to the scanner (Cote *et al.*, 2009). The instrument then calculates the range to the target as follows:

$$Range\ (m) = \frac{t\ \times C}{2} \tag{2.2}$$

Where *t* is the time of flight and *C* is the speed of light.

The range and the angle at which the light pulse was emitted are used to determine the 3D coordinates of that specific point on the target's surface in relation to the LiDAR scanner position. Modern time-of-flight scanners have high accuracy and also long range. A phase-shift scanner emits a sinusoidal laser pulse and determines the time of travel by calculating the phase-shift between the emitted and returned pulse (Balduzzi *et al.*, 2010). The instrument uses the calculated time to measure the range to the target and determine the 3D coordinates of that specific point on the target's surface. Phase-shift scanners have a very high rate of points measured per second. However, this is at the expense of the instrument's range which is relatively lower than that of discrete pulse time-of-flight scanners. A time-of-flight full waveform scanner emits laser pulses, then records the full time trace of the energy of the returned pulses, known as the full waveform (Lovell *et al.*, 2011). The instrument then uses a similar approach as the time-of-flight discrete return scanners to measure the range to the points in the surrounding environment after post-processing the full waveforms. However, a major difference from the discrete pulse scanners is that full waveform scanners record the full intensity trace of the backscattered laser pulses. This leads to more information being available from the point clouds, which can be useful in analysing very complicated scan scenes.

TLS instruments have been widely used for high resolution measurements of vegetation canopies during the last two decades, especially in forests, allowing a comprehensive description of forest biophysical characteristics (Henning and Radtke, 2006; Takeda *et al.*, 2008; Moskal and Zheng, 2011; Ramirez *et al.*, 2013; Newnham *et al.*, 2015; Disney, 2019). Forest biophysical attributes obtained using TLS data include, but are not limited to, tree height (Hilker *et al.*, 2010; Olofsson *et al.*, 2014; Laurin *et al.*, 2019; Tian *et al.*, 2019), stem diameter (Lovell *et al.*, 2011; Pitkänen *et al.*, 2019), above ground biomass (Yu *et al.*, 2013; Kaasalainen

et al., 2014; Srinivasan *et al.*, 2014; Calders *et al.*, 2015; Greaves *et al.*, 2015), leaf area density (Takeda *et al.*, 2008), leaf area distribution (Béland *et al.*, 2011), directional gap fraction (Danson *et al.*, 2007; Ramirez *et al.*, 2013; Chen and Wang, 2016; Zheng *et al.*, 2016), and canopy LAI (Moorthy *et al.*, 2008; Antonarakis *et al.*, 2010; Zheng *et al.*, 2013; Vincent *et al.*, 2015; Meng *et al.*, 2019). Further applications include leaf – wood separation (Béland *et al.*, 2014; Douglas *et al.*, 2015; Ma *et al.*, 2016; Zhu *et al.*, 2018), tree 3D modelling (Pfeifer *et al.*, 2004; Côté *et al.*, 2009; Eysn *et al.*, 2013; Hackenberg *et al.*, 2015; Raumonen *et al.*, 2015), and realistic 3D forest plot reconstruction (Calders *et al.*, 2016; Calders *et al.*, 2018). The former two applications allowed the realistic representation of trees in 3D RTMs (Widlowski *et al.*, 2015), which can improve the accuracy of their simulation of canopy reflectance (Zhu *et al.*, 2019). On the other hand, less attention has been paid to utilising intensity data recorded by the TLS instruments to estimate important vegetation biochemical characteristics, such as EWT, at leaf and canopy level.

2.4.1 TLS intensity data

TLS instruments not only provide information on canopy structure, but also record intensity data that is a function of the reflectance of the scanned object (Penasa *et al.*, 2014). Thus, by using a shortwave infrared wavelength instrument, the recorded intensity can theoretically be used to provide 3D estimates of EWT at leaf and canopy level (Gaulton *et al.*, 2013; Zhu *et al.*, 2017). However, the scanned object reflectance is not the only parameter that influences the TLS recorded intensity data. Numerous other factors influence the intensity, including instrumental effects, and the scan geometry (Krooks *et al.*, 2013; Kashani *et al.*, 2015). Thus, radiometric correction is needed prior to linking the intensity to EWT. The instrumental effects refer to the instrument internal processing that alters the intensity values to enhance the visualization of the point cloud and/or improve the range measurement using algorithms that are unknown to the end-user (Danson *et al.*, 2014). The scan geometry effects include the range and the incidence angle effects. The laser equation (Höfle and Pfeifer, 2007), derived from the radar equation (Jelalian, 1992), summarizes the aforementioned factors as follows:

$$P_r = \frac{P_t D^2 \rho \cos(\theta)}{4 R^2} \eta_{sys} \eta_{atm} \tag{2.3}$$

Where P_r is the received backscattered signal, P_t is the emitted signal, D is the receiver aperture diameter, ρ is the target reflectance coefficient, θ is the incidence angle, η_{sys} corresponds to the instrumental effects, η_{atm} corresponds to the atmospheric effects, and R is the range to target.

Parameters P_t, D and η_{sys}, all being sensor-related, and ρ, being a characteristic of the scanned target, are theoretically constant during a single scan (Höfle and Pfeifer, 2007; Jutzi and Gross, 2009), while η_{atm} can be neglected for close-range TLS (Kaasalainen *et al.*, 2011; Fang *et al.*, 2015). Thus, in a single scan, the scan geometry remains the major element affecting the TLS recorded intensity (Krooks et al., 2013).

The range effect refers to how the distance between the instrument and the scanned object affects the backscattered laser pulse magnitude, which is then recorded as intensity data (Kaasalainen *et al.*, 2011; Tan *et al.*, 2016). Typically, the farther the laser pulse travels, the more energy it loses, and the lower the recorded backscattered intensity will be, in comparison to similar objects nearer to the instrument (Kashani *et al.*, 2015). According to the laser equation, the recorded intensity is inversely proportional to the square of the measured range. However, numerous authors reported that this relationship is only theoretical and that the actual relationship between intensity and range must be studied separately for each instrument. Kaasalainen *et al.* (2011) showed that the intensity-range relationship for the FARO LS880 and Leica HDS 6100 scanners only follow the $1/R^2$ relationship after 10 m. Blaskow and Schneider (2014) reported high deviation in the intensity-range relationship from the $1/R^2$ prediction for the Riegl LMS Z420i scanner, while the Z+F Imager 5006i scanner follows the $1/R^2$ relationship only after 5 m. Fang *et al.* (2015) reported the same observation for the Z+F Imager 5006i scanner. Tan *et al.* (2016) found a deviation from the laser equation at both near and far ranges for the Faro Focus^{3D} 120 scanner. The deviation in the intensity-range relationship from the laser equation was explained to be a result of the instruments being equipped with a near-distance intensity reducer to protect the optics and/or far-distance amplifiers to enhance the range measurements for far targets (Jutzi and Gross, 2009; Kaasalainen *et al.*, 2011; Blaskow and Schneider, 2014; Fang *et al.*, 2015; Tan *et al.*, 2016; Calders *et al.*, 2017). TLS instruments accurately record the coordinates of each point in the point cloud, which can be used to calculate the range of each point to be used in the radiometric calibration. Typically, external reference targets with known reflectance can be used to develop the intensity correction models (Pfeifer *et al.*, 2008; Kaasalainen *et al.*, 2009; Kaasalainen *et al.*, 2011; Blaskow and Schneider, 2014; Kashani *et al.*, 2015).

The incidence angle of the laser beam is the angle between the incident laser beam and the object's surface normal (Kaasalainen *et al.*, 2016). According to the laser equation, the TLS recorded backscattered intensity is directly proportional to the cosine of the incidence angle for a Lambertian surface (Kaasalainen *et al.*, 2016). The effect of the incidence angle primarily

depends on the target surface characteristics (Tan and Cheng, 2016). However, Lambertian cosine law (Equation (2.4)) can often sufficiently describe the incidence angle effect, whether the scanned target can be approximated as a Lambertian surface or not (Kaasalainen *et al.*, 2011). This does not apply for surfaces with high irregularity (Krooks *et al.*, 2013).

$$I_{reflected} = I_{incident} \cos\theta \tag{2.4}$$

Where $I_{reflected}$ is the intensity reflected from the target's surface and $I_{incident}$ is the intensity incident on the target's surface.

Hancock *et al.* (2017) and Kaasalainen *et al.* (2018) showed the effects that incidence angle has on TLS recorded backscattered intensity of leaf samples, which can cause a significant bias in TLS estimation of leaf biochemical traits if no radiometric corrections are applied. To correct for such effects using the Lambertian law, the incidence angle of the laser beam for each point in the point cloud needs to be determined first. TLS instruments do not record the incidence angles automatically and the incidence angle needs to be determined by the end-user. This is achievable by fitting surface planes to the points and calculating the surface normal vector for each point, then calculating the incidence angle using the normal vector and the point vector between the point and the scanner. However, in a complex vegetation canopy, it is not trivial to use such an approach to calculate the incidence angle for each leaf/needle in the point cloud (Hancock *et al.*, 2017), making it a challenge to accurately calibrate for the incidence angle effect with a single wavelength (Béland *et al.*, 2014). The approach is time and computational resource consuming, plus, the accuracy of the normal vector estimation can be of concern, especially at greater ranges where there might be insufficient points per leaf to fit a plane. Alternatively, the Normalized Difference Index (NDI) of two laser wavelengths, typically NIR and SWIR (Equation (2.5)), in the same context of NDWI and NDII used in optical RS data, can be used to minimize the incidence angle effect (Hancock *et al.*, 2012; Hancock *et al.*, 2017). Here the two wavelengths must be similarly affected by the incidence angle (Eitel *et al.*, 2014b; Hancock *et al.*, 2017), or else radiometric correction will still be needed (Zhu *et al.*, 2015).

$$NDI = \frac{\rho_{NIR} - \rho_{SWIR}}{\rho_{NIR} + \rho_{SWIR}} \tag{2.5}$$

Where ρ_{NIR} is the reflectance at a NIR wavelength, and ρ_{SWIR} is the reflectance at a SWIR wavelength.

TLS instruments typically operate at a single wavelength, and despite successful attempts to calibrate the intensity data to apparent reflectance for various TLS instruments (Höfle and Pfeifer, 2007; Jutzi and Gross, 2009; Kaasalainen *et al.*, 2011; Krooks *et al.*, 2013; Blaskow and Schneider, 2014; Anttila *et al.*, 2016; Tan and Cheng, 2016; Zhu *et al.*, 2017; Tan *et al.*, 2018; Bolkas, 2019), using a single wavelength TLS instrument to estimate EWT at the canopy level remains a challenge as a result of the incidence angle effects. Another factor that complicates the use of single wavelength TLS in EWT estimation is leaf internal structure effects. Leaf thickness and LMA influence the shortwave infrared reflectance, and their variation within canopy and between different trees in a vegetation plot can complicate the retrieval of EWT (Ceccato *et al.*, 2001). Also, the partial canopy hits (edge returns), which occur when a leaf does not fully occupy the laser beam footprint, can affect the accuracy of the TLS estimation of leaf biochemical characteristics (Eitel *et al.*, 2010). Dual- and multi-wavelength TLS systems, also known as multispectral and hyperspectral LiDAR systems, have recently been developed in an attempt to overcome the limitations of single-wavelength TLS (Danson *et al.*, 2014).

2.4.2 Multispectral and hyperspectral LiDAR

Multispectral and hyperspectral LiDAR systems, typically non-commercial full-waveform instruments, have been developed specifically for use in vegetation applications. As the instruments record the full-waveform of the backscattered intensity, and thus can detect multiple objects on the laser beam path, they are capable of providing more detailed information about canopy structure, especially the canopy interior, than the commercial single-wavelength pulsed TLS systems (Danson *et al.*, 2014; Douglas *et al.*, 2015). Furthermore, as they operate at two or more wavelengths, spectral indices can be derived from the intensity data, similar to vegetation indices derived from multispectral and hyperspectral optical RS data. As discussed in Section 2.4.1, such spectral indices can minimize the incidence angle and leaf internal structure effects. This allows utilizing the data to measure EWT and other vegetation biochemical traits (Gaulton *et al.*, 2013), and also allows better leaf – wood separation results than using a single wavelength (Danson *et al.*, 2018), which can lead to more accurate estimation of forest above ground biomass.

A number of multispectral and hyperspectral LiDAR instruments have been developed in the last decade, mainly for scientific research purposes. Chen *et al.* (2010) developed a prototype dual-wavelength instrument, operating at 600 nm and 800 nm wavelengths, with the purpose of deriving NDVI from the TLS data to distinguish between vegetation and non-living objects.

Wei *et al.* (2012) developed a four-wavelength instrument (555 nm, 670 nm, 700 nm, and 780 nm) to measure vegetation nitrogen and chlorophyll content. Hakala *et al.* (2012) developed a hyperspectral TLS system that employs eight wavelengths between 500 nm and 1100 nm, optimized for measuring vegetation biochemical traits. The study showed the potential of deriving spectral indices from the TLS instrument data, including the modified chlorophyll absorption ratio index, NDVI, and WI. Eitel *et al.* (2014b) introduced a dual-wavelength TLS system that employed green (532 nm) and red (658 nm) wavelengths for leaf nitrogen content estimation. Li *et al.* (2014) designed a hyperspectral LiDAR system with 32 wavelength bands covering the range between 409 nm and 914 nm to estimate leaf chlorophyll, nitrogen, and carotenoid concentrations. Sun *et al.* (2014) and Du *et al.* (2016) developed similar hyperspectral LiDAR systems for the same purpose. Wang *et al.* (2018) developed an eight-wavelength hyperspectral LiDAR instrument, covering the spectral range between 540 nm NIR to 1460 nm SWIR wavelengths. The development of the instrument aimed at including SWIR bands, as the majority of the available multi- and hyperspectral LiDAR systems operated at visible and NIR wavelengths only. The aforementioned instruments have been mainly utilized in lab or small-scale experiments.

Two dual-wavelength TLS instruments have been developed and then deployed, not only in lab experiments but also in field campaigns: the Dual Wavelength Echidna LiDAR (DWEL) (Douglas *et al.*, 2015) and the Salford Advanced Laser Canopy Analyser (SALCA) (Danson *et al.*, 2014). DWEL was developed by the University of Boston, University of Massachusetts, Boston, University of Massachusetts, Lowell, USA, and CSIRO, Australia (Douglas *et al.*, 2015), while SALCA was developed by the University of Salford, UK and Halo Photonics Ltd (Danson *et al.*, 2014). Both instruments are full waveform TLS systems, with SALCA operating at 1064 nm NIR and 1545 nm SWIR wavelengths, and DWEL employing 1064 nm and 1548 nm wavelengths. Spectral indices calculated using NIR and SWIR wavelengths, such as NDI, can minimize the incidence angle effects, as investigated and confirmed by Hancock *et al.* (2017) using leaf samples from a variety of species. NDI was also found to be sensitive to EWT (Gaulton *et al.*, 2013). Thus, the instruments have been utilized for leaf-wood separation at single tree and forest stand levels, as using spectral indices such as NDI made leaves distinguishable from non-photosynthetic woody materials in the point cloud (Figure 2-4) (Brodu and Lague, 2012; Douglas *et al.*, 2015; Newnham *et al.*, 2015; Danson *et al.*, 2018; Li *et al.*, 2018).

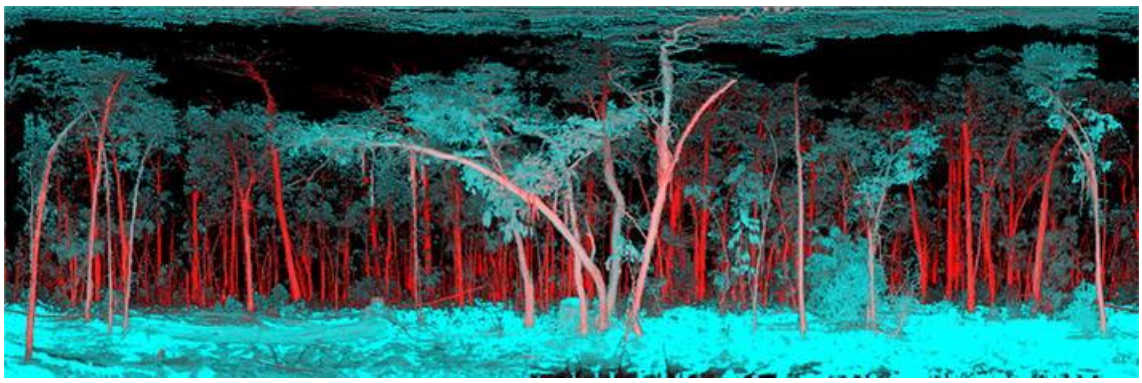

Figure 2-4. NDI pointcloud derived from DWEL data in an open eucalyptus forest at Tumbarumba, Australia, showing the distinctive difference between leaves (blue) and wood (red). This figure was adapted from Newnham *et al.* (2015).

Despite their potential in estimating the vegetation biochemical and biophysical characteristics, multispectral and hyperspectral TLS systems are still a proof-of-concept, not commercially available, and need further development of data extraction algorithms to make full use of the information they provide (Danson *et al.*, 2014).

2.4.3 TLS and vegetation biochemical traits

A few recent successful attempts to utilize TLS intensity data to estimate vegetation biochemical traits can be found in the literature. Eitel *et al.* (2010) and (2011) showed the potential of using TLS intensity data to estimate vegetation biochemical characteristics at leaf and canopy level. Green laser (532 nm) intensity, utilized in the Leica ScanStation-2 TLS instrument, was found to be highly correlated (R^2 = 0.77) to foliar chlorophyll content of bur oak (*Quercus macrocarpa*) and sugar maple (*Acer saccharum*) leaf samples (Eitel *et al.*, 2010), and to total foliar nitrogen (R^2 = 0.68) of spring wheat (*Triticum aestivum L.*) leaf samples (Eitel *et al.*, 2011). Wei *et al.* (2012) used four-band multispectral LiDAR to estimate nitrogen content of leaf samples from seven different species, finding a strong relationship between three derived laser intensity indices and foliar nitrogen content (R^2 = 0.72, 0.78 and 0.82 respectively). Eitel *et al.* (2014a) used a Leica ScanStation-2 TLS instrument (532 nm) to determine winter wheat crop nitrogen status during early season growth. Eitel *et al.* (2014b) used a green (532 nm) and red (658 nm) dual wavelength TLS and derived green-red intensity ratio spectral indices to estimate foliar nitrogen content, achieving good accuracy (R^2 = 0.71). Magney *et al.* (2014) used 532 nm green wavelength utilized in the Leica ScanStation-2 TLS instrument to measure xanthophyll pigments (xanthophylls are pigments that play a role in photosynthesis and in autumn, when chlorophyll levels decline, give leaves their red, yellow, and brown colours) as

an early indicator of vegetation stress using leaves from five different plant species (winter wheat (*Triticum aestivum L.*), bur oak (*Quercus macrocarpa*), paper birch (*Betula papyrifera Marshall*), aspen (*Populus tremuloides Michx.*), and sunflowers (*Helianthus annuus L.*)).

Nevalainen *et al.* (2014) used an eight-channel multispectral LiDAR (500 to 1300 nm), described in Hakala *et al.* (2012), to estimate chlorophyll concentrations in Scots pine shoots with high accuracy (R^2 = 0.88). Hakala *et al.* (2015) used the same instrument to derive spectral indices to estimate chlorophyll content for pine plantation at leaf, branch and tree levels. Li *et al.* (2016) used vegetation indices derived from a 32-channel multispectral LiDAR, described in Li *et al.* (2014), to estimate leaf nitrogen content, chlorophyll content, and carotenoid content, finding a strong relationship between the indices and the biochemical characteristics (R^2 = 0.71, 0.83 and 0.77 respectively). Du *et al.* (2016) and (2018) used data from a 32-channel hyperspectral LiDAR to derive spectral indices and estimate leaf nitrogen content of rice under controlled lab conditions and four different levels of fertilization, reporting a strong correlation (R^2 = 0.75). Using the 32-channel hyperspectral LiDAR described in Sun *et al.* (2014), Sun *et al.* (2018) reported that combining hyperspectral LiDAR data with inversion of PROSPECT can improve the accuracy of retrieving leaf chlorophyll content.

A number of studies have successfully linked TLS intensity data to estimate EWT. Gaulton *et al.* (2013) found a strong relationship (R^2 = 0.80) between EWT of leaf samples from three different species: *Brassica oleracea* (cabbage), *Spathiphyllum* (peace lily), and *Fallopia japonica* (Japanese knotweed), and the NDI of 1064 nm and 1545 nm wavelengths employed by the SALCA instrument. Zhu *et al.* (2015) used a RIEGL VZ-400 scanner (1550 nm shortwave infrared) to investigate the relationship between EWT of leaf samples from eight species and the instrument intensity data, reporting a strong correlation (R^2 = 0.76). Zhu *et al.* (2017) used data from the same instrument to retrieve the EWT vertical profiles for 20 plants from five different species: *Schefflera arboricola compacta* (dwarf schefflera), *Ficus benjamina twilight* (weeping fig), *Ficus microcarpa* (Chinese banyan), *Ficus benjamina Danielle* (ficus), and *Zamioculcas zamiifolia* (Zanzibar gem), reporting a good relationship at leaf level (R^2 = 0.66) and at canopy level (mean error of 4.46%). Vertical heterogeneity in the canopy EWT was also reported, as all trees had higher EWT in the canopy top than in the canopy bottom. However, as a single wavelength was used, radiometric correction for the incidence angle effects on the intensity data was needed, which was achieved using reference targets with known reflectance.

Junttila *et al.* (2016) reported a very strong relationship (R^2 = 0.93) between the NDI of red (690 nm) and shortwave infrared (1550 nm) wavelengths, utilized in phase-based Leica HDS6100 and FARO X330 instruments respectively, and EWT of 101 leaf and needle samples from five different species: *Tilia cordata L.* (small-leaved lime), *Betula pendula L.* (silver birch), *Acer platanoides L.* (Norway maple), *Picea abies L.* (Norway spruce), and *Pinus sylvestris L.* (scots pine). The relationship between EWT of Norway spruce seedlings and the NDI of 905 nm and 1550 nm wavelengths, utilized in the FARO S120 and the FARO X330 TLS instruments respectively, was investigated by Junttila *et al.* (2018) and a strong relationship (R^2 = 0.91) was reported. Junttila *et al.* (2019) used the same instruments to detect *Ips typographus L.* (European spruce bark beetle) infestation symptoms in 29 mature Norway spruce trees, successfully classifying the trees into three classes (no, low, and moderate infestation levels) with overall accuracy of 66%. Higher accuracy was obtained (90%) when the trees were classified into two classes only: infested or not infested. Additionally, FMC was reported to be a better indicator of European spruce bark beetle infestation symptoms than EWT.

Although the aforementioned studies demonstrated the potential of using TLS intensity data to estimate vegetation biochemical traits, these studies, with the exception of Junttila *et al.* (2019), investigated the relationship between TLS data and vegetation biochemical traits at leaf level only, or at leaf and canopy levels in controlled environments. The multispectral and hyperspectral TLS systems used in these studies can still be considered a proof-of-concept, and are not commercially-available. Danson *et al.* (2014) highlighted that processing methods for accurate calibration and registration of the data from such systems are still needed in order for the data to be usable at larger scales. Furthermore, the majority of multispectral and hyperspectral TLS systems employ wavelengths that cover the visible and NIR regions only, making them more suitable for estimating leaf chlorophyll, nitrogen, and carotenoid contents.

Commercial single-wavelength TLS systems that utilize SWIR wavelengths can be suitable for estimating EWT at leaf level, or at canopy level for small trees in laboratory settings. However, using such systems to estimate EWT at the canopy level in complex vegetation environments such as forests will be limited by the incidence angle and leaf internal structure effects. Combining the data from two different commercially-available TLS systems, operating at NIR and SWIR wavelengths, has the potential to minimize such effects, thus rendering this method applicable in a real forest environment. However, accurate aligning of the point clouds from the two different instruments can be challenging, and although Junttila *et al.* (2019) applied this

approach in a Norway spruce forest plot, no 3D EWT point clouds or EWT vertical profiles were generated, most likely as a result of the complications associated with aligning the point clouds and estimating EWT on a point-by-point basis. No successful attempts to utilize TLS data to generate 3D EWT estimates at the canopy level in forest stands, tree plots, or agricultural sites appear to have been reported in the literature to date.

2.5 Summary

This chapter has reviewed the use of optical RS data for estimating EWT, identified its limitations, and investigated the potential of using TLS to address such issues. Previous studies that used vegetation indices and/or RTMs to estimate EWT from optical RS data were examined. This revealed that vegetation indices were highly correlated to EWT at leaf level, and some studies showed that they can also be used to successfully retrieve canopy EWT at landscape level. However, vegetation indices were reported to be sensor- and site-specific, and their use cannot be generalized. For example, NDII was designed to retrieve EWT from Landsat data, while NDWI was designed for MODIS data. Thus, using these vegetation indices to retrieve EWT from other sensors required either modifying them to suit the spectral bands utilized in that sensor, or designing similar indices specifically for the sensor. In addition, numerous studies highlighted that the accuracy of use of vegetation indices for retrieval of canopy EWT at the landscape level was highly influenced by canopy structure, especially canopy LAI.

RTMs were reported to be able to overcome these limitations, as they are based on physical principles and thus are transferrable to any vegetation site. RTMs also take the canopy structural parameters into account, and numerous studies showed that inverting the models can successfully retrieve canopy EWT at the landscape level, as a product of EWT and LAI. However, some authors showed that the use of RTMs must be accompanied by some previous knowledge of canopy biochemical and biophysical traits in the site of interest, in order to improve the accuracy of the model inversion. Complex 3D RTMs have been developed to account for the vertical and horizontal heterogeneity in canopy structure, instead of assuming a homogenous canopy. However, the vertical heterogeneity in canopy biochemical traits, including EWT, remained unaccounted for, with few studies attempting to measure it by destructive sampling and taking spectroscopy measurements at multiple canopy layers. These studies further showed that EWT, chlorophyll content, and nitrogen content exhibited vertical heterogeneity that varied between species. The effect of such heterogeneity on the canopy reflectance and on the accuracy of canopy EWT estimation still needs to be further investigated,

as the few studies found in the literature that looked into such effects reported that the vertical heterogeneity should not be ignored as it highly influences the canopy reflectance (Kuusk, 2001; Wang and Li, 2013; Quan *et al.*, 2017).

Another issue that was highlighted in the literature, associated with the retrieval of EWT from optical RS data in general, was that collecting a sufficient number of leaf samples from the canopy top layers in sampling plots that match the sensor's pixel size to calibrate and validate the estimation models can be very challenging. Two gaps were identified in the literature: (1) a fast, non-destructive approach to estimate canopy EWT at plot level, and to provide EWT estimates of the upper canopy layers, is needed, (2) a more practical method is needed to measure the vertical heterogeneity in canopy biochemical traits in order to investigate its effect on the canopy reflectance.

Previous studies have shown that TLS can provide accurate measurements of canopy structure, but fewer studies have investigated using TLS intensity data to measure EWT and other vegetation biochemical traits. This is a result of the limitations associated with using a single-wavelength TLS instrument to estimate vegetation biochemical traits, with the two main issues being correction of the intensity data for incidence angle effects and for the leaf internal structure effects at the canopy level. To overcome these limitations, a number of multi- and hyperspectral TLS instruments have been developed for scientific research and were successfully used to estimate EWT, chlorophyll content, nitrogen content, and carotenoid content. As these instruments are not available commercially, other studies used intensity data from commercially available TLS instruments, typically by combining the data from two different instruments into a spectral index, and successfully estimated EWT, chlorophyll content, and nitrogen content. However, the number of studies that used TLS to estimate EWT, and vegetation biochemical traits in general, is very low, and all the studies found in the literature were conducted in laboratory conditions at leaf level only, or at leaf level and small, individual canopy level. Only one recent study to date has used TLS to estimate EWT in a real forest environment to detect signs of pest infestation, but no 3D EWT point clouds or vertical profiles of EWT were generated. There remains a gap in the literature regarding the use of TLS, especially commercial instruments, in the 3D estimation of EWT at the canopy level in challenging vegetation environments, such as forest stands and agricultural sites, where the canopy structure, wind, and partial canopy hits can greatly complicate the process.

Chapter 3. Combining TLS intensity data from different instruments in the NDI

3.1 Introduction

Accurate estimation of EWT in 3D at the canopy level, using dual-wavelength terrestrial laser scanning, depends on a number of factors. Firstly, the intensity data from the two instruments need to be calibrated to apparent reflectance accurately. Secondly, the two wavelengths utilised in the NDI must be affected similarly by the incidence angle so that combining them in the NDI would minimize the incidence angle effects with no need for radiometric corrections. In addition, NDI needs to be able to minimize the leaf internal structure effects, or else, radiometric corrections will be needed for each wavelength separately. Finally, accurate alignment of the point clouds from the two different instruments is required, so that NDI can be calculated correctly on a point-by-point basis and 3D EWT point clouds can be generated with low errors.

This chapter is dedicated to address the aforementioned factors. Firstly, the TLS instruments used in this study are described. Then, the method for combining the data from different TLS instruments to generate 3D estimates of EWT is described. Afterwards, details of the calibration work for each instrument are given. Finally, the ability of NDI to minimize the incidence angle and leaf internal structure effects is investigated.

3.2 TLS instruments

Four different TLS instruments were used in this research, a Leica P20, two different Leica P40 instruments, named hereafter as Leica $P40_a$ and the Leica $P40_b$, and a Leica P50 (Figure 3-1). The Leica $P40_a$ and the Leica $P40_b$ were different instruments of the same model, manufactured in two different years, 2016 and 2017. The specifications of each of the four instruments are described in Table 3-1.

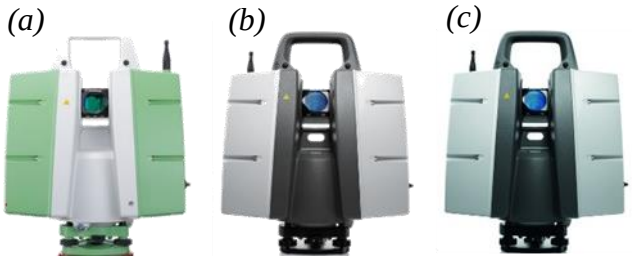

Figure 3-1. The TLS instruments used in this research: *(a)* the Leica P20, *(b)* the Leica $P40_a$ and $P40_b$ and *(c)* the Leica P50.

Table 3-1. Nominal specifications of the TLS instruments used in this research.

	Leica P20	Leica $P40_a$ and $P40_b$	Leica P50
Measurement type	Time-of-flight	Time-of-flight	Time-of-flight
Wavelength	808 nm	1550 nm	1550 nm
Beam divergence	0.20 mrad	0.23 mrad	0.23 mrad
Beam diameter at exit	2.8 mm	3.5 mm	3.5 mm
Beam diameter at 10 m	4.8 mm	5.8 mm	5.8 mm
Beam diameter at 20 m	6.8 mm	8.1 mm	8.1 mm
Maximum range	120 m at 18% reflectivity	120 m at 8% reflectivity 180 m at 18% reflectivity 270 m at 34% reflectivity	120 m at 8% reflectivity 270 m at 34% reflectivity 570 m at 60% reflectivity 1 km at 80% reflectivity
Scan rate	up to 1,000,000 points/second	up to 1,000,000 points/second	up to 1,000,000 points/second
Highest resolution (point spacing)	0.8 mm at 10 m	0.8 mm at 10 m	0.8 mm at 10 m

The Leica P20, operating at 808 nm NIR wavelength, was involved in all the experiments and data collection campaigns conducted in this research. The P20 wavelength lies in a region in the leaf reflectance spectra that is known to be insensitive to change in EWT but sensitive to changes in leaf structure (Hunt and Rock, 1989; Gao, 1996; Liu *et al.*, 2014). The three other instruments operate at 1550 nm SWIR wavelength, which is very sensitive to the change in EWT (Gaulton *et al.*, 2013; Junttila *et al.*, 2016; Zhu *et al.*, 2017). The data from the P20 was combined in the NDI with the data from each of the three SWIR instruments, depending on their availability, as shown in Table 3-2. The NDI of NIR and SWIR wavelengths was previously reported to be very sensitive to the change in EWT (Hunt and Rock, 1989; Ceccato *et al.*, 2001; Gaulton *et al.*, 2013), to be able to minimize the incidence angle effects (Hancock *et al.*, 2017), and to be insensitive to the leaf internal structure effects (Ceccato *et al.*, 2001). However, this has not been investigated for the two wavelengths involved in this study, the 808 nm and 1550 nm wavelengths.

Table 3-2. The TLS instruments usage in the data collection campaigns.

Data collection campaign	Indoors dataset, Chapter 4	Forest dataset, Chapter 5	Willow dataset, Chapter 6	Park dataset, Chapter 6
Instruments used	Leica P20 Leica $P40_a$	Leica P20 Leica $P40_b$	Leica P20 Leica $P40_a$	Leica P20 Leica P50

In addition to having suitable wavelengths for a NDI highly correlated to EWT, the instruments have similar chassis and laser beam exit location (Figure 3-1). They use a similar scanning mechanism, with the ability to capture up to 1,000,000 points per second. Thus, consecutive scanning of a target with the P20 instrument, followed by one of the three SWIR instruments, mounted on the same tripod and occupying the same survey station, can result in very similar scan geometry. Although Table 3-1 shows some differences in beam diameter at exit and beam divergence between the P20 instrument and the SWIR instruments, the aforementioned similarities and scan setup can lead to achieving sufficient overlap between the laser beams. This can lead to a high registration accuracy of the point clouds from the different instruments, which is necessary for estimating EWT on a point-by-point basis.

3.3 TLS data processing to generate 3D EWT point clouds

3.3.1 Scan setup

Combining the intensity data from the P20 and any of the three SWIR instruments required the correct scan setup to take advantage of the similarities between the instruments, to achieve the highest possible overlap between the point clouds. For this, a tripod was fixed on a survey point, and the P20 was mounted on the tripod to scan the object of interest, being a single tree or a group of trees. Afterwards, the $P40_a$, the $P40_b$ or the P50 was mounted on the same tripod to scan the object of interest, adopting the same scanning resolution used with the P20. The tripod was then moved to the next survey point and the process was repeated. A minimum of three Leica black and white registration targets were placed around the object of interest, at different heights, in order to link each pair of scans.

Figure 3-2 shows a 50% SphereOptics Spectralon panel scanned indoors by the P20 instrument, followed by the $P40_a$ instrument, using the aforementioned scan setup and scanning resolution (point spacing) of 0.8 mm at 10 m. The average distance between the points from the two point clouds, calculated using the cloud to cloud distance compute module in CloudCompare v. 2.6.2 software, was 0.2 mm. For the tree canopies scanned indoors (Chapter 4), this distance was

found to be 1.3 mm, while it was found to be 5 mm for the scans conducted in a real forest environment (Chapter 5).

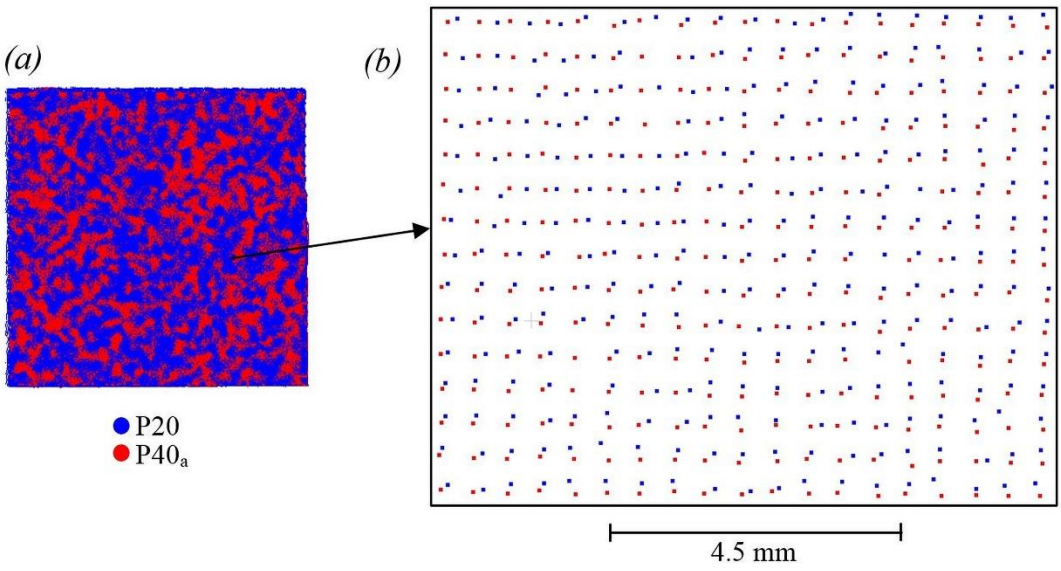

Figure 3-2. A 50% Spectralon panel scanned by the P20 and the $P40_a$ instruments: *(a)* the point clouds, coloured in blue for the P20 and in red for the $P40_a$ and *(b)* a close up to show the point distance between each point in the P20 point cloud and the corresponding point in the $P40_a$ point cloud, with the average distance being 0.2 mm.

Processing the data to generate the 3D EWT point cloud followed the steps shown in Figure 3-3.

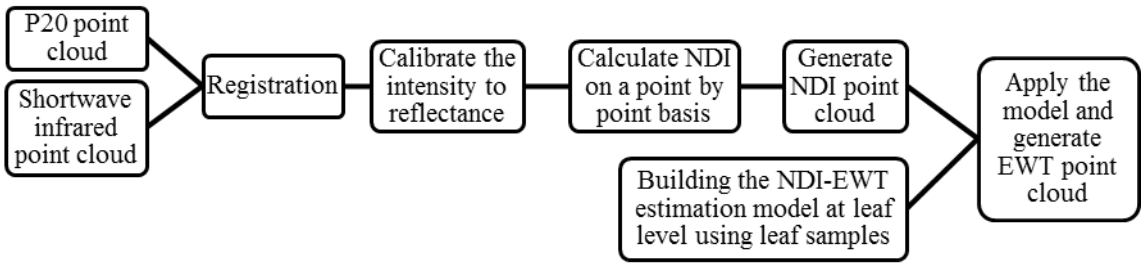

Figure 3-3. A flowchart of the TLS data processing pipeline used to generate 3D EWT point clouds.

3.3.2 Point cloud registration

The point clouds were extracted from each instrument using Leica Cyclone 9.1 (Leica Geosystems HDS) software. To reduce the number of partial hits (edge returns) in the point

clouds, the mixed pixel filter in Leica Cyclone was used on medium (default) setting. The filter searched for points that had a measured range that was actually a mixture of various observed ranges. The filter then disregarded these points, as they occurred when the edge of the object partially occupied the laser footprint.

Each scanner had its own local coordinate system, thus, the point clouds needed to be aligned. This was done in Leica Cyclone using the registration targets placed in the scans. The point cloud from the SWIR instrument was considered as the reference in the registration process. The Cyclone registration module detected the registration targets that co-existed in both scans and used them as constraints to derive a transformation matrix. For this, the targets needed to be labelled correctly while collecting the data so that the registration module could recognize them and use them to link the scans. The transformation matrix was then applied to the P20 point cloud to align it to the corresponding SWIR point cloud. The accuracy of the registration was evaluated and reported by Leica Cyclone in a form of Root Mean Squared Error (RMSE). The registered point clouds were then exported as ASCII files for further processing. The next step was to separately calibrate the intensity from each instrument to apparent reflectance. This is described in details in Section 3.4 in this chapter. All of the processes described in the subsequent sections were implemented in MATLAB (The MathWorks Inc., USA, 2016).

3.3.3 Point matching and NDI calculation

Despite the similarities between the instruments, resulting point clouds did not have the same number of points. A P20 point cloud had more points than a corresponding point cloud collected by the $P40_a$, the $P40_b$ or the P50 instruments, because of the presence of different number of partial hits and the slight differences in laser beam footprint and beam divergence. To account for this, two sets of point cloud filtering were applied as follows:

(1) The P20 point cloud was filtered to match the same number of points in a corresponding SWIR point cloud. For this, a 3D nearest neighbour function was applied in MATLAB, using the SWIR point cloud as a reference. The function used an exhaustive search algorithm to compute the distances in 3D between each point in the SWIR point cloud and all the points in the corresponding P20 point cloud. The function then generated an index matrix that defined the nearest neighbour in the P20 point cloud to each point in the SWIR point cloud. The index matrix was then used to filter the P20 point cloud, retaining only the nearest neighbour points and disregarding the remaining points, and generating a conjugate point cloud containing the same number of points as the corresponding SWIR point cloud.

(2) A threshold of 3 cm was applied, that is, any pair of neighbour points > 3 cm apart was removed from the P20 point cloud and the corresponding SWIR point cloud. This was required because the nearest neighbour function tried to find the nearest neighbour in the P20 point cloud to each point in the SWIR point cloud, regardless of how far that nearest neighbour was. The 3 cm threshold was chosen on the basis of 97% of the nearest neighbour distances being < 3 cm apart, while 99% of distances were < 6 cm apart. Applying the threshold disregarded points from both the SWIR and P20 point clouds. Figure 3-4 shows a histogram of closest points within 3 cm after applying the two sets of filtering to a P20 point cloud and its corresponding $P40_b$ point cloud, collected in Wytham Woods forest plot (Chapter 5).

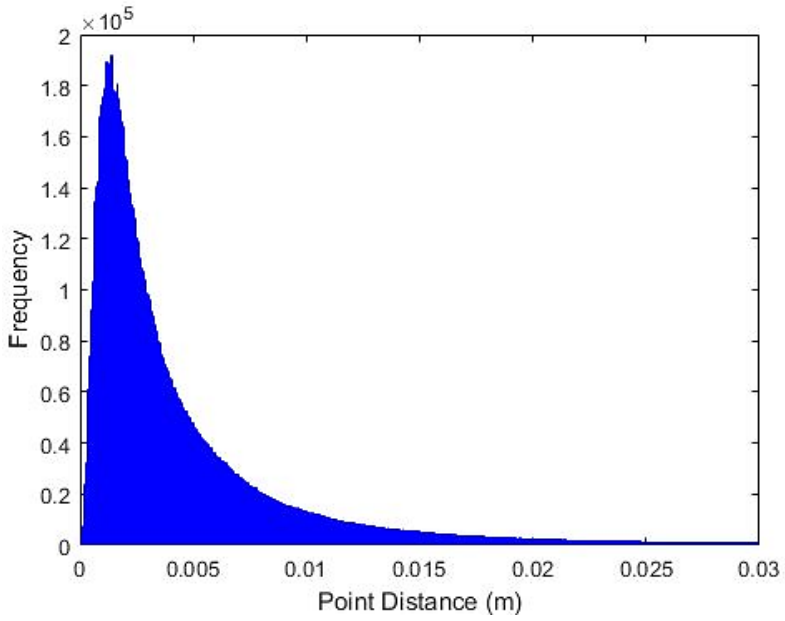

Figure 3-4. Histogram of closest points within 3 cm after filtering a P20 point cloud and its corresponding $P40_b$ point cloud, collected in Wytham Woods forest plot (Chapter 5).

NDI was then calculated on a point-by-point basis (Equation (2.5)) to generate the NDI point cloud.

3.3.4 Building the NDI – EWT estimation model

After generating the NDI point cloud, an NDI – EWT relationship was needed to convert the NDI point cloud to 3D EWT point cloud. For this, leaf samples were collected from the scanned trees in the data collection site. The number and species of the samples depended on the experiment. The leaf samples were labelled and the fresh weight of each sample was measured, immediately on collection, using a precise scale (0.001 g division). Afterwards, the leaf samples were suspended in a wooden frame with thin black threads, positioned at a fixed distance from

a tripod. The leaves were scanned by the P20 instrument, followed by the SWIR instrument used in the experiment. Throughout the scans, the vertical and horizontal incidence angle effects were minimized by ensuring the wooden frame was as normal as possible to the laser beam direction. The intensity values of each leaf sample were then extracted from the scans and calibrated to apparent reflectance, using the intensity correction models described in Section 3.4. The NDI of each leaf was calculated according to Equation (2.5).

Next step was to calculate the EWT of each leaf sample. For this, the surface area of each leaf sample was obtained using Image-J 1.50i software (Schneider et al., 2012) after dividing them into groups and scanning each group and a scale with an Epson Perfection photo scanner. Afterwards, the leaves were dried in an oven for 48 hours at 60° Celsius until no change in weight was recorded. The dry weight of each leaf was measured using the same precise scale used to obtain the fresh weight. The EWT of each leaf sample was calculated following Equation (2.1).

NDI values of the leaf samples were plotted against the corresponding EWT values and reduced major axis regression was used to determine the NDI – EWT relationship. Reduced major axis regression was used instead of least squares regression because the latter assumes that only the dependent variable in the regression (EWT in this case) is subject to errors. Least squares regression then attempts to minimize the sum of squared errors of the vertical distance between the actual dependent variable values (y values) and their corresponding predictions. However, as both NDI and EWT were subject to errors, which violated the least squares regression assumptions, reduced major axis regression was considered a more suitable approach. Reduced major axis regression is a method specifically formulated to account for errors in both the dependent and independent variables by attempting to minimize both vertical and horizontal distances between data points and their predicted values (Smith, 2009). Furthermore, unlike least squares regression, reduced major axis regression is symmetric, meaning that the resulting regression equation can be back solved to predict the dependent variable from the independent variable if needed.

3.3.5 Generating the EWT point cloud

The NDI – EWT relationship derived at leaf level was then applied on a point-by-point basis to the NDI point cloud and the EWT point cloud was generated. Further processing was needed to remove the woody materials and noise, which depended on the type and size of dataset and thus is described in detail in the corresponding data collection chapters.

3.4 TLS intensity data calibration

As discussed in Section 2.4.1, the range and incidence angle are the two main parameters that influence the TLS recorded backscattered intensity data. This section is dedicated to describing the range effect calibration models, while the incidence angle effects are covered in Section 3.5.

3.4.1 Concept of range effect intensity calibration models

The aim of the range effect calibration model was to calibrate the instrument's recorded intensity to reflectance, as close as possible to the scanned target's apparent reflectance, regardless of how far the target was from the scanner. The calibration model thus conducted two tasks: 1) calibrating the intensity data for the range effect and 2) transforming the calibrated intensity to apparent reflectance. To achieve the first task, the intensity-range relationship for each instrument was investigated by scanning a reference target with known reflectance at various ranges from the scanner. The target's intensity at each range was extracted and plotted against the corresponding range to obtain the intensity-range curve. Polynomial functions were then fitted to the curve and considered a reference for the range calibration model. The next step was to choose an intensity value at any range to serve as a reference intensity for the calibration model (I_{ref}), to which the intensity values at the remaining ranges were calibrated.

To achieve the second calibration task, the intensity-reflectance relationship for each instrument needed to be determined at the range of I_{ref}. This was achieved by scanning reference targets with different apparent reflectance, or a multi-step reference target, at I_{ref} range. The targets' intensity values were then plotted against the targets' known reflectance to obtain the intensity-reflectance relationship of the instrument. The intensity-reflectance relationship was used to transform the calibrated intensity at all ranges to apparent reflectance.

In this research, five SphereOptics Spectralon panels, almost ideal Lambertian surfaces according to the manufacturer, were used to build and validate the calibration models of the P20 instrument, the $P40_a$ instrument and the $P40_b$ instrument. The nominal and true reflectance of the panels are shown in Table 3-3. The calibration experiments for the P50 instrument were conducted using a multi-step SphereOptics Zenith Lite Diffuse reflectance target (Table 3-4), as the Spectralon panels were not available. Throughout all the calibration experiments described in the upcoming sections of this chapter, the scanner's laser beam exit location approximately faced the centre of the panel, while the surface of the panel was almost perpendicular to the laser beam direction. This aimed at minimizing the incidence angle effects, so that the backscattered intensity would be affected by the range only.

Table 3-3. Actual reflectance from Spectralon panels at P40 and P20 wavelengths.

Spectralon	5%	20%	50%	90%	95%
P40 (1550 nm)	4.7%	24.2%	41.8%	90.2%	94.7%
P20 (808 nm)	4.5%	22.6%	43.5%	92.2%	96.1%

Table 3-4. Actual reflectance of the multi-step reference target used for the P50 calibration.

Panel	5%	20%	50%	90%
P50 (1550 nm)	5.5%	20.5%	47.7%	91.8%

3.4.2 Determining the intensity-range relationships

The intensity-range relationship was investigated separately for each scanner. A range calibration experiment was conducted indoors for each instrument, by mounting a reference target on a tripod and scanning it at various ranges. Table 3-5 shows the details of the calibration experiment of each instrument.

Table 3-5. Details of the range calibration experiments of the TLS instruments.

Instrument	Reference target	Start range	End range	Step	I_{ref} range
Leica P20	50% Spectralon panel	2 m	36 m	1 m	15 m
Leica $P40_a$	50% Spectralon panel	2 m	36 m	1 m	18 m
Leica $P40_b$	50% Spectralon panel	2 m	36 m	1 m	20 m
Leica P50	50% panel*	2 m	22 m	1 m	15 m

* Part of a multi-step panel.

3.4.3 Determining the intensity-reflectance relationships

An individual experiment was conducted for each instrument to determine the intensity-reflectance relationship. The five Spectralon panels described in Table 3-3 were scanned consecutively using the P20, the $P40_a$ and the $P40_b$ instruments at I_{ref} range from the scanner (Table 3-5). For the P50 instrument, the multi-step reference panel (Table 3-4) was scanned at I_{ref} range (15 m) away from the scanner.

3.4.4 Validating the intensity calibration models

For each instrument, an independent reference target was scanned indoors at various ranges, as shown in Table 3-6. The developed calibration models were used to calibrate the intensity values at each range for the range effect and to apparent reflectance. The accuracy of the models were evaluated by comparing the estimated reflectance at each range to the reference target's

true reflectance. The relative error (E %, Equation (3.1)) and the RMSE (Equation (3.2)) were calculated. For the P20, two different validation experiments were conducted, one prior to the indoors experiment (Chapter 4), and the other before the forest data collection campaign (Chapter 5). This aimed at a direct comparison between the accuracy achieved using the P20 and that achieved using the corresponding P40 that was to be used in the data collection.

Table 3-6. Details of the validation experiments of the TLS instruments.

Instrument	Reference target	Start range	End range	Step
Leica P20	90% Spectralon panel	2 m	15 m	1 m
Leica P20	20% Spectralon panel	2 m	15 m	1 m
Leica $P40_a$	90% Spectralon panel	2 m	18 m	1 m
Leica $P40_b$	20% Spectralon panel	2 m	22 m	1 m
Leica P50	20% panel*	2 m	22 m	1 m

* Part of a multi-step panel.

$$E\ \% = \left(\frac{\hat{y} - y}{y}\right) \times 100 \tag{3.1}$$

$$RMSE = \sqrt{\frac{\sum_{i=1}^{n}(\hat{y}_i - y_i)^2}{n}} \tag{3.2}$$

Where $\hat{y}$ and y are the estimated and true values respectively.

Prior to carrying out the main data collection campaign in a forest plot in Wytham Woods, Oxford, UK (Chapter 6), additional validation experiments were conducted for the two instruments that were to be used in the data collection, the P20 and the $P40_b$ instruments. The additional experiments were conducted using a wooden multi-step painted board. The board was 0.75 × 0.50 m, divided into six approximately equal panels, each of them painted in a different shade of grey. The shades of grey were obtained by mixing black and white matte emulsion paint with different ratios. Prior to painting the board, thirty different black and white combinations were painted on a test board. The reflectance of each combination was measured at the 1550 nm and 808 nm wavelengths using an ASD field Spectroradiometer with a contact probe, then six combinations were chosen and used to paint the multi-step board. The combinations were selected so that they would cover a reflectance range between 10% and 70%. Afterwards, five ASD measurements were taken for each of the six panels of the multi-step board, and the reflectance of each panel at each wavelength equalled the average of the measurements, as shown in Table 3-7.

Table 3-7. Actual reflectance of each of six panels in the multi-step painted board.

Wavelength	Panel 1	Panel 2	Panel 3	Panel 4	Panel 5	Panel 6
1550 nm	12%	23.8%	36.5%	48.4%	57.7%	64.8%
808 nm	14.6%	28.9%	42.9%	55.1%	64.3%	70.7%

The multi-step painted board was scanned indoors by each scanner separately at a random range of 7.32 m. The board was also scanned outdoors at 4.4 m, 6 m and 8.6 m. The calibration models were used to calibrate the intensity values of each panel in the multi-step board for the range effect and to apparent reflectance. The estimated reflectance was compared to the panels' actual reflectance for accuracy evaluation.

3.5 The ability of NDI to minimize the incidence angle effects

To investigate the ability of the NDI of the 808 nm and 1550 nm to minimize the incidence angle effects, an experiment was conducted in a laboratory setting using eighteen leaf samples from six different tree species, three samples from each species. The leaf samples included: grey alder (*Alnus incana*), common lime (*Tilia x europaea*), common alder (*Alnus glutinosa*), hornbeam (*Carpinus betulus*), poplar (*Populus sp.*) and cherry (*Prunus avium*). The leaf samples were collected from Peel Park in Salford, Manchester, UK. The experiment was conducted using the P20 and the $P40_a$ instruments. There was no need to repeat the experiments using the $P40_b$ and the P50 instruments, as the incidence angle effect is a factor of the wavelength and the scanned target surface characteristics, and not of the instrument itself.

The leaf samples were divided into three groups, each group containing six leaf samples, one sample from each species. Each group of leaves was suspended in a wooden frame by thin black threads. The frame (Figure 3-5) was positioned at a fixed scan range of 6.5 m. A clear space of 2 m was ensured behind the frame to avoid any influence of the energy reflected from the rear wall on the leaf sample's backscattered intensity. The whole frame was rotated between scans, increasing the incidence angle from 0 to 60 degrees, with scans conducted at 20 degree intervals. A total of 24 scans were conducted. The intensity values of each leaf, at each incidence angle, for each scanner, were extracted. The points near the edges of the leaves were manually removed as they corresponded to partial hits. The intensity values were calibrated into apparent reflectance using the calibration models described in Section 3.4. NDI was calculated at each incidence angle for each leaf.

Figure 3-5. The wooden frame used in the leaf incidence angle experiment.

3.6 The ability of NDI to minimize the leaf structure effects

A leaf has a complicated internal structure, which significantly affects the interaction of radiation with foliage (Jacquemoud and Baret, 1990). The ability of NDI to minimize the leaf internal structure effects is a key parameter in successfully using NDI to estimate EWT at canopy level, especially in forest environments, as the leaf internal structure varies between different species and also within each individual species (Lichtenthaler et al., 1981).

Figure 3-6 shows an example of the leaf internal structure. The mesophyll layers are where the photosynthesis take place. The palisade mesophyll cells are packed together and are responsible for the majority of the photosynthesis, while the spongy mesophyll cells contribute less to the photosynthesis and have gaps between them, filled with air or water. The number and thickness of the mesophyll layers, in addition to the cellular arrangement within them, varies between individual leaves within each species and also between different species (Jacquemoud and Baret, 1990). If the leaf is fully dry, that is, it has zero water content, the weight of the leaf can be considered the leaf dry weight, which when divided by the leaf surface area results in the LMA (Poorter et al., 2009) (Equation (3.3)). The leaf mesophyll structure and LMA, in addition to EWT, are the major elements affecting the interaction of NIR and SWIR wavelengths with foliage (Ceccato *et al.*, 2001; Gaulton *et al.*, 2013). Thus, these three elements were the focus of this research, while the remaining leaf structure components were ignored. To investigate the effects of the aforementioned elements on the 808 and 1550 nm wavelengths, and on the NDI, PROSPECT simulations were conducted.

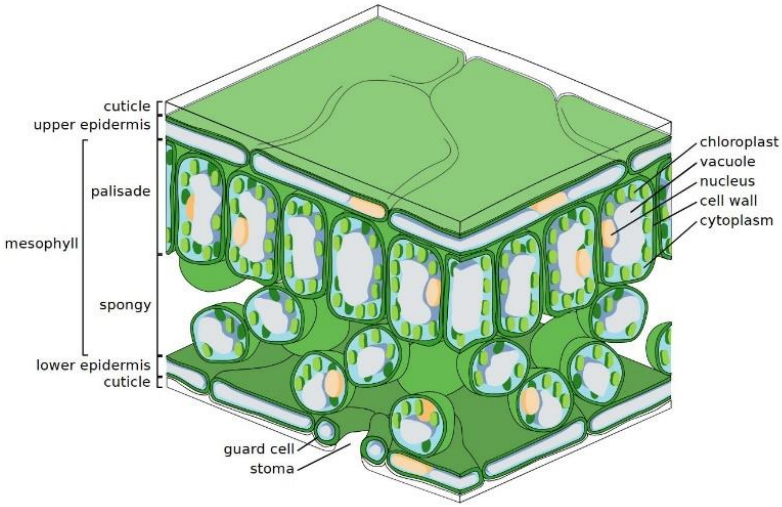

Figure 3-6. Leaf internal structure and cellular arrangements.

$$LMA\ (g\ cm^{-2}) = \frac{Leaf\ DW}{Leaf\ SA} \tag{3.3}$$

3.6.1 PROSPECT model

PROSPECT (Jacquemoud and Baret, 1990) is a radiative transfer model capable of simulating the optical properties of plant leaves over the visible, near infrared and shortwave infrared regions of the electromagnetic spectrum (400 nm to 2500 nm). The version used in this research was PROSPECT-5 (Feret et al., 2008), which modelled the leaf optical properties using six parameters: leaf structure coefficient (N), chlorophyll a and b content (C_{ab}), carotenoid content (C_{ar}), brown pigment content (C_b), leaf water content (C_w), and dry matter content (C_m). The values of C_{ab}, C_{ar} and C_b were kept constant at the model defaults, 47.7 µg cm^{-2}, 4.4 µg cm^{-2} and 0 respectively, as they have minor effects on the NIR and SWIR wavelengths (Ceccato *et al.*, 2001; Gaulton *et al.*, 2013). Zarco-Tejada *et al.* (2003) also used generic, fixed values for the aforementioned variables while conducting PROSPECT and SAIL simulations to determine the suitability of MODIS data to estimate canopy EWT at the landscape level. C_w will be referred to as EWT in the upcoming sections. C_m represents the leaf dry matter content and is quantified in the model as LMA (Feret et al., 2008). C_m will be referred to as LMA hereafter.

3.6.2 The effects of leaf structure coefficient on the NDI

N is the leaf mesophyll structure coefficient and is related to number and thickness of the mesophyll cell layers and the cellular arrangement within them (Figure 3-6), covering a range of values between 1 and 3 (Jacquemoud and Baret, 1990). To study how N affected the NDI, the values of EWT and LMA were kept constant, each at an average value of 0.01 g cm^{-2}, while

N was incrementally increased from 1.5 to 2.5, with an interval of 0.1. N values < 1.5 correspond to monocot leaves, which were outside the interest of this research, while N values > 2.5 indicate that leaves are senescent (Jacquemoud and Baret, 1990). The NDI was calculated for each N value.

3.6.3 The effects of LMA on the NDI

N and EWT values were kept constant at 2 (dimensionless) and 0.01 g cm^{-2} respectively. LMA values covered the range between 0.0017 and 0.0157 g cm^{-2}, based on the minimum and maximum values reported in the LOPEX93 dataset (Feret et al., 2008), with an interval of 0.001 g cm^{-2}. The NDI was calculated for each LMA value.

3.6.4 The effects of leaf structure coefficient on the NDI-EWT relationship

A total number of 111 EWT values, ranging between 0.0046 and 0.0162 g cm^{-2}, which resulted from actual leaf sample EWT measurements conducted in this research and fully described in Chapters 4 and 5, were used. LMA was kept constant at 0.01 g cm^{-2}, and for each EWT value, N was changed between 1.5 and 2.5, with an interval of 0.1, resulting in 1221 combinations of N and EWT. The NDI was calculated for each combination.

3.6.5 The effects of LMA on the NDI-EWT relationship

The same EWT dataset was used as described in Section 3.6.4. For each EWT value, LMA changed between 0.0017 and 0.0157 g cm^{-2}, with an interval of 0.001 g cm^{-2}. N was kept constant at 2 in all simulations. The NDI was calculated for each of the 1665 combinations of LMA and EWT.

3.7 Results and discussion

3.7.1 TLS intensity data calibration

The intensity-range relationship for the four instruments deviated from the $1/R^2$ component of the laser equation (Figure 3-7). The intensity-range relationships also varied between the instruments, despite being built by the same manufacturer. Additionally, there was also a clear difference between the $P40_a$ and the $P40_b$ instruments, although they were of the same model. All instruments were found to be equipped with a near-distance intensity reducer to protect the optics, which reduced the intensity for ranges less than 4 m (5 m for the P50 instrument). A drop was seen in the intensity values up to around 7.5 m range for the $P40_a$ and the P50 instruments, and 9 m for the P20 and the $P40_b$ instruments, after which the intensity values gradually increased.

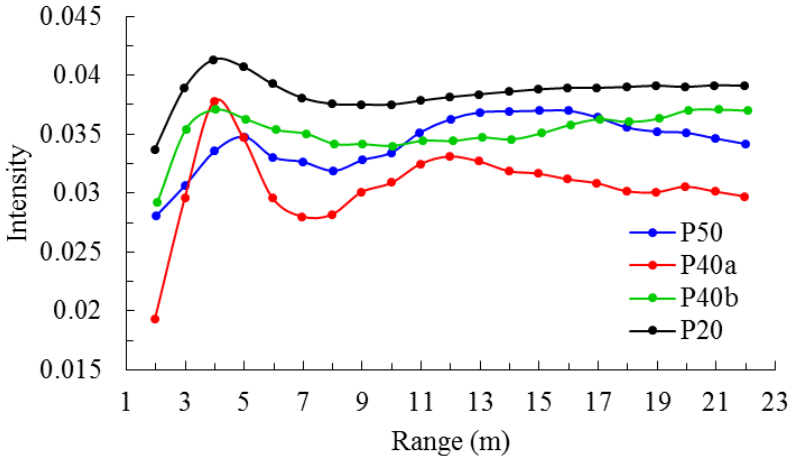

Figure 3-7. The intensity-range relationships for the four instruments used in this study.

The P20 and the $P40_b$ instruments then showed similar behaviour as the intensity values continued to gradually increase, before tending to level out after 15 m for the P20 and 20 m for the $P40_b$. For the $P40_a$ and the P50 instruments, the intensity values increased more significantly, before starting to experience another drop after 12 m and 15 m respectively. The intensity values then tended to level out for the $P40_a$ instrument after 18 m range, with a slight increase at 20 m range. The intensity-range relationship was not investigated for the P50 instrument beyond 22 m as it was not needed for the data collection campaign carried out with the instrument. For the remaining instruments, the intensity values remained constant until the end range of the experiment (36 m). The intensity levelling out suggested that the instruments were equipped with on-board range calibration adjustments that attempted to calibrate for the range effect after 15 m for the P20, 18 m for the $P40_a$ and 20 m for the $P40_b$. Thus, these ranges were chosen for I_{ref} in the range calibration model (Table 3-5). A similar observation was reported for the Faro Focus3D 120 scanner which internally calibrated for the range effect after 15 m (Tan *et al.*, 2016).

For all of the instruments, it was not possible to fit a single polynomial function to the intensity-range relationship. Thus, two polynomial functions were used for each instrument. The split point for the polynomial function was selected for each instrument to achieve a smooth transition between the two functions. The degrees of the polynomial functions were chosen so that the highest possible fitting accuracy could be achieved. Table 3-8 shows the degrees of the polynomial functions for each instrument. It is worth mentioning that for the P20 and the $P40_a$ instruments, polynomial functions were fitted only up to 15 m and 18 m ranges respectively, as the instruments were to be used in indoor experiments and outdoors to scan willow plots, both

involving scanning trees at near ranges, as described in Chapter 4 and Chapter 6 respectively. The P20 instrument was recalibrated and new polynomial functions were fitted up to 36 m range to use the instrument in the forest data collection campaign (Chapter 5). As shown in Table 3-8, a 3rd degree polynomial function was fitted between 2 and 5 m for the $P40_b$ instrument, unlike the other instruments, for which a 2nd degree polynomial function was sufficient. This was done to achieve a smooth transition between the two fitted polynomial function at the split point, and this could not be achieved for the $P40_b$ instrument when a 2nd degree function was fitted at near range. This difference between the instruments may be a result of them being equipped with different near-distance intensity reducers. Figure 3-8 shows the fitted polynomial functions for the $P40_b$.

Table 3-8. Properties of the polynomial functions for the calibration models.

Scanner	Polynomial function	Split point	Fitting accuracy (R^2)
P20	6th degree function between 2 and 15 m	----	97%
P20*	2nd degree function between 2 and 5 m	5 m	99%
	6th degree function between 5 and 36 m		99%
$P40_a$	2nd degree function between 2 and 4 m	4 m	99%
	6th degree function between 4 and 18 m		98%
$P40_b$	3rd degree function between 2 and 5 m	5 m	99%
	6th degree function between 5 and 36 m		97%
P50	2nd degree function between 2 and 5 m	5 m	99%
	6th degree function between 5 and 22 m		99%

*Recalibration for the forest data collection campaign.

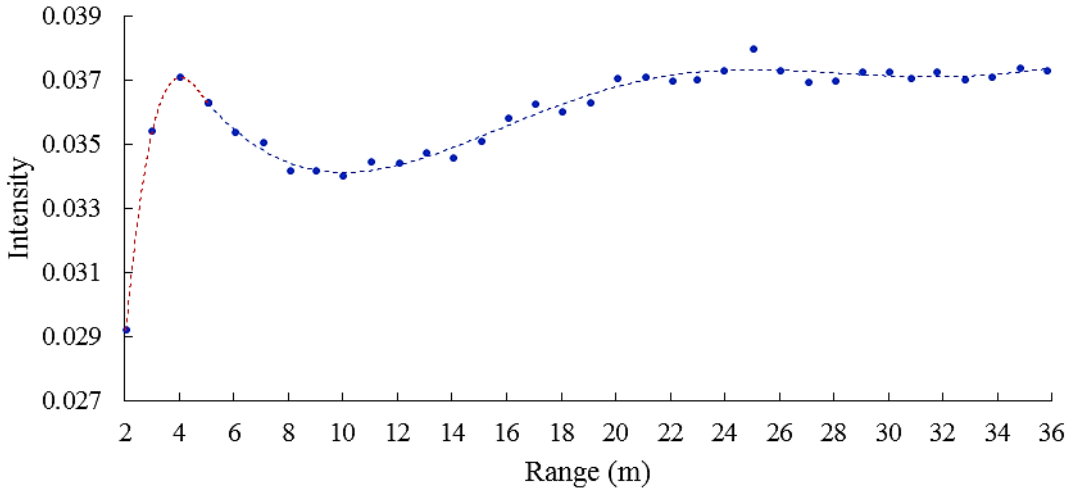

Figure 3-8. The $P40_b$ fitted polynomial functions for near ranges (red, 3rd degree function) and for remaining ranges (blue, 6th degree function) with 5 m range chosen as the split point.

The polynomial functions can be described as follows:

For the P20 instrument:

$$I_P = 0.0000005983 \times R^6 - 0.0000167105 \times R^5 - 0.0000791961 \times R^4 + 0.0070609346 \times R^3 - 0.0854688734 \times R^2 + 0.3909688599 \times R + 0.0336314008 \quad (3.4)$$

For the P20 recalibration:

$$I_P = -0.0014419055 \times R^2 + 0.0123301563 \times R + 0.015072154, \text{ for } R \leq 5 \text{ m} \quad (3.5)$$

$$I_P = 0.0000000005 \times R^6 - 0.0000000751 \times R^5 + 0.0000041012 \times R^4 - 0.0001139564 \times R^3 + 0.0016819488 \times R^2 - 0.0122517431 \times R + 0.071853401, \text{ for } R > 5 \text{ m} \quad (3.6)$$

For the $P40_a$ instrument:

$$I_P = -0.0167555733 \times R^2 + 0.2475767475 \times R - 0.12114732, \text{ for } R \leq 4 \text{ m} \quad (3.7)$$

$$I_P = -0.0000033794 \times R^6 + 0.0002243391 \times R^5 - 0.0058804139 \times R^4 + 0.0766866501 \times R^3 - 0.5126008324 \times R^2 + 1.6048373581 \times R - 1.2338424945, \text{ for } R > 4 \text{ m} \quad (3.8)$$

For the $P40_b$ instrument:

$$I_P = 0.0004042365 \times R^3 - 0.006086872 \times R^2 + 0.029380775 \times R - 0.0089245614, \text{ for } R \leq 5 \text{ m} \quad (3.9)$$

$$I_P = -0.00000000012 \times R^6 + 0.0000000133 \times R^5 - 0.0000004981 \times R^4 + 0.0000045267 \times R^3 + 0.0001134455 \times R^2 - 0.0022367096 \times R + 0.0443796256, \text{ for } R > 5 \text{ m} \quad (3.10)$$

For the P50 instrument:

$$I_P = -0.0003583715 \times R^2 + 0.0048220578 \times R + 0.01973043, \text{ for } R \leq 5 \text{ m} \quad (3.11)$$

$$I_P = -0.000000023 \times R^6 + 0.0000018088 \times R^5 - 0.0000550102 \times R^4 + 0.0008050998 \times R^3 - 0.0057017687 \times R^2 + 0.0170650149 \times R + 0.0204361395, \text{ for } R > 5 \text{ m} \quad (3.12)$$

Where I_P is the intensity from the polynomial function at a range R.

Figure 3-9 shows the relationship between the intensity values and the reference panels' true reflectance for all instruments. In Figure 3-9a, which shows the relationships for the $P40_a$ and the P20 instruments, the intensity values cover the range between 0 and 1, as they were internally stretched by the instruments to enhance the visual appearance of the point clouds.

This intensity alteration was done automatically by the instruments and access to the original recorded intensity values before the alteration was not possible. According to the manufacturer, the intensity alteration was constant, and thus, the intensity-reflectance relationship can be used to calibrate the intensity to reflectance in any scan conducted by the same instrument. The intensity-reflectance relationships could only be described as non-linear, and a 2nd degree polynomial function was fitted to each intensity-reflectance curve with $R^2 > 0.99$.

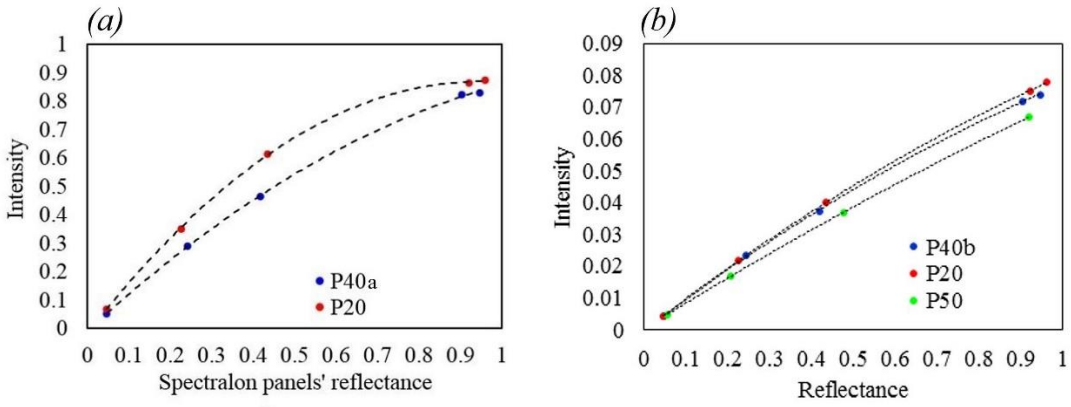

Figure 3-9. The intensity-reflectance relationships of the instruments used in this study.

Figure 3-9b shows the intensity-reflectance relationships for the $P40_b$, the P20 (recalibration), and the P50 instruments, in which the intensity values were not altered by the instruments to enhance the visual appearance. This was achieved by using an intensity map editor provided by the manufacturer, Leica Geosystems, which reversed the intensity alteration and restored the original recorded intensity values. The relationship between the intensity values and the panels' true reflectance, for the three instruments, can be described as linear ($R^2 > 0.99$). However, there was a slight nonlinearity that could lead to overestimation of reflectance if a linear model was used, especially for the reflectance region less than 50%, where most of leaf reflectance was expected to be. An overestimation of reflectance can lead to a significant error in EWT estimation. It was therefore preferable to fit 2nd degree polynomial functions to the intensity-reflectance relationships ($R^2 > 0.99$) to better account for the nonlinearity.

The polynomial functions that describes the intensity-reflectance relationships of the different instruments are as follows:

For the P20 instrument:

$$I = -0.9877937688 \times \rho^2 + 1.8706814918 \times \rho - 0.0175632763 \quad (3.13)$$

For the P20 recalibration:

$$I = -0.0260691455 \times \rho^2 + 0.1067444694 \times \rho + 0.0003190931 \quad (3.14)$$

For the $P40_a$ instrument:

$$I = -0.4714314827 \times \rho^2 + 1.3390038055 \times \rho - 0.0092605544 \quad (3.15)$$

For the $P40_b$ instrument:

$$I = -0.0225515506 \times \rho^2 + 0.0997507219 \times \rho - 0.0000788046 \quad (3.16)$$

For the P50 instrument:

$$I = -0.010138882 \times \rho^2 + 0.0816307988 \times \rho + 0.0003966758 \quad (3.17)$$

Where I refers to the intensity and ρ is the reflectance.

3.7.2 Validating the intensity calibration models

Table 3-9 shows the errors in the reflectance estimation for each validation experiment. For the Spectralon panels experiments, the estimated reflectance at each range of the experiment was compared to the panel's true reflectance and the relative error (E %) was calculated following Equation (3.1). The results revealed high errors at 2 m range, shown in Table 3-9 as max error[(a)], and generally higher errors at ranges ≤ 4 m than at the remaining ranges. This can be a result of the calibration models not being fully able to calibrate the intensity for the near-distance intensity reducer effects. The average of the relative errors at all ranges was the lowest for the P20, followed by the $P40_a$ and the P50, then the $P40_b$, with all average errors being < 4%. When ranges ≤ 4 m were excluded, as no leaf-scanning experiments were planned at such near ranges, the max error dropped, shown in Table 3-9 as max error[(b)]. RMSE was not used for direct comparison between all validation experiments, because the datasets had different mean and numerical scales as a result of using 90% and 20% reference targets for validation. However, RMSE was higher for the $P40_a$ than for the P20 (90% Spectralon panel used in both experiments). This can be a result of the high error in the reflectance estimation at 2 m range (12.3%). When measurements ≤ 4 m were excluded, RMSE was found to be equal in the two experiments. For the P20 recalibration, the $P40_b$ and the P50, for which a reference target with a nominal 20% reflectance was used, RMSE was higher for the $P40_b$ than the P50 and the P20 and also dropped when ranges ≤ 4 m were excluded.

Table 3-9. Errors in the reflectance estimation in the validation experiments. For the Spectralon panels, Max error[(a)], average error[(a)] and RMSE[(a)] correspond to all ranges, while max error[(b)], average error[(b)] and RMSE[(b)] correspond to ranges > 4 m. For the painted board, max error[(a)], average error[(a)] and RMSE[(a)] correspond to all panels, while max error[(b)], average error[(b)] and RMSE[(b)] correspond to panels with reflectance < 60%.

Scanner	Validation experiment	Min error (%)	Max error[(a)] (%)	Average error[(a)] (%)	RMSE[(a)]	Max error[(b)] (%)	Average error[(b)] (%)	RMSE[(b)]
P20	90% panel	0.6	1.5	1.1	0.011	1.5	1.2	0.011
P20*	20% panel	0	7.4	1.6	0.006	1.7	1	0.002
	Painted board	1.1	8.3	5.1	0.043	5.3	3.6	0.020
P40a	90% panel	0.3	12.3	1.7	0.025	1.7	1.2	0.011
P40b	20% panel	1.7	8.3	3.4	0.009	4.6	2.9	0.007
	Painted board	1.5	7.2	3.3	0.022	5	3.1	0.012
P50	20% panel	0.1	6.9	1.8	0.005	3.2	1.1	0.003

*Additional validation for the forest data collection campaign.

For the additional validation experiments conducted for the P20 and $P40_b$ instruments using the multi-step painted board, the average of the relative errors was 3.3% and 5.1% for the $P40_b$ and the P20 instruments respectively. For the $P40_b$, the error was consistent in the two different validation experiments, which suggested that the wavelength of the instrument was not affected by the change in the target surface properties between the Spectralon panel and the wooden painted board. However, for the P20, the error in the multi-step painted board validation experiment was higher than that in the Spectralon panel experiment, suggesting that the NIR wavelength utilized in the instrument was affected by the target surface characteristics. The errors were higher in the two panels with reflectance > 60% than the remaining four panels. When these panels were excluded, as reflectance > 60% was highly unlikely to be encountered when scanning foliage, the errors dropped to 3.1% and 3.6% for the $P40_b$ and the P20 respectively. RMSE also dropped from 0.022 to 0.012 for the $P40_b$ and from 0.043 to 0.02 for the P20.

The average of the relative errors observed in all the validation experiments was 2.6%, which dropped to 2% when ranges < 4 m and multi-step painted board panels with reflectance > 60% were excluded. Thus, the accuracy of the calibration was considered suitable for the purpose of this study. It is worth mentioning that the intensity correction models were developed using almost perfect Lambertian panels, while in reality leaf and canopy reflectance is bidirectional and can be described by the Bidirectional Reflectance Distribution Function (BRDF). Leaf

BRDF not only depends on leaf surface spectral characteristics, but also on the direction of the incident light and the direction of scattered light. This means that the laser beam incidence angle and the TLS instrument viewing angle affect the amount of reflected energy that will reach the sensor and then be recorded as backscattered intensity. Similar to the incidence angle effects, accounting for leaf BRDF effects will be mandatory when using a single wavelength to estimate EWT, as leaves in different parts of the canopy will have different reflectance, not only because they have different EWT, but also because of their orientation in space in relation to the sensor. However, the use of NDI can minimize such effects, similar to the use of vegetation indices to minimize the effects of sun position and sensor viewing angle on satellite estimation of EWT. Radiative transfer models also approximate leaves as Lambertian surfaces, considering that combining multiple spectral bands can minimize leaf BRDF effects. Based on this assumption, models such as PROSPECT, PROSAIL, and GeoSAIL have been successfully utilized in estimating EWT from optical remote sensing data, as discussed in Section 2.3.2.

3.7.3 The ability of NDI to minimize the incidence angle effect

The effect of the incidence angle on both wavelengths was large in all species sampled (Figure 3-10), as the change in incidence angle between zero and 60 degrees reduced the SWIR reflectance by an average of 47% and the NIR reflectance by an average of 52%. The change in reflectance varied between species, with minimum and maximum changes being 29% (hornbeam) and 67% (poplar) respectively in SWIR reflectance, and 36% (hornbeam) and 68% (poplar) respectively in NIR reflectance. The effect of incidence angle was higher on NIR wavelength than in SWIR, agreeing to the observations reported in Hancock *et al.* (2017). Using NDI largely minimized the incidence angle effects for all six species (Figure 3-10c). Changing the incidence angle between zero and 40 degrees caused an average change in NDI of 6.7% across all leaf samples, with the change in NDI ranging between 0.2% (hornbeam) and 12% (grey alder). Changing the incidence angles between zero and 60 degrees caused an average change of 13.7% in NDI, with the change in NDI varying between 3.7%, and up to 19% in the grey alder leaf samples. One reason for the more significant change in NDI at 60 degrees incidence angle can be that leaves are not perfectly Lambertian surfaces, meaning they only follow the cosine law to an extent. Furthermore, at 60 degrees incidence angel it became very difficult to accurately distinguish between points corresponding to leaf samples and those corresponding to the edge of the frame, because of the partial hits between the leaves and the frame. This has contributed to the deviation observed.

Overall, the average change in NDI for all species and incidence angles, including the deviations at 60 degrees for the grey alder leaves, was 9%. For the same leaf samples, the change in NDI caused by the change in EWT between minimum and maximum was 53%, showing that EWT had more significant impact on NDI than the remaining effects of the incidence angle. Hancock *et al.* (2017) reported similar observations for NDI of 1064 nm and 1545 nm, also observing deviations at 10, 40, and 60 degrees incidence angles for some leaf samples, which was more than the deviation observed at 60 degrees in this study, and concluding that the change in NDI caused by the change in EWT was more significant than that caused by the incidence angle effects.

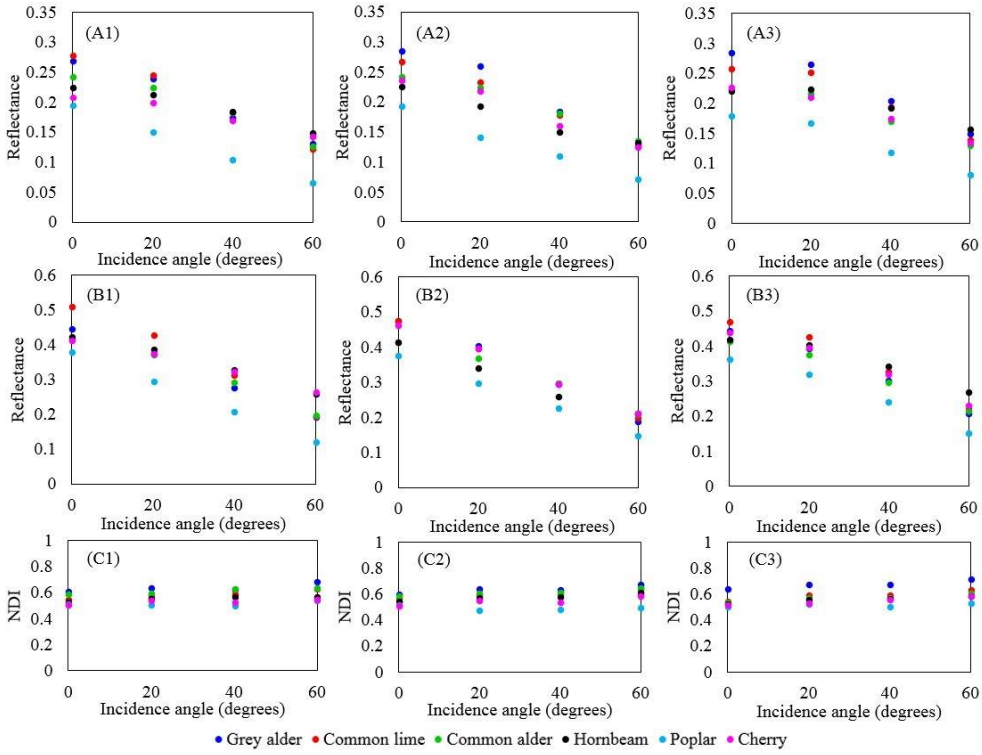

Figure 3-10. The reflectance-incidence angle relationship for leaf samples for the 1550 nm wavelength: (A1) group 1, (A2) group 2 and (A3) group 3; the reflectance-incidence angle relationship for the 808 nm wavelength: (B1) group 1, (B2) group 2 and (B3) group 3, and the NDI-incidence angle relationship: (C1) group 1, (C2) group 2 and (C3) group 3.

3.7.4 The ability of NDI to minimize the leaf structure effects

Changing N affected the modelled leaf reflectance in the visible, NIR and SWIR regions of the electromagnetic spectrum, with higher values of N leading to an increasing reflectance (Figure 3-11a). The two wavelengths in the scope of this study, 808 nm and 1550 nm, showed similar sensitivity to the change in N (Figure 3-11b). Combining the two wavelengths in the NDI

minimized the effects of N. However, it did not entirely eliminate these effects (Figure 3-11b). A leaf with a more compact mesophyll structure would have a slightly higher NDI value than a leaf with a more differentiated structure, even if they both had an identical EWT.

LMA affected the leaf reflectance in the NIR and SWIR regions only, with the least effect being around the water absorption wavelengths of 1400 nm, 2500 nm, and especially 1900 nm. Increasing LMA resulted in a lower leaf reflectance (Figure 3-12a). The 808 nm and the 1550 nm wavelengths were both sensitive to the change in LMA, and combining them in the NDI minimized, but did not eliminate, the effects (Figure 3-12b). A leaf with respectively lower dry matter content would have a slightly lower NDI than a leaf with higher dry matter content that has the same surface area and EWT value.

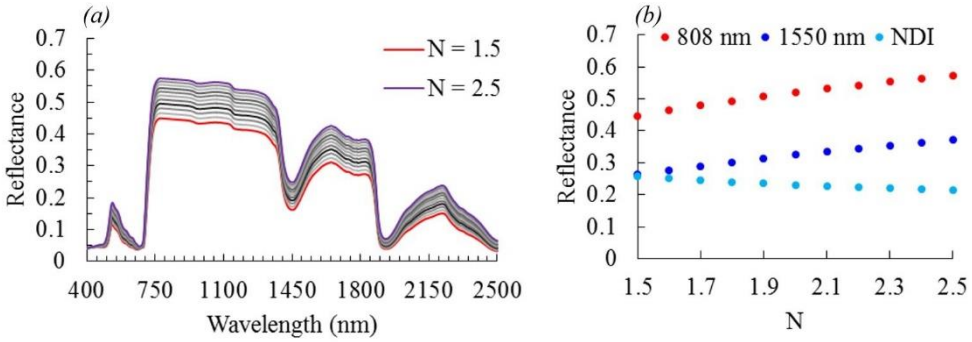

Figure 3-11. *(a)* Effects of N on the leaf reflectance in the visible, NIR and SWIR regions of the electromagnetic spectrum, and *(b)* effects of N on 808 nm wavelength, 1550 nm wavelength and NDI.

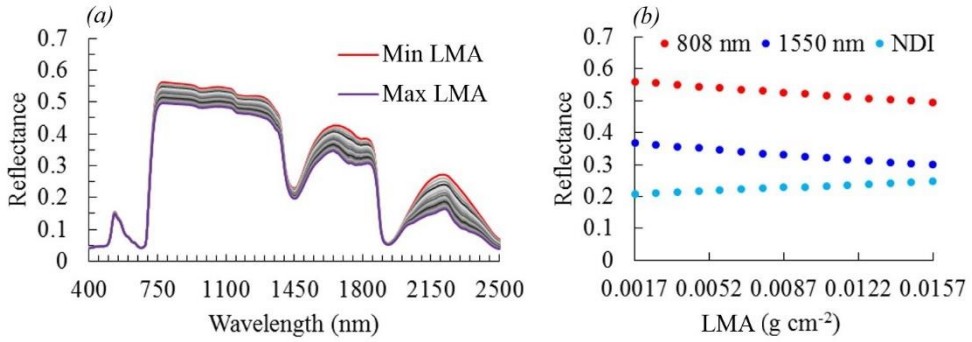

Figure 3-12. *(a)* Effects of LMA on the leaf reflectance in the visible, NIR and SWIR regions of the electromagnetic spectrum and *(b)* effects of LMA on 808 nm wavelength, 1550 nm wavelength and NDI.

The NDI – EWT relationship was affected by the change in N, with an increase in N leading to a shift in the trendline of the NDI – EWT relationship downwards (Figure 3-13). The effects of N appeared to be larger for higher EWT values. The relationship was also affected by the LMA value, with an increase in LMA value causing the trendline of the NDI – EWT relationship to be shifted up (Figure 3-14). Unlike N, the effects of LMA were slightly larger for lower EWT values. It is worth mentioning that although N and LMA were considered uncorrelated parameters in the simulations, for the sake of studying their effects on NDI individually, they are highly correlated in reality. N is correlated to the Specific Leaf Area (SLA) parameter, which is the leaf surface area divided by the leaf dry mass, and an increase in SLA leads to a decrease in N (Jacquemoud and Baret, 1990). Thus, N is also highly correlated to LMA, as LMA is the reciprocal of SLA. A thinner leaf would frequently have a lower N value than a thicker leaf, and correspondingly a lower LMA value. Although the PROSPECT simulations revealed that both N and LMA individually slightly affected NDI, when their effects were combined they would be minimized as they would cancel each other out. Thus, a change in NDI would be mainly caused by a change in EWT, with some minor influence of N and LMA. Thus, the NDI has the potential to be used to estimate EWT at canopy level in forest plots with mixed species, as the leaf internal structure would have a minimal effect on the estimation.

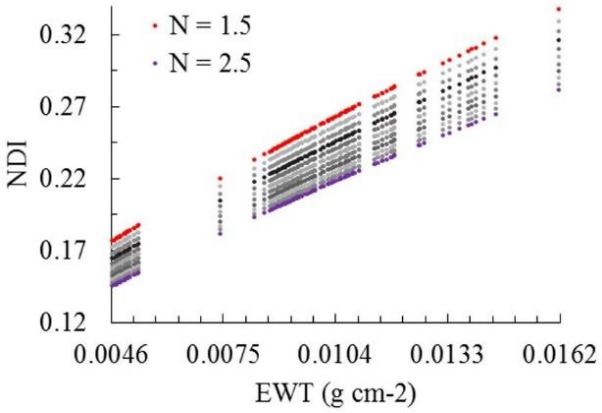

Figure 3-13. Effects of leaf structure coefficient on the NDI – EWT relationship.

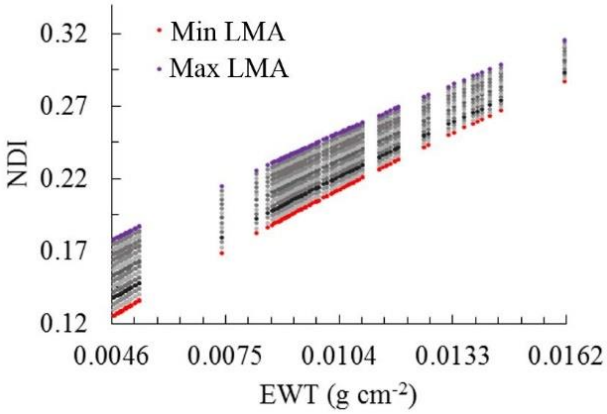

Figure 3-14. Effects of LMA on the NDI – EWT relationship.

3.8 Summary

This chapter described the characteristics of the TLS instruments used in this study and the method for combining their data to produce 3D EWT estimations. The details of the calibration work for each instrument were given, then the ability of the NDI of 808 nm and 1550 nm wavelengths to minimize the incidence angle and leaf internal structure effects was investigated.

The intensity data from the four TLS instruments involved in this research was found to be heavily affected by the range effect. None of the intensity – range relationships followed the laser equation. In addition, each TLS instrument was found to have its unique intensity-range relationship, thus, each instrument needed its own calibration model. The instruments were found to be equipped with a near-distance intensity reducer. Plus, they also seemed to be equipped with far-distance intensity amplifiers and on-board range calibration adjustments, which attempted to calibrate the intensity for the range effect starting from a specific range, which differed between the instruments. The calibration models developed were found to be able to calibrate the intensity for the range effect and to apparent reflectance with low errors. Although the errors observed at ranges < 4 m were higher than the remaining ranges, this was not considered a problem as none of the scans planned in the data collection campaigns were to be conducted at such near ranges.

The incidence angle had a severe influence on the intensity data of both the near and the shortwave infrared wavelengths. Using NDI minimized the incidence angle effect with no need for further radiometric calibration for a variety of leaf samples from different tree species. Some deviation, however, was observed at 60 degrees incidence angle, which may introduce some

errors while applying this method at the canopy level in real forest environments, as laser beams will hit the leaves at all possible incidence angles (Kaasalainen *et al.*, 2018).

PROSPECT simulations revealed that the leaf internal structure, defined in the model as the leaf mesophyll structure coefficient (N) and LMA, affected the reflectance at both the 808 nm and the 1550 nm wavelengths. Increasing N resulted in a higher leaf reflectance while increasing LMA reduced the leaf reflectance. The simulations also revealed that combining the two wavelengths in the NDI can minimize, but not entirely normalize, such effects. EWT was found to be the main parameter affecting NDI, but there remained some minor influences of N and LMA, which may reduce the accuracy of EWT estimation in mixed-species sites that exhibit significant variation in N and LMA, for instance, sites that combine green and senescent leaves.

The experiments described in this chapter and the results obtained showed the possibility of retrieving reflectance data from the four TLS instruments tested with low errors, and also demonstrated the ability of NDI of the two wavelengths in the scope of this research to minimize the incidence angle and leaf internal structure effects. Such ability can allow the use of NDI to estimate EWT at the canopy level without the need for radiometric corrections for the incidence angle effects, and for the variation in the leaf internal structure within each individual species or between different species. This can allow the use of NDI to estimate EWT in 3D at canopy level.

Chapter 4. EWT estimation in indoors dry-down experiment

4.1 Introduction

This chapter describes a dry-down experiment conducted in a laboratory setting using four small trees from two different species. The instruments used in the experiment were the Leica P20 and the $P40_a$. The aim of the experiment was to investigate the ability of NDI to estimate EWT at leaf level, and the possibility of upscaling the estimations to canopy level. Challenges associated with the estimation of EWT at the canopy level were studied, which included the accuracy of the registration, the possibility of calculating NDI on a point-by-point basis, and the effect of the woody materials on the EWT estimation accuracy. The experiment also examined the vertical distribution of EWT at the canopy level and the ability of the proposed approach to detect the change in EWT over a short period of time. Additionally, the experiment investigated how the drying pattern varied between the two different species. However, the experiment can only be considered a proof-of-concept as it included one deciduous and one conifer species, and 3D EWT point clouds were generated for a single tree from each species. The experiment was a step towards transferring the EWT estimation approach to a real forest environment. The content of this chapter was published in Elsherif *et al.* (2018).

4.2 Experimental setup

The dry-down experiment was conducted at the School of Environment and Life Sciences, Salford University, Manchester, UK. The trees involved in the experiment were two deciduous Snake-bark maple (*Acer davidii*), with an approximate height of 2.6 m each (Figure 4-1a), and two Corsican pine (*Pinus nigra*) conifers, approximately 0.9 m in height (Figure 4-1b). The duration of the experiment was eight days for the deciduous canopies and nine days for the conifer canopies. For each species, one tree served as a control unit and was watered regularly, whilst the other acted as a dry-down unit and was left to dry naturally.

The trees, together with a 50% Spectralon panel, were placed 6.5 m away from a tripod, ensuring a clear space of at least 1 m between them and the wall behind. Neither the trees nor tripod were moved during the entire period of the experiment, thereby ensuring the scanners occupied the same survey point in all scans and faced the trees from the same viewing angle. The canopies were scanned by the P20 instrument followed by the $P40_a$ instrument on each day of the experiment, except for two days on which access to the building was not granted, resulting in 6 scans for the deciduous canopies and 7 for the conifer canopies. For consistency,

all scans were conducted at 11 am, with a duration of 10 minutes for each instrument, and leaf sampling (Section 4.3) was carried out immediately after the scans to ensure that the leaf samples represented canopy EWT at the time of the scan, as leaves lose moisture during the day as a result of photosynthesis. No scans were conducted predawn, and all the scans were carried out with the instruments' highest point spacing (0.8 mm at 10 m).

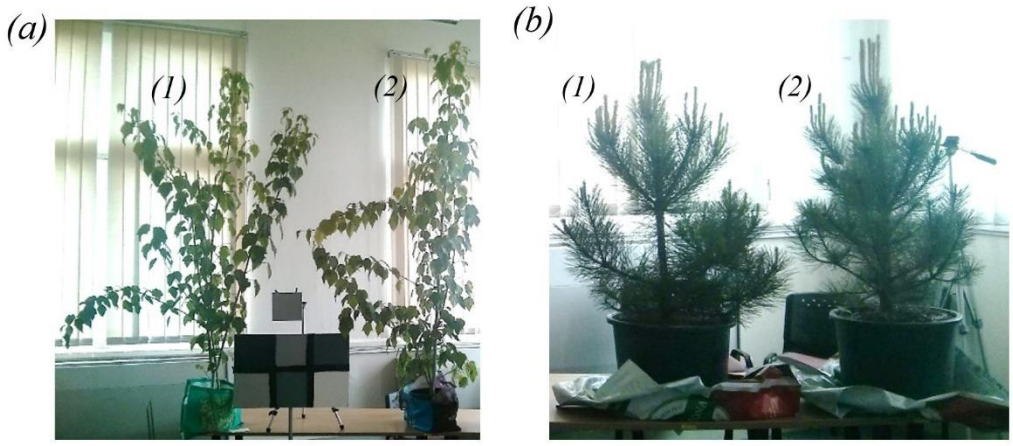

Figure 4-1. The trees involved in the indoors dry-down experiment: (*a*) the deciduous canopies and (*b*) the coniferous canopies, while (*1*) indicates the control units and (*2*) indicates the dry-down units.

4.3 Leaf sampling and biochemistry measurements

4.3.1 Deciduous leaves

Three leaf samples were collected daily from the dry-down unit, except for days 4 and 7, resulting in a total of 18 leaf samples. Collecting more daily samples was not possible in order to avoid defoliation of the small canopy. To add species variety to the experiment, nine additional leaf samples were collected randomly from five different species in Peel Park in Salford, Manchester. The leaf samples included: three leaves of grey alder (*Alnus incana*), two leaves of common lime (*Tilia x europaea*), one leaf of common alder (*Alnus glutinosa*), one leaf of poplar (*Populus sp.*), and one leaf of cherry (*Prunus avium*). Processing the leaf samples followed the steps described in Section 3.3.4. The fresh weight of each leaf was measured immediately on collection, then the leaves were suspended in a wooden frame and successively scanned by the P20 and $P40_a$ scanners, at a distance of 6.5 m. NDI was calculated following Equation (2.5) after calibrating the intensity to apparent reflectance using the calibration models described in Section 3.7.1. EWT of each leaf was calculated following Equation (2.1) after measuring the surface area and dry weight of each leaf sample.

4.3.2 Conifer needles leaves

Three needle samples were collected daily from the dry-down unit, except for days 5 and 8. Each sample consisted of 25 to 45 needles. The weight of the needles in the sample was measured and considered the sample fresh weight. The needles in each sample were then taped together, side by side from the top, to form a wider surface that could be scanned. They were scanned as a single unit by both the P20 the $P40_a$ scanners. The surface area of each sample was considered the summation of the surface areas of the needles in the sample, while the surface area of each individual needle was estimated as the length of the needle multiplied by the needle width (estimated at 1 mm). To measure the needle samples' dry weight, the samples were dried in an oven for eight days at 60 degrees Celsius. Samples were weighed every two days until no change in weight was detected. EWT of each needle sample was calculated according to Equation (2.1). Similar to the broadleaf samples, NDI of the reflectance was calculated for each needle sample following Equation (2.5).

4.4 Canopy level data processing and analysis

4.4.1 Point cloud processing

Processing the canopy level point clouds to produce an NDI point cloud on each day of the experiment followed the steps described in Sections 3.3.2 and 3.3.3. The scans were imported into Leica Cyclone and the partial canopy hits were reduced from the point clouds using the Cyclone partial hits filter on medium setting. Each $P40_a$ and P20 point cloud pair was registered in Leica Cyclone. The P20 point clouds were then filtered to match the same number of points in the corresponding $P40_a$ point clouds using a nearest neighbour function, as described in Section 3.3.3.

The registered point clouds were then calibrated for the range effect on a point-by-point basis using the calibration models described in Section 3.7.1. NDI was calculated for each pair of $P40_a$/P20 scans on a point-by-point basis and an NDI point cloud for each day of the experiment was generated. Mean NDI at canopy level was compared to the mean EWT of the leaf samples of the dry-down unit on each day of the experiment. The NDI point clouds were then transformed to EWT point clouds by applying Equation (4.1) and Equation (4.2), on a point-by-point basis, for the deciduous and conifer canopies respectively, derived in Section 4.5.1.

4.4.2 Removing the woody materials

The histogram of the EWT distribution at canopy level on day 1 was used to separate the woody materials from the leaves by choosing a separation threshold by trial and error, until few points

corresponding to leaves were incorrectly filtered as woody materials. The threshold was then applied to the point clouds on all days of the experiment. In the case of the conifer canopies, the threshold incorrectly extracted too many points corresponding to needles in the point cloud of day 9, as they represented very dry needles that were misclassified as wood. Thus, the identified woody points for day 1 were used as a reference, and were compared to the filtered points on day 9. The cloud-to-cloud distance module in CloudCompare v.2.6.2 software package was used to identify the filtered points on day 9 that were less than 1 mm away from the corresponding filtered points on day 1. These points corresponded to the stem and branches. The remaining points were extracted and re-added to the needle point cloud.

4.4.3 Studying the effect of wood on the EWT estimations

The average estimated EWT for each day of the experiment was calculated from the point cloud of the dry-down unit, as the summation of the water content of all points in the EWT point cloud, divided by the number of points. The estimated EWT at canopy level, before and after filtering the woody materials, was compared to EWT from leaf samples on each day of the experiment, not with the aim of validating the estimation, which requires destructively sampling the whole canopy, or collecting a different set of leaf samples for the sole purpose of validating the EWT estimates, but to study the effect of the presence of woody materials on upscaling EWT estimation from leaf to canopy level.

4.4.4 Detecting the change in EWT

The estimated EWT of the control and dry-down units, on each day of the experiment, after removing the woody materials, was plotted against the corresponding day to investigate the ability of the proposed approach to detect the change in EWT.

4.4.5 Studying the EWT vertical profiles

To study the vertical heterogeneity of the EWT, after filtering the woody materials, the EWT point clouds of the dry-down unit on all days of the experiment were divided into 9 horizontal layers (5 horizontal layers for the conifer canopy) and the average EWT for each layer was calculated and plotted against the corresponding height.

4.5 Results and discussion

4.5.1 Leaf level results

A strong linear relationship between NDI and EWT was found for the Snake-bark maple leaf samples (Figure 4-2a, $R^2 = 0.82$, $P < 0.05$). The following equation was derived from the relationship, which can be used to estimate EWT from NDI for this species:

$$EWT\ (g\ cm^{-2}) = 0.0594 \times NDI - 0.0052 \quad (4.1)$$

A strong linear relationship was also found between NDI and EWT for the additional nine leaf samples (Figure 4-2b, $R^2 = 0.94$, $P < 0.05$). The strong relationship holds ($R^2 = 0.91$, $P < 0.05$) when all the leaf samples were combined together (Figure 4-2c).

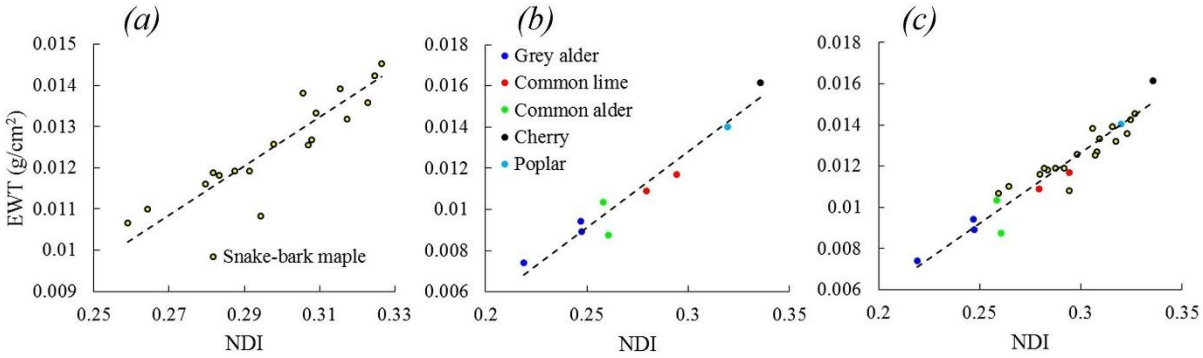

Figure 4-2. Leaf level results of NDI against EWT for (*a*) Snake-bark maple leaf samples, (*b*) the additional leaf samples and (*c*) all leaf samples combined.

For the conifer needles, NDI was found to be highly correlated to EWT (Figure 4-3, $R^2 = 0.74$, $P < 0.05$). The relationship between NDI and EWT for this species had significantly different slope and intercept than that of the deciduous species, as a result of the different leaf internal structure between broadleaf and needles. The NDI – EWT relationship can be described as:

$$EWT\ (g\ cm^{-2}) = 0.1148 \times NDI - 0.0022 \quad (4.2)$$

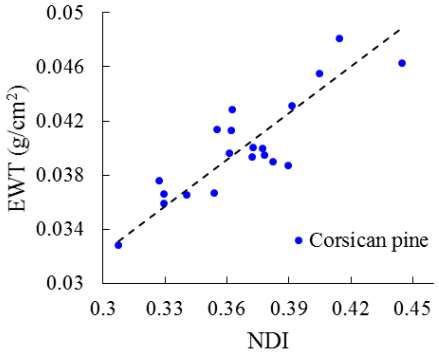

Figure 4-3. Leaf level results of NDI against EWT for the conifer samples.

4.5.2 Canopy level EWT estimation

The registration accuracy, reported by Leica Cyclone, of the $P40_a$/P20 point clouds obtained on all days of the experiment was very similar, as the scan geometry was constant. RMSE of the registration ranged between 0.7 and 0.8 mm for all the scans, which was very close to the

utilised scan resolution (0.8 mm at 10 m). Figure 4-4 shows a 3D EWT point cloud for the control and dry-down units of the deciduous canopies on day 8, alongside the histogram of the water content distribution. Figure 4-5 shows the same for the conifer canopies on day 9. Visual inspection of the EWT point clouds and histogram on all days revealed that the woody materials had higher water content than the leaves in the deciduous canopies, possibly because the trees were young and the woody materials were green. Green wood can have similar moisture content to leaves or even higher (Waterman *et al.*, 1983). In the case of the conifer canopies, the woody materials (brown and mature) had lower water content than the needles. The visual inspection also showed some stress in the bottom part of the dry-down canopies in comparison to the control canopies.

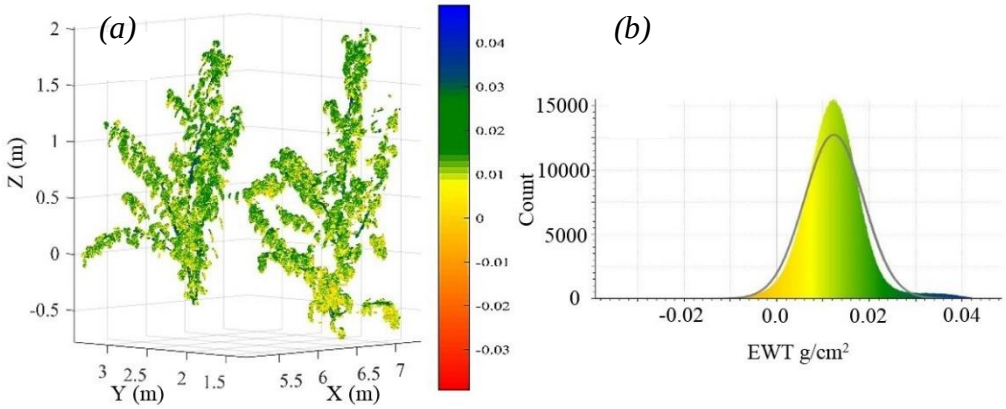

Figure 4-4. For the deciduous canopies, (*a*) 3D EWT (g/cm^2) distribution of the control unit (left) and the dry-down unit (right) on day 8 and (*b*) the histogram of the EWT (g/cm^2) distribution for the dry-down and control units combined.

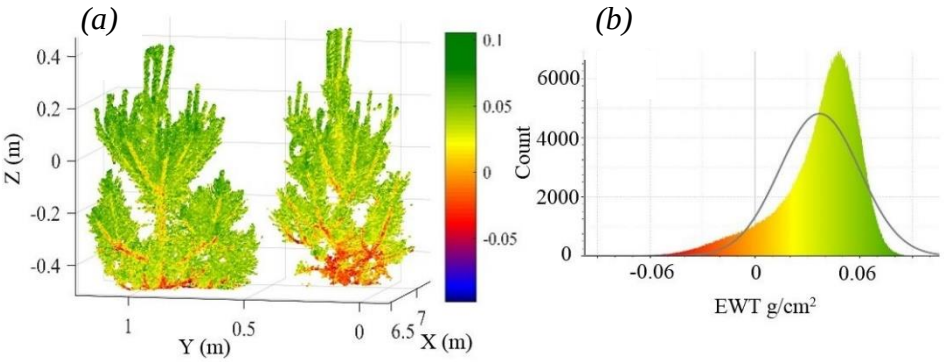

Figure 4-5. For the conifer canopies, (*a*) 3D EWT (g/cm^2) distribution of the control unit (left) and the dry-down unit (right) on day 9 and (*b*) the histogram of the EWT (g/cm^2) distribution for the dry-down and control units combined.

Thresholds of 0.028 g/cm^2 for the deciduous trees was applied to the EWT point clouds to extract the woody materials, which had EWT > 0.028 g/cm^2. For the conifers, the woody materials were found to have EWT < 0.011 g/cm^2 and the threshold was used for leaf/wood separation. Figure 4-6 illustrates the extracted woody materials of the EWT point clouds shown in Figure 4-4 and Figure 4-5.

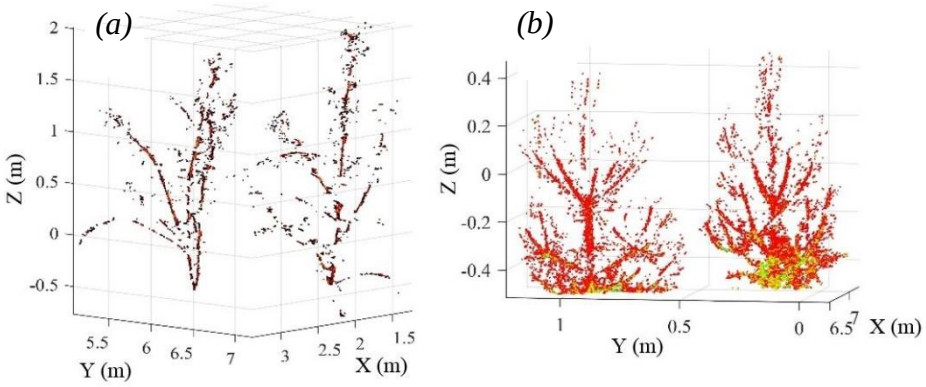

Figure 4-6. The extracted woody materials, (*a*) the deciduous canopies on day 8 and (*b*) the conifer canopies on day 9, many needles were incorrectly filtered as wood in the conifer dry-down unit.

NDI at canopy level for the dry-down units, before and after extracting the woody materials, were plotted against EWT of leaf samples (Figure 4-7). The results revealed a linear relationship with R^2 of 0.57 and 0.48 for the deciduous and conifer canopies respectively before filtering the woody materials ($P > 0.05$). Filtering the woody materials had little effect on the NDI – EWT relationship for the deciduous canopy, but improved the relationship for the conifer canopy ($R^2 = 0.73$, $P < 0.05$). In addition, the NDI – EWT relationship for the deciduous canopy was affected by the measured EWT of the leaf samples on day 6 being higher than the previous days (see Figure 4-8), but would be expected to be lower as the canopy had dried more. Excluding the results of day 6, likely to result from a laboratory measurement error, improved the correlation ($R^2 = 0.89$, $P < 0.05$).

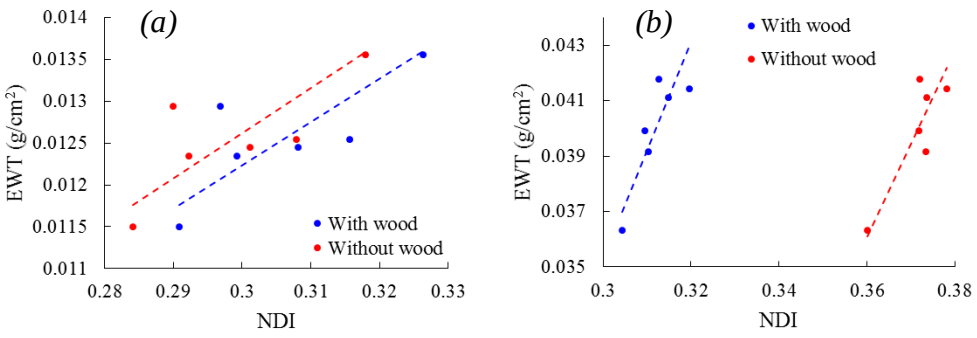

Figure 4-7. NDI at canopy level against EWT of leaf samples for the dry-down units, (*a*) the deciduous canopies and (*b*) the conifer canopies. The outlier on day 6 is included.

4.5.3 Studying the effect of wood on the EWT estimations

The estimated EWT at canopy level for the dry-down units were compared to EWT of leaf samples (Figure 4-8) and the relative error was calculated. The results revealed an overestimation on all days for the deciduous canopy when woody material was included, except for day 6, with an average of relative errors being 4.9%, and significant underestimation for the conifer canopy, with an average of relative errors equalling 16.6%. Studying the errors, alongside the histograms and point clouds of the EWT distribution, revealed that the higher error in EWT estimation in the conifer canopy seemed to be a result of the canopy having mature wood and a higher wood to leaf ratio than the deciduous canopy.

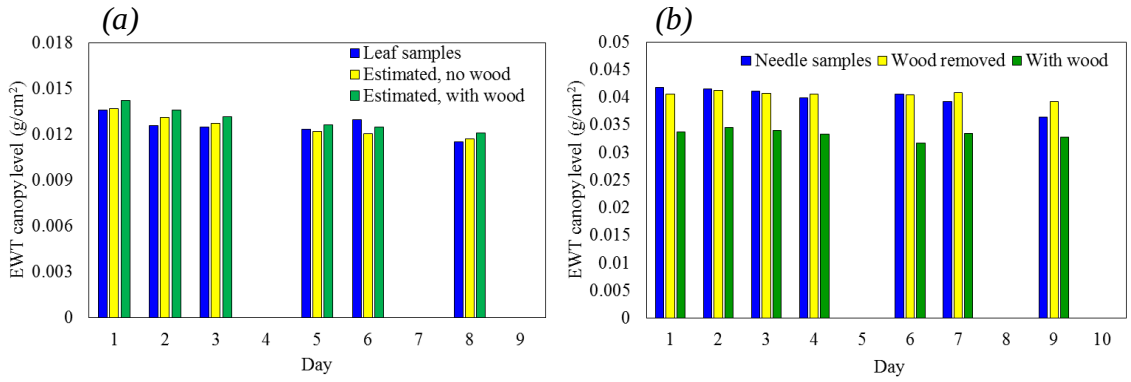

Figure 4-8. Estimated EWT at canopy level with and without the woody materials against EWT of leaf samples for the dry-down unit, (*a*) deciduous and (*b*) conifer.

Filtering of the woody materials reduced the average error in EWT estimation to 2.9% for the deciduous canopy, and significantly decreased the average error in the estimation to 2.6% for the conifer canopy. This revealed the strong effect of the presence of the woody materials on the upscaling of the TLS estimation of EWT from leaf to canopy level, especially when the wood was brown and mature.

4.5.4 Detecting the change in EWT

Figure 4-9 shows how the estimated EWT from the TLS measurements changed between the first and last day of the experiment for the control and the dry-down deciduous canopies, while Figure 4-10 shows the same for the conifer canopies. For the deciduous canopies, the control unit showed an almost constant EWT, with a slight increase in the first two days then a slight decrease in the remaining days. The dry-down unit, on the other hand, lost EWT throughout the days of the experiment, with EWT on the last day of the experiment being 15% less than that on the first day. The change in EWT appeared to be more significant in the first two days, as the canopy lost 7.3% of EWT, while it lost a total of 7.9% EWT between the third and last day of the experiment. In addition, a logarithmic model with $R^2 > 0.99$ can describe the drying pattern of the tree and could possibly be used to predict EWT beyond the duration of the experiment.

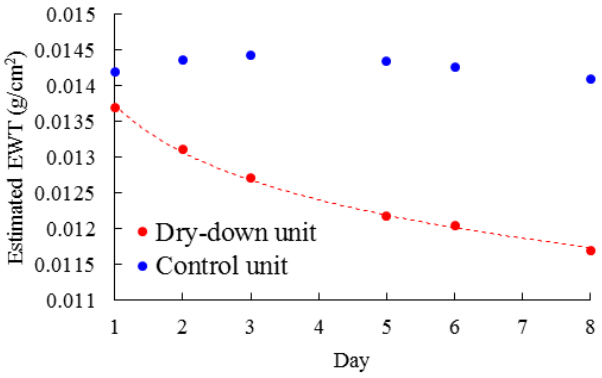

Figure 4-9. The change in the estimated EWT from TLS measurements over the duration of the experiment for the deciduous canopies.

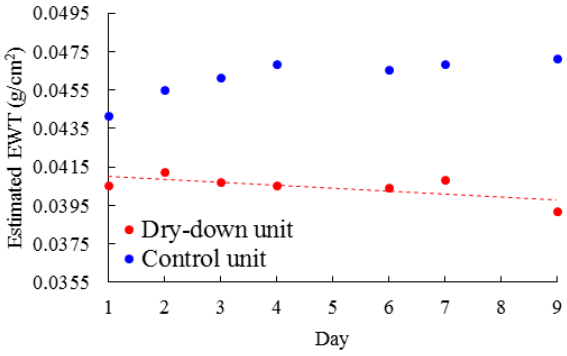

Figure 4-10. The change in the estimated EWT from TLS measurements over the duration of the experiment for the conifer canopies.

Furthermore, TLS could detect the daily change in EWT for the deciduous tree, showing that the tree lost approximately 3.7% EWT per day in the first two days in the experiment, and 1.6% EWT per day in the remaining five days. The ability of TLS to detect such fine changes in EWT suggested that there could be a potential in using TLS to detect canopy EWT changes throughout the day, and compare predawn EWT to midday EWT to quantify how much moisture plants lose during photosynthesis.

For the conifer canopies, a 6% increase in EWT occurred between day 1 and day 4 for the control unit, before EWT tended to be almost constant throughout the remaining days of the experiment. This could be a result of the tree receiving more daily water than it was getting in the nursery and/or the tree already being stressed before the start of the experiment. For the dry-down unit, the overall trend shows a slight decrease in EWT throughout the days of the experiment, with EWT on day 9 being 3.4% less than EWT on day 1. This was expected as conifer canopies are drought tolerant and use water efficiently (Moran *et al.*, 2017), suggesting that nine days were not enough time to cause severe stress.

4.5.5 Studying the EWT vertical profiles

Figure 4-11 compares the vertical distribution of EWT for the dry-down units on the first and last day of the experiment. The results revealed that the canopies had higher water content in the upper canopy than the lower canopy. For the deciduous canopy, the bottom of the canopy had 35% lower water content than the top on day 1, and 39.7% lower water content on day 8. For the conifer canopy, the bottom of the canopy had 33% lower water content than the top on day 1, and 40% lower water content on day 9.

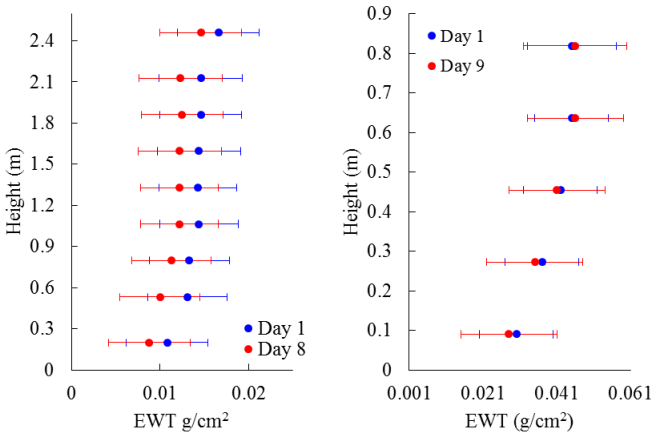

Figure 4-11. The vertical distribution of EWT for the dry-down units, (*a*) deciduous and (*b*) conifer, after filtering the woody materials.

Comparing the EWT vertical profile on day 1 and on the last day revealed that the deciduous canopy lost moisture from all parts of the canopy relatively evenly as it dried, with slightly greater water loss from the lower canopy. For conifer canopy, upper canopy EWT remained almost constant over the course of the experiment, with slightly greater water loss from the lower canopy. Although the deciduous and coniferous canopies were not fully destructively sampled to validate the EWT vertical profiles, the observations obtained agreed with the findings reported in Chavana-Bryant *et al.* (2016), a study in which younger leaves, typically in canopy top layers, were reported to have higher EWT than older leaves for 1099 leaf samples collected from 12 lowland Amazonian trees. Zhu *et al.* (2017) also reported EWT vertical heterogeneity in 20 small plants from five different species: dwarf schefflera, weeping fig, Chinese banyan, ficus, and Zanzibar gem, highlighting that EWT was always higher in canopy top than in canopy bottom. This was also explained as a result of new leaves at the top of the canopy having higher water content than older leaves (Mooney *et al.*, 1977). The EWT vertical heterogeneity and its possible causes are further investigated in Section 5.5.4.

4.6 Summary

This chapter described an indoor dry-down experiment conducted using two deciduous snake-bark maple canopies and two Corsican pine conifer canopies. The experiment aimed at investigating the relationship between the NDI of the 808 nm and the 1550 nm wavelengths and the EWT at leaf level and the possibility of using NDI to produce 3D EWT estimates at canopy level.

NDI was found to be highly linearly related to broadleaf EWT across various tree species, and also to needle EWT of the Corsican pine conifer canopy. However, as the experiment included samples from a single conifer species, the results obtained can only be considered preliminary and further experiments that include various conifer species are necessary in order to determine whether the NDI-EWT relationship will hold or not.

At the canopy level, a high registration accuracy was obtained for each $P40_a$/P20 point cloud pair on each day of the experiment, because of the similarity in the scan geometry. NDI estimated EWT on a point-by-point basis for the deciduous and conifer canopies, generating 3D distributions of EWT that revealed some vertical heterogeneity. The young leaves and needles in the upper canopy had higher water content than the older leaves/needles in the lower canopy. This, if also observed in a forest environment, can affect passive optical spaceborne or airborne sensor estimation of EWT, as measurements from such instruments will be dominated

by the canopy top (Liu *et al.*, 2015) (see Section 5.5.4 for EWT vertical profiles in forest canopies).

NDI overestimated the EWT for the deciduous canopy, and underestimated it for the conifer canopy on all days of the experiment, with the errors in the EWT estimation being proportional to the amount of woody material in the point cloud. Filtering the woody material significantly improved the EWT estimation accuracy for the conifer canopy, while having a minimum effect for the deciduous canopy, most likely because the wood was young and green in the deciduous canopy, but was brown and mature in the conifer canopy.

The 3D EWT estimates showed that the two different species had different drying patterns. The deciduous tree seemed to be equally losing EWT from all layers in the canopy while the tree dried between the first and last day of the experiment. On the other hand, the conifer canopy maintained an almost constant EWT in the upper canopy layers while losing water from the bottom layers. It was also possible to detect the change in EWT between the days of the experiments, with the change being more obvious in the deciduous canopy than the conifer canopy.

This experiment showed the potential of dual-wavelength TLS methods to better characterise and study heterogeneity in biochemistry within tree canopies, which can provide a new insight into tree stress and physiology. However, experiments in real forest environments need to be conducted to assess the applicability of the proposed EWT estimation approach in larger canopies and outdoor conditions (for example in the presence of wind). This was investigated in fieldwork campaigns, described in Chapters 5 and 6.

Chapter 5. Mapping of forest canopy EWT in three dimensions

5.1 Introduction

Forests are of great importance for humankind and the environment because of the essential ecological, economic and social services they provide (Yao *et al.*, 2014). They play a major role in the global carbon and hydrological cycles (Pan *et al.*, 2011), and influence the climate as a result of exchanging water, energy, carbon dioxide, and other chemicals with the atmosphere (Bonan, 2008). However, natural and anthropogenic threats, such as climate change, drought, disease infections, pest infestations, wildfires, land use change and deforestation, threaten forest health (Lewis *et al.*, 2015; Millar and Stephenson, 2015). Forest health monitoring is critical to understand how forests react to such stressors (Ferretti, 1997; Trumbore *et al.*, 2015), and also for early detection of drought stress, symptoms of disease, and risk of wildfire (Meentemeyer *et al.*, 2008).

As discussed in Section 2.3, optical RS data, airborne and spaceborne, have been widely adopted in estimating canopy EWT as a vegetation stress indicator to overcome the limitations of *in-situ* approaches (destructive methods and field spectroscopy), which are time and effort consuming and impractical for large areas (Pu *et al.*, 2003; Dash *et al.*, 2017). However, the effects of EWT vertical heterogeneity on the optical RS estimation of EWT still needs to be investigated. The results obtained in Chapter 4 showed the potential of using dual-wavelength TLS for estimating canopy EWT in 3D and generating EWT vertical profiles that can be used to quantify and study the EWT vertical heterogeneity within a canopy. However, the relationship between NDI and EWT at canopy level was investigated for small individual trees in a controlled environment only. In this chapter, the method was transferred to a real forest environment, and NDI was used to produce 3D estimations of EWT in a mixed-species broadleaf deciduous forest plot in Wytham Woods, Oxford, UK. The aims of the data collection campaign were to: (i) test the ability of NDI to generate 3D EWT estimates in a real forest environment where partial canopy hits, wind effect, and variation of leaf internal structure between species can affect the accuracy of the EWT estimates, and (ii) examine the vertical variation of EWT within forest canopies. The content of this chapter was published in (Elsherif *et al.*, 2019d). Prof. Yadvinder Malhi and Dr Alexander Shenkin, Environmental Change Institute, University of Oxford, have contributed to the results interpretation presented in Sections 5.5.1 and 5.5.4.

5.2 Study area and TLS scanning setup

The data collection campaign took place in Wytham Woods near Wytham village (51.78° N, 1.31° W) in Oxfordshire, UK, between 22nd and 31st of May 2017. Wytham Woods is approximately 400 ha and consists of ancient woodland and naturally-regenerated secondary woodland, in addition to nineteenth and twentieth-century plantations (Morecroft *et al.*, 2008). It has been owned by the University of Oxford since 1942 and is considered one of the most important sites for ecological research in the world (Morecroft *et al.*, 2001). The fieldwork data were acquired in a 35 × 45 m rectangular plot around the treetop canopy walkway in the 18 ha Wytham core plot (Figure 5-1 and Figure 5-2). Wytham core plot is a permanent sample plot, established in the woodland for research purposes (McMahon *et al.*, 2015).

The site was dominated by *Quercus robur* (oak) and *Acer pseudoplatanus* (sycamore) trees, in addition to a number of *Fagus sylvatica* (beech) and *Fraxinus excelsior* (ash) trees. The fieldwork campaign took place in non-windy, non-rainy conditions at an average temperature of 21° Celsius. Thirteen trees around the canopy walkway were selected for sampling, based on how accessible their leaves were from the canopy walkway (Figure 5-2). Ten scanning positions were set around the walkway in locations corresponding to low density canopy cover to reduce the effect of occlusion by lower branches and obtain as much detail (laser beam returns) as possible from the thirteen sampled trees (Figure 5-2).

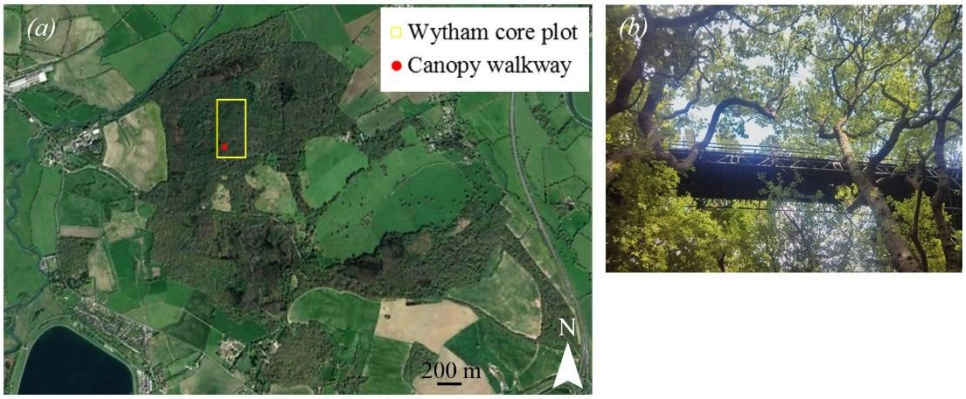

Figure 5-1. The study area: *(a)* Wytham woods and the location of Wytham core plot and *(b)* the treetop canopy walkway.

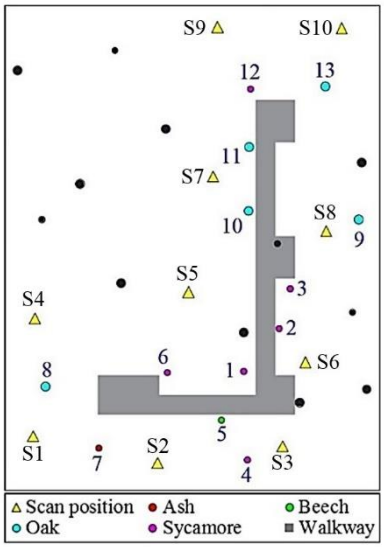

Figure 5-2. The 35 × 45 m rectangular plot and the thirteen sampled trees (indicated by numbers assigned during fieldwork). Black indicates trees that were not sampled.

At each scan position, full-hemisphere scans (360° × 270°) were conducted by the $P40_b$ and the P20 instruments, mounted consecutively on the same tripod, with a resolution (point spacing) of 3 mm at 10 m. Four Leica black and white registration targets were used to link each pair of consecutive scanning positions. The scans were conducted over a period of two days. On the first day, TLS data were collected from scanning positions S1 to S6, with the duration of each scan being approximately fifteen minutes for each instrument. Scanning began at 10 AM and the total scanning duration, including the time needed to move the instruments between different scanning positions, was approximately two hours. This was followed by leaf sampling, for the purpose of validating the EWT estimation (Section 5.3.2), from trees number 1, 2, 3, 4, 5, 6, and 8. No samples for validation were collected from the ash tree, labelled 7, as it was the only ash tree accessible from the treetop canopy walkway, and samples for building the EWT estimation model were collected from it (Section 5.3.1). It was acknowledged that canopy EWT may have undergone some changes over the two hours of scanning, as trees lost moisture during photosynthesis, and that the ideal leaf sampling approach was to collect the samples at the same time of scanning, ensuring that they accurately represented the canopy EWT at the time. However, this was not possible due to lack of personnel. On the second day, scans were carried out from scanning positions S7 to S10, starting at 10 AM and lasting for approximately 90 minutes, followed by collecting leaf samples for validation from trees number 9, 10, 11, 12, and 13. Afterwards, leaf samples for building the EWT estimation models were collected and processed as described in Section 5.3.1.

5.3 Leaf sampling and biochemistry measurements

5.3.1 Samples for building the EWT estimation model

Eighty-four leaf samples were collected randomly from various trees in the plot. The priority in sampling leaves for the EWT estimation model was to ensure a representative and broad sample of species, leaf types and EWT. Samples were collected from low branches in the canopy bottom that were accessible from ground using a tree pruner, and also from the canopy top, which was accessible using the treetop canopy walkway. The canopy top leaf samples predominantly represented sun leaves, while the canopy bottom leaf samples predominantly represented shade leaves. Sun leaves grow in the well-lit regions of the canopy and are usually thicker and have higher photosynthetic rates than shade leaves (Lichtenthaler *et al.*, 1981; Terashima *et al.*, 2005). The leaf samples included: 18 oak leaf samples, 22 beech leaf samples, 20 sycamore leaf samples, and 24 ash leaf samples. The ash leaf samples were individual leaflets of the compound leaves. Leaf sampling was carried out for each species separately. That is, the oak leaf samples were collected first, and the fresh weight of each sample was measured in field, immediately on collection, using an electronic balance (one milligram precision). The samples were then suspended in a wooden frame, positioned 8.6 m away from a tripod, and were scanned in field using the $P40_b$, followed by the P20 instrument, with a resolution (point spacing) of 0.8 mm at 10 m. The time gap between collecting the samples and scanning them was less than fifteen minutes, and the duration of the scan was approximately five minutes for each instrument. Afterwards, the same sampling approach was repeated for each species, one after another.

The leaf samples were then transferred to the laboratory and processed as described in Section 3.3.4 to measure their surface area, dry weight, EWT, and NDI. It is worth mentioning that before drying the samples in an oven, they were left to dry naturally over a period of two weeks. Afterwards, they were further dried in an oven for 48 hours at 60° Celsius and were considered fully dry as no change in weight was observed when they were weighed after 40, 44, and 48 hours. In addition to measuring EWT of each leaf sample (Equation (2.1)), LMA was measured according to Equation (3.3). Reduced major axis regression was used to determine the NDI – EWT relationship for each individual species, and also for all species combined.

5.3.2 Samples for validation of the EWT estimation

A total of 274 leaf samples were collected from twelve out of the thirteen trees shown in Figure 5-2, as the ash tree, labelled 7, was excluded from validation. Table 5-1 shows the number of leaf samples collected from each tree. The leaf samples were collected from two canopy layers:

the canopy top layer and the canopy bottom layer. This allowed the areas sampled for validation to be explicitly identified in the TLS point cloud. The canopy top layer was 1 m above the canopy walkway level (12 m), with a depth of one metre, while the canopy bottom layer consisted of the low branches that were accessible from the ground. EWT and LMA of each leaf sample were measured following the steps described in Section 5.3.1.

Table 5-1. Details of the species, locations and numbers of the leaf samples for the EWT estimation validation. The samples from the ash tree, labelled 7, were excluded.

Tree label	Species	Number of leaf samples	
		Canopy top layer	Canopy bottom layer
1	Sycamore	20	18
2	Sycamore	18	10
3	Sycamore	20	20
4	Sycamore	--	20
5	Beech	19	--
6	Sycamore	20	--
8	Oak	--	24
9	Oak	20	--
10	Oak	20	--
11	Oak	15	--
12	Sycamore	15	--
13	Oak	15	--
Total number		182	92

5.4 TLS point cloud processing

5.4.1 Point cloud registration and filtering

The point clouds from each instrument were registered in Leica Cyclone, using the registration targets, to build the forest plot. The registered P20 scans were then aligned to the registered $P40_b$ scans. The outcome was a pair of $P40_b$/P20 aligned point clouds at each scanning positions. Points corresponding to ground and understory vegetation were removed to reduce the size of the point clouds.

The P20 point cloud at each scanning position was filtered to match the same number of points in the corresponding $P40_b$ point cloud using a nearest neighbour function as described in Section 3.3.3. As the nearest neighbour function tried to find the nearest neighbour in the P20 point cloud to each point in the $P40_b$ point cloud, regardless of how far that nearest neighbour was, further filtering was required. A threshold of 3 cm was applied, that is, any pair of $P40_b$/P20 neighbour points > 3 cm apart was removed from the point cloud. The 3 cm threshold was

chosen on the basis of 96% of the nearest neighbour distances being < 3 cm apart, while 99% of distances were < 6 cm apart.

5.4.2 Generating the EWT point clouds

The filtered point clouds were calibrated to apparent reflectance and NDI was calculated for each pair of $P40_b$/P20 scans on a point-by-point basis. The NDI point clouds from the ten scanning positions were merged into a single point cloud that covered the entire 35 × 45 m rectangular plot. The sampled trees (Table 5-1) were manually extracted from the NDI point cloud. They were divided into three groups according to their species, sycamore, oak and beech. The species-specific NDI – EWT relationship found at leaf level, as described in Section 5.5.1 was applied to the NDI point clouds of each group, Equations (5.1), (5.2) and (5.3) for sycamore, oak, and beech respectively, and EWT point clouds were generated. In addition, the pooled NDI – EWT relationship that combined all species (Equation (5.5)) was applied to the NDI point clouds of the twelve trees, regardless of their species, to investigate the possibility of using a pooled EWT estimation model in a mixed-species forest plot without the need to classify the trees according to their species.

5.4.3 Validating the EWT estimations

Visual inspection of the NDI point cloud and histogram of each tree showed that foliage NDI was clustered around 0.3, while for wood it was clustered around zero. Wood typically is expected to have higher SWIR reflectance than green foliage, as it contains less moisture, while their NIR reflectance is expected to be similar at the wavelength used in this study (808 nm). This caused the lower NDI values of wood components. Applying the NDI – EWT estimation models, trained solely using green foliage, would then cause the majority of points corresponding to woody materials to have EWT value equal to or below zero, even if they had higher moisture in reality. The same applies to noise points, resulting from wrongly assigned nearest neighbours, that is, a full hit being assigned to a partial hit, resulting in a very low or a very high NDI value.

As the focus of this study was to estimate EWT of foliage only, a threshold of zero was used to disregard the points corresponding to wood and noise. Afterwards, using visual inspection, points that clearly corresponded to wood (being part of the trunk or primary branches) but which were wrongly classified as leaves, were manually removed. In addition, it was possible to visually identify and remove many of the points corresponding to lateral branches. However, it was not possible to identify and remove smaller branches and twigs. Additionally, a Gaussian

distribution was fitted to the EWT histogram and a threshold equal to twice the mean value was applied to filter points with very high EWT (Figure 5-3).

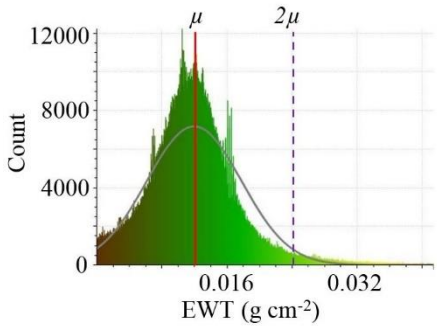

Figure 5-3. Example of using the mean *(μ)* of the fitted EWT histogram Gaussian distribution to remove the noise by applying a threshold equal to *2μ* (purple).

The layers from which the leaf samples were collected were extracted from each individual tree point cloud. The estimated EWT of each layer was compared to the actual EWT of the leaf samples collected from that layer and the relative error was calculated according to Equation (3.1).

The EWT point cloud of each tree was divided into a number of horizontal layers, each 1 m deep, after removing the woody materials. EWT of each layer was plotted against the corresponding height to produce the EWT vertical profile of the tree. The EWT vertical profiles were produced from the EWT point clouds generated using the pooled EWT estimation model (Equation (5.5)).

5.5 Results and discussion

5.5.1 Leaf level results

For each individual species, moderate correlation was observed between NDI and EWT (R^2 = 0.55, 0.57, 0.59 and 0.68 for the beech, ash, oak and sycamore species respectively, $P < 0.05$). Some differences in the slope, and more obviously in the intercept, of the NDI – EWT relationships were observed between the different species (Figure 5-4). This can be a result of the remaining effects of the leaf internal structure on the NDI, as PROSPECT simulations revealed that NDI can minimize but not entirely normalize such effects (Section 3.7.4). For instance, Figure 5-4 shows that there are numerous leaf samples with EWT around 0.0095 g/cm^2; however, they have NDI values varying between 0.21 and 0.25. Theoretically, they should have had similar NDI values, if there were no remaining effects for the leaf internal structure on NDI. Another factor that affected the slope and intercepts of the NDI – EWT

relationships was the narrow range of EWT values within each individual species, especially in beech, and it was not possible to determine the exact NDI – EWT relationship of each individual species using such small EWT ranges. Thus, a dry-down experiment may be needed if the aim was to determine the accurate NDI – EWT relationship for each species individually. The species-specific NDI – EWT relationships can be described as:

$$EWT\ (g\ cm^{-2}) = 0.0488 \times NDI - 0.0016, \text{ for sycamore} \quad (5.1)$$

$$EWT\ (g\ cm^{-2}) = 0.0553 \times NDI - 0.0031, \text{ for oak} \quad (5.2)$$

$$EWT\ (g\ cm^{-2}) = 0.0327 \times NDI - 0.0002, \text{ for beech} \quad (5.3)$$

$$EWT\ (g\ cm^{-2}) = 0.0534 \times NDI - 0.0032, \text{ for ash} \quad (5.4)$$

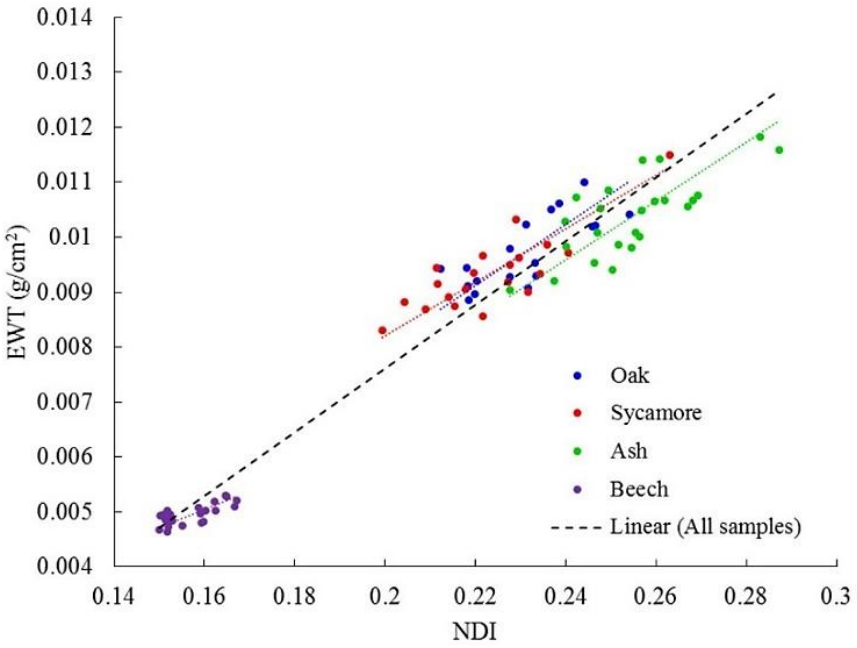

Figure 5-4. The species-specific and pooled NDI – EWT relationships.

It was possible to fit a linear model to all leaf samples combined ($R^2 = 0.94$, $P < 0.05$) (Figure 5-4). It is acknowledged that there remained a gap in the EWT values, between 0.0055 g/cm^2 and 0.008 g/cm^2, thus the high correlation can potentially be misleading as the samples were not normally distributed. However, the consistency of trends between the general and individual species models gave confidence it was suitable for application at the canopy scale. The pooled NDI – EWT model can be described as:

$$EWT\ (g\ cm^{-2}) = 0.0579 \times NDI - 0.0039 \quad (5.5)$$

The leaf samples collected for the purpose of validating the EWT estimates revealed a vertical heterogeneity in EWT within canopies. The average EWT of all leaf samples collected from the canopy top layer was 20% higher than that of the leaf samples collected from the canopy bottom layer (Figure 5-5). In addition, LMA of leaf samples from the canopy top layer was 42% higher than that of the canopy bottom layer, suggesting that the observed higher EWT in the canopy top was caused by the leaves having higher LMA, increasing their ability to hold moisture. To further investigate, the relationship between EWT and LMA was studied at leaf level (Figure 5-6), revealing that EWT and LMA were highly correlated (R^2 = 0.92, 0.61, 0.60 and 0.63 for beech, ash, oak and sycamore respectively), and that the relationship between EWT and LMA was species-specific. Junttila *et al.* (2019) also reported that EWT and LMA were highly correlated at the leaf level. Additionally, studying the EWT – LMA relationship within each species revealed some differences between the individual trees (Figure 5-6).

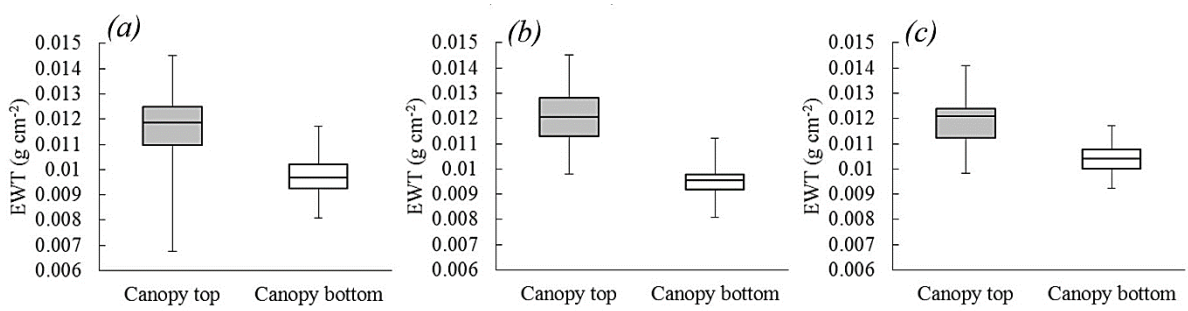

Figure 5-5. A boxplot of the EWT of the leaf samples in canopy top and canopy bottom layers: *(a)* all leaf samples combined, *(b)* sycamore, and *(c)* oak. The whiskers are the minimum and maximum values.

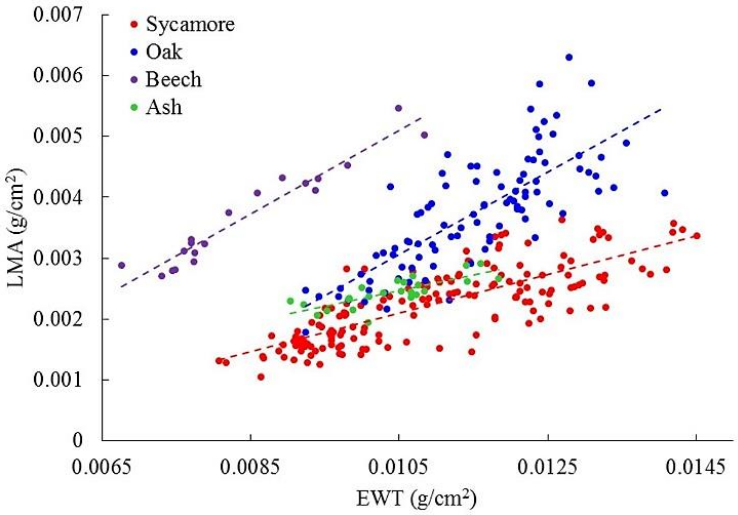

Figure 5-6. The EWT – LMA relationships at leaf level.

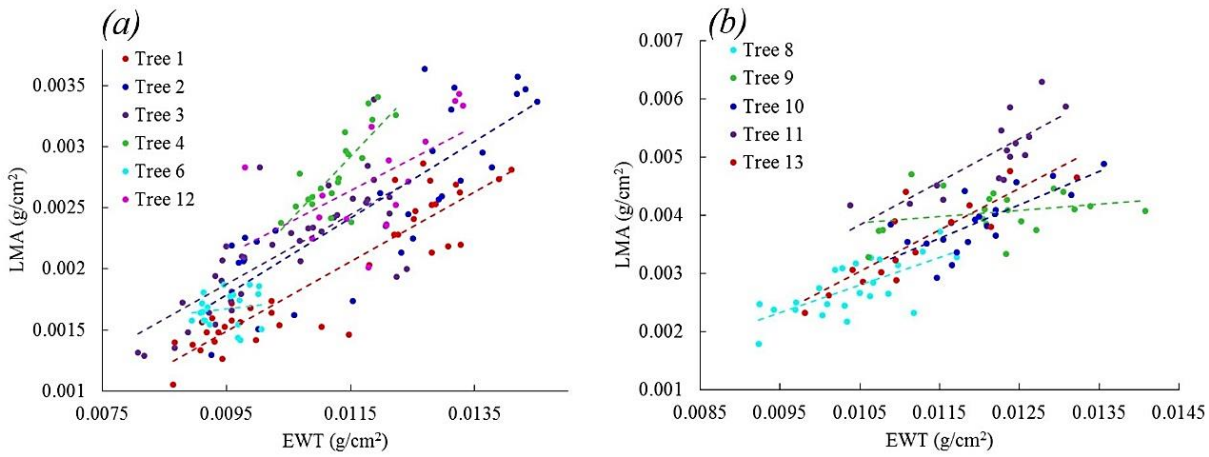

Figure 5-7. The EWT – LMA relationships of the individual trees: *(a)* sycamore and *(b)* oak.

Furthermore, the EWT – LMA relationship was investigated at the canopy level (Figure 5-8), which further showed that EWT and LMA were highly correlated and that the relationship between them was species-specific. Arellano *et al.* (2017) and Gara *et al.* (2018) also investigated the relationship between EWT and LMA at canopy level using destructive sampling, reporting that canopy layers with higher LMA had higher EWT.

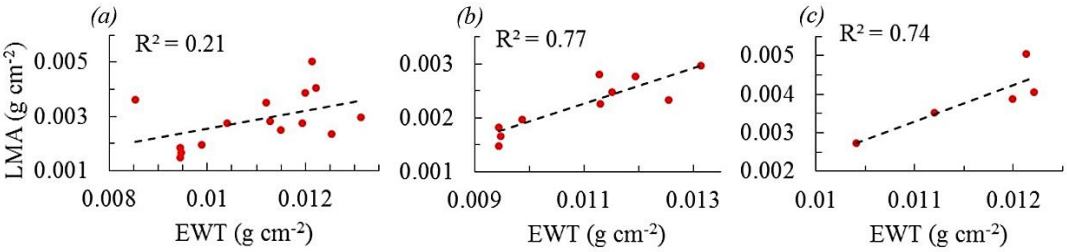

Figure 5-8. The relationship between EWT and LMA at canopy level: *(a)* all species combined, *(b)* Sycamore and *(c)* Oak.

5.5.2 EWT point clouds

The RMSE of the point cloud registration, reported by Leica Cyclone, was 3 mm for each instrument separately. As the scans were conducted at a resolution of 3 mm at 10 m, the registration accuracy was considered sufficient. The RMSE of the registration of the P20 point clouds to the P40 point clouds was 1 mm. The high accuracy was a result of the similarities between the two instruments in terms of their scanning mechanism and laser beam exit location, and also a result of the similar scanning geometry. Another key factor was the absence of wind. Scanning in more windy conditions would be expected to significantly reduce the registration

accuracy (see the willow dataset, Section 6.3.2). The high registration accuracy allowed the generation of 3D EWT point clouds, as shown in Figure 5-9 and Figure 5-10.

Figure 5-9. The 3D EWT distribution of the sampled trees.

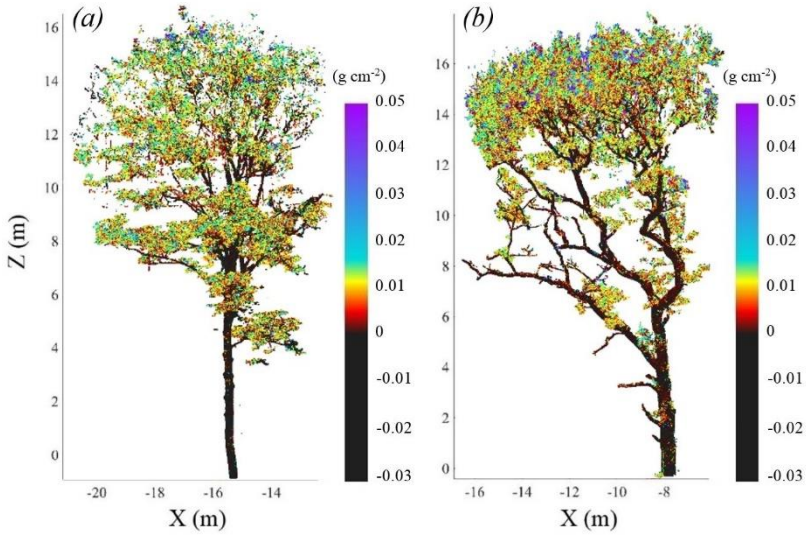

Figure 5-10. Examples of the 3D EWT distribution of individual trees: *(a)* Sycamore tree, labelled (6), and *(b)* Oak tree, labelled (11).

The point clouds revealed a significant difference between the leaf and wood EWT, showing some potential of using the 3D EWT distribution in separating the leaf from the wood using zero EWT as a separation threshold. However, testing this method revealed that many points that clearly corresponded to wood (e.g. trunk, primary branches, lateral branches) had above zero EWT, and thus were mistakenly classified as leaves. Attempting to filter these points using a higher threshold resulted in removing points clearly corresponding to leaves. Thus, these

points had to be removed manually, which rendered this leaf – wood separation method impractical at the plot scale. In addition, it was not possible to visually identify and manually remove misclassified points that corresponded to small branches and twigs. Additionally, numerous points corresponding to leaves were also classified as wood, as they had below zero EWT. This could be a result of wrongly assigned nearest neighbours, as discussed in Section 5.4.3. It was possible to filter these points using the statistical outlier removal tool in the CloudCompare v. 2.6.2 software, as they were sparse points in comparison to the very dense points in the trunk and branches. However, this method may also filter small branches and twigs, and as no field measurements were conducted to validate this leaf-wood separation approach, it was not possible to determine its accuracy.

5.5.3 Validating the EWT estimations

Comparing the estimated EWT to the actual EWT from the leaf samples revealed a relative error of 7.7% on average in the EWT estimations for the species-specific models and 6.3% for the pooled model. Table 5-2 summarizes all the observed errors. All errors were < 10%, except for the errors obtained in the canopy top layer in sycamore trees number 2 and 12, and in the canopy bottom layer in oak tree number 8, in addition to a high error (-21%) in the beech tree. This high error in the beech tree can be a result of the narrow range of EWT in the leaf samples used to build the EWT estimation model, which was insufficient to accurately determine the slope and intercept of the NDI – EWT relationship. In the dry-down experiment (Chapter 4), the Snake-bark maple species-specific model produced errors < 3% when applied at the canopy level, mainly because the model covered a wide range of EWT values, being calibrated using leaf samples collected while the canopies were drying down. This suggested that if the aim was to use a species-specific model to estimate EWT at the canopy level, carrying out a dry-down experiment would be recommended. This can be conducted by scanning the leaf samples and measuring their weight once collected, then leaving them to dry naturally over a period of at least one week, while scanning them and measuring their weight at fixed intervals. The leaves can then be dried in the oven to measure their dry weight, then the NDI – EWT model can be calibrated. This can ensure that the model covered a wide range of NDI and EWT values for this species, which can then lead to a more accurate estimation of EWT at the canopy level using the species-specific model.

Table 5-2. EWT estimation errors in the twelve trees, for the canopy top and bottom layers. The signs of the errors were ignored while calculating the average and total errors.

Tree	Species	Relative error in EWT estimations			
		Species-specific models		Pooled model	
		Canopy top	Canopy bottom	Canopy top	Canopy bottom
1	Sycamore	-5.9%	9.2%	-5.3%	7.2%
2	Sycamore	-13.5%	6%	-13.5%	4.3%
3	Sycamore	-2.5%	6.9%	-2.7%	4.3%
4	Sycamore	---	9.3%	---	7.3%
5	Beech	-21%	---	-2.8%	---
6	Sycamore	-0.7%	---	-1%	---
8	Oak	---	12.5%	---	10.2%
9	Oak	8%	---	6.7%	---
10	Oak	3.7%	---	2.1%	---
11	Oak	-0.6%	---	-2.4%	---
12	Sycamore	-12%	---	-13.3%	---
13	Oak	-3%	---	-5.4%	---
Average error		7.1%	8.8%	5.5%	6.7%
Total error		7.7%		6.3%	

When the pooled model was used, the error in the EWT estimation for the beech tree dropped to - 2.8%, further showing that the species-specific model of beech was inaccurate. The errors in sycamore trees number 2 and 12 slightly increased, with the errors being higher than those observed in the remaining sycamore trees. As EWT was underestimated, this suggested lower NDI values, which can be a result of the remaining effects of the leaf internal structure on the NDI, if leaf samples from these two trees were thicker than the leaves used to build the EWT estimation model, according to PROSPECT simulations. This was reflected in the average LMA value of the leaf samples collected from the two trees, which was 0.0029 g cm^{-2}, being higher than the average LMA of the leaf samples collected from the remaining sycamore trees (0.0021 g cm^{-2}). On the other hand, the error in the EWT estimation in oak tree 8 dropped when the pooled model was used, but remained higher than the errors observed in the remaining oak trees. The overestimation of EWT suggested that leaf samples collected from that specific tree were thinner than the leaf samples used to build the EWT estimation model. This was also reflected in the average LMA of the leaf samples collected from the tree (0.0027 g cm^{-2}), which was lower than the average LMA of the leaf samples collected from the remaining oak trees (0.0041 g cm^{-2}). The observed EWT estimation errors showed the possibility of using a pooled NDI – EWT model to successfully estimate EWT in a mixed forest plot without needing a NDI – EWT estimation model for each individual species. Using a pooled EWT model can then be more applicable as it does not require prior tree species classification. However, further

experiments that include measuring leaf thickness are still needed to better understand the source of the high errors observed in some trees.

5.5.4 EWT vertical profiles

The EWT vertical profiles (Figure 5-11) revealed a vertical variation in the EWT distribution in all twelve trees, agreeing with the leaf sampling results (5.5.1). Figure 5-11 also shows the advantage of using TLS data in mapping the EWT in forest plots over the destructive sampling approach. TLS can estimate EWT in all canopy layers, which requires tree climbers and extensive destructive sampling to be achieved using traditional approaches. Assuming that the leaves in the top part of the canopy were sun leaves, and those in the bottom were shade leaves, the vertical profiles of EWT showed a gradual transition between sun leaves and shades leaves, with sun leaves having higher EWT, and correspondingly higher LMA, than shade leaves.

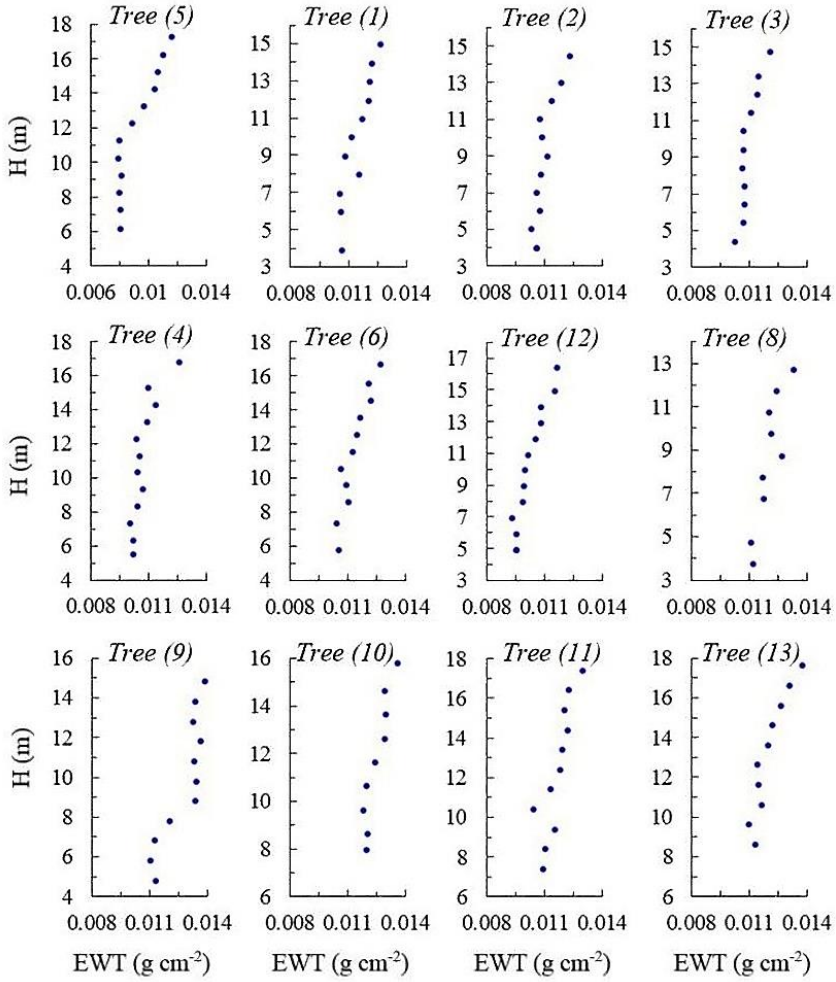

Figure 5-11. The EWT vertical profiles. Tree (5) is beech, trees (1, 2, 3, 4, 6 and 12) are sycamore and trees (8, 9, 10, 11 and 13) are oak.

All trees had higher EWT in the upper canopy than in the shaded lower canopy. The upper canopy in all trees had an average of 24.2% more EWT than the lower canopy. However, the errors presented in Table 5-2 showed that the EWT estimation model overestimated the EWT in the canopy bottom layer and, in most cases, underestimated the EWT in the canopy top layer, suggesting that the actual difference between EWT of upper and lower canopy can be higher than 24.2%. The highest observed variation in EWT was in the beech tree, labelled (5), where EWT in the upper canopy was 44% higher than the bottom canopy. The lowest variation was observed in the oak tree, labelled (10), where EWT was 13.6% higher in the upper canopy than in the lower. Similarities were observed in the vertical profiles of the sycamore trees, with the upper canopy layer having an average of 20% higher EWT than the lower canopy. The vertical profile of the beech tree was more distinctive. The vertical profiles of the oak trees showed some variations from each other, with EWT being 25.4% higher in upper canopy than in lower canopy, which suggested that the EWT vertical profile can vary within a species, depending on each individual tree structure.

The vertical profiles observed in the forest plot concurred with the findings of Zhu *et al.* (2017), Arellano *et al.* (2017) and Gara *et al.* (2018), all reporting higher EWT in the canopy top than in the canopy bottom in a variety of species. Zhu *et al.* (2017) and Gara *et al.* (2018) studied the EWT vertical profiles in small, individual trees from various species: *weeping fig*, *Ficus benjamina*, *Camellia japonica*, *Chamaedorea elegans*, and *Fatshedera lizei*, in controlled environments. On the other hand, Arellano *et al.* (2017) examined the EWT vertical heterogeneity in forest plots in Amazonian forest in Ecuador. The results also agreed with the vertical profiles observed in the dry-down experiment (Chapter 4). Typically, top layers of canopy receive the majority of irradiance and trees tend to grow sun leaves in these layers to optimize photosynthesis (Chazdon and Fetcher, 1984). Trees also tend to dedicate more nutrients and water to sun leaves than to the shaded leaves in the canopy bottom for the same purpose (Hirose and Werger, 1987; Hikosaka, 2004). The observed vertical distribution of EWT can then be related to the distribution of sun/shade leaves within the canopy. As sun leaves typically have higher LMA than shade leaves, and as EWT was found to be highly correlated to LMA as discussed in Section 5.5.1, the EWT vertical profiles shown in Figure 5-11 also reflected the vertical variation in LMA within canopies. Arellano *et al.* (2017) and Gara *et al.* (2018) also showed that EWT and LMA vertical profiles showed similarities.

5.6 Summary

This chapter was dedicated to investigate the possibility of using the NDI of the 808 nm NIR wavelength and the 1550 nm SWIR wavelength to generate 3D EWT estimations at the canopy level in a real forest environment. It described in detail a data collection campaign that took place in a mixed deciduous forest plot in Wytham Woods, Oxford, UK, and resulted in mapping the EWT in the forest plot in 3D.

At leaf level, moderate correlation was observed between NDI and EWT across four broadleaf tree species: oak, sycamore, beech and ash. It was also possible to fit a pooled EWT estimation model that combined all species, but more leaf samples still need to be added to the model to fill the gap in the low EWT region of the model. At the canopy level, it was possible to achieve a high registration accuracy for the point clouds, despite the difference in the laser beam footprint and beam divergence between the two instruments. This was a result of the similarity in the chassis of the instruments and their laser beam exit locations, in addition to the similarity in the scan geometry. NDI was successfully used to generate 3D estimations of EWT in the scanned forest plot, using species-specific models in addition to a pooled EWT model, with a relative error of 7.7% and 6.3% in the EWT estimation respectively.

The generated 3D distributions of EWT revealed some vertical heterogeneity in all the sampled trees. All the trees were found to have higher EWT in the canopy top than the canopy bottom, with EWT gradually becoming lower towards the canopy bottom. Such variation in EWT can be a result of the leaves in the top of the canopy, predominantly sun leaves, having higher LMA than shaded leaves in the bottom of the canopy, as EWT and LMA were found to be highly correlated. The observed EWT vertical variation in the forest plot may affect the estimation of EWT using passive optical spaceborne or airborne sensors, because measurements from such instruments will be dominated by the canopy top, which, according to this study, has higher EWT than the lower layers in the canopy. This was further investigated in Chapter 7 using radiative transfer modelling.

Chapter 6. Transferability of the EWT estimation approach to different sites

6.1 Introduction

Chapter 4 showed the potential of using NDI of the 808 nm and the 1550 nm wavelengths to generate 3D estimates of EWT at the canopy level, with errors < 4%. However, the experiment was conducted in a controlled indoor environment, using healthy individual trees, and with no effect of wind or occlusion. When the method was transferred to a real forest environment, as shown in Chapter 5, EWT was successfully estimated with errors < 8%. The higher errors were caused by the lower registration accuracy because of the slight movements of trees due to wind, in addition to occlusion, remaining partial hits, remaining effects of leaf internal structure, and the remaining woody materials that could not be filtered manually. Nevertheless, the conditions in which the data collection campaign took place were considered very suitable for laser scanning, as strong wind was absent.

This chapter is dedicated to investigating the transferability of the EWT estimation approach to two additional sites with more challenging conditions. The first site consisted of six willow (*Salix spp.*) bioenergy crop plots and was scanned to study the effects of wind and senescence of leaves on the accuracy of the EWT estimation. The second site was a mixed-species urban tree plot that was scanned twice, at the end of a heatwave and two months later, to further investigate the leaf senescence effect and also to study the ability of the EWT estimation approach to detect temporal changes in EWT. Furthermore, the ability of NDI to directly estimate FMC at the canopy level was investigated, as a proof-of-concept for future work. The results of the willow dataset have been published in Elsherif *et al.* (2019b). The results of Exhibition Park dataset have been published in Elsherif *et al.* (2019a). The 3D FMC results have been published in Elsherif *et al.* (2019c).

6.2 Willow dataset

6.2.1 Study area

The study area was at the Newcastle University Cockle Park Farm in Ulgham, Northumberland, UK (Figure 6-1). Cockle Park Farm is approximately 262 hectares and has been part of Newcastle University since 1896. It is a working farm that offers a unique opportunity for interdisciplinary research in agriculture, including food security and the generation and efficient use of bioenergy. The data collection took place in part of the 10 hectares devoted to short

rotation coppiced willow crops (55.2° N, 1.69° W) (Figure 6-1) which are used for bioenergy generation. The 10 hectares are divided into four main plots, with each plot containing thirteen subplots planted with different willow varieties, with a nominal width of 6 m each (Figure 6-2). Six willow subplots of different varieties were chosen for the data collection, labelled as Endeavour (E), Terra Nova (TE), Beagle (B), Stott (S), Tordis (T), and Nimrod (NI) (Figure 6-2). As the data collection took place in October, the leaves were already senescent, as shown in Figure 6-3.

Figure 6-1. The study area and the location of the 10 hectares devoted to the willow crops, indicated by red.

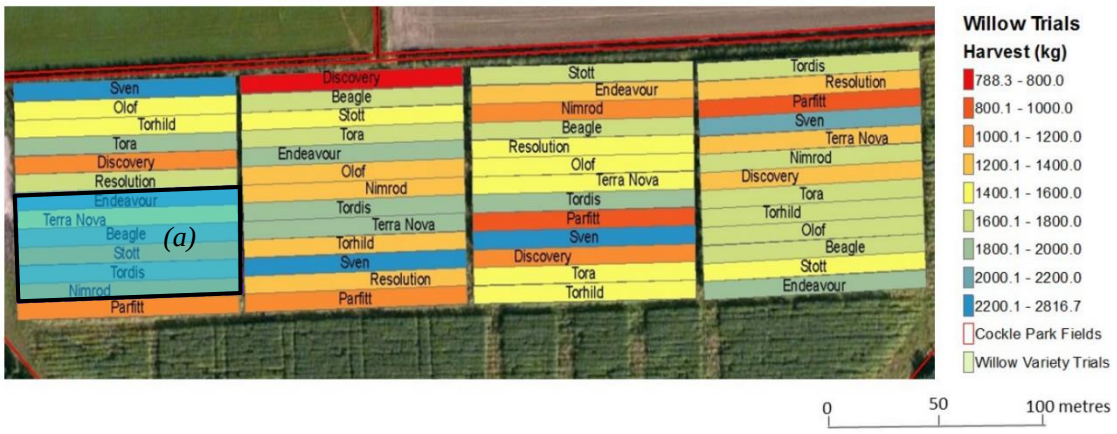

Figure 6-2. The willow subplots and varieties, coloured by their harvested weight (Kg) in March 2015, after four years of growth. Shaded area *(a)* indicates the six willow subplots used in the data collection. The figure was adapted from Gaulton *et al.* (2015).

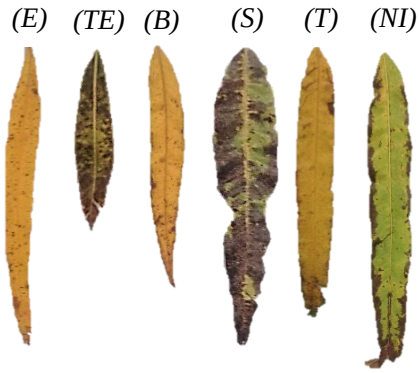

Figure 6-3. The willow varieties. All leaves were already senescent.

6.2.2 Experiment setup

Two scanning positions were set at a range of 15 m away from the plots, covering three adjacent plots each. The first scanning position covered plots ‘E’, ‘TE’ and ‘B’, while the second covered plots ‘S’, ‘T’ and ‘NI’. The plots were scanned from one side from each scanning position with the $P40_a$ and P20 scanners. The scans were conducted with a resolution of 3 mm at 10 m. Four Leica black and white registration targets were placed in each scan to be used in aligning the P20 point cloud to the $P40_a$ point cloud. In addition, reflectors were mounted on wooden sticks and used to mark the approximate boundaries of each willow plot. The scans were conducted in windy conditions. Figure 6-4 shows a view of the plots covered from scan position one. Table 6-1 shows the height and width of the scanned side of the plots. Figure 6-5 shows the P20 point clouds collected from the two scanning positions.

Figure 6-4. A view of the three plots covered from scanning position one, left is plot ‘E’, middle is plot ‘TE’, and right is part of plot ‘B’. Three out of four Leica black and white registration targets can be seen, in addition to the reflectors used to mark the approximate boundaries of each plot.

Table 6-1. Height and width of the scanned side of the plots.

Plot	E	TE	B	S	T	NI
Height (m)	4.7	4.1	3	3	4.5	3.5
Width (m)	5.5	6.3	5.6	6	7.7	5.2

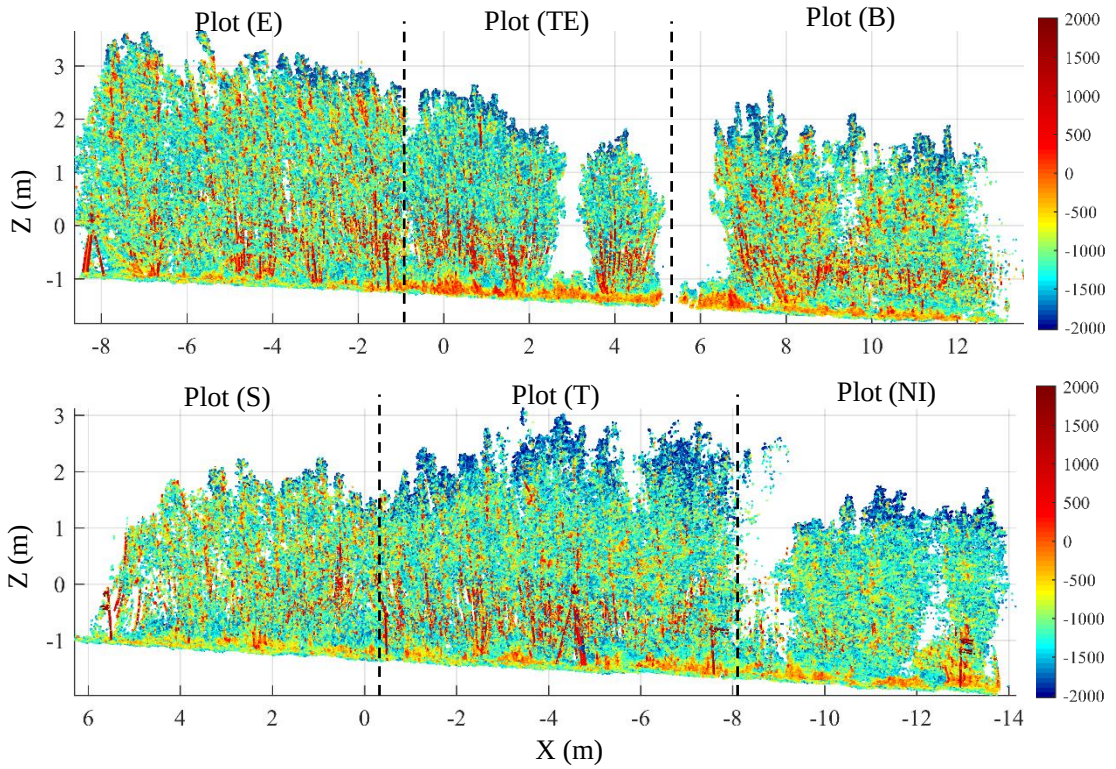

Figure 6-5. The P20 point clouds of scan position one (top) and scan position two (bottom). The point clouds show only the front side of the plots, 1 m deep into the canopy. The colour ramps show the uncalibrated intensity (dimensionless).

6.2.3 Leaf sampling and biochemistry measurements

For each plot, six leaf samples were collected randomly to be used in building the EWT estimation model. Six additional leaf samples were collected from a sampling layer with a thickness of one metre, located 1.5 m above ground, for the validation of the EWT estimation. The total number of leaf samples collected was 72 samples. The leaf samples were processed as described in Section 3.3.4 to measure their EWT.

To build the EWT estimation model, the six leaf samples collected for this purpose from each plot were suspended in a wooden frame and scanned by the P20, followed by the $P40_a$, at a range of 7 m. The wooden frame was normal to the laser beam direction to minimize the incidence angle effects. The intensity values of each leaf were calibrated to apparent

reflectance, using the calibration models described in Section 3.7.1. NDI was calculated for each leaf following Equation (2.5). NDI values of the leaf samples were plotted against EWT values to determine the NDI – EWT relationship for each plot.

6.2.4 Point cloud processing

The P20 point clouds were aligned to the $P40_a$ point clouds in Leica Cyclone using the registration targets. Afterwards, the aligned point clouds were calibrated to apparent reflectance on a point-by-point basis, and reflectance point clouds were generated, using the calibration models described in Section 3.7.1. The reflectance point clouds were used to estimate EWT of each plot using two different approaches.

The first approach followed the steps described in Section 3.3.3 and NDI point clouds were generated on a point-by-point basis. Afterwards, the NDI - EWT estimation model of each willow variety was used to generate EWT point cloud of each plot. The layer from which leaf samples were collected for validation were then extracted from the EWT point cloud of each plot. Removing the woody materials and cleaning the noise followed the same method used in the forest dataset, as described in Section 5.4.3. Estimated EWT of each layer was compared to actual EWT of the leaf samples collected from that layer to evaluate the accuracy of the estimation.

Due to the strong wind during scanning, which was expected to have severe effects on the accuracy of the point cloud registration and the estimation of EWT on a point-by-point basis, a second approach to estimate EWT was also used. The approach aimed at estimating the average EWT of the canopy layer from which leaf samples for validation were collected. For each plot, the sampled canopy layer was extracted from the P20 and the $P40_a$ point clouds, and average reflectance of the layer was calculated for each wavelength. Average NDI of the layer was calculated using the average P20 and $P40_a$ reflectance values instead of calculating NDI on a point-by-point basis. The average EWT of the layer was estimated using the average NDI value. To validate the estimation, the sampled layer estimated EWT of each plot was compared to the mean EWT of the leaf samples collected from that layer.

6.3 Willow dataset results and discussion

6.3.1 Leaf level

Moderate to high correlation was observed between NDI and EWT (Figure 6-6 and Table 6-2). The correlation was significant ($P < 0.05$) except for plot ‘S’. Some differences in the slopes and intercepts of the NDI – EWT relationships of the different plots were observed, with the

most significant differences being in plots ‘E’ and ‘S’ (Table 6-3). For plot ‘E’, the NDI – EWT relationship had clearly different slope and intercept in comparison to the remaining plots. This significant difference can be a result of leaf internal structure effects, if the two leaves that had the highest and lowest EWT values were at different levels of senescence in comparison to the remaining four leaves. Another reason can be a laboratory measurement error in the two leaf samples corresponding to the lowest and highest EWT.

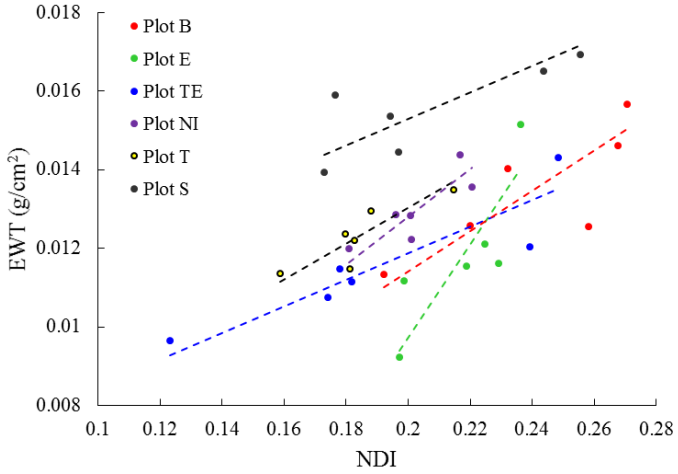

Figure 6-6. The relationship between NDI and EWT of each willow plot.

Table 6-2. The correlation between NDI and EWT.

Plot	E	TE	B	S	T	NI
R^2 (NDI – EWT), $P < 0.05$	0.66	0.82	0.64	0.62	0.76	0.72

Table 6-3. Slopes and intercepts of the NDI – EWT relationships.

Plot	E	TE	B	S	T	NI
Slope	0.1187	0.0337	0.0514	0.0336	0.0457	0.0609
Intercept	-0.0140	0.0051	0.0011	0.0086	0.0039	0.0006

For plot ‘S’, the intercept was different than the other plots. The leaf samples had lower NDI than the leaf samples from other varieties that had almost the same EWT. According to PROSPECT simulation results (Section 3.7.4), this can be a result of the leaf samples having higher N, corresponding to a significantly different mesophyll structure. However, in healthy leaves, higher N usually corresponds to higher LMA (Jacquemoud and Baret, 1990). Higher N would cause a decrease in NDI, while higher LMA would cause an increase in NDI. If the two

effects were almost similar, a slight change in NDI would be observed between species. The significant decrease in NDI for plot 'S' suggested that N had a much more substantial effect on NDI than LMA, concurring that leaf samples from plot 'S' had significantly different mesophyll structure than the remaining leaves. A possible reason for this can be that the leaves were more senescent, as the more senescent the leaves were, the higher their N value would be (Jacquemoud and Baret, 1990).

The variety-specific NDI – EWT relationships can be described as:

$$EWT\ (g\ cm^{-2}) = 0.1187 \times NDI - 0.0140, \text{ for plot 'E'} \quad (6.1)$$

$$EWT\ (g\ cm^{-2}) = 0.0337 \times NDI + 0.0051, \text{ for plot 'TE'} \quad (6.2)$$

$$EWT\ (g\ cm^{-2}) = 0.0514 \times NDI + 0.0011, \text{ for plot 'B'} \quad (6.3)$$

$$EWT\ (g\ cm^{-2}) = 0.0336 \times NDI + 0.0086, \text{ for plot 'S'} \quad (6.4)$$

$$EWT\ (g\ cm^{-2}) = 0.0457 \times NDI + 0.0039, \text{ for plot 'T'} \quad (6.5)$$

$$EWT\ (g\ cm^{-2}) = 0.0609 \times NDI + 0.0006, \text{ for plot 'NI'} \quad (6.6)$$

It was also possible to fit a pooled NDI – EWT model for all leaf samples combined, excluding plot 'S' ($R^2 = 0.57$, $P < 0.05$), which can be described as follows:

$$EWT\ (g\ cm^{-2}) = 0.0532 \times NDI + 0.0020 \quad (6.7)$$

Both the variety-specific models and the pooled model were used to estimate EWT at the canopy level.

6.3.2 Canopy level

RMSE of the $P40_a$/P20 point cloud registration for scan positions one and two, reported by Leica Cyclone, was 1.6 cm and 1.7 cm respectively. Such errors were considered high in comparison to the errors obtained in the indoor experiment (Chapter 4, RMSE = 0.8 mm) and the forest dataset (Chapter 5, RMSE = 3 mm). The lower registration accuracy was a result of the wind effect. The errors in the registration severely affected the accuracy of retrieving EWT on a point-by-point basis, and very high errors were observed, using the variety-specific models and also the pooled EWT model (Table 6-4). The errors were a result of the nearest neighbour function, while attempting to calculate NDI on a point-by-point basis, wrongly assigning the nearest neighbours because of leaf and branch movement between the scans. Eighty percent of the selected nearest neighbours were < 3 cm apart, while only 36% were < 1 cm apart. In the

indoor experiment (Chapter 4), all the nearest neighbours were < 3 cm apart and 99.6% of them were < 1 cm apart, while in the forest dataset (Chapter 5), 96% were < 3 cm apart, and 80% were < 1 cm apart.

Table 6-4. Errors in the EWT estimation. Approach one refers to estimating EWT on a point-by-point basis, while approach two refers to using the average NDI to estimate the average EWT.

	Relative error in EWT estimations			
	Approach one		Approach two	
Plot	Variety-specific model	Pooled model	Variety-specific model	Pooled model
NI	45.2%	23.7%	-10.4%	-10.1%
T	24.7%	15.2%	-4.2%	-9%
S	10.5%	N/A	-9.3%	N/A
B	26.3%	21.3%	-9.1%	0.5%
TE	23.3%	27.4%	2.6%	7.1%
E	52.2%	24.8%	-17.6%	6.4%
Average	30.4%	22.5%	8.9%	6.6%

When calculations were not done on a point-by-point basis and the average NDI was used to estimate the average EWT, the average errors in the EWT estimation dropped to 8.9% and 6.6% for the variety-specific and pooled models respectively (Table 6-4). For plot 'E', the error obtained using the pooled model was much lower than the error obtained using the variety-specific model (6.4% and -17.6% respectively). This suggested that the variety-specific NDI – EWT relationship for plot 'E', which had different slope and intercept than the remaining plots, was either influenced by the leaf samples being at different levels of senescence, or was caused by laboratory measurement error. High correlation was observed between the average estimated EWT of the sampled layer in each plot and the actual EWT of the leaf samples collected from the layer, using both the variety-specific models and the pooled model (R^2 = 0.73, RMSE = 0.0013 g/cm^2 and R^2 = 0.62, RMSE = 0.001 g/cm^2 respectively) (Figure 6-7). The correlation was significant in both cases ($P < 0.05$).

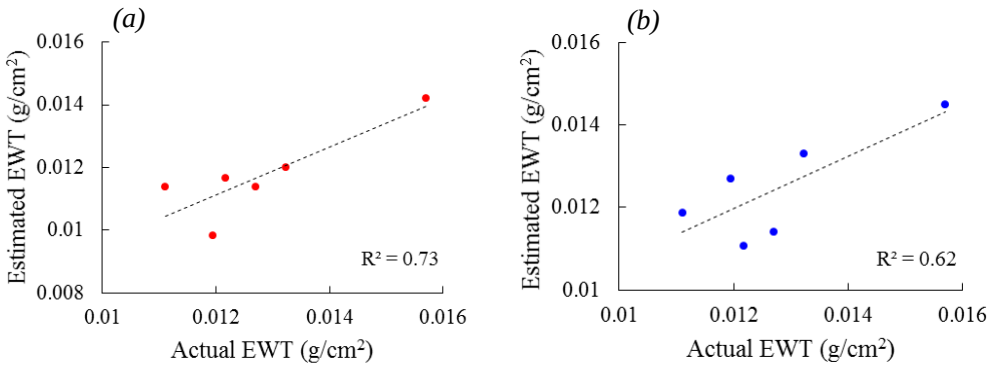

Figure 6-7. The relationship between the estimated EWT of the sampled layers and the actual EWT: *(a)* for the variety-specific models and *(b)* for the pooled model.

No significant difference in reflectance between leaf and wood was observed in the $P40_a$ point clouds of all plots, as shown in Figure 6-8b for plot 'T' as an example. This can be a result of the wood having high water content as willows are known to have bark filled with watery sap, which is used in numerous medical applications (Orémusová *et al.*, 2012). The EWT point cloud of the plot (Figure 6-8d) concurred with this observation and showed that the wood had higher EWT than leaves. This agreed with the results obtained for the young, deciduous trees in Chapter 4 and showed that the SWIR wavelength may not be suitable for leaf/wood separation if the bark was green or had high water content. Attempting to extract the woody materials from the EWT point cloud using a threshold by trial and error resulted in some points corresponding to leaves being classified as wood (Figure 6-8f). On the other hand, clear difference in reflectance between leaf and wood was observed in the P20 point cloud (Figure 6-8a) as wood had higher reflectance than leaves. Attempting to extract the wood using a threshold produced a visually-better result than using EWT, as fewer points corresponding to leaves were misclassified (Figure 6-8e). This showed the potential of using the 808 nm NIR wavelength in leaf/wood separation in willows, which can be useful in biomass estimations.

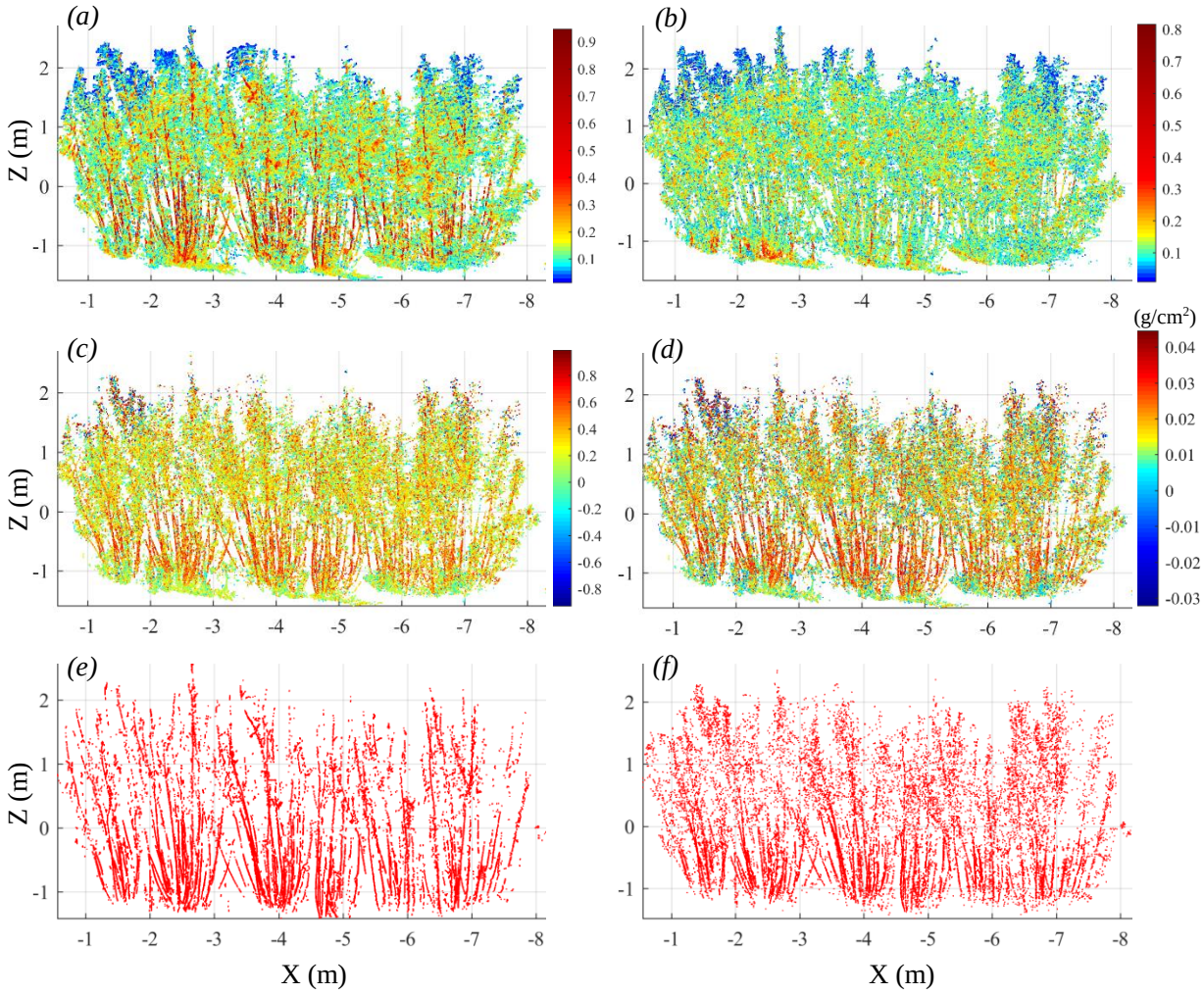

Figure 6-8. Plot 'T' point clouds: *(a)* the P20 reflectance, *(b)* the P40 reflectance, *(c)* NDI point cloud, *(d)* EWT point cloud, *(e)* woody materials extracted from the P20 reflectance point cloud using 0.35 threshold and *(f)* woody materials extracted from EWT point cloud using 0.03 g/cm^2 threshold. Thresholds were chosen by trial and error until changing the threshold did not visually improve the results.

6.4 Exhibition Park dataset

6.4.1 Study area

The study area was a mixed-species tree plot (35 m × 39 m) in Exhibition Park, Newcastle upon Tyne, UK (54.98° N, 1.62° W) (Figure 6-9). The tree species included: *Ilex aquifolium* (holly), *Acer pseudoplatanus* (sycamore), *Sorbus intermedia* (Swedish whitebeam), *Fraxinus excelsior* (ash), *Aesculus hippocastanum* (horse chestnut), *Fagus sylvatica* (beech), and *Tilia x europaea* (lime). A single scanning position was set in the centre of the plot, corresponding to a wide gap in canopy cover, aimed at obtaining as many laser beam returns as possible from the canopy top. The scanning position covered nine trees: two holly trees, two ash trees, two Swedish

whitebeam tress, one beech tree, one sycamore tree, and one horse chestnut tree. The horse chestnut tree was suffering from horse-chestnut leaf miner (*Cameraria ohridella*) and thus was excluded from any further processing.

Figure 6-9. The Exhibition Park dataset study area: *(a)* Exhibition Park and *(b)* the scanned tree plot.

The plot was scanned on 7th of August 2018, at the end of the 2018 heatwave that hit the British Isles between 23rd of June and 7th of August, as part of the 2018 European heatwave, making summer 2018 the joint-warmest summer in recorded in the UK, and the second warmest summer in the North East England region. Temperatures in Newcastle upon Tyne reached 26 °C, significantly higher than the 15 °C recorded average summer temperature. Scans were conducted with the P20 and the P50 instruments mounted consecutively on the same tripod, on the same surveying point (scanning position). Three Leica black and white registration targets were placed in the plot at different heights for the purpose of aligning the P20 and P50 point clouds. A full-hemisphere scan (360° × 270°) was conducted with each instrument with a resolution (point spacing) of 3 mm at 10 m. The duration of the scan was approximately fifteen minutes for each instrument. The plot was scanned again on 22nd of October 2018 while leaves were senescing, using the same scanning set-up. Average temperature in October was 13 °C, with periods of rainfall throughout the month. On each date, leaf samples were collected immediately after scanning to link the TLS data to EWT, as described in Section 6.4.2.

6.4.2 Leaf sampling and biochemistry measurements

On each date, two sets of leaf samples were collected, one for the purpose of building the NDI – EWT estimation model, and the other for the validation of the EWT estimates. As the study

area was in a public park, extensive destructive sampling of the trees was not possible. The total number of leaf samples collected in August dataset was 50 samples, while the total number of samples collected in October dataset was 38 samples. Leaf sampling details are given in Table 6-5. Samples for building the EWT estimation model were collected randomly from the plot. On the other hand, leaf samples for validation were collected from a small volume, approximately 0.5 m × 0.5 m × 0.5 m, with a known crown location in a specific tree from each species. Sycamore leaf samples were found to be covered with grey powdery material, indicating that the tree suffered from powdery mildew disease. This severely affected the NDI – EWT relationship as discussed in Section 6.5.1, and thus the tree was excluded in October data collection. Leaf samples of holly were thicker than the other species, in addition, they had glossy, waxy surface. The lime tree was on the edge of the plot, fully occluded by two ash trees, thus, no leaf samples were collected for validation and samples were only collected to add species variety to the EWT estimation model in August. In October, the tree had already lost its leaves.

Table 6-5. Leaf samples collected to build the EWT estimation model and validate the estimation in August and October datasets.

Date	August		October	
Type of samples	EWT model	Validation	EWT model	Validation
Swedish Whitebeam	5	5	5	5
Ash	3	5	5	4
Beech	6	5	5	5
Holly	4	5	4	5
Sycamore	3	4	---	---
Lime	5	---	---	---
Total number of leaf samples	26	24	19	19

The fresh weight and surface area of each leaf sample was measured as described in Section 3.3.4. The leaf samples were then left to dry naturally over a period of five days (a week for October dataset), then were further dried in an oven for 72 hours at 60 °C. Holly leaf samples were oven-dried for an additional six days until no change in their weight was observed, ensuring that they were fully dry. The dry weight of each leaf sample was measured using the same scale used to measure the fresh weight, and EWT was calculated according to Equation (2.1).

Samples for building the EWT estimation model on each date were scanned by both the P20 and P50, immediately after measuring their fresh weight, at ranges of 6 m and 7 m for August and October datasets respectively. NDI was calculated for each leaf after calibrating the intensity values to apparent reflectance using the calibration models described in Section 3.7.1. For the August dataset, different pooled NDI – EWT relationships were examined, in addition to species-specific relationships. Firstly, a pooled NDI – EWT model was fitted to all species combined. Next, the diseased sycamore leaf samples were excluded, and a second pooled NDI – EWT model was fitted to the remaining species. The next step was to exclude holly leaf samples from the pooled EWT model to account for their thickness and surface characteristics that differed from the remaining species. The remaining leaf samples were then combined with the leaf samples measured in Chapter 4, and a third pooled NDI – EWT model was fitted in an attempt to develop a species-independent EWT estimation model for leaves from park environments, collected from different sites. For the October dataset, a pooled NDI – EWT model was fitted to leaf samples from all species combined. In addition, holly leaf samples were excluded, and a second pooled EWT model was fitted to the remaining species. Furthermore, the leaf samples were combined with the willow leaf samples (Section 6.2.3) in an attempt to derive a site- and species-independent NDI – EWT relationship for senescent leaves.

6.4.3 Point cloud processing

The P20 and P50 point clouds on each date were aligned in Leica Cyclone. NDI point cloud of the plot on each date was generated on a point-by-point basis (Section 3.3.3). Individual trees were then manually extracted and species-specific and pooled NDI – EWT models on each date were used to generate the EWT point clouds. The woody materials were removed as described in Section 5.4.3. To validate the EWT estimates, the sections from which leaf samples for validation were collected (0.5 m × 0.5 m × 0.5 m volume) were extracted from the corresponding trees in the EWT point clouds and the estimated EWT was compared to the actual EWT measured from destructive leaf sampling and relative errors in the EWT estimations were calculated.

The temporal change in EWT (increase/decrease) between August and October was measured for each tree from the TLS estimated EWT, and also from the destructive sampling EWT, to investigate the accuracy of TLS in detecting such changes. Afterwards, the EWT point-cloud of each tree was split into multiple horizontal layers, 1 m each. Average EWT of each layer was calculated and plotted against height at the centre of the layer to produce a vertical profile of EWT distribution in the canopy. The EWT vertical profiles produced for each tree in August

and October datasets were compared, to study how the vertical distribution of EWT varied temporally.

6.5 Exhibition Park dataset results and discussion

6.5.1 Leaf level

A significant correlation ($P < 0.05$) was found between NDI and EWT for each species on both dates (Table 6-6 and Figure 6-10). Some differences in slopes and intercepts of the NDI – EWT relationships were observed between the different species, being a result of the remaining leaf internal structure effects on NDI and/or the small number of leaves used to derive the NDI – EWT relationships, which was insufficient to accurately determine the correct slopes and intercepts.

On both dates, the trendline of the NDI – EWT relationship of holly was significantly shifted up in comparison to the other species, similar to what was observed for plot 'S' in the willow dataset. As discussed in Section 6.3.1, this can be a result of a significantly different leaf internal structure of holly in comparison to the other species. Holly leaves were clearly thicker than the leaves of the other species, and although their leaf thickness was not measured, their average LMA (0.0164 g cm^{-2}) was 129 % higher than average LMA of ash leaf samples (0.0071 g cm^{-2}), 117 % higher than average LMA of Swedish whitebeam leaf samples (0.0075 g cm^{-2}), and 192 % higher than average LMA of beech leaf samples (0.0056 g cm^{-2}). Gaulton *et al.* (2013) reported a similar observation when two *Fallopia japonica* (Japanese knotweed) leaf samples were attached together to form a sample with double thickness and were found to deviate from the NDI – EWT relationship of the remaining species. It is worth mentioning that the shiny surface of holly leaf samples could also have been a factor that contributed to the deviation of the NDI – EWT relationship of this species. Zhu *et al.* (2017) showed that at 1550 nm wavelength, shiny leaves had stronger specular reflection than matt leaves at zero incidence angle. Higher reflectance at the 1550 nm wavelength would reduce the NDI value, causing the upward shift of the trendline of the NDI – EWT relationship of holly in comparison to the other matt leaves.

Table 6-6. The correlation between NDI and EWT for the species-specific models.

	Beech	Swedish	Ash	Holly	Sycamore	Lime
R^2 (August)	0.65	0.94	0.92	0.67	0.85	0.88
R^2 (October)	0.93	0.59	0.76	0.74	N/A	N/A

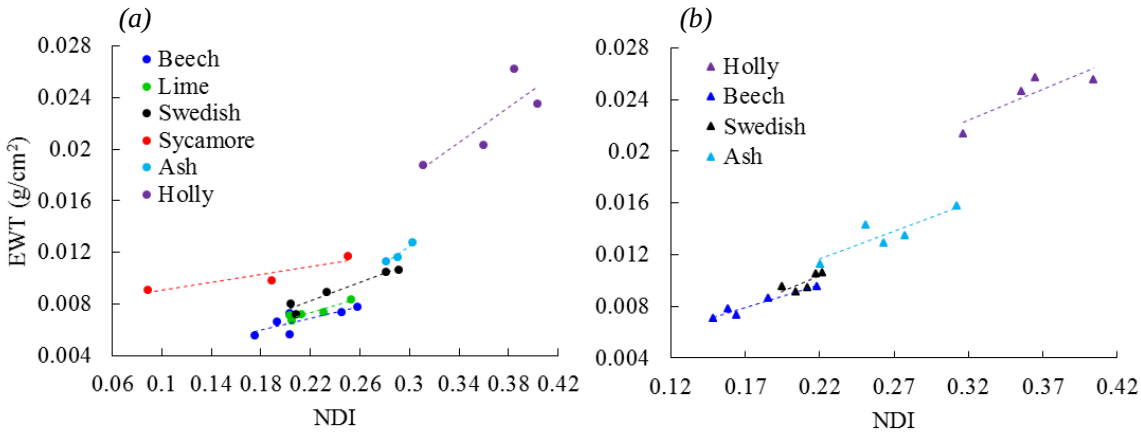

Figure 6-10. Species-specific NDI – EWT relationships: *(a)* August and *(b)* October.

The NDI – EWT relationship of diseased sycamore leaves appeared to be affected by the low NDI value (0.08) of one sycamore leaf. Another sycamore leaf also had lower NDI value than leaves from other species with similar EWT. The two leaves had lower NIR reflectance, 0.31 and 0.36 respectively, than all the other leaf samples, which had NIR reflectance between 0.43 and 0.56. On the other hand, the SWIR reflectance of the two leaves, 0.26 and 0.24 respectively, was within the minimum and maximum values observed in the leaf sampling, 0.19 and 0.35 respectively. The low NDI values were therefore a result of the low NIR reflectance, which could have been caused by the powdery mildew that covered the leaves' surface. Yuan *et al.* (2014) reported similar observation in winter wheat, showing a decrease in NIR reflectance and a slight increase in SWIR reflectance in leaves infected with powdery mildew in comparison to healthy leaves. In general, diseases are known to reduce leaf reflectance in NIR (Nilsson, 1991), and NIR wavelengths have been adopted in detecting powdery mildew infections in winter wheat (Zhang *et al.*, 2012; Yuan *et al.*, 2014) and grape (Beghi *et al.*, 2017). However, powdery mildew in wheat is caused by different fungus than in sycamore and further investigation is still needed by scanning healthy and diseased sycamore leaves.

The species-specific NDI – EWT models can be described as follows for August dataset:

$$EWT\ (g\ cm^{-2}) = 0.0289 \times NDI + 0.0006, \text{ for beech} \quad (6.8)$$

$$EWT\ (g\ cm^{-2}) = 0.0362 \times NDI + 0.0002, \text{ for Swedish whitebeam} \quad (6.9)$$

$$EWT\ (g\ cm^{-2}) = 0.0711 \times NDI - 0.0088, \text{ for ash} \quad (6.10)$$

$$EWT\ (g\ cm^{-2}) = 0.0836 \times NDI - 0.0083, \text{ for holly} \quad (6.11)$$

$$EWT\ (g\ cm^{-2}) = 0.0166 \times NDI + 0.0073, \text{ for sycamore} \quad (6.12)$$

$$EWT\ (g\ cm^{-2}) = 0.0287 \times NDI + 0.0010, \text{ for lime} \quad (6.13)$$

The species-specific models are as follows for October dataset:

$$EWT\ (g\ cm^{-2}) = 0.0366 \times NDI + 0.0017, \text{ for beech} \quad (6.14)$$

$$EWT\ (g\ cm^{-2}) = 0.0632 \times NDI - 0.0034, \text{ for Swedish whitebeam} \quad (6.15)$$

$$EWT\ (g\ cm^{-2}) = 0.0492 \times NDI + 0.0006, \text{ for ash} \quad (6.16)$$

$$EWT\ (g\ cm^{-2}) = 0.0558 \times NDI + 0.0042, \text{ for holly} \quad (6.17)$$

For the August dataset, it was possible to fit a pooled NDI – EWT model for all leaf samples combined ($R^2 = 0.7$, $P < 0.05$) (Figure 6-11). However, the trendline appeared to be affected by the low NDI values of the sycamore leaves. Excluding the sycamore leaves and fitting a second pooled EWT model improved the correlation ($R^2 = 0.88$, $P < 0.05$) (Figure 6-12, Equation (6.18)). Similarly, a linear model was fitted to all leaf samples combined in the October dataset ($R^2 = 0.93$, $P < 0.05$) (Figure 6-12, Equation (6.19)). Comparing the pooled EWT models on the two different dates showed similarity in the slopes, but a difference in the intercept, with the trendline of the October model being shifted up in comparison to the trendline of the August model. This is likely to be a result of the difference in leaf internal structure between green leaves (August) and senescent leaves (October), as senescence changes leaf cell structure (Jacquemoud and Baret, 1990).

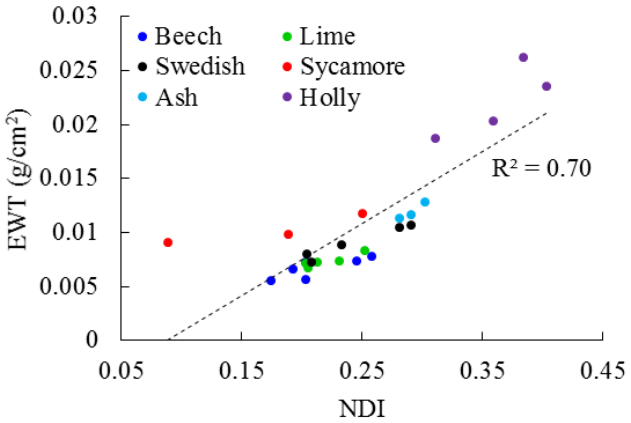

Figure 6-11. Pooled NDI – EWT model for August dataset. The trendline was affected by the Sycamore low NDI values.

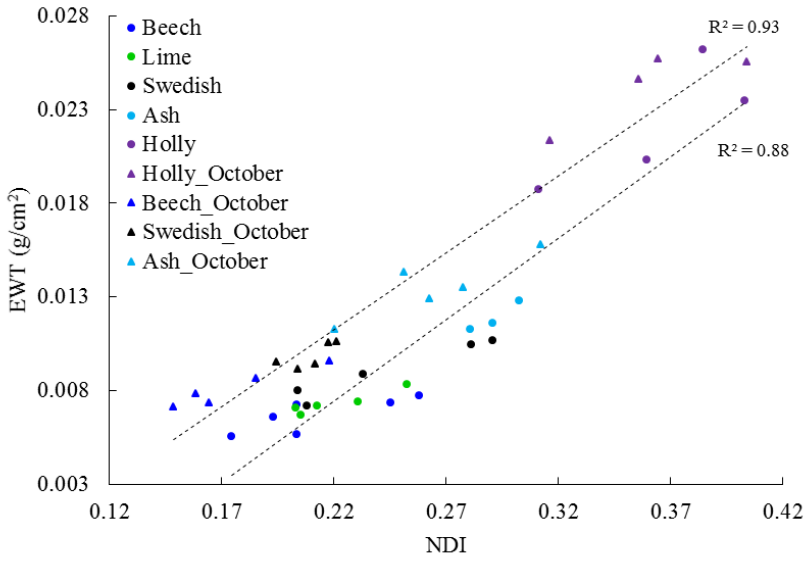

Figure 6-12. Pooled NDI – EWT models for August (bottom), excluding the Sycamore leaves, and for October (top). A shift can be seen between the two trendlines, caused by the leaf senescence.

The pooled EWT models can be described as follows:

$$EWT\ (g\ cm^{-2}) = 0.0925 \times NDI - 0.0131, \text{ for August} \quad (6.18)$$

$$EWT\ (g\ cm^{-2}) = 0.0852 \times NDI - 0.0076, \text{ for October} \quad (6.19)$$

Additionally, the leaf samples collected in August were combined with the leaf samples collected in the indoor dry-down experiment described in Chapter 4, in an attempt to find a species-independent EWT estimation model for healthy leaves in park environments. However, a single model could not be fitted accurately without excluding the holly and the sycamore leaf samples (Figure 6-13). This concurred with the observation that the holly leaf samples did not follow the same NDI – EWT relationship of the other species, as a result of their thickness or different surface characteristics, and neither did the diseased sycamore leaves, as a result of their different surface characteristics. In a similar manner, the holly leaf samples in the October dataset were excluded, and a new pooled EWT model was fitted to the remaining species (Figure 6-14). The pooled EWT model was shifted up in comparison to the model for the August dataset as a result of the leaf senescence (Figure 6-14). The pooled EWT models after excluding the holly leaf samples can be described as:

$$EWT\ (g\ cm^{-2}) = 0.0631 \times NDI - 0.0064, \text{ for August} \quad (6.20)$$

EWT (g cm^{-2}) = 0.0576 × NDI – 0.0019, for October (6.21)

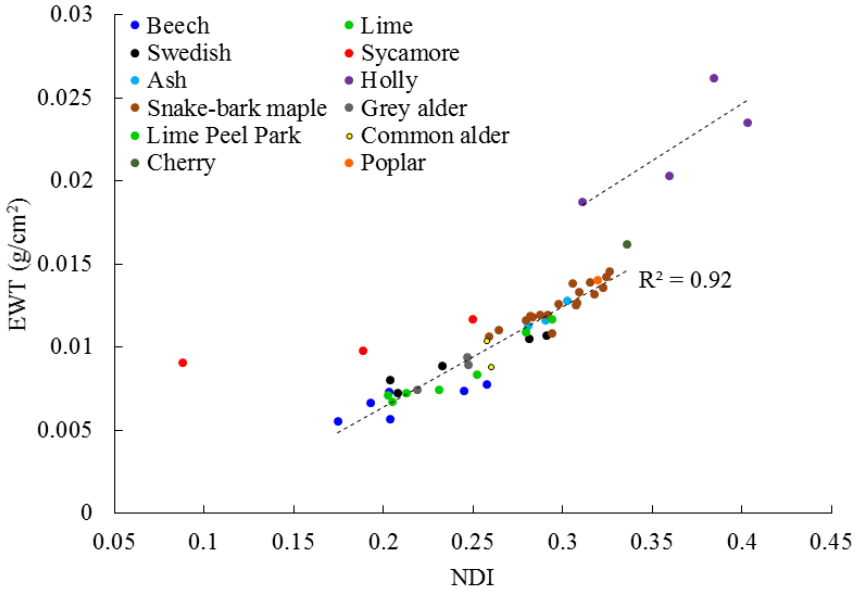

Figure 6-13. Pooled NDI – EWT model for August leaf samples combined with leaf samples collected in the indoor dry-down experiment (Chapter 4). Two of the diseased Sycamore leaves appear as outliers, while the Holly leaf samples have their own EWT model.

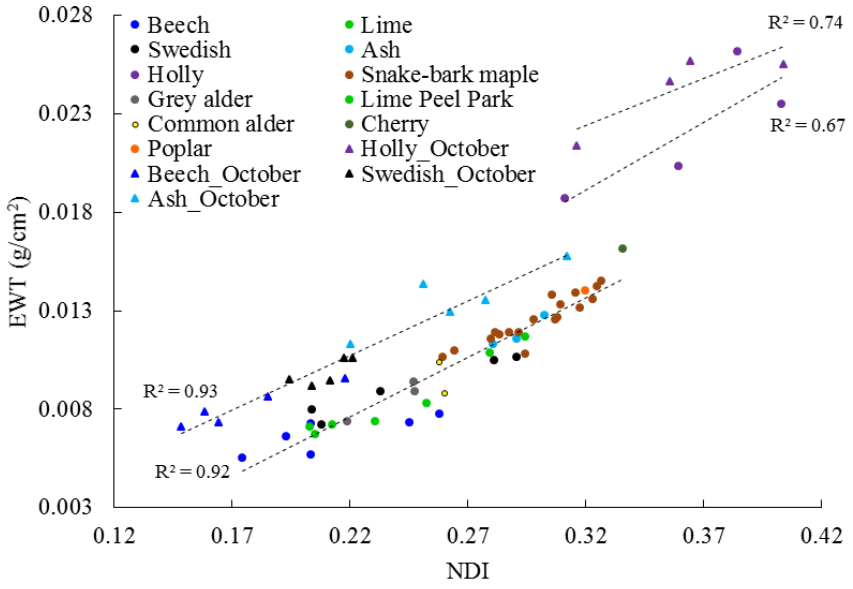

Figure 6-14. Pooled NDI – EWT models for August (bottom) and for October (top), after excluding Holly leaf samples. The shift in trendlines of the NDI – EWT relationships was caused by the leaf senescence.

Next step was to investigate the possibility of fitting a site- and species-independent EWT estimation model for senescent leaves. For this, the leaf samples from October dataset were combined with the willow leaf samples (Figure 6-15). This showed a difference in the slopes and intercepts of the NDI – EWT relationships between the willow leaf samples and October dataset. The trendlines of willow were shifted up, suggesting that the willow leaves were more senescent than the October dataset leaves. Additionally, some willow leaves, including a leaf from plot 'B', a leaf from plot 'TE', and three leaves from plot 'E', appeared to be following the NDI – EWT relationship of October dataset more than that of the willow dataset. Furthermore, it seemed to be possible to fit an NDI – EWT model for plot 'S' and Holly leaf samples combined. These observations revealed that the NDI – EWT relationship may not be dependent on the species as much as it is dependent on the internal structure of leaves. It was not possible to fit a general EWT estimation model for senescent leaves, as they appeared to be at different levels of senescence.

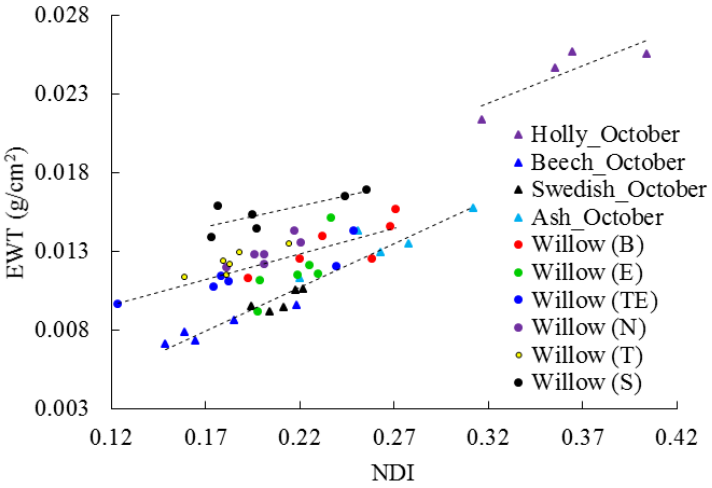

Figure 6-15. Pooled NDI – EWT models for October dataset (bottom), for willow dataset (middle), and for willow plot 'S' and Holly leaf samples (top).

6.5.2 Canopy level

The visual inspection of the EWT point cloud of the plot in both dates, and the histogram of EWT distribution, showed differences in EWT between species, suggesting that the EWT point cloud can be useful in species classification in mixed tree plots (Figure 6-16). Using the species-specific models to estimate EWT at canopy level resulted in relative errors in the estimation < 10% in all species in both dates, except for beech and sycamore in the August dataset (Table 6-7). The errors in the EWT estimation for each species varied between the two different dates, being higher in the August dataset than in the October dataset, except for holly.

This concurred with the observations obtained in the forest dataset (Section 5.5.3) that the accuracy of using species-specific models to estimate EWT at the canopy level depended mainly on how accurate the slope and intercept of the model were. For the sycamore tree, severe error was observed in the EWT estimation (- 31.5%). This suggested that the species-specific model derived at the leaf level did not represent the NDI – EWT relationship at the canopy level.

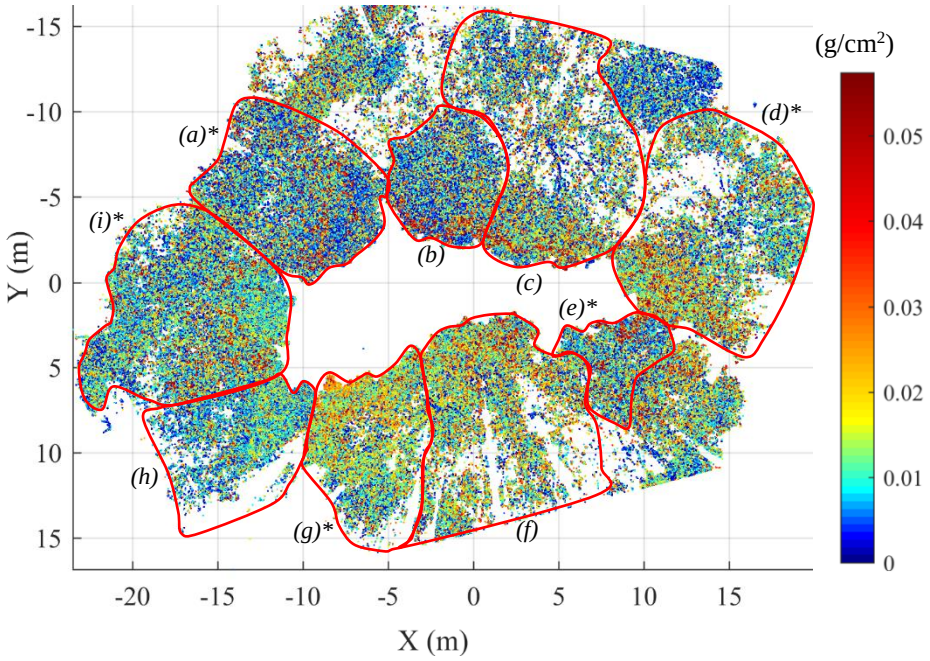

Figure 6-16. Top view of the EWT point cloud of the plot in August and the approximate boundaries of the trees: *(a)* Swedish Whitebeam tree 1, *(b)* Swedish Whitebeam tree 2, *(c)* Ash tree 1, *(d)* Ash tree 2, *(e)* Beech tree, *(f)* Holly tree 1, *(g)* Holly tree 2, *(h)* Horse chestnut tree and *(i)* Sycamore tree. * indicates that samples were collected form the tree for EWT validation.

Table 6-7. The errors in EWT estimations for the species-specific models, pooled model 1, which refers to the pooled EWT model with holly leaf samples included, and pooled model 2, which refers to the pooled EWT model without holly leaf samples.

	Relative error in EWT estimations					
	August dataset			October dataset		
Species	Species-specific	Pooled model 1	Pooled model 2	Species-specific	Pooled model 1	Pooled model 2
Swedish Whitebeam	-9.6%	23.4%	-2.2%	-1.2%	17.8%	6.3%
Ash	-3.2%	25.5%	-4%	-1%	-4.2%	-5.6%
Beech	-14.1%	56.2%	12%	8.5%	-17.6%	7.3%
Holly	-4.4%	1%	---	5.8%	2.4%	---
Sycamore	-31.5%	-46.7%	---	---	---	---

Using the pooled EWT model that included the holly leaf samples, Equations (6.18) and (6.19) for August and October datasets respectively, resulted in severe errors in the EWT estimation in both dates, except for the ash tree in October and the holly tree in both dates (Table 6-7). This revealed that although the models had high fitting accuracy (R^2 = 0.88 and 0.93 for August and October datasets respectively), the models did not represent the NDI – EWT relationship at the canopy level, except for the holly species, and thus produced significant errors in the EWT estimation. When the pooled EWT models that excluded the holly species were used, Equations (6.20) and (6.21) for the August and October datasets respectively, the errors dropped significantly (Table 6-7). Thus, care must be taken while fitting a pooled EWT estimation model that is to be applied at the canopy level in a mixed-species plot, and species that have thicker leaves or different surface characteristics than the remaining species need to be excluded from the model.

In the case of the diseased sycamore tree, both pooled EWT models failed to correctly estimate EWT at the canopy level, with the first model producing severe error in the EWT estimation (- 46.7 %), and the second model producing a below zero EWT value. This suggested that this EWT estimation approach can be inapplicable if leaves were covered with a material that did not affect the two wavelengths included in NDI in a similar manner. However, such diseased trees will appear as outliers in the NDI – EWT relationship in comparison to the healthy trees and thus, this approach can help in detecting diseased trees in tree plots. Following the unsuccessful attempts to estimate EWT of the sycamore tree, the tree was not included in October dataset.

Overall, the errors in August were less than the errors in October, except for the beech tree, which may have been a result of leaf senescence. Senescence effect on leaf internal structure is known to vary between species, and can also vary between leaves from the same species if they were at different levels of senescence (Buchanan-Wollaston, 1997). Thus, it can be more challenging to build a NDI – EWT model that can accurately represent all levels of senescence in the plot. Another source of errors was the wind effect. Although the plot was scanned in non-windy conditions on both dates, there was a gentle breeze in October during the scan. This may have reduced the accuracy of aligning the point clouds from the two instruments in the October dataset, leading to higher errors in estimating EWT on a point-by-point basis. However, this was not obvious in the RMSE of point cloud alignment, which was 3 mm in both datasets.

6.5.3 Detecting the temporal changes in EWT

Table 6-8 shows the change in EWT between August and October for the four trees used in validating the EWT estimates. The destructive sampling results showed an increase in EWT for the Swedish whitebeam, ash and beech trees. The highest increase in EWT was observed in the beech tree, whilst the ash tree showed the least change in EWT between the two dates. On the other hand, some decrease in EWT was observed in the holly tree. However, the change in EWT was measured only for the sections of the trees from which leaf samples for validation were collected and did not necessarily represent the change in EWT for the whole canopy, which would require collecting leaf samples from all canopy layers (see Section 6.5.4 for EWT vertical profiles).

Using the pooled EWT estimation model to detect the change in EWT resulted in an overestimation of the increase in EWT for the Swedish whitebeam, indicating that EWT increased by 26.7 % in this section of the tree, while leaf sampling showed that it only increased by 17.4 %, with 9.3 % difference between them. On the other hand, it underestimated the increase in EWT for the beech tree, which had an increase in EWT by 20.6 % according to leaf sampling, and by 15.8 % according to TLS (4.8 % difference). The change in EWT was detected more accurately for the ash and holly trees as shown in Table 6-8, with the difference between actual and estimated EWT change (%) being 1.2 % and 1.6 % respectively.

Using the species-specific EWT estimation models also resulted in an overestimation of the difference between EWT in August and October for the Swedish whitebeam, ash and beech trees, and underestimation for the holly tree. The overestimation was very significant in the beech tree. Overall, the pooled EWT model detected the change in EWT more accurately than the species-specific models. Table 6-8 summarizes the observed temporal change in EWT and the accuracy of detecting such change using TLS data.

The accuracy of detecting the change in EWT was mainly a function of the EWT estimation errors on both dates. An overestimation or underestimation of EWT in both dates, with similar magnitude of errors, produced the most accurate estimation of the change in EWT. A higher magnitude of error in one dataset than in the other produced less accurate estimates of the change in EWT, while overestimating EWT in one dataset and underestimating it in the other produced the least accuracy, as observed in the Swedish whitebeam tree. Overall, the direction and magnitude of the change in EWT was successfully characterized using TLS in the four sampled trees, showing the potential of this method to be used in detecting the impact of drought

on vegetation. With the very high temporal resolution of TLS, being independent on solar illumination or limited by cloud coverage, it can be used to fill the gaps in time series produced using optical RS spaceborne sensors.

Table 6-8. Temporal changes in EWT between August and October.

		Swedish Whitebeam	Ash	Beech	Holly
Actual EWT (g/cm^2)	August	0.0092	0.0127	0.0068	0.0266
	October	0.0108	0.0139	0.0082	0.0239
	Difference	0.0016	0.0012	0.0014	-0.0027
	Difference (%)	17.4%	9.4%	20.6%	-10.2%
Estimated EWT (g/cm^2) species-specific	August	0.0084	0.0122	0.0058	0.0268
	October	0.0106	0.0138	0.0089	0.0245
	Difference	0.0022	0.0016	0.0031	-0.0023
	Difference (%)	26.2%	13.1%	53.4%	-8.6%
Estimated EWT (g/cm^2) pooled model 2	August	0.0091	0.0121	0.0076	---
	October	0.0114	0.0131	0.0088	---
	Difference	0.0023	0.001	0.0012	---
	Difference (%)	25.3%	8.3%	15.8%	---

The temporal change in EWT was also observed in the visual inspection of the point clouds of the trees on both dates, as shown in Figure 6-17 for Swedish Whitebeam tree 1 as an example.

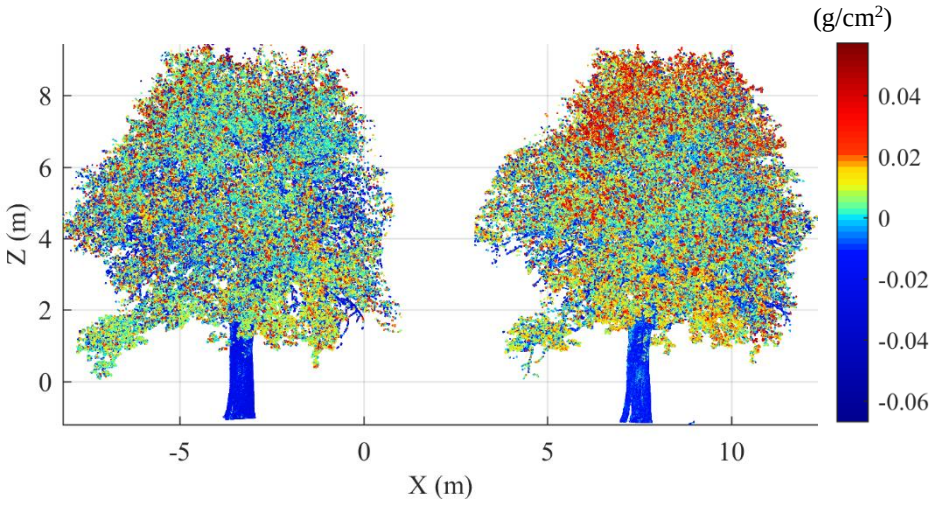

Figure 6-17. EWT pointcloud of Swedish Whitebeam tree 1 in August (left) and in October (right). An increase in EWT was observed in October.

6.5.4 Vertical profiles of EWT

Figure 6-18 shows the vertical profiles of EWT for six trees in the plot: two ash trees, two Swedish whitebeam trees, and two holly trees. The sycamore tree was excluded following the

severe errors in EWT estimation. The beech tree was partially occluded by an ash tree and a holly tree, resulting in few laser beam returns from the middle and upper canopy, and thus it was not possible to generate a vertical profile of EWT.

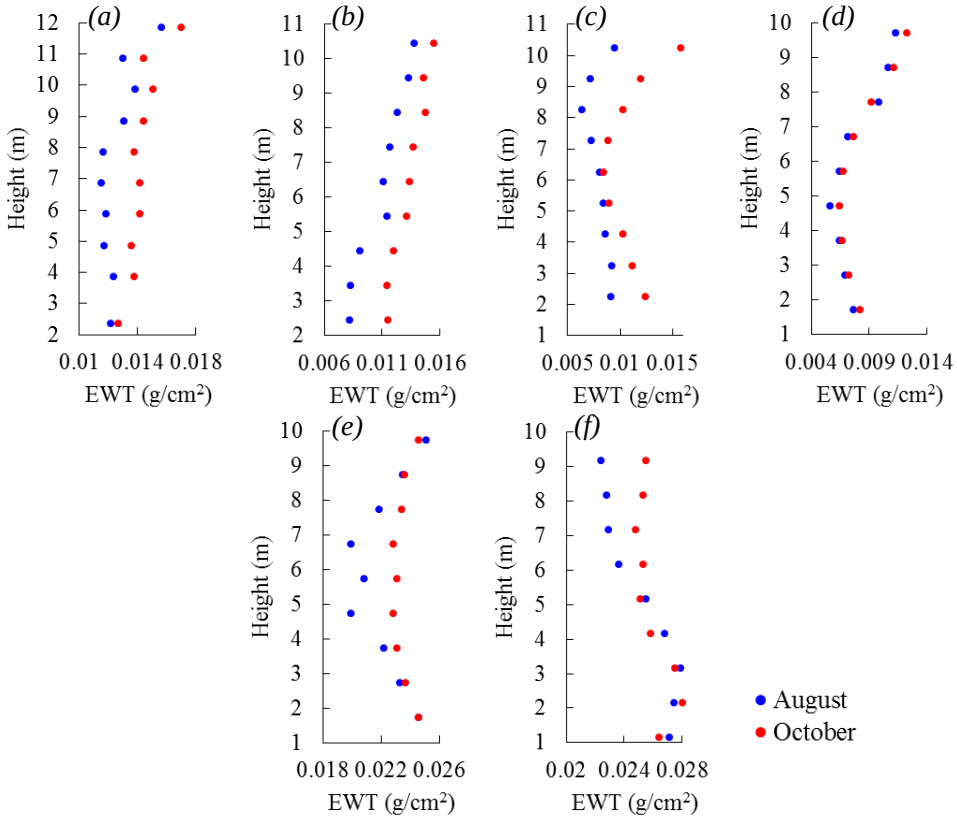

Figure 6-18. EWT vertical profiles in August and October: *(a)* Ash tree 1, *(b)* Ash tree 2, *(c)* Swedish Whitebeam tree 1, *(d)* Swedish Whitebeam tree 2, *(e)* Holly tree 1 and *(f)* Holly tree 2.

Both ash trees, in August and October, had higher EWT in the canopy top than in the canopy bottom, agreeing with the findings of the indoor dry-down experiment (Chapter 4) and the forest dataset (Chapter 5). For ash tree 1, EWT was 29% higher in the canopy top than in the canopy bottom in August, and 34% higher in the canopy top than in the canopy bottom in October, whilst for ash tree 2, EWT was 67% higher in the canopy top in August and 34% higher in the canopy top in October. Both trees had higher EWT in October than in August in all layers, suggesting that when the trees were stressed in August, they lost EWT from all layers, agreeing with the findings of the indoor dry-down experiment in which the deciduous snake-bark maple tree was losing EWT from all layers while being dried down over a period of eight days (Chapter 4). Additionally, the vertical profiles showed that ash tree 2 had lower EWT than ash tree 1 and also was more stressed during the heatwave in August, losing more EWT than ash tree 1, especially in the canopy bottom.

The Swedish whitebeam trees showed different behaviour to the ash trees. Both trees had higher EWT in the canopy top than in the canopy bottom in both dates, except for tree 1 in August in which canopy layers between 7 m and 10 m had the lowest EWT. However, the vertical profiles of EWT were hourglass shaped with the lowest EWT being in middle canopy layers. For tree 1, EWT was higher in October than in August and comparing the EWT vertical profiles in both dates revealed that there was almost no change in EWT in middle canopy layers, while EWT increased in the top and bottom layers in October. In August, EWT was higher in the canopy top than in the canopy bottom by only 4%, while it was higher by 27% in October. For tree 2, slight change in EWT was detected between August and October, with EWT in October being slightly higher. EWT was higher in the canopy top than in the canopy bottom by 48% and 49% in August and October respectively. The tree either was not affected by the heatwave, or had not yet recovered from the stress caused by the drought, considering that overall it had lower EWT in October than tree 1.

Similar to the Swedish whitebeam trees, holly tree 1 had hourglass EWT vertical profiles in August and October, with EWT in middle layers being less than that in the top and bottom of canopy. However, contrary to the behaviour observed in Swedish whitebeam tree 1, holly tree 1 maintained the same EWT in the top and canopy bottom during and after the heatwave, while middle canopy layers showed an increase in EWT in October. However, holly tree 2 had different EWT vertical profiles than holly tree 1 and also than all the other species. EWT was lower in the canopy top than in the canopy bottom in both August and October by 17% and 4% respectively. Also, there was a slight change in EWT between the two dates in the canopy bottom, while EWT increased in the canopy top in October.

It was unclear why two trees of the same species, in the same plot, had substantially different vertical profiles of EWT and also reacted in a different manner to stress during a heatwave. A possible explanation is the illumination conditions of the plot, which may have caused the two trees to be illuminated in different ways, thus resulting in the trees growing sun/shade leaves in different canopy layers. Typically, sun leaves grow in the canopy top because the top layers of the canopy receive the majority of irradiance (Chazdon and Fetcher, 1984). However, as there was a wide gap in the canopy in the middle of the plot, sun leaves were not necessarily in the canopy top only, depending on how the trees were illuminated. Holly is known to be able to grow different types of leaves depending on the position of leaves in the canopy, with shaded, canopy bottom leaves having sharp prickles to protect them from animals and insects, while sun leaves are smaller and smoother (Herrera and Bazaga, 2013). However, despite all leaf

samples being collected from the canopy bottom in both dates, among the eighteen leaf samples collected only four were prickly, while fourteen were smooth, suggesting that the canopy bottom layers were sun leaves. This can explain why the two holy trees in the plot had high EWT in canopy bottom layers, and also attempted to maintain the EWT in these layers unchanged when the trees were stressed, while losing moisture from middle canopy layers in holly tree 1, and from the canopy top in holly tree 2.

6.6 Species- and site-independent EWT estimation model

The leaf level results discussed in section 6.5.1 showed that it was not possible to fit a general, site-independent EWT estimation model for senescent leaves, if they were at different levels of senescence. However, it was possible to fit a pooled, species- and site-independent EWT model for green leaves, described in Equation (6.20), combining the leaf samples collected in the August dataset with the leaf samples collected in the indoor dry-down experiment (Chapter 4). To further investigate this finding, the leaf samples collected in the forest dataset (Chapter 5) were added to the model (Figure 6-19), resulting in a very high fitting accuracy (R^2 = 0.91). The model can be described as:

$$EWT\ (g\ cm^{-2}) = 0.0543 \times NDI - 0.0034 \quad (6.22)$$

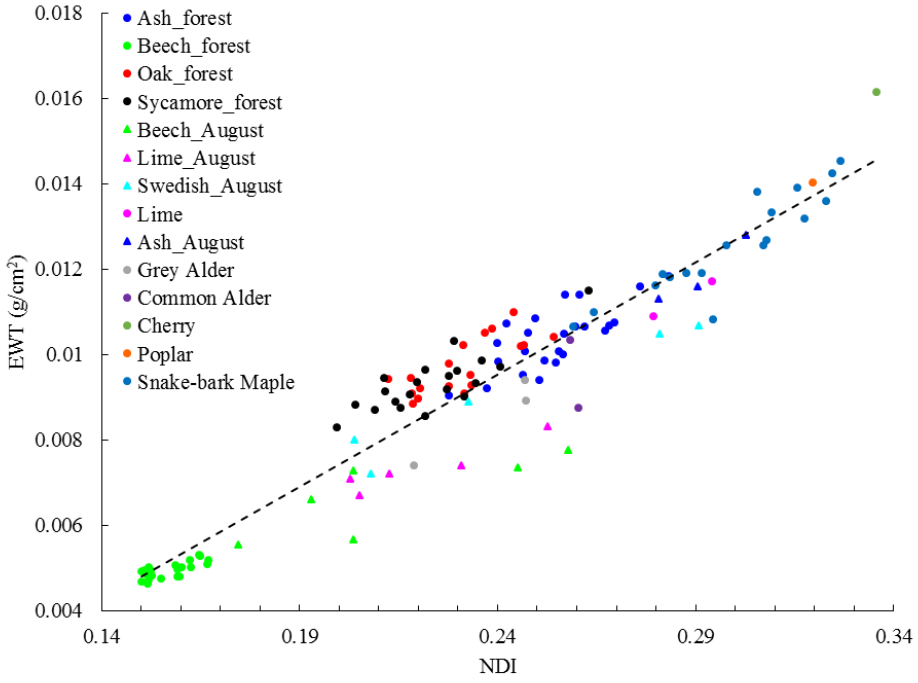

Figure 6-19. The general, species- and site-independent pooled NDI – EWT model that combined all leaf samples.

The all-samples pooled EWT model further showed that the NDI – EWT relationship was not driven by species as much as it was driven by the variation in leaf internal structure. Variation in NDI values of leaves with similar EWT was in some cases more significant within individual species than it was between different species, as observed in the beech and lime leaf samples. Another example was the sycamore and oak leaf samples, as at similar EWT values, NDI of some sycamore leaves was more similar to that of oak leaves than to other sycamore leaves. The same was observed in ash leaf samples. The high fitting accuracy of the model suggested that such variation in NDI was insignificant; however, as discussed in Section 6.5.1, a high fitting accuracy of the EWT estimation model at the leaf level does not necessarily reflect the accuracy of the model at the canopy level. Thus, the all-samples pooled model was tested at the canopy level in both forest and August datasets. Errors in the EWT estimations are shown in Table 6-9 for the August dataset and Table 6-10 for the forest dataset.

Table 6-9. For August dataset, a comparison between the errors observed in the EWT estimation using the all-samples pooled EWT model and the Park-only EWT model.

	Relative error in EWT estimations	
Species	All samples EWT model	Park only EWT model
Swedish Whitebeam	5.3%	-2.2%
Ash	-1.8%	-4%
Beech	25%	12%

Table 6-10. For forest dataset, a comparison between the errors observed in the EWT estimation using the all-samples pooled EWT model and the forest-only EWT model.

		Relative error in EWT estimations			
		All samples EWT model		Forest only EWT model	
Tree	Species	Canopy top	Canopy bottom	Canopy top	Canopy bottom
1	Sycamore	-9.1%	3%	-5.3%	7.2%
2	Sycamore	-16%	0.2%	-13.5%	4.3%
3	Sycamore	-6.6%	0.3%	-2.7%	4.3%
4	Sycamore	---	3.2%	---	7.3%
5	Beech	-6.3%	---	-2.8%	---
6	Sycamore	-4.9%	---	-1%	---
8	Oak	---	5.8%	---	10.2%
9	Oak	2.3%	---	6.7%	---
10	Oak	-2.1%	---	2.1%	---
11	Oak	-6.3%	---	-2.4%	---
12	Sycamore	-16%	---	-13.3%	---
13	Oak	-9.1%	---	-5.4%	---
Average error		7.9%	2.5%	5.5%	6.7%
Total error		6.6%		6.3%	

For the August dataset, the EWT estimation accuracy obtained using the all-samples pooled EWT model was comparable to the park-only pooled EWT model, except for the beech tree. The overestimation of the beech tree EWT indicated that the tree had leaves significantly thinner, or with different mesophyll structure, than the leaves of the other trees in the plot. Although leaf thickness was not measured, LMA measurements showed that beech leaf samples had lower LMA than ash and Swedish Whitebeam leaves (0.0056, 0.0071 and 0.0075 g/cm^2, respectively), suggesting, but not confirming, that they were thinner.

For the forest dataset, the average of the relative errors in the EWT estimation using the all-samples pooled model was 6.6%, insignificantly higher than the error observed when the forest-only pooled model was used (6.3%). However, many of the errors in the canopy top layer increased and the errors in the canopy bottom layers decreased, as a result of the EWT estimation model containing many canopy-bottom leaves. Error in each individual tree was < 10 %, except for sycamore trees 2 and 12, for which EWT was underestimated. The high errors and the EWT underestimation in the two trees indicated that their leaves were thicker, which was reflected in their higher LMA in comparison to the leaves from the other sycamore trees (0.0029 g/cm^2 for sycamore trees 2 and 12 and average of 0.0021 g/cm^2 for the remaining Sycamore tree, ranging between 0.0017 and 0.0024 g/cm^2). The results revealed that the all-samples pooled EWT model was species-independent, but site-independent only to an extent.

6.7 3D mapping of FMC

Typically, FMC and EWT are correlated water status metrics, as FMC can be quantified as EWT divided by LMA. FMC is linked to the potential of fire ignition and propagation (Viegas *et al.*, 1992), in addition to the fire spread rate (Nelson Jr, 2001). Thus, it has been widely used in wildfire modelling and early detection of wildfire risk (Danson and Bowyer, 2004). Following the successful estimation of EWT in 3D using NDI, FMC of leaf samples collected in the October dataset was measured, following Equation (6.23), and was directly linked to NDI. NDI – FMC relationships were established at the leaf level and applied at the canopy level to investigate the possibility of generating 3D FMC point clouds and FMC vertical profiles. Figure 6-20 shows the NDI – FMC relationships established at the leaf level.

$$FMC\ (\%) = \left(\frac{FW\ -\ DW}{DW}\right) \times 100 \tag{6.23}$$

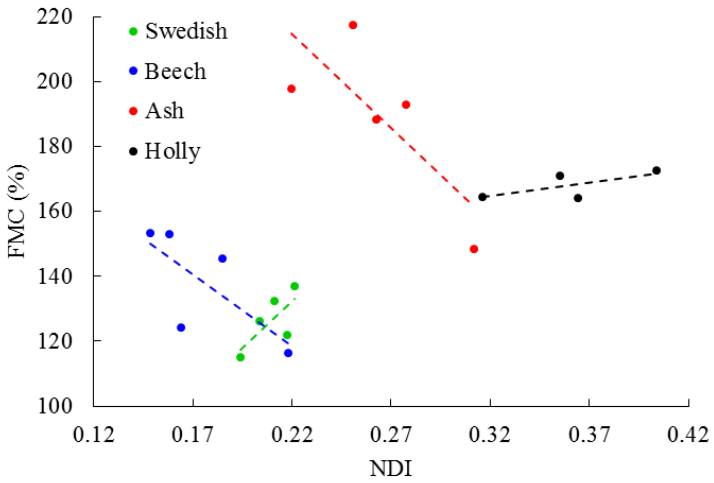

Figure 6-20. The NDI – FMC relationships at leaf level for October dataset leaf samples.

The highest FMC was observed in ash leaf samples (189 %), followed by holly leaf samples (168 %). The beech leaf samples had a lower FMC (138 %), whilst FMC observed in the Swedish whitebeam samples was the lowest (126 %). This differed from the observation obtained for EWT of the same leaf samples, which showed that holly had the highest EWT and beech had the lowest. Moderate linear correlation was observed between NDI and FMC for all species (R^2 = 0.53, 0.51, 0.60 and 0.45 for Swedish whitebeam, beech, ash and holly, respectively), and the correlation was lower than that achieved in the NDI – EWT relationships. This was expected, as EWT is known to be more correlated to reflectance in the optical domain than FMC (Ceccato *et al.*, 2001). NDI and FMC were found to be directly proportional for Swedish whitebeam and holly species, but inversely proportional for ash and beech (Figure 6-20). The NDI – FMC relationship was found to be species-dependent and it was not possible to fit a pooled, species-independent FMC estimation model. This observed variation in the NDI – FMC relationships between species was caused by the difference in LMA between them, as FMC is sensitive to the change in LMA (Riaño *et al.*, 2005; Yebra *et al.*, 2008). This agreed with the findings of Ceccato *et al.* (2001), reporting that EWT and FMC were not always directly related, as they are two different ways to define vegetation water content, and observing an inverse relationship between them in some species, as a result of the LMA effects.

The species-specific NDI – FMC models can be described as follows:

$$\text{FMC (\%)} = 581.46 \times \text{NDI} + 4.58, \text{ for Swedish whitebeam} \quad (6.24)$$

$$\text{FMC (\%)} = -445.18 \times \text{NDI} + 216.27, \text{ for beech} \quad (6.25)$$

$$FMC\ (\%) = -580.57 \times NDI + 342.55, \text{ for ash} \quad (6.26)$$

$$FMC\ (\%) = 83.86 \times NDI + 137.86, \text{ for holly} \quad (6.27)$$

At the canopy level, FMC was estimated with errors < 8 % in the four trees used for validation, with the average error in the estimation being 4.5 % (Table 6-11). 3D FMC point clouds were generated for the same six trees shown in Figure 6-18. Figure 6-21 shows the 3D FMC point cloud of Swedish whitebeam tree 1. Similar to the 3D EWT point clouds, the FMC point clouds revealed a difference between leaf and wood, and also showed vertical heterogeneity in FMC distribution within canopy.

Table 6-11. The errors in the FMC estimations at canopy level.

Species	Actual FMC (%)	Estimated FMC (%)	Relative error (%)
Swedish whitebeam	146.8	135.5	-7.7
Ash	189.7	186.4	-1.6
Beech	137.5	128.6	-6.4
Holly	166.1	169.8	2.2

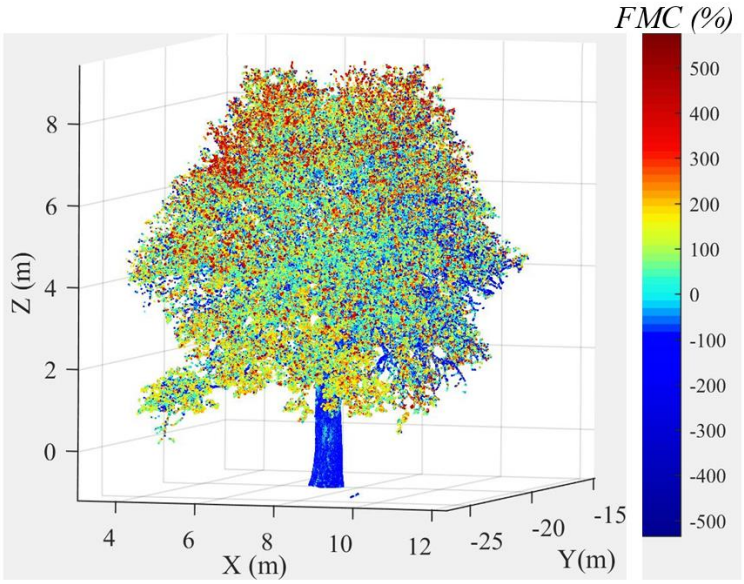

Figure 6-21. 3D FMC point cloud of Swedish whitebeam tree 1.

FMC vertical profile was generated for each tree (Figure 6-22). FMC vertical profiles concurred with the visual inspection of point clouds and revealed some vertical variation in all trees. The vertical profiles of FMC varied between species, and also showed some variation between the two trees from each species. For the Swedish whitebeam trees, the trees displayed hour-glass shaped FMC distribution, similar to their EWT vertical profiles, with the lowest FMC being

located in the middle of the canopy, which was more obvious in tree 1 than in tree 2. The two trees had similar FMC in the upper canopy (layers > 6 m), whilst tree 1 had a higher FMC in the lower canopy than tree 2. Overall, tree 1 had 28 % higher average FMC than tree 2 (138 % and 108 %, respectively).

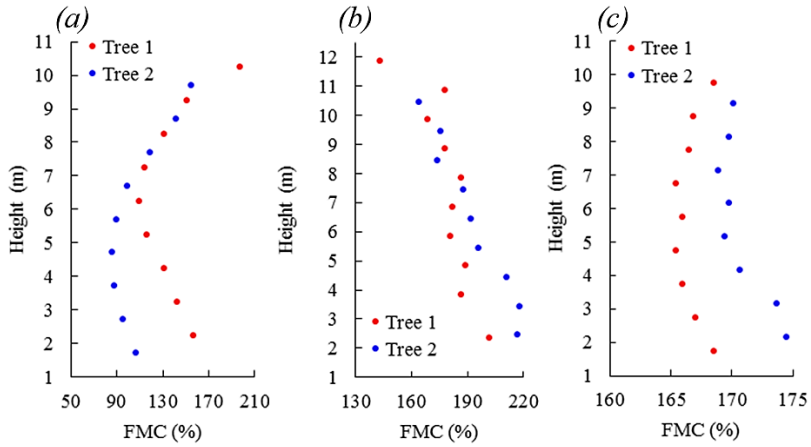

Figure 6-22. FMC vertical profile for six trees in the plot: *(a)* Swedish whitebeam trees 1 and 2, *(b)* ash trees 1 and 2, and *(c)* holly trees 1 and 2.

For ash trees, the two trees had similar FMC in the upper canopy (layers > 7 m), while tree 2 had higher FMC in the lower canopy than tree 1. However, the difference in the mean FMC between the trees was less significant than that in the Swedish whitebeam trees, as tree 2 had only approximately 7 % higher FMC than tree 1. Also, the highest observed FMC in ash trees was in the canopy bottom, while the lowest was in the upper canopy, showing different FMC vertical profiles than the hour-glass shaped FMC vertical profiles observed in the Swedish whitebeam trees. The FMC vertical profiles were also the opposite to the EWT vertical profiles, as a result of NDI being inversely proportional to FMC for ash. Holly trees showed the least vertical variation in FMC. Tree 1 had an hour-glass shaped FMC vertical profile, with FMC in the middle canopy being slightly lower than that in the upper and lower canopy. However, tree 2 showed a different behaviour, as FMC in the upper and middle canopy was almost constant, while FMC was slightly higher in the lower canopy. The FMC vertical profiles matched the EWT vertical profiles.

Although the results obtained from this dataset were promising, more experiments that include leaf samples for validation from multiple canopy layers are needed to validate the accuracy of the 3D FMC estimates. The method also needs to be tested in a real forest environment, and the data collected in Wytham dataset (Chapter 5) was insufficient for this, as LMA measurements

were carried out in the upper and lower canopy only, while LMA vertical profiles are needed to fully validate this approach. Combining TLS data with multispectral or hyperspectral imagery can lead to better quantifying of the LMA vertical heterogeneity in forest canopies, and thus allowing the use of TLS to provide 3D FMC point clouds in forest stands. Overall, FMC was outside the scope of this research, which focuses mainly on EWT, and this dataset can only be considered a proof-of-concept for future work.

6.8 Summary

This chapter investigated the transferability of the EWT estimation approach to two different sites: willow bioenergy crop plots and a mixed-species tree plot. The experiments described in this chapter aimed at studying the effects of wind and senescence of leaves on the accuracy of the EWT estimation, and investigating the possibility of using the proposed EWT estimation approach to detect temporal changes in EWT.

Regarding the wind effects, as expected, it was found that in windy conditions mapping EWT in 3D was not possible because of the low registration accuracy of the point clouds from the two TLS instruments. However, it was still possible to estimate the average EWT in the whole canopy or in individual layers of the canopy, as long as calculations were not done on a point-by-point basis.

Leaf senescence was found to significantly affect the NDI – EWT relationship, as it alters the leaf internal structure in a way that seemed to vary depending on the leaf level of senescence. It was not possible to fit a pooled, site-independent NDI – EWT model. However, it was possible to fit a pooled, site-specific EWT estimation model for leaf samples that were at similar levels of senescence. On the other hand, for green leaves, a species-, site-independent EWT estimation model was derived, and was found to be able to estimate EWT with accuracy very close to that obtained using site-specific models. However, care must be taken when applying the model, as large errors in EWT estimation would be obtained in trees that have leaves with significantly different internal structure (thinner/thicker) than the majority of leaves used in building the model.

It was possible to detect the temporal change in EWT using TLS data. The accuracy depended mainly on the errors obtained in EWT estimation in the different dates. Consistent errors in both dates resulted in high accuracy in detecting the change in EWT. However, less accuracy was obtained when EWT was overestimated in one dataset and underestimated in the other.

Although the results obtained were very promising, the method needs to be tested in a real forest environment to investigate the ability of TLS data to detect the change in EWT in such a challenging environment.

Chapter 7. Integrating the 3D EWT estimates in radiative transfer modelling

7.1 Introduction

The results obtained in Wytham Woods (Chapter 5) revealed vertical heterogeneity in EWT in the forest plot, with the upper canopy having an average of 24% higher EWT than the lower canopy. As discussed in Chapter 2, the effects of such vertical heterogeneity on the accuracy of EWT estimation using optical remote sensing data is often ignored, as it is difficult to measure and to account for in EWT estimation models. This chapter is dedicated to integrating the 3D EWT estimates obtained in Chapter 5 into the 3D RTM DART. Two groups of simulations were conducted to study the effects of woody materials, understory, and EWT vertical heterogeneity on the Bottom of the Atmosphere (BOA) reflectance and the NDWI, using two different forest scenes. Additionally, example scenarios of water stress, that affected the whole canopy or started in the lower canopy then spread upward, were simulated to investigate which canopy layers dominated the forest plot reflectance. Such water stress can be caused by drought or infections by pests or diseases that affect the lower canopy first, such as oak anthracnose, oak leaf blister, sycamore anthracnose, and ash dieback (Downer, 2006; Horst and Horst, 2013; Pokorny, 2015). To link the simulations to real satellite data, the simulated reflectance and NDWI were compared to actual values retrieved from Sentinel-2A near- and shortwave-infrared bands (864 nm and 1613 nm, respectively).

7.2 DART concept and background

DART (Gastellu-Etchegorry *et al.*, 1996) is a 3D RTM which has been developed in the CESBIO (CEntre for the Study of the BIOsphere from space) laboratory since 1992. DART is capable of simulating the radiative budget in any user-defined Earth-atmosphere system, as acquired by airborne and spaceborne optical sensors, in the visible and infrared (near, shortwave, and thermal) regions of the electromagnetic spectrum (Gastellu-Etchegorry *et al.*, 2004). Radiative budget refers to the balance between solar radiation entering an Earth-atmosphere system and reflected radiation and thermal emissions from the system (Kiehl and Trenberth, 1997). DART computes the radiation propagation through the system, simulating the radiation scattering and absorption by the atmosphere and Earth landscape, plus thermal emissions from both of them, and produces a 3D radiative budget, in addition to images at various altitudes. Simulated images are produced at BOA and Top of the Atmosphere (TOA) for any user-defined sensor, viewing angles, sun illumination angles, and spectral bands, in

addition to images at any other sensor altitude specified by the user. Simulated images are coupled with Look Up Tables (LUTs) that contain BOA and TOA spectral products, including scene radiance, irradiance, albedo, and reflectance, for all specified sensors and configurations. Irradiance refers to the incident radiation, radiance is the reflected radiation, albedo is the ratio between radiance and irradiance, while reflectance is the same fraction for a single incidence angle (sun position) (Wanner *et al.*, 1997). TOA products resemble satellite sensor measurements and are influenced by atmospheric effects (scattering and absorption), and thus require radiometric corrections in real-life scenarios. Among the aforementioned DART products, BOA reflectance was the focus of this study, as it is the product being used in deriving vegetation indices. The numerous other spectral products that DART provides are described in detail in Gastellu-Etchegorry *et al.* (2015).

DART simulation is conducted using four modules: Direction, Phase, Maket, and Dart. The inputs for the Direction module are the sensor characteristics, viewing angle, spectral bands, and sun angular position (azimuth and zenith angles). The module then computes discrete directions of light propagation to be used in flux tracking during the simulation. For the Phase module, the atmospheric parameters need to be defined, including gas and aerosol (solid or liquid particles suspended in the air) density profiles, which can be defined manually, imported into the model, or selected from the model database. In addition, the optical properties of all objects in the scene need to be specified. Optical properties can be manually defined or selected from the DART database. The Phase module uses the inputs to calculate scattering phase functions for elements in the Earth landscape and the atmosphere, based on their pre-defined optical properties and geometry. A scattering phase function defines how radiation is scattered by an element at a given wavelength (Seinfeld and Pandis, 2016).

In the Maket module, urban, natural or mixed 3D Earth scenes, with different levels of complexity, can be constructed as a set of 3D cells (voxels) that contain the scene elements. The dimensions of the cells affect the processing time and define the output spatial resolution. 3D objects in the scene can be created in the module or imported into it, then their optical properties, pre-defined in the Phase module, are assigned. 3D objects consist of turbid cells, facets (triangles), or a combination of both, depending on the type of the object. For example, tree trunks and urban features are constructed as facets, while water and vegetation bodies (grass, crop fields, and foliage) are approximated as turbid mediums. A vegetation turbid medium is a set of infinitely small flat surfaces, defined by their leaf angle distribution, volume density, and optical properties. Vegetation foliage can also be modelled as facets, defined by

their orientation in space and surface area. In addition to creating the Earth scene and the 3D objects in it, the atmosphere geometry needs to be specified. DART models the atmosphere as three major sections: Lower Atmosphere (LA), Mid Atmosphere (MA), and High Atmosphere (HA). LA has the height and cell size of the Earth landscape. MA is modelled as a number of cells while HA is modelled as a number of layers. The dimensions of the MA cells and HA layers can be defined by the end-user, or DART default atmosphere geometry (Table 7-1) can be used, depending on the aims of the simulations.

Finally, the Dart module uses the outputs from the Direction, Phase, and Maket modules, and computes radiation propagation and interactions through the atmosphere and the Earth scene, by tracing iteratively radiation fluxes per cell (voxel), and generates the scene 3D radiative budget, simulated images, and spectral products. Gastellu-Etchegorry *et al.* (2015) provides a full description of the DART model, including the physical principles of the model, flux-tracking approaches, different products, and how to define and simulate terrestrial and airborne optical and LiDAR sensors. Figure 7-1 shows a representation of a DART Earth-atmosphere system. The model used in this study was DART 5.6.7.

Table 7-1. DART default atmosphere geometry.

Atmosphere height	MA height	MA cell size	HA height	HA layer thickness
84 km	4 km	100 m × 100 m × 500 m	80 km	2 km

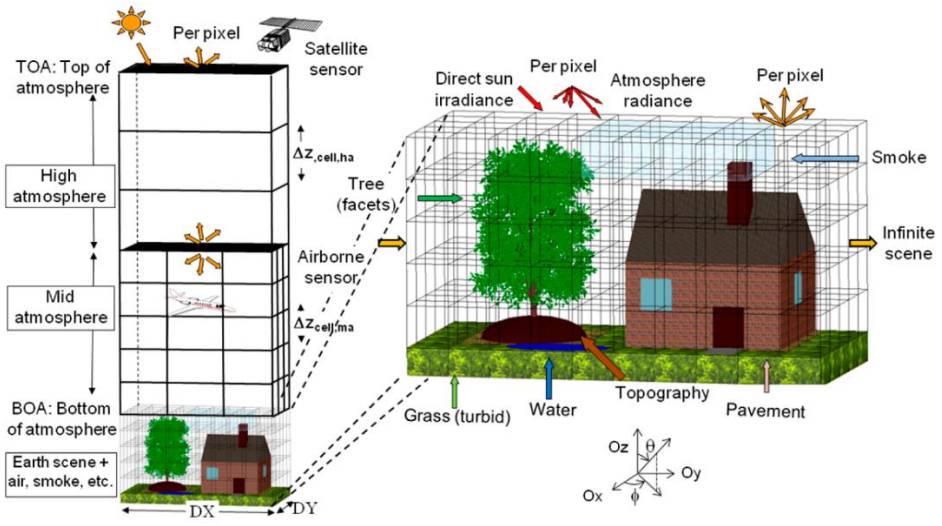

Figure 7-1. DART representation of Earth-atmosphere system. Figure is adapted from Gastellu-Etchegorry *et al.* (2015).

Numerous previous studies have successfully coupled DART simulations with airborne and spaceborne optical data to retrieve vegetation biophysical and biochemical characteristics. SPOT and Ikonos imagery were used for estimating forest LAI, crown coverage, and leaf chlorophyll content through inversion of DART (Gascon *et al.*, 2004). Sepulcre-Canto *et al.* (2009) used ASTER (Advanced Spaceborne Thermal Emission and Reflection Radiometer) satellite imagery and DART simulations to successfully differentiate between irrigated and rain-fed olive orchards. Hernández-Clemente *et al.* (2012) coupled airborne multispectral data with DART simulations to examine the performance of carotenoid vegetation indices at leaf and canopy levels in a pine forest. Banskota *et al.* (2013) estimated forest LAI using AVIRIS hyperspectral data with high accuracy through inversion of the DART model. Malenovský *et al.* (2013) derived a new leaf chlorophyll content vegetation index from the AISA Eagle airborne imaging spectrometer data using DART simulations. Yáñez-Rausell *et al.* (2015) used CHRIS-PROBA images and DART simulations to successfully estimate leaf chlorophyll content of a Norway spruce stand, validating the estimation using AISA Eagle airborne imagery of the same stand. Ferreira *et al.* (2018) combined AISA Eagle airborne imagery with DART simulations to successfully estimate individual tree crowns' structural and biochemical traits (chlorophyll and carotenoid contents) in a diverse tropical forest.

Other applications of the DART model have included designing satellite sensors (Durrieu *et al.*, 2013), studying canopy heterogeneity in Amazonian forests (Barbier *et al.*, 2010), studying variation in tropical forest texture and canopy structure (Barbier *et al.*, 2012), estimating tropical forests biomass (Proisy *et al.*, 2012), and modelling vegetation canopies' 3D distribution of photosynthesis rates (Guillevic and Gastellu-Etchegorry, 1999). No apparent previous studies have modelled the vertical variation in vegetation biochemical characteristics (including EWT) in 3D RTMs, including DART.

7.3 Parametrizing the model

Two spectral bands were defined and used in all simulations, corresponding to Sentinel-2A near- and shortwave-infrared bands (bands 8A and 11, respectively). The first band had a central wavelength of 864 nm and a bandwidth of 33 nm, while the second band had a central wavelength of 1613 nm and a bandwidth of 143 nm. Although DART produces spectral products for various sensor viewing angles, the results presented in this study corresponded to zero zenith and azimuth sensor viewing angles. DART default sun angular position was used (30º zenith angle and 225º azimuth angle). The number of discrete light propagation directions and the number of iterations for flux tracking were 100 and 6 respectively, as recommended by

the developer of the model for the spectral range in the scope of this study. The U.S. standard atmosphere 1976 model (DART database) was used to parametrize how pressure, temperature and density of the atmosphere change with altitude, defining the gas and aerosol vertical profiles and optical properties. As the aim of the simulations was not to study the atmospheric effects on TOA reflectance, it was not necessary to accurately define the atmosphere, and using a standard atmosphere model was considered sufficient, as it was kept constant in all simulations. Optical properties of the understory were predefined as two Lambertian models (DART database). The first resembled healthy grass (Figure 7-2a), and the second resembled leaf litter (Figure 7-2b). For the woody materials, bark-deciduous Lambertian model (DART database) was used (Figure 7-3).

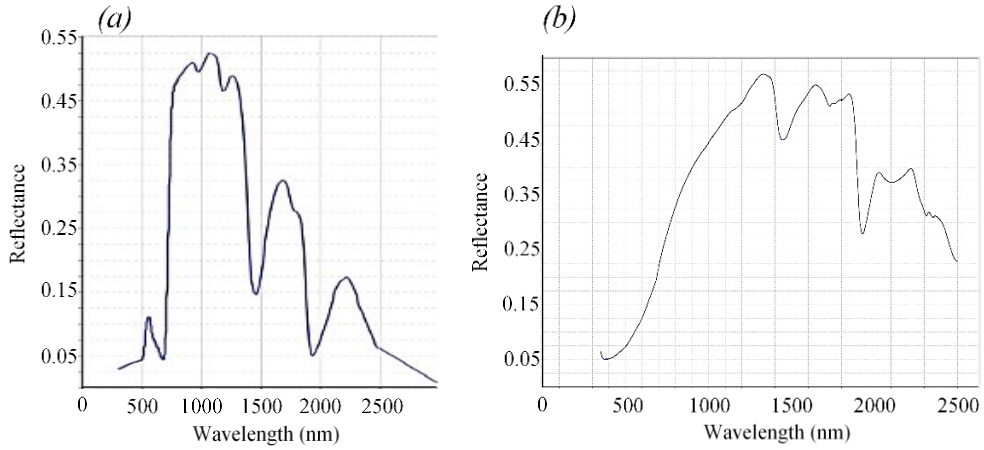

Figure 7-2. Pre-defined understory optical properties: *(a)* healthy grass, and *(b)* litter.

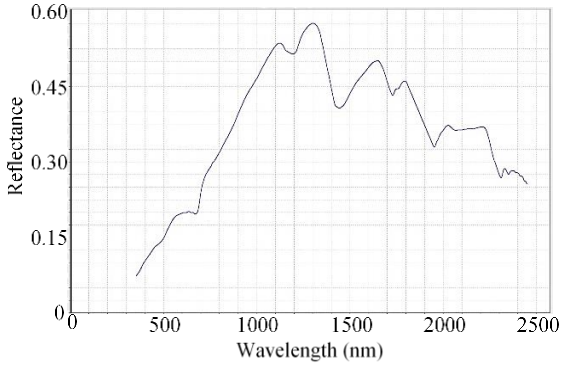

Figure 7-3. Pre-defined bark-deciduous optical model used for woody materials.

Leaf optical properties were simulated using the PROSPECT model, implemented in DART, using the model parameters shown in Table 7-2, unless otherwise stated, and changing EWT depending on the simulation. The leaf structure coefficient was defined based on the values retrieved from field spectroscopy measurements conducted in the forest, as reported in Calders

et al. (2018). LMA was defined based on the destructive sampling conducted in the forest (Chapter 5). Methods to implement the vertical variation of EWT in the model are presented in Section 7.4. It is worth mentioning that leaves were modelled as objects with double-face optical properties. That is, light rays were allowed to scatter on the front face, transmit through leaves, and scatter again on the back face. On the other hand, woody materials were modelled as objects with single-face optical properties, meaning that light rays only scattered on the outer surface of objects.

Table 7-2. PROSPECT parameters used to simulate leaf optical properties.

Leaf structure coefficient	Chlorophyll ($\mu g\ cm^{-2}$)	Carotenoid ($\mu g\ cm^{-2}$)	Brown pigment	LMA ($g\ cm^{-2}$)	EWT ($g\ cm^{-2}$)
1.5	47.7	4.4	0.0	0.0028	variable

Two forest scenes (Sections 7.4 and 7.5) were constructed, having the dimensions of 35 m × 45 m and 40 m × 40 m respectively, and average heights of 16.5 m and 27.6 m respectively. Default values for the scene cell (voxel) dimensions were used (0.3 m × 0.3 m × 0.3 m). DART default atmosphere geometry (Table 7-1) was utilized, keeping the atmosphere optical and geometric characteristics constant in all simulations.

7.4 Forest scene 1

Forest scene 1 represented a mixed-species (sycamore and oak) forest plot, based on the TLS data obtained in the data collection campaign conducted in Wytham Woods (Chapter 5). All the processes described in this section were conducted in CloudCompare v. 2.6.2 software, unless otherwise stated. To build the forest scene, tree stem locations were determined from the TLS point cloud. First, a slice was taken slightly above ground in the plot point cloud, which contained the ground and approximately 20 cm of the stems. Then, the approximate coordinates of the centre of each stem at ground level were acquired and considered as the tree location. As the aim of the planned simulations was to investigate the effects of EWT vertical heterogeneity on BOA reflectance and NDWI, and not to investigate the effects of tree structure variation, it was not necessary to model all the trees in the plot. Instead, to reduce computation time, one sycamore tree and one oak tree were chosen from the plot TLS point cloud to be used in reconstructing the forest scene. The selection of the trees and generation of 3D tree models were performed as follows:

1) The point clouds of the twelve sampled trees around the canopy walkway (Figure 5-2 and Table 5-1) were visually inspected, and six trees (four sycamores and two oaks), which visually suffered the least occlusion, were selected.

2) Leaf and wood in each tree were already separated for EWT estimation (Section 5.4.2). The leaf point cloud was also already divided into multiple layers to generate EWT vertical profiles (Section 5.5.4). A Poisson surface reconstruction model, which generates a triangle mesh from a set of oriented 3D points, using the algorithm described in Kazhdan and Hoppe (2013), was used to reconstruct 3D objects (meshes) from leaf layers and wood point clouds of each tree. According to the developer of the model, the model is recommended for application on closed 3D shapes, thus applying it to leaf and wood point clouds resulted in highly distorted 3D objects, as the model attempted to produce closed shapes, disregarding the shape of leaves and tree branches (Figure 7-4b and Figure 7-5b). However, the model generated the density histogram of the points involved in creating each triangle in the mesh. The density histogram was used to clean the 3D objects and remove the triangles that had very low density by choosing a threshold, based on visual inspection of the meshes and original point clouds. Figure 7-4 shows an example of generating a 3D object from the TLS point cloud for Sycamore tree 1 woody materials. Figure 7-5 shows the same for a single leaf layer in the same tree.

3) The average number of triangles in each tree 3D object was 41 million, as a result of the very dense point clouds used to generate the 3D models. Using 3D objects that had such a high number of triangles was not practical, because of software and hardware limitations, which required reducing the number of triangles. For this, each tree 3D object was imported into MATLAB and the standard MATLAB function ‘reducepatch’ was applied to reduce the number of triangles. The function maintained the boundaries of each shape, attempting to preserve the surface area, and merged the triangles inside the shape to reduce their number. The input was a reduction coefficient (percentage). This was decided by trial and error, by measuring the total mesh surface area before and after applying different reduction coefficients. It was found that the module was able to reduce the number of triangles by approximately 96% with only a slight reduction in the mesh surface area. The average number of triangles in the tree objects after reduction was approximately 1.3 million. This number was still considered high. However, using a higher reduction coefficient was not possible, as it was found to have more impact on the surface area.

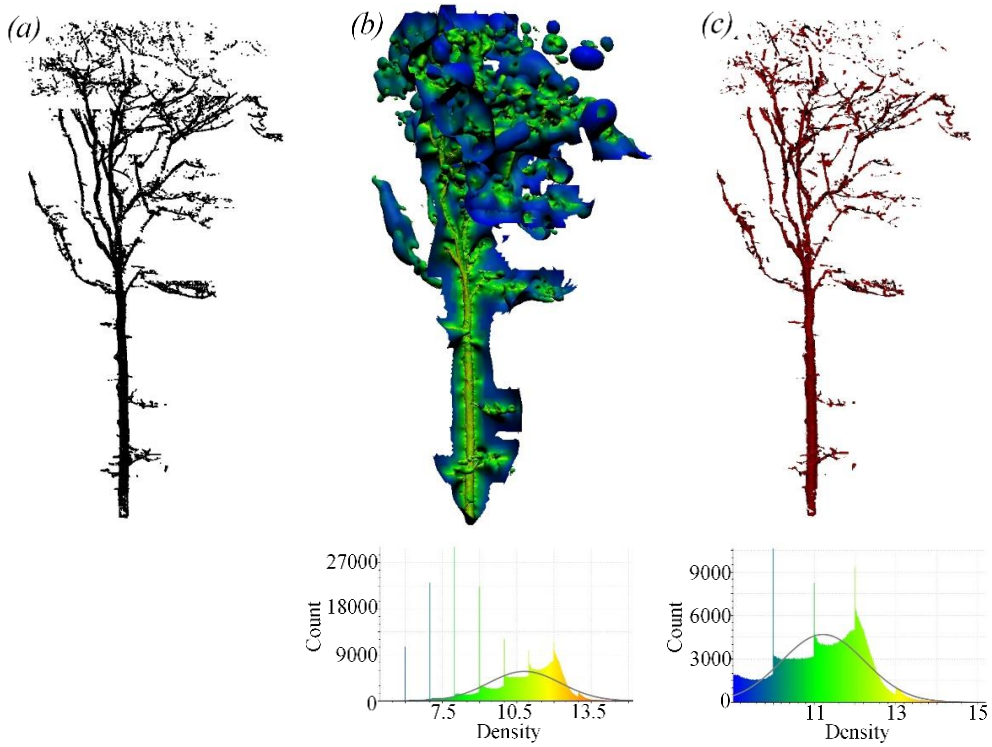

Figure 7-4. Creating 3D object for Sycamore tree 1 woody materials: *(a)* wood point cloud, *(b)* outcome of applying Poisson surface reconstruction model and the histogram of point density in mesh triangles, and *(c)* the final 3D object after removing the noise using the density histogram, guided by visual inspection of the original point cloud.

4) Leaf layer 3D objects of each tree were used to estimate individual tree LAI. First, the total one-sided surface area of the triangles in each layer was calculated. Afterwards, to calculate the canopy projected area, a polygon was interactively fit to the canopy outer perimeter by manually drawing a polyline. The polygon was then projected on a horizontal plane using AutoCAD 2016 and the area inside the polygon was calculated and considered the canopy projected area. LAI of the canopy was calculated as the summation of the one-sided surface area of triangles divided by the canopy projected area (Table 7-3). Sycamore tree 1 and oak tree 10 (Figure 7-6) were chosen to be used in DART simulations as they had the closest LAI to the global average LAI for deciduous forests, which ranges between 3.9 and 5.1, as reported in Asner *et al.* (2003), and in the region of 3-6, as reported in Kozlowski and Pallardy (1996).

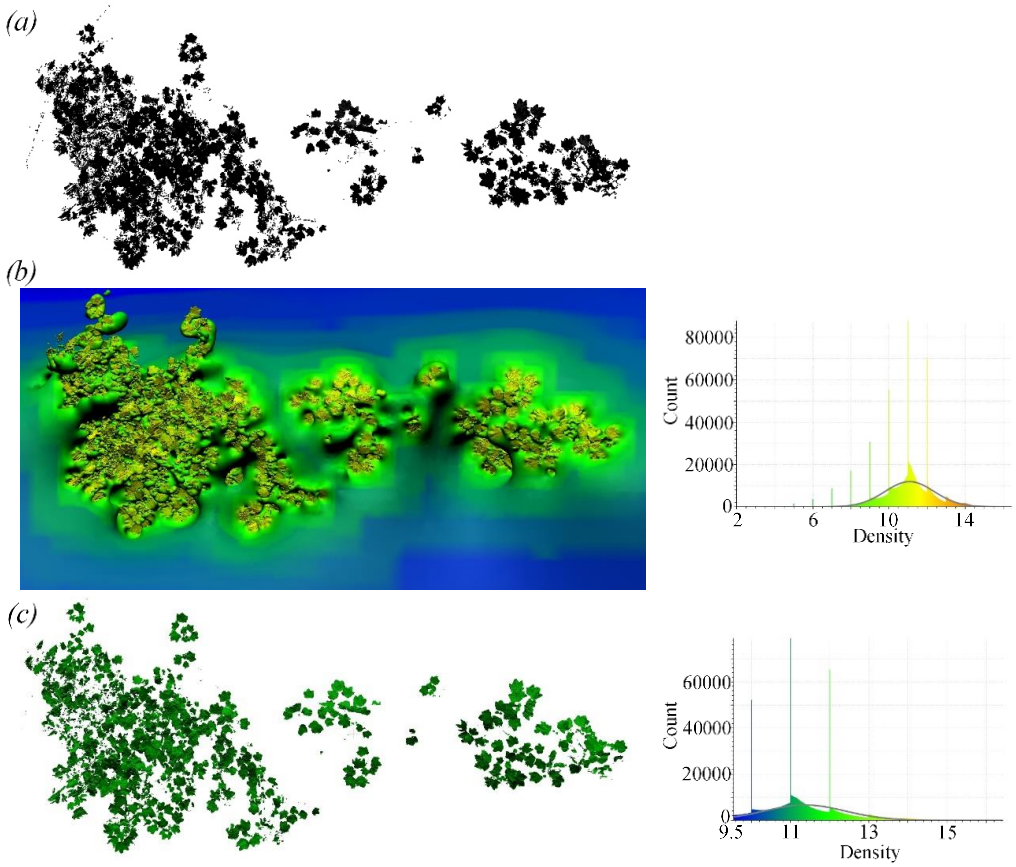

Figure 7-5. Creating 3D object for a leaf layer in Sycamore tree 1: *(a)* layer point cloud, *(b)* outcome of applying Poisson surface reconstruction model and the histogram of point density in mesh triangles, and *(c)* the final 3D object after removing the noise.

Table 7-3. LAI estimated from the trees 3D models.

Tree label	Species	Height (m)	LAI
1	Sycamore	15.80	3.42
2	Sycamore	15.40	2.62
6	Sycamore	17.25	3.01
12	Sycamore	17.42	2.31
10	Oak	16.49	3.03
11	Oak	17.90	1.85

5) To import the trees into DART, 3D objects of each tree (leaf layers and wood) were combined into a single group of objects that resembled the whole tree. The species and coordinates of each tree in the plot were used to distribute the 3D tree objects in the scene. In each location that corresponded to a sycamore tree, the 3D model of sycamore tree 1 was placed, and in each location that corresponded to an oak tree, the 3D model of oak tree 10 was placed. DART considered each tree object a single object that consisted of multiple groups (leaf layers and

wood), making it possible to assign specific optical properties to each layer in the tree to model the vertical variation of EWT. For this, an average EWT vertical profile of the sycamore trees in the plot (Table 7-4) and an average EWT vertical profile of the oak trees in the plot (Table 7-4) were generated from the EWT vertical profiles retrieved in Chapter 5. For each canopy layer, a PROSPECT simulation was conducted, using the parameters shown in Table 7-2, and EWT of the layer, and the resulting optical model was assigned to the layer. Figure 7-7 shows a 3D view of the forest scene.

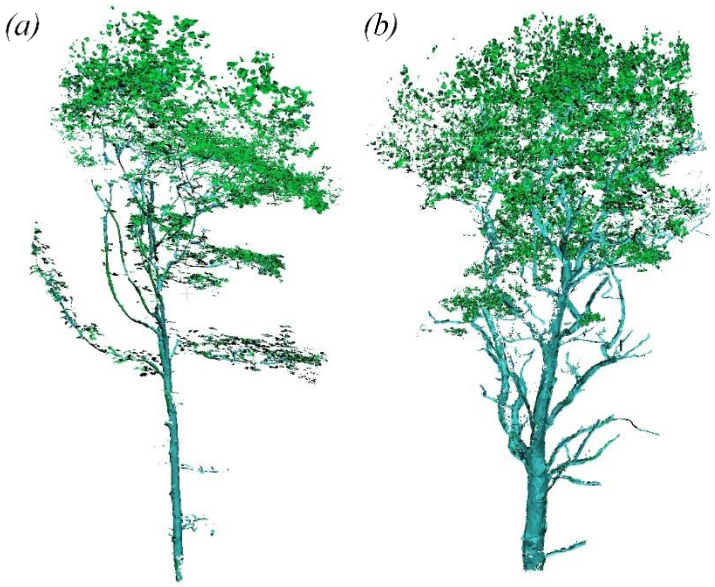

Figure 7-6. The 3D tree objects used to build forest scene 1: *(a)* Sycamore tree 1, and *(b)* oak tree 10.

Table 7-4. The EWT vertical profiles for the 3D models of the Sycamore and Oak trees, used to build forest scene 1. Height was measured to the centre of each layer.

Sycamore			Oak		
Layer	Height (m)	EWT (g cm^{-2})	Layer	Height (m)	EWT (g cm^{-2})
1	15.1	0.0130	1	15.62	0.0131
2	13.9	0.0125	2	14.25	0.0130
3	12.9	0.0122	3	13.25	0.0128
4	11.9	0.0121	4	12.25	0.0122
5	10.9	0.0119	5	11.25	0.0120
6	9.9	0.0115	6	10.25	0.0119
7	8.9	0.0108	7	9.25	0.0114
8	7.9	0.0105	8	7.75	0.0106
9	6.9	0.0107	N/A	N/A	N/A
10	5.9	0.0106	N/A	N/A	N/A

Figure 7-7. 3D view of forest scene 1.

7.5 Forest scene 2

Forest scene 2 was a 40 m × 40 m subset of the 3D model of a one hectare forest stand in Wytham Woods, Oxford, UK, described in detail in Calders *et al.* (2018). The one hectare 3D model was reconstructed using data collected with a RIEGL VZ-400 TLS instrument in leaf-on and leaf-off conditions (Calders *et al.*, 2016). Reconstructing the 3D model is described thoroughly in Calders *et al.* (2018), and followed three main steps: (1) tree segmentation, (2) tree structure modelling, and (3) leaf insertion. Tree segmentation was done using the *treeseg* open-source software (Burt *et al.*, 2018), using the leaf-off point cloud. Tree structure modelling was done by converting each extracted individual tree point cloud to a Quantitative Structure Model (QSM), which is a geometrical model that describes the complete tree woody components in an hierarchical order, including the higher order branches (Hackenberg *et al.*, 2015). For this, cylinders were fitted to the tree point clouds, according to the skeleton of each tree, following the procedure described in Calders *et al.* (2015). Leaves were then added to each tree QSM using the Foliage and Needles Naïve Insertion (FaNNI) algorithm (Åkerblom *et al.*, 2018), by defining the leaf shape, target leaf area, leaf area density distribution, leaf size distribution, and leaf orientation distribution, using the leaf-on point cloud as a guidance, as described in Calders *et al.* (2018).

The subset used in this research contained 44 trees from three different species: sycamore (*Acer pseudoplatanus*), ash (*Fraxinus excelsior*), and hazel (*Corylus avellana*). To reconstruct the forest scene in DART, each tree leaf point cloud was divided into a number of layers, each 1 m deep, depending on the canopy height. For the woody materials, each tree QSM defined the woody components as cylinders, with each cylinder defined as two vertices, top and bottom

respectively, and a radius. As DART is not capable of reconstructing 3D models from such data type, the cylinders were reconstructed in MATLAB, using the free add-on 'cylinder between two points' function. The outcome was one or more cylinder meshes for each wood component in each tree, which were then merged together to build the tree woody materials 3D models (Figure 7-8a). The woody materials 3D models and the leaf layers 3D models were then grouped and imported into DART to build the forest scene (Figure 7-8b).

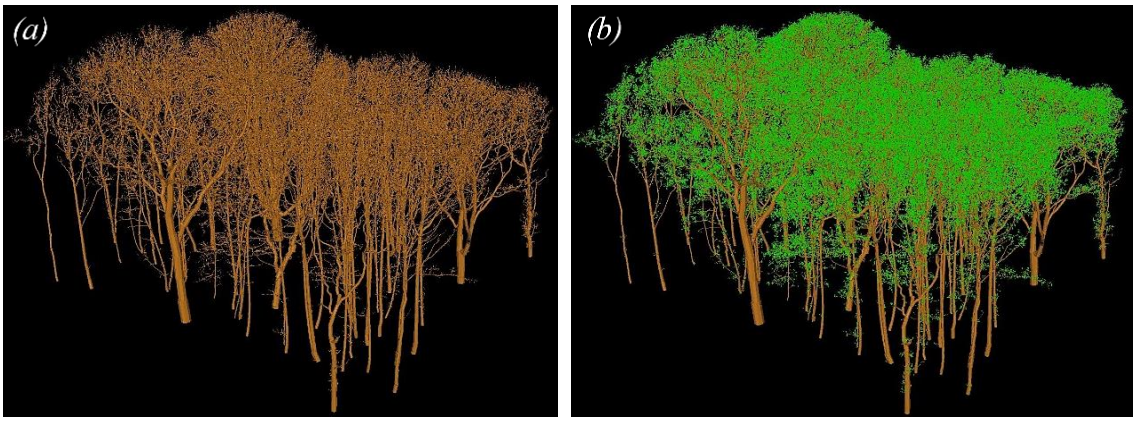

Figure 7-8. 3D view of forest scene 2: *(a)* woody materials 3D objects and *(b)* plot 3D objects, combining wood and leaf 3D models.

The forest scene was a realistic representation of the original forest plot, in terms of the tree species, structure, and locations, unlike forest scene 1, which was reconstructed using only two tree models representing two species. Plus, as the woody materials were modelled as QSMs derived from leaf-off TLS data, the small branches and twigs in the upper canopy were accounted for, whilst they were absent in the tree models used to build forest scene 1 as a result of occlusion in the TLS leaf-on data. In addition, the average height of the scene was 27.6 m, being higher than that of forest scene 1 (16.5 m). This variation in tree structure and species between the two forest scenes can be useful to investigate its effect on the plot reflectance and the NDWI. As no EWT measurements were conducted in this forest plot, and no EWT vertical profiles were generated, EWT was assumed to equal 0.014 g cm^{-2} in all canopy layers, based on EWT retrieved from destructive sampling of sycamore and ash trees (Chapter 5). EWT was then modified to simulate different case scenarios, as discussed in Section 7.6. For each canopy layer, a PROSPECT simulation was conducted using the parameters shown in Table 7-2, except for LMA that was changed to 0.0022 g cm^{-2} in this plot, based on the field spectroscopy conducted in this part of the forest (Calders *et al.*, 2018). Assigning optical properties to each

canopy layer in the 44 trees was time consuming. This further showed the challenges associated with modelling the vertical variation in vegetation biochemistry traits.

7.6 Simulations

Two groups of simulations were carried out. The first group aimed at studying how foliage, woody materials, and understory contributed to the forest plot BOA reflectance and NDWI (Table 7-5). In forest scene 1, EWT was kept constant at 0.013 g cm^{-2} in all canopy layers, being the average EWT of canopy top observed in leaf destructive sampling, while it was kept constant at 0.014 g cm^{-2} in all canopy layers of forest scene 2. Sim 1.1 aimed at measuring the BOA reflectance and NDWI resulting from foliage only, and thus zero reflectance Lambertian optical models were assigned to the woody materials and understory. Sim 1.2 and 1.3 measured the contribution of woody materials and understory, respectively, to the plot BOA reflectance and NDWI, while Sim 1.4 combined both contributions. The results of the simulations were compared to Sim 1.1 results and the change in reflectance and NDWI was calculated. Sim 1.5 investigated how changing the understory from healthy grass to dry litter would affect the plot reflectance and cause a change in NDWI. Thus, the results of Sim 1.5 were compared to the results of Sim 1.4 to calculate the change in reflectance and NDWI.

Table 7-5. Group 1 simulations. EWT value was 0.014 g cm^{-2} for forest scene 2.

	Sim 1.1	Sim 1.2	Sim 1.3	Sim 1.4	Sim 1.5
Foliage PROSPECT reflectance model EWT value (g cm^{-2})	0.013	0.013	0.013	0.013	0.013
Understory reflectance model	Zero	Zero	Healthy grass	Healthy grass	Litter
Woody materials reflectance model	Zero	Bark deciduous	Zero	Bark deciduous	Bark deciduous

The predefined optical models: healthy grass (Figure 7-2a), litter (Figure 7-2b), and bark-deciduous (Figure 7-3), were used in the simulations, as shown in Table 7-5. It is worth mentioning that assigning zero reflectance optical models to ground and/or woody materials meant that light rays that would reach the ground or wood components would be terminated. In a real life scenario, part of the light rays reflected from the ground and wood components can be scattered again by foliage, and thus add to the canopy reflectance. So, it was expected that the results obtained in simulations that included assigning zero reflectance optical properties to ground and/or woody materials would contain a bias.

The second group of simulations aimed at studying the effect of the EWT vertical heterogeneity on the BOA reflectance and the NDWI, and to determine which canopy layers dominated the plot reflectance (Table 7-6). Bark-deciduous Lambertian model was assigned to the woody materials, and healthy grass was assigned to the understory, except for Sim 2.10 in which the understory was modelled as dry litter. In Sim 2.1, it was assumed that EWT dropped in all canopy layers from 0.013 g cm^{-2} (0.014 g cm^{-2} in forest scene 2) to 0.008 g cm^{-2} (38% and 43% drop in EWT for forest scenes 1 and 2 respectively), simulating a water stress condition. In Sim 2.2, canopy layers were dried more, simulating a more severe stress, and lower EWT value was used (0.004 g cm^{-2}, 69% and 71% drop in EWT from its original value for forest scenes 1 and 2 respectively). In simulations 2.1 and 2.2, the vertical heterogeneity in EWT was ignored, and it was assumed that all canopy layers dried simultaneously. Sim 2.3 modelled the vertical variation in EWT. For forest scene 2, as there were no actual EWT vertical profile measurements of the trees, Sim 2.3 was not carried out. Simulations 2.4 to 2.9 aimed at investigating which canopy layers contributed the most to the plot reflectance, by applying different alterations to the EWT in canopy bottom layers, as shown in Table 7-6, simulating scenarios of water stress that started in the bottom of the canopy and then spread upwards.

Table 7-6. Group 2 simulations.

Sim	Forest scene 1	Forest scene 2
2.1	0.008 g cm^{-2} in all canopy layers	0.008 g cm^{-2} in all canopy layers
2.2	0.004 g cm^{-2} in all canopy layers	0.004 g cm^{-2} in all canopy layers
2.3	Vertical profiles in Table 7-4	N/A
2.4	Top five layers: EWT vertical profiles 0.008 g cm^{-2} in remaining layers	Top five layers: 0.014 g cm^{-2} 0.008 g cm^{-2} in remaining layers
2.5	Top four layers: EWT vertical profiles 0.008 g cm^{-2} in remaining layers	Top four layers: 0.014 g cm^{-2} 0.008 g cm^{-2} in remaining layers
2.6	Top three layers: EWT vertical profiles 0.008 g cm^{-2} in remaining layers	Top three layers: 0.014 g cm^{-2} 0.008 g cm^{-2} in remaining layers
2.7	Top five layers: EWT vertical profiles 0.004 g cm^{-2} in remaining layers	Top five layers: 0.014 g cm^{-2} 0.004 g cm^{-2} in remaining layers
2.8	Top four layers: EWT vertical profiles 0.004 g cm^{-2} in remaining layers	Top four layers: 0.014 g cm^{-2} 0.004 g cm^{-2} in remaining layers
2.9	Top three layers: EWT vertical profiles 0.004 g cm^{-2} in remaining layers	Top three layers: 0.014 g cm^{-2} 0.004 g cm^{-2} in remaining layers
2.10	Top four layers: EWT vertical profiles 0.004 g cm^{-2} in remaining layers Understory changed to litter	Top four layers: 0.014 g cm^{-2} 0.004 g cm^{-2} in remaining layers Understory changed to litter

7.7 Model validation

This research focused on DART simulation of vegetation reflectance, which has been successfully validated using ground and airborne validation data (Gastellu-Etchegorry *et al.*, 1999). In addition, de Castro Oliveira *et al.* (2017) assessed DART simulation accuracy of Eucalyptus plantations reflectance, by comparing it to reflectance extracted from high resolution Pleiades satellite imagery, reporting absolute error < 2%. Plus, as part of the RAdiation transfer Model Intercomparison (RAMI) experiment, DART simulations of vegetation reflectance were cross-validated against other, independently developed, 3D RTMs, including FLIGHT, SPRINT, Librat, and Raytran (Pinty *et al.*, 2001; Pinty *et al.*, 2004; Widlowski *et al.*, 2007; Widlowski *et al.*, 2008; Widlowski *et al.*, 2013; Widlowski *et al.*, 2015). DART Earth-atmosphere radiative coupling was validated successfully using simulations of the MODTRAN (MODerate resolution atmospheric TRANsmission) atmosphere RTM (Gascon *et al.*, 2001; Grau and Gastellu-Etchegorry, 2013).

To evaluate how close the results obtained from the simulations conducted in this study were to real satellite imagery, and how the assumptions used in parametrizing the model affected the accuracy of the results, Sentinel-2A imagery that covered Wytham Woods was acquired from the Copernicus Open Access Hub, processed to BOA reflectance. The imagery was collected on 22nd of May 2017, which corresponded to the data collection campaign (22nd to 31st of May 2017), in which TLS data collection and leaf EWT measurements were conducted (Chapter 5). The average zenith angle of the satellite imagery was 2.7º, and the sun zenith angle was 32.4º, both being close to their assumed values in the simulations, which were 0.0º and 30º, respectively. Pixels corresponding to the 18 ha Wytham core plot (Figure 5-1) were extracted from the NIR and SWIR bands (bands 8A and 11, respectively) in the satellite imagery, using the coordinates specified in Butt *et al.* (2009). Minimum, maximum, and average reflectance in the extracted pixels were determined. In addition, NDWI was calculated on a pixel-by-pixel basis, then the minimum, maximum, and average NDWI values in the plot were determined. The calculated values were compared to Sim 1.4 results of forest scenes 1 and 2.

7.8 Results and discussion

7.8.1 Comparing the simulated reflectance to Sentinel-2A data

Sim 1.4 results obtained from forest scenes 1 and 2 were compared to the actual BOA reflectance and NDWI retrieved from the Sentinel-2A satellite imagery (Figure 7-9). The results revealed that the simulated NIR reflectance was lower than the average reflectance obtained

from the satellite data, referred to as the average actual reflectance hereafter, by 14.8 % and 7.6 % in forest scenes 1 and 2 respectively. As discussed in Section 7.4, forest scene 1 suffered from occlusion, as 3D tree models used in the scene were reconstructed from leaf-on TLS scans, making their canopy LAI less than the actual value in the real forest plot. This can explain the simulated NIR reflectance being less than the actual NIR reflectance obtained from the satellite data. One approach to solve this issue is by combining TLS data and airborne LiDAR data in order to achieve a better coverage of canopy top, and thus reduce the occlusion effects.

On the other hand, the simulated SWIR reflectance in both forest scenes was very close to the average actual reflectance, indicating that the EWT measurements used in the simulations, retrieved from the TLS data and destructive sampling, were realistic. The simulated SWIR was 6.6 % less than the average actual reflectance in forest scene 1, and 6.4 % higher than the average actual reflectance in forest scene 2. The simulated NDWI obtained from forest scene 1 was 8 % lower than the average actual NDWI, while forest scene 2 simulated NDWI was 12.5 % lower than average actual NDWI. Both simulated NDWI values were affected by the simulated NIR reflectance being lower than the actual NIR reflectance. Furthermore, simulated NDWI of forest scene 2 could have also been influenced by the simulated SWIR reflectance being higher than its actual value. No EWT measurements were conducted in field for forest scene 2 and EWT was assumed to equal 0.014 g cm^{-2} in all the canopy layers, based on the EWT retrieved from destructive sampling in forest scene 1, as discussed in Section 7.5.

Overall, the results showed that the simulated reflectance and NDWI in both forest scenes can be considered realistic, despite the approximations used in parametrizing the forest scenes. It is worth mentioning that the minimum, maximum, and average satellite reflectance and NDWI were calculated from all the pixels corresponding to the 18 ha Wytham core plot, and not from the exact pixels corresponding to the locations of the simulated forest plots, as the accurate coordinates of the plots were not available.

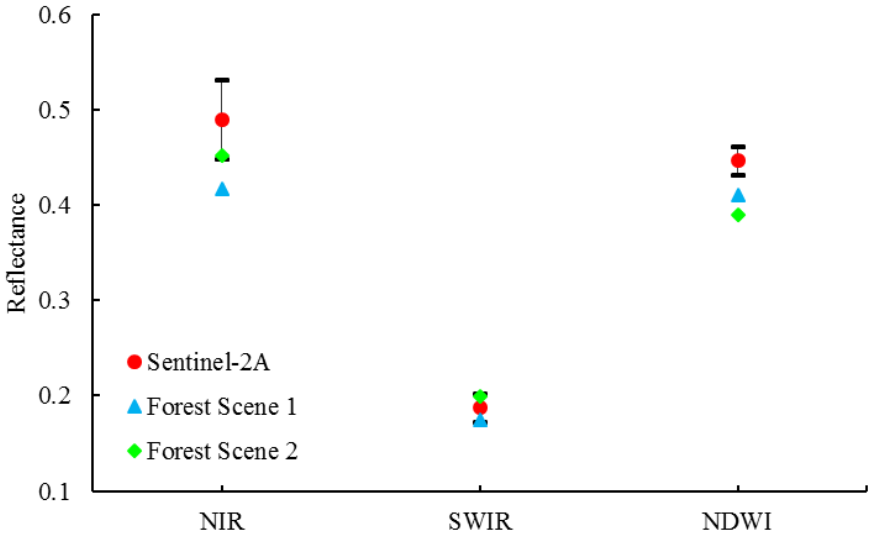

Figure 7-9. Comparison between the simulated NIR reflectance, SWIR reflectance, and NDWI, and the actual mean values retrieved from Sentinel-2A satellite imagery of the plot. Whiskers represent one standard deviation.

7.8.2 Group 1 simulations

Table 7-7 shows the simulated 864 nm NIR and 1613 nm SWIR reflectance, and the corresponding NDWI, resulting from both forest scenes.

Table 7-7. Group 1 simulations results. The change in reflectance and NDWI was calculated in regard to Sim 1.1, except for Sim 1.5.

Forest scene 1						
Sim	NIR reflectance	NIR reflectance change (%)	SWIR reflectance	SWIR reflectance change (%)	NDWI	NDWI change (%)
1.1	0.3301	---	0.1489	---	0.3782	---
1.2	0.3364	1.9	0.1505	1.1	0.3818	1
1.3	0.4018	21.7	0.1720	15.5	0.4004	5.9
1.4	0.4169	26.3	0.1747	17.3	0.4093	8.2
1.5	0.3948	- 5.3*	0.1965	12.5*	0.3354	- 18.1*
Forest scene 2						
1.1	0.3991	---	0.1863	---	0.3635	---
1.2	0.4448	11.5	0.1977	6.1	0.3846	5.8
1.3	0.4042	1.3	0.1876	0.7	0.3660	0.7
1.4	0.4524	13.4	0.1991	6.9	0.3887	6.9
1.5	0.4497	- 0.6*	0.2005	0.7*	0.3834	- 1.4*

* Change in reflectance and NDWI was calculated in regard to the results of Sim 1.4.

7.8.3 Effects of the woody materials on the plot reflectance

For forest scene 1, the results revealed that the woody materials (Sim 1.2) had made minimal contribution to the plot reflectance. In comparison to Sim 1.1, the plot reflectance in the NIR and SWIR bands, and NDWI remained almost unchanged. The negligible effects of the woody materials on the plot reflectance and NDWI may be a result of the missing branches and small twigs in the top of the canopy, in the 3D models used to build the forest scene (Figure 7-4), as a result of occlusion in the TLS data. In a similar study, Malenovský *et al.* (2008) used DART simulations, coupled with AISA Eagle imagery, to study the influence of woody materials on Norway spruce canopy reflectance, reporting that when only trunks and first order branches were taken into account, a negligible change (< 1 %) was observed in the canopy reflectance. When small branches and twigs were incorporated into the model, a decrease in the canopy reflectance was reported, which varied between spectral bands (2% in visible and 4% in NIR). Another reason may be the woody materials being occluded by the leaves in the canopy top, thus having a low contribution to top of the canopy reflectance, and to NDWI as a result. A similar observation was reported by Verrelst *et al.* (2010), when PROSPECT and FLIGHT RTM simulations were used to study the influence of woody materials on canopy reflectance for three coniferous plots, which varied in age and structure. It was reported that the woody materials' effects were negligible in the dense, young plot, but were significant in the old-growth plots, concluding that the woody materials' influence must be taken into consideration for mature or partly defoliated forest plots. However, these studies included coniferous forest plots only, while this research focuses on deciduous broadleaf forest plots, for which there is a gap in the literature regarding the contribution of the woody materials to the plot reflectance.

By contrast, the results obtained in forest scene 2 showed that the woody materials had some influence on the plot reflectance and NDWI. NIR reflectance increased by 11.5 %, while SWIR reflectance increased by 6.1 %, resulting in a 5.8 % increase in NDWI. Unlike forest scene 1, tree models used in this forest scene did not suffer from occlusion, meaning that higher order branches and twigs in the canopy, especially in the canopy top, were accounted for and modelled. This difference in the tree models used in the forest scenes can be the reason for the different observations obtained in the results.

7.8.4 Effects of the understory on the plot reflectance

The understory had a high contribution to the plot reflectance in forest scene 1 (Sim 1.3). The NIR and SWIR reflectance increased by 21.7 % and 15.5 % respectively, in comparison to Sim 1.1, causing an increase in NDWI by 5.9 %. On the other hand, the understory had no effect on

the plot reflectance and NDWI in forest scene 2. The observed differences between the two forest scenes was due to the presence of canopy gaps in forest scene 1, while forest scene 2 had no canopy gaps, and canopy gap distribution is known to affect the contribution of understory to forest plot reflectance (Guyot *et al.*, 1989; Spanner *et al.*, 1990; Miller *et al.*, 1997; Zarco-Tejada *et al.*, 2001; Rautiainen and Lukeš, 2015; Landry *et al.*, 2018). Furthermore, forest scene 1 had less leaves and woody materials in the canopy top than the real forest, because of occlusion in the TLS data used to reconstruct the plot as previously discussed, which allowed more irradiance to reach the understory, which in return resulted in the understory having high contribution to the plot reflectance. In a similar study, Eriksson *et al.* (2006) used Forest Reflectance and Transmittance (FRT) RTM to study how understory contributed to top of the canopy reflectance of 20 forest stands (14 deciduous and six coniferous) in southern Sweden, 30 m × 30 m in size each. It was reported that reflectance values varied by up to ± 18% in the red region and up to ± 10% in the near infrared region due to the understory. This suggested that the observed increase in simulated reflectance in forest scene 1 due to the understory was exaggerated as a result of the missing leaves and branches in the upper canopy layers.

When the effects of woody materials and understory were combined (Sim 1.4), NDWI increased by 8.2 %, in comparison to Sim 1.1, in forest scene 1, and by 6.9 % in forest scene 2. When the understory was changed from healthy grass in Sim 1.4 to litter in Sim 1.5, NIR reflectance dropped by 5.3 % and SWIR reflectance increased by 12.5 % in forest scenes 1, causing an 18 % drop in NDWI. The NIR, SWIR, and NDWI of forest scene 2 remained almost unchanged. This showed that NDWI can only detect water stress in the understory if canopy gaps existed in the forest plot.

More simulations are still needed, with different types of understory (understory being modelled as turbid cells with different dimensions, density, and optical properties), to further investigate the contribution of the understory to forest plot reflectance and NDWI. Additionally, simulations that include bare soil, or add a soil layer beneath the understory, can be used to study the effects of soil on reflectance.

7.8.5 Group 2 simulations

Table 7-8 shows the simulated SWIR reflectance in both forest scenes, whilst Table 7-9 shows the simulated NDWI. Sim 1.4 results were used as a reference to calculate the change in SWIR reflectance and NDWI. NIR reflectance was not included in the results, as it remained unchanged. The results revealed that the SWIR reflectance and NDWI changed considerably

when EWT was decreased in all canopy layers to 0.008 g cm^{-2} in Sim 2.1, and to 0.004 g cm^{-2} in Sim 2.2, with the SWIR reflectance increasing and NDWI decreasing. Such change in NDWI was expected, as NDWI is very sensitive to the change in vegetation moisture content (Serrano *et al.*, 2000; Jackson, 2004; Dennison *et al.*, 2005; Chakraborty and Sehgal, 2010).

Table 7-8. Group 2 simulated reflectance. The change in reflectance was calculated in regard to Sim 1.4. Blue corresponds to changing EWT to 0.008 g cm^{-2}, whilst grey corresponds to changing EWT to 0.004 g cm^{-2}.

	Forest scene 1		Forest scene 2	
Sim	SWIR reflectance	SWIR reflectance change (%)	SWIR reflectance	SWIR reflectance change (%)
1.4	0.1747	---	0.1991	---
2.1	0.2137	22.3	0.2537	27.4
2.2	0.2615	49.7	0.3112	56.3
2.3	0.1786	2.2	---	---
2.4	0.1809	3.5	0.2087	4.8
2.5	0.1839	5.3	0.2115	6.2
2.6	0.1905	9	0.2194	10.1
2.7	0.1838	5.2	0.2183	9.6
2.8	0.1916	9.7	0.2238	12.4
2.9	0.2072	18.6	0.2402	20.6
2.10	0.2168	24.1	0.2255	13.3

Table 7-9. Group 2 simulated NDWI. The change in NDWI was calculated in regard to Sim 1.4. Blue corresponds changing EWT to 0.008 g cm^{-2}, whilst grey corresponds to changing EWT to 0.004 g cm^{-2}.

	Forest scene 1		Forest scene 2	
Sim	NDWI	NDWI change (%)	NDWI	NDWI change (%)
1.4	0.4093	---	0.3887	---
2.1	0.3237	- 20.9	0.2831	- 27.2
2.2	0.2319	- 43.3	0.1865	- 52
2.3	0.4002	- 2.2	---	---
2.4	0.3947	- 3.6	0.3689	- 5.1
2.5	0.3879	- 5.2	0.3629	- 6.6
2.6	0.3728	- 8.9	0.3470	- 10.7
2.7	0.3881	- 5.2	0.3503	- 9.9
2.8	0.3701	- 9.6	0.3385	- 12.9
2.9	0.3360	- 17.9	0.3075	- 20.9
2.10	0.2864	- 30	0.3328	-14.4

Sim 2.3 showed that the EWT vertical heterogeneity almost had no effect on the plot reflectance and NDWI, both changing by 2.2%. Possible reasons for this were that the vertical heterogeneity was not significant enough to cause a change in reflectance and NDWI, or that the upper canopy layers, in which there was minimal vertical heterogeneity, dominated the plot reflectance. The results of simulations 2.4 to 2.9 confirmed that the top four canopy layers contributed the most to the plot reflectance and to the change in NDWI. For forest scene 1, Sim 2.4 showed that reducing EWT to 0.008 g cm^{-2} in the canopy layers below the top five layers, while leaving EWT in top five layers unchanged, increased the SWIR reflectance by only 3.5%, and caused NDWI to drop by 3.6%. This showed that the canopy layers below the top five layers made a minimal contribution to the plot reflectance and NDWI. When EWT in canopy layer five was reduced (Sim 2.5), the magnitude of the change in reflectance and NDWI increased slightly. Reducing EWT in canopy layer four (Sim 2.6) increased the magnitude of the change in reflectance to 9%, and that of the change in NDWI to 8.9 %. This revealed that reducing EWT in canopy layer four alone almost had the same effect on reflectance and NDWI as reducing EWT in all canopy layers below it combined. Furthermore, comparing the change in NDWI that was observed when all canopy layers were dried down to 0.008 g cm^{-2} to the change observed when the top four canopy layers remained healthy (20.9 % drop and 5.2 % drop, respectively), further showed that NDWI was mainly detecting the change in EWT in canopy top layers.

Simulations 2.7 to 2.9 further confirmed this, showing that reducing EWT to 0.004 g cm^{-2} in canopy layer four alone almost had the same effect on reflectance and NDWI as reducing EWT in all lower canopy layers combined. The simulations also showed that when EWT in all canopy layers was reduced to 0.004 g cm^{-2}, NDWI dropped by 43.3 %, while it only dropped by 9.6 % when the top four canopy layers remained healthy, and all the remaining canopy layers were dried down. Results obtained in forest scene 2 were consistent with forest scene 1 results, with some differences in the magnitude of the change in reflectance and NDWI, and thus only forest scene 1 results were discussed to avoid repetition.

Simulations 2.4 to 2.9 assumed that a water stress started in the canopy bottom then spread upward, whilst the understory remained healthy, for the sake of studying the effects of reducing EWT in the lower canopy on the plot reflectance and NDWI. In reality, a water stress caused by drought conditions will also affect the understory. Sim 2.10 accounted for this, by drying all canopy layers below the top four canopy layers to 0.004 g cm^{-2}, and modelling the understory as dry litter. The simulation was a repeat of Sim 2.8, with the only change being modelling the

understory as litter instead of healthy grass. Comparing the results of the two simulations in forest scene 1 showed that drying the understory had a significant effect on the NDWI, while it had a minimal effect on the NDWI in forest scene 2. As discussed in Section 7.8.4, forest scene 1 had less leaves and branches in the canopy top than in reality, which increased the contribution of the understory to the plot reflectance and NDWI, whilst Forest scene 2 was a more realistic representation of the forest.

Overall, results of group 2 simulations showed that care must be taken while using spaceborne and airborne optical RS data to monitor forest health and early-detect the risk of wildfires, especially in dense forests, as the upper canopy layers, which have more moisture, were found to dominate the forest plot reflectance. In the case of moderately dense and open forests, NDWI may reflect the severity of the water stress, even if the upper canopy layers remained healthy, as a result of the understory contribution to the plot reflectance and NDWI. On the other hand, in dense forests, a spaceborne sensor will not be able to detect a severe water stress in the understory and lower canopy until the upper canopy layers begin to get stressed.

The results presented in this chapter cannot be generalized until more forest plots, sensors, and case studies are simulated. Also, similar case studies need to be simulated using other 3D RTMs for cross-comparison with the results obtained from DART. The results of RTM simulations are very sensitive to the phase function used in single and multiple scattering of radiation in the canopy, and also to the number of successive orders of scattering (Widlowski *et al.*, 2015). The results of the RAMI-IV experiment, in which highly realistic forest scenes were simulated, showed variation in the simulated spectra between the different 3D RTM models tested (Widlowski *et al.*, 2013).

7.9 Summary

This chapter integrated the vertical heterogeneity of forest canopy EWT in the RTM DART, aiming at investigating how such heterogeneity would affect the forest plot reflectance and the NDWI. In addition, various case scenarios were simulated to study the effects of woody materials and understory on the plot reflectance, and also to examine how sensitive NDWI was to the change in the plot EWT. Simulations that included decreasing EWT in all canopy layers simultaneously, and others that involved drying the canopy bottom layers only, were conducted and compared, in an attempt to determine which canopy layers dominated the plot reflectance and contributed the most to the change in NDWI. Two forest scenes were used in the simulations, each of them representing a different forest plot in the same forest. The forest

scenes had different tree structure and species, and their tree 3D models were reconstructed from TLS data using two different approaches. The 3D leaf models of the trees were divided into a number of layers, with a thickness of 1 m each, in order to assign different optical properties to each layer, based on the EWT of it, and thus modelling the vertical variation of EWT in the forest plot.

The NIR and NDWI calculated from Sentinel-2A satellite imagery showed that the simulated reflectance and NDWI of the two forest scenes were realistic, lying within the minimum and maximum values observed in the satellite imagery, and not far from the mean. Forest scene 2 was more efficient in terms of the required processing time and computational resources. Each simulation required approximately six hours of processing time using forest scene 1, while the same simulation required approximately one hour and 15 minutes to complete using forest scene 2, using the same PC.

The results of the simulations revealed that the understory had a high contribution to the forest plot reflectance and affected the NDWI in forest scene 1, which suffered from occlusion and contained canopy gaps, while it had a minimal effect on the reflectance and the NDWI in forest scene 2, which was a more realistic representation of the forest. These findings agreed to what was previously reported in the literature, and further showed that the effects of the understory on the forest plot reflectance must be accounted for in moderately dense and open forests. The woody materials had a minimal effect on the plot reflectance and NDWI in forest scene 1, mainly because the woody materials in upper canopy were missing from the tree 3D models used in reconstructing the plot. On the other hand, the woody materials had some influence on forest scene 2 reflectance and NDWI, but the effects were minimal in comparison to the changes in NDWI caused by reducing EWT.

Modelling the vertical heterogeneity of EWT had a negligible effect on the plot reflectance, in comparison to assuming a uniform EWT in all canopy layers. However, it was found that this was caused by the top four canopy layers dominating the plot reflectance. Drying the canopy layers below the top four layers, while maintaining upper canopy layers healthy, changed NDWI in a way that did not reflect the severity of the water stress and that the lower canopy layers lost approximately 70 % of their EWT. This may cause misjudgements while monitoring the forest health, during drought conditions or in case of water stress that started in the canopy bottom then spread upward, caused by disease or pest invasion. The drying patterns of forest canopies still need to be studied using TLS to examine how the EWT vertical profiles would

change during drought conditions, and to investigate whether the trees would lose moisture equally from all canopy layers, or would attempt to maintain the upper canopy layers healthy to optimize photosynthesis.

The results obtained in this chapter may be specific to the forest under study, or to the species in the forest, or specifically to broadleaf deciduous forests, and thus cannot be generalized, unless more forest types and species are studied. Also, similar case studies need to be simulated using other RTMs for cross-comparison with the results obtained from DART.

Chapter 8. Discussion and conclusions

8.1 Research motivation

Determining the vegetation water status can reflect the physiological status of vegetation, thus, it has significant importance for various agricultural and forestry applications (Peñuelas *et al.*, 1994; Chaves *et al.*, 2003). It can help in early detection of vegetation stress, symptoms of disease, and signs of pest infestations in forests and agricultural crops (Carter, 1993; Datt, 1999; Trumbore *et al.*, 2015). Additional applications in forestry include early detection of wildfire risk, forest fire modelling, and studying wildfire regimes (Ustin *et al.*, 1998; Chuvieco *et al.*, 2004a; Danson and Bowyer, 2004; Yebra *et al.*, 2008). Furthermore, in agricultural crops, monitoring vegetation water status is important for drought assessment, irrigation scheduling, and crop yield estimation (Peñuelas *et al.*, 1992; Sepulcre-Cantó *et al.*, 2006).

Optical RS data, both spaceborne and airborne, have been widely utilized in monitoring the vegetation water status at a landscape level (Dash *et al.*, 2017). Typically, canopy EWT is estimated directly from optical RS data and used as an early indicator of vegetation stress. However, the accuracy of estimating EWT from optical RS data is influenced by canopy structure, background soil and understory reflectance, atmosphere, and shadows (Ali *et al.*, 2016). Although using RTMs to estimate EWT instead of using simple vegetation indices can overcome these limitations, the models do not account for the vertical heterogeneity in canopy biophysical and biochemical traits. Such heterogeneity plays a role in the canopy reflectance, and ignoring it can reduce the accuracy of the estimation of vegetation biochemical traits (Kuusk, 2001; Wang and Li, 2013). Methods to quantify such heterogeneity are still needed. Also, there is a need for a fast and reliable method to measure canopy EWT in sampling plots that match the pixel size of satellite sensors to be used in the calibration and validation of the EWT estimation models. The *in-situ* destructive sampling approaches currently being used are insufficient, especially for satellites with large pixel size such as MODIS. Another limitation of using optical RS data to estimate EWT is that EWT cannot be measured predawn, which is a more reliable indicator of vegetation water status (Améglio *et al.*, 1999). Dual-wavelength TLS was identified as a tool that can overcome the limitations associated with optical RS estimation of EWT, by providing 3D EWT estimates that can be used to study the EWT vertical heterogeneity. TLS can also serve as a calibration and validation tool for satellite estimation of EWT. In addition, EWT can be estimated both predawn and at midday, as TLS instruments are active sensors.

8.2 Revisiting research aim and objectives

The main aim of this research was to estimate canopy EWT in 3D using commercial dual-wavelength TLS, both in a laboratory experiment and multiple field campaigns, to quantify and better understand the canopy EWT vertical heterogeneity. The intensity data from commercially available TLS instruments, operating at NIR wavelength (the Leica P20) and SWIR wavelength (the Leica P40 and P50) was combined into a vegetation index (NDI), after developing robust methods to calibrate the intensity to apparent reflectance (Chapter 3). NDI was used to generate 3D canopy EWT estimates in an indoors dry-down experiment (Chapter 4) and four data collection campaigns. The main data collection campaign was in a mixed-species forest plot in Wytham Woods, Oxford, and is named hereafter as the Wytham dataset (Chapter 5). The second data collection campaign was in a willow crop site in Newcastle University Cockle Park Farm in Ulgham, Northumberland, and is named hereafter as the willow dataset (Chapter 6). The third and fourth campaigns were carried out in a mixed-species tree plot in Exhibition Park, Newcastle. The plot was scanned at the end of a heatwave (August 2018) and two months later (October 2018), resulting in two datasets, named hereafter as Exhibition Park August dataset and Exhibition Park October dataset (Chapter 6). Vertical profiles of EWT were generated and compared within and across species.

Additional aims included: (1) detecting EWT temporal changes in 3D, which was addressed using the indoors dry-down experiment (Chapter 4) and Exhibition Park datasets (Chapter 6), and (2) investigating how EWT vertical heterogeneity affected forest plot reflectance and received satellite signal, which was addressed by modelling the 3D EWT estimates of the Wytham dataset in the DART model (Chapter 7). Four TLS instruments were utilized in this study: a Leica P20 instrument, two Leica P40 instruments, and a Leica P50 instrument. This research had seven main objectives, which were addressed as follows:

Objective one: to develop robust methods to calibrate the intensity data from commercially-available TLS instruments to apparent reflectance.

This objective was addressed in Chapter 3. The intensity – range relationship was investigated separately for each instrument using external reference targets with known reflectance, revealing that the four instruments deviated from the $1/R^2$ component of the laser equation. This was caused by the near-distance intensity reducer that aimed at protecting the optics and the on-board range calibration adjustments that attempted to correct the intensity for the range effect after a specific range, which varied between the instruments. This deviation from the laser

equation was expected, as similar observations were previously reported for numerous commercial TLS instruments, e.g., the Faro LS880 and Leica HDS 6100 (Kaasalainen *et al.*, 2011), the Riegl LMS Z420i (Blaskow and Schneider, 2014), the Z+F Imager 5006i (Blaskow and Schneider, 2014; Fang *et al.*, 2015), the Faro Focus3D 120 (Tan *et al.*, 2016), the Riegl VZ400i (Xu *et al.*, 2018), and the Riegl VZ4000 (Tan *et al.*, 2019). As each of the four instruments used in this study was found to have its own unique intensity – range relationship, an intensity correction model was developed for each instrument separately. The intensity – reflectance relationship was then investigated for each instrument. This revealed non-linear relationships as a result of the internal adjustments performed by the instruments to alter the intensity values and enhance the visual appearance of the point clouds. When the raw intensity data were extracted from the instruments using an intensity map editor provided by the manufacturer, the relationship was found to be almost linear, with some slight non-linearity.

The intensity correction models were validated using independent reference targets. The average error observed in all validation experiments at all ranges tested was 2.6 %, while the minimum and maximum average errors were 1.1 % (RMSE = 0.011) and 5.1 % (RMSE = 0.043) respectively. The errors observed at ranges less than 4 m, especially at 2 m range, were higher than all remaining ranges, with errors > 10 %. This was a result of the intensity correction models not being able to fully correct the intensity for the near distance intensity reducer effects. This must be considered if scans were planned at near ranges, or if objects of interest were less than 4 m away from the instrument, such as the understory vegetation surrounding the scanning positions in a forest plot. The accuracy of the intensity correction models was considered sufficient for the application, which was further confirmed with the high correlation obtained between NDI and EWT at leaf and canopy levels, as described in the upcoming sections.

Objective two: to investigate the ability of NDI to minimize the effects of incidence angle and leaf internal structure without the need for further radiometric corrections.

This objective was addressed in Chapter 3. For the incidence angle effects, eighteen leaf samples from six different tree species, including grey alder, common lime, common alder, hornbeam, poplar, and cherry, were scanned. The incidence angle was changed between 0 and 60 degrees, with scans conducted at 20 degrees intervals, and NDI was calculated for each incidence angle. The incidence angle effect on each wavelength separately was severe, as the change in incidence angle between zero and 60 degrees reduced the SWIR reflectance by an

average of 47 % and the NIR reflectance by an average of 52 %. Using NDI largely minimized the incidence angle effects for all six species. Changing the incidence angle between zero and 40 degrees caused an average change in NDI of 6.7 % across all leaf samples, whilst changing it between zero and 60 degrees caused an average change of 13.7% in the NDI. One reason for the more significant change in NDI at 60 degrees incidence angle was that leaves were not perfectly Lambertian surfaces, and the reflectance – incidence angle relationships deviated more from the cosine law as the incidence angle increased towards 60 degrees.

For the same leaf samples, the change in NDI between minimum and maximum EWT values was 53 %. In the Wytham dataset, the change in EWT caused 79 % change in NDI, and overall in all leaf samples measured in this study, excluding holly leaf samples, the change in EWT caused a 127 % change in NDI. This showed that EWT had more significant impact on NDI than the remaining effects of the incidence angle. Hancock *et al.* (2017) reported similar observations for NDI of 1064 nm and 1545 nm, also observing deviations at some incidence angles, for instance, at 10, 40, and 60 degrees incidence angles, which was higher than the deviation observed at 60 degrees in this study. It was concluded that the change in NDI caused by the incidence angle effects was negligible in comparison to the change in NDI caused by EWT. However, at the canopy level in complex vegetation environments such as forests, the remaining effects of the incidence angle on NDI may contribute to the errors in estimating EWT, as the laser beams will hit the leaves at all possible incidence angles (Kaasalainen *et al.*, 2018).

The ability of NDI to minimize the leaf internal structure effects was investigated by conducting 2886 PROSPECT simulations to examine how the leaf structure coefficient (N), representing leaf thickness and leaf internal cellular arrangements, and LMA affected the NDI – EWT relationship. LMA was found to have a minimal effect on NDI, as the maximum change in LMA across all species examined caused only a 7 % increase in NDI. N at the canopy level was found to range between 1.5 and 2 for green canopies, and was ≥ 2.5 for senescent canopies, as shown in Figure 8-1. Increasing N between 1.5 and 2 would result in a 10 % decrease in NDI according to the PROSPECT simulations. As N and LMA are correlated variables, with an increase in N typically corresponding to an increase in LMA, their combined effects on NDI would be further reduced as the effects have opposite directions. However, the effects would not entirely cancel each other out, and N would have some remaining effects on NDI. This can be a factor contributing to the variation of EWT estimation errors observed at the canopy level in Wytham and Exhibition Park datasets. However, this did not prevent the use of a pooled

EWT estimation model to successfully estimate EWT at the canopy level in mixed-species sites. Increasing N to 2.5 would cause a 17 % decrease in NDI, while increasing it to 3 would cause a 22 % decrease in NDI. Thus, species that had significantly thicker leaves than the other species in the plot, for instance, holly leaves in Exhibition Park dataset, needed their own NDI – EWT estimation model. Furthermore, an NDI – EWT relationship developed using green leaves could not be applied to senescent leaves.

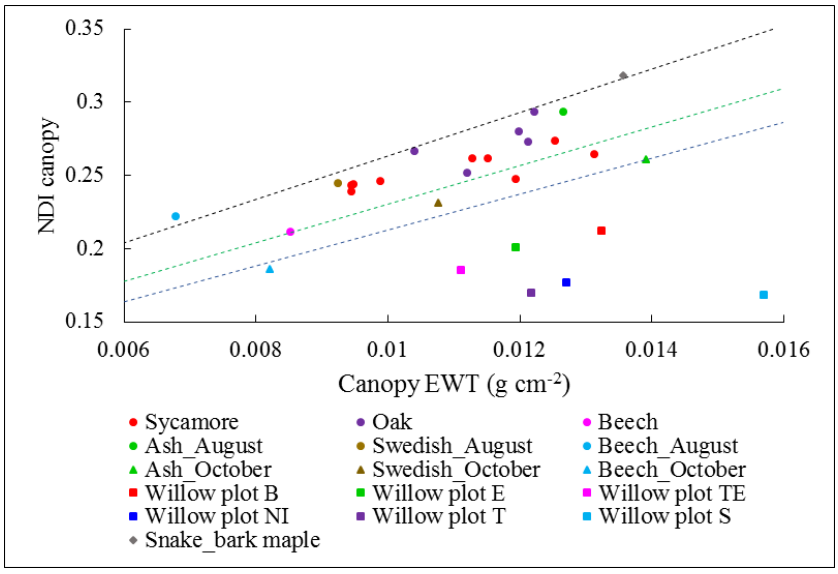

Figure 8-1. The NDI – EWT relationship for N = 1.5 (black), N = 2 (green), and N = 2.5 (blue), resulted from PROSPECT simulations, in addition to the NDI – EWT relationship at canopy level for all scanned trees in this study, excluding holly trees.

Overall, the experiments conducted in this study showed that EWT was the main factor deriving the change in NDI, whilst the incidence angle and leaf internal structure remaining effects on NDI may affect the accuracy of EWT retrieval at the canopy level.

Objective three: to examine the relationship between NDI and EWT at the leaf level across a range of species.

This objective was addressed in Chapter 4, Chapter 5, and Chapter 6. A total of 192 leaf samples were collected, scanned, and their NDI and EWT measured. The samples represented thirteen different species as follows: snake-bark maple, grey alder, common lime, common alder, poplar, cherry, sycamore, oak, beech, ash, Swedish whitebeam, holly, and six varieties of willows. Among the 192 leaf samples, 137 leaves were green, 19 leaves were senescing, meaning they had started to change colour but were still relatively green (Exhibition Park October dataset), and 36 leaves were senescent, meaning they had already changed colour and

lost nutrients and chlorophyll content (willow dataset). For each individual species, moderate to high correlation was observed between NDI and EWT, with R^2 ranging between 0.55 and 0.94.

For green leaves, site-specific species-independent pooled NDI – EWT models were fitted with high accuracy (R^2 ranging between 0.88 and 0.94), in addition to a site- and species-independent pooled NDI – EWT model that combined all leaf samples (R^2 = 0.91, Figure 6.19). This concurred with the results obtained from the PROSPECT simulations and showed that the remaining effects of leaf internal structure on the NDI – EWT relationship did not prevent fitting pooled NDI – EWT models with high accuracy. This suggested that the NDI – EWT relationship was species-independent, agreeing with the results obtained in Gaulton *et al.* (2013) for NDI of 1064 nm NIR and 1545 nm SWIR laser wavelengths. On the other hand, NDII and NDWI, the vegetation indices equivalent to NDI in optical RS data, have also been previously linked to EWT in mixed-species sites (Cheng *et al.*, 2008a; Yilmaz *et al.*, 2008; De Jong *et al.*, 2014). However, other studies highlighted that in the case of a large variation in leaf thickness and LMA between species, the accuracy of NDII and NDWI estimation of EWT can be significantly reduced (Zarco-Tejada *et al.*, 2003; Zhang and Zhou, 2015). For NDI, this was observed in holly leaf samples, which was the only species that did not fit in the pooled NDI – EWT models. Holly leaves were clearly thicker than the leaves of the other species, and had 145 % higher LMA than the average LMA measured for the other species in this study. In addition, the shiny surface of holly leaves also contributed to the deviation of the NDI – EWT relationship of this species from that of the other matt leaves, as Zhu *et al.* (2017) showed that at 1550 nm wavelength, shiny leaves had stronger specular reflection. The higher reflectance at the 1550 nm wavelength reduced the NDI and thus contributed to the deviation in the NDI – EWT relationship.

The sycamore leaves diseased with powdery mildew also did not follow the NDI – EWT relationship of healthy leaves, and similar to holly leaves, did not fit in the pooled NDI – EWT models. The powdery mildew that covered sycamore leaf samples decreased the NIR reflectance but had a minimal effect on the SWIR reflectance, resulting in very low NDI values in comparison to NDI of healthy leaves. This concurred with the findings of Yuan *et al.* (2014) for winter wheat powdery mildew. In general, diseases are known to reduce leaf reflectance in NIR (Nilsson, 1991), and NIR wavelengths have been adopted in detecting powdery mildew infections in winter wheat (Zhang *et al.*, 2012; Yuan *et al.*, 2014) and grape (Beghi *et al.*, 2017).

However, further investigation is still needed as fungus that causes powdery mildew differs between plant species.

For the senescent leaves, they did not follow the NDI – EWT relationship of green leaves, mainly because senescence is known to significantly change the leaf internal cell structure (Jacquemoud and Baret, 1990; Buchanan-Wollaston, 1997), and such changes were found to influence the NDI – EWT relationship, as shown in Figure 8-1. It was possible to fit site-specific pooled NDI – EWT models for the Exhibition Park October dataset and willow dataset separately, but not a site-independent pooled model that combined all senescent leaves, most likely because they were at different levels of senescence.

The leaf level results obtained in this research showed that the NDI – EWT relationship was site- and species-independent to an extent, but highlighted that leaf surface characteristics, leaf senescence, and leaf thickness must be taken in consideration while deriving pooled, multi-species NDI – EWT models.

Objective four: to use NDI to generate 3D EWT estimates at the canopy level in a controlled laboratory experiment, as well as in field campaigns.

This objective was addressed in Chapter 4, Chapter 5, and Chapter 6. Canopy EWT was successfully estimated in an indoors dry-down experiment and four field campaigns, with errors in EWT estimates for individual trees ranging between 1 % and 13.5 %. The average errors observed in the dry-down experiment were 2.9 % and 2.6 % for the deciduous and coniferous canopies respectively. The average errors obtained in the Wytham dataset, willow dataset, Exhibition Park August dataset, and Exhibition Park October dataset were 7.7 %, 8.9 %, 7.8 %, and 4.2 % respectively, using the species-specific NDI – EWT models. When the site-specific pooled NDI – EWT models were used, the errors were 6.3 %, 6.6 %, 4.8 %, and 5.4 % for the Wytham dataset, willow dataset, Exhibition Park August dataset, and Exhibition Park October dataset respectively. It is worth mentioning that for the willow dataset, it was not possible to estimate EWT on a point-by-point basis as a result of the low registration accuracy resulting from the strong wind on the day of the scan, and it was only possible to estimate the average EWT in each plot.

The site- and species-independent pooled NDI – EWT model that combined all green leaves (Figure 6.19, Equation 6.22) was also successfully used to retrieve canopy EWT estimates in the Wytham dataset and Exhibition Park August dataset, with average errors of 6.6 % and 10 %

respectively. The advantage of using pooled EWT estimation models over using species-specific models is that it does not require prior tree species classification, thus reducing the processing time, as a single model will be applied to the whole NDI point cloud at once. However, the results obtained using the site- and species-independent pooled NDI – EWT model showed that the NDI – EWT relationship was site-specific to an extent, as severe error in EWT estimation was observed in one beech tree (25 %) when the model was used, in comparison to a 12 % error in EWT estimation when the site-specific pooled model was used. As shown in Figure 8-1, this specific beech tree had the lowest EWT and the thinnest leaves (N < 1.5). Further experiments that include accurate measurements of leaf thickness are still needed to determine the boundaries outside which pooled NDI – EWT models should not be used. The powdery mildew that covered the leaves of sycamore trees in the Exhibition Park August dataset rendered this EWT estimation approach inapplicable at the canopy level as high error was obtained (47 %). This showed that this EWT estimation approach cannot be applied if leaves were covered with a material that did not affect the two wavelengths included in the NDI in a similar manner. However, as the diseased trees would appear as outliers in comparison to the healthy trees in the canopy level NDI – EWT relationship, this approach can serve as a fast, non-destructive method to detect diseased trees, which would be identified by their very low NDI values (Figure 8-2).

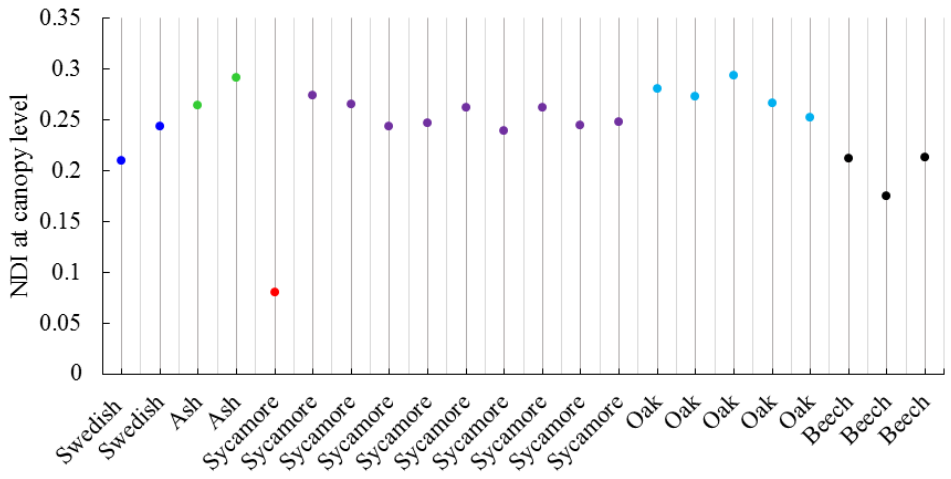

Figure 8-2. Using NDI to detect diseased trees. The Sycamore tree, diseased with powdery mildew (red), had significantly lower NDI than the healthy trees.

The errors obtained at the canopy level in the field campaigns were higher than the errors reported in Zhu *et al.* (2017) (mean error of 4.46 %), which, to our knowledge, was the only previous study in which 3D EWT estimates were generated at the canopy level using TLS.

However, the aforementioned study was conducted in controlled laboratory settings, utilized a single-wavelength TLS (1550 nm), required radiometric corrections for the incidence angle effects, and involved small, individual canopies. Junttila *et al.* (2019) successfully used dual-wavelength TLS to detect European spruce bark beetle infestation symptoms in Norway spruce trees in field campaigns, but 3D EWT estimates at the canopy level were not generated. Overall, very high correlation was observed between TLS estimated canopy EWT and actual canopy EWT measured from destructive sampling (Figure 8-3, $R^2 = 0.95$, RMSE = 0.0008 g cm^{-2}). The results of the conifer tree in the dry-down experiment were excluded, as the tree had very high EWT, and including the results would have biased the regression and increased R^2 to 0.99. Similarly, holly trees also had relatively higher EWT than all the remaining species. When holly trees were excluded, the correlation remained high ($R^2 = 0.82$, RMSE = 0.0008 g cm^{-2}). The accuracy of the EWT estimation at the canopy level was considered high and was comparable to the accuracy reported in the literature using optical RS data (R^2 ranging between 0.7 and 0.92) (Champagne *et al.*, 2003; Zarco-Tejada *et al.*, 2003; Cheng *et al.*, 2008a; Yilmaz *et al.*, 2008). However, the accuracy of this EWT estimation approach still needs to be investigated at the plot level for a more accurate comparison to the accuracy of spaceborne and airborne optical RS estimation of canopy EWT, which will require coupling the EWT estimates with canopy LAI measurements.

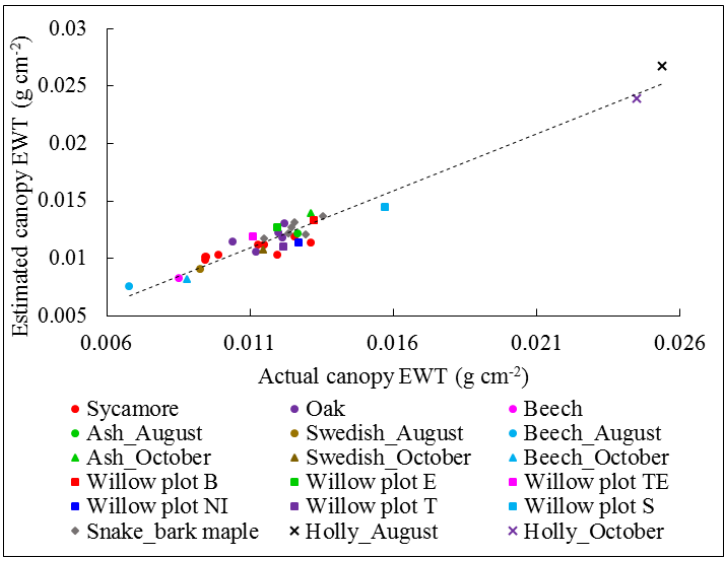

Figure 8-3. The relationship between TLS estimated canopy EWT and actual canopy EWT measured from destructive sampling for all trees involved in this study.

Overall, the results obtained in this study showed that dual-wavelength TLS can successfully retrieve canopy EWT in field campaigns conducted in sites that were heterogeneous in terms

of species and canopy structure. Such heterogeneous sites are more challenging when it comes to estimating canopy EWT because of the variation in canopy LAI and leaf internal structure between species (Zarco-Tejada *et al.*, 2003).

Objective five: to study EWT vertical heterogeneity within canopy and determine how it varies across different species and also between individual trees within each species.

This objective was addressed in Chapter 4, Chapter 5, and Chapter 6. Vertical profiles of EWT were generated for deciduous snake-bark maple and coniferous Corsican pine canopies in the indoors dry-down experiment, for twelve forest canopies from three different species in the Wytham dataset (sycamore, oak, and beech), and for six trees from three different species in the Exhibition park datasets, with vertical profiles being generated twice, once in August and once in October (ash, Swedish whitebeam, and holly). Vertical heterogeneity in canopy EWT was observed in all twenty trees. This concurred with the findings reported in the few studies found in the literature that investigated the vertical distribution of EWT at the canopy level (Liu *et al.*, 2015; Arellano *et al.*, 2017; Zhu *et al.*, 2017; Gara *et al.*, 2018), all reporting vertical heterogeneity.

One reason for the observed EWT heterogeneity was that leaves at different heights within the canopy contribute differently to the total canopy photosynthesis (Aber, 1979; Ellsworth and Reich, 1993), and trees tend to dedicate more nutrients and water to sun leaves in the canopy top than to the shaded leaves in the canopy bottom, to optimize photosynthesis (Hirose and Werger, 1987; Hikosaka, 2004). This can explain the behaviour observed in the snake-bark maple and Corsican pine canopies in the indoors dry-down experiment, in the twelve forest canopies in the Wytham dataset, and in the two ash trees in the Exhibition Park datasets, in which EWT was higher in the canopy top, gradually getting lower towards the canopy bottom. Previous studies in the literature also reported that EWT was always higher in the canopy top than in the canopy bottom (Liu *et al.*, 2015; Arellano *et al.*, 2017; Zhu *et al.*, 2017; Gara *et al.*, 2018). Mooney *et al.* (1977) and Chavana-Bryant *et al.* (2016) showed that leaf age also played a role in EWT distribution within a canopy, reporting that younger leaves in the canopy top had higher EWT than older leaves in the canopy bottom. However, the two Swedish whitebeam and the two holly trees in the Exhibition Park datasets showed different behaviour, as EWT was not always the highest in the canopy top and the lowest in the canopy bottom as observed in all other trees. Typically, sun leaves grow in the canopy top because the top layers of the canopy receive the majority of irradiance (Chazdon and Fetcher, 1984). However, in the Exhibition

Park tree plot, there was a wide gap in the canopy in the middle of the plot, thus sun leaves were not necessarily in the canopy top only, depending on how the trees were illuminated.

The EWT vertical profiles observed could also be a result of the LMA distribution within the canopy, as EWT and LMA were found to be highly correlated in the destructive sampling conducted in Chapter 5, suggesting that a leaf with higher LMA, typically thicker, would be able to hold more moisture than a thinner leaf of the same species. This agreed with the findings of Junttila *et al.* (2019), also reporting high correlation between EWT and LMA at the leaf level. Arellano *et al.* (2017) and Gara *et al.* (2018) showed that EWT and LMA vertical profiles showed similarities, with canopy layers with higher LMA having higher EWT. This can again be related to the illumination conditions and the distribution of sun/shade leaves within the canopy, as sun leaves are typically thicker and have higher LMA than shade leaves (Lichtenthaler *et al.*, 1981).

Objective six: to investigate the potential of using TLS to detect temporal changes in EWT due to drought conditions.

This objective was addressed in Chapter 4 with an indoors dry-down experiment and in Chapter 6 with the Exhibition Park August and October datasets. In the dry-down experiment, TLS was able to detect the change in EWT over a period of eight days for the deciduous snake-bark maple tree and over a period of nine days for the coniferous Corsican pine tree, while the trees were drying naturally. TLS estimated a 15 % drop in EWT between the first and last days of the experiment for the deciduous tree, and a 3.4 % decrease in EWT for the conifer tree. Furthermore, TLS could detect the daily change in EWT for the deciduous tree, showing that the tree lost approximately 3.7 % EWT per day in the first two days of the experiment, and 1.6 % EWT per day in the remaining five days. The ability of TLS to detect such fine changes in EWT suggested that there could be a potential in using TLS to detect canopy EWT changes throughout the day, and compare predawn EWT to midday EWT to quantify how much moisture plants lose during photosynthesis. Spaceborne and airborne optical RS sensors can neither measure such fine changes in EWT because of their temporal resolution limitations, nor can they provide predawn EWT estimates. Also, determining the predawn vegetation water status by measuring predawn leaf water potential using a pressure chamber is a very challenging process if the aim was to determine the water status of a large number of plants (Vila *et al.*, 2011), and TLS can be a more efficient alternative approach.

Although the measured daily change in EWT in the dry-down experiment was less than the errors observed in canopy EWT estimates in the field campaigns, this did not necessarily indicate that TLS cannot detect the fine changes in EWT in outdoors conditions. For instance, scanning a forest plot predawn and rescanning it at midday, from the exact same scanning positions and in non-windy conditions, can theoretically lead to similar errors in canopy EWT estimates predawn and midday, which can lead to accurate detection of the EWT fine changes. This has not been tested in this study, and although the ability of TLS to detect EWT temporal changes in outdoors conditions was examined in the Exhibition Park datasets, the experiment involved green and senescent leaves, which required the use of two different EWT estimation models to account for the significant changes in leaf internal structure. This reduced the accuracy of detecting the change in EWT and thus the results obtained could not be considered a reference to determine the ability of TLS to measure EWT fine changes.

In the Exhibition Park datasets, the errors in EWT estimates in the August dataset (average error of 4.8 %) were less than the errors in the October dataset (average error of 5.4 %), which could have been a result of leaf senescence. The effect of senescence on leaf internal structure is known to vary between species, and can also vary between leaves from the same species if they were at different levels of senescence (Buchanan-Wollaston, 1997). Thus, it can be more challenging to build a NDI – EWT model that can accurately represent all levels of senescence in the plot. Another source of errors was the wind effect, as there was a gentle breeze in October during the scan.

The change in EWT between August and October was detected for seven trees from four different species: ash, Swedish whitebeam, beech and holly. The results showed that the direction and magnitude of the change in EWT was successfully characterized using TLS. This showed the potential of this method to be used in detecting the impact of drought on vegetation. With the very high temporal resolution of TLS, being independent of solar illumination or limited by cloud coverage, it can be used to fill the gaps in time series produced from optical RS data. The accuracy of detecting the change in EWT appeared to be mainly a function of the EWT estimation errors on both dates. An overestimation or underestimation of EWT in both dates, with similar magnitude of errors, produced the most accurate estimation of the change in EWT. A higher magnitude of error in one dataset than in the other, or overestimating EWT in one dataset and underestimating it in the other, resulted in less accurate estimates of the change in EWT.

Objective seven: to develop methods to utilise the 3D EWT estimates in the DART model and simulate the effects of EWT vertical heterogeneity on satellite signal.

This objective was addressed in Chapter 7. Two forest plots were reconstructed in the DART model, based on TLS data collected in Wytham Woods: a mixed-species oak and sycamore plot, named hereafter as forest plot 1, and a mixed-species sycamore, ash, and hazel plot, named hereafter as forest plot 2. Forest plot 1 was reconstructed using the leaf-on TLS point clouds collected in the Wytham dataset, thus there were missing leaves and wood components in the canopy top as a result of occlusion. Forest plot 2 was reconstructed from leaf-off scans conducted with a Riegl VZ-400 TLS instrument, which was used to build the wood component 3D models, then a leaf insertion algorithm was used to add leaves to the 3D models, based on leaf-on scans conduced with the same instruments (full details in Calders *et al.* (2018)).

Simulations were carried out to investigate which canopy layers dominated the forest plot reflectance by assuming equal EWT in all canopy layers, then reducing EWT in canopy bottom layers only while maintaining EWT constant in canopy top layers. This was achieved by splitting each tree model as a number of horizontal layers, and assigning different optical properties to each layer separately. Sentinel-2A NIR and SWIR bands were simulated, and NDWI was calculated for each case study. The results obtained in the two forest plots revealed that the plot reflectance, NDWI, and the change in NDWI, were dominated by the reflectance from the top four meters of canopy. Reducing EWT in all canopy layers by 70 %, simulating a severe drought condition, caused a 52 % drop in NDWI, which reflected the severe vegetation water stress. However, reducing EWT by 70 % in all layers below the top four metres of canopy, whilst the top four metres maintained the high EWT values, resulted in only a 13 % drop in NDWI, which may not indicate that the forest plot was at risk of wildfire.

Furthermore, comparing the simulated reflectance and NDWI when EWT was equal in all canopy layers to the simulated reflectance and NDWI when the actual EWT vertical profile was used showed that the EWT vertical heterogeneity had no effect on the satellite-measured reflectance or NDWI. This was a result of the majority of the plot reflectance resulting from the top four metres of the canopy, in which there was minimal vertical heterogeneity. It is worth mentioning that drying the canopy bottom layers only while maintaining the canopy top layers healthy did not necessarily represent the real drying patterns of trees during drought conditions, which still needs to be examined in forest canopies. Overall, the simulations showed that care must be taken while using spaceborne optical RS data in monitoring forest health and early-

detection of wildfire risk, especially in dense forests, as the upper canopy layers, which have more moisture, were found to dominate the forest plot reflectance. In dense forests, a spaceborne sensor will not be able to detect severe water stress in the understory and lower canopy until the upper canopy layers begin to get stressed. However, more 3D RTMs still need to be tested, as the results of RTM simulations are very sensitive to the phase function used in single and multiple scattering of radiation in the canopy, and also to the number of successive orders of scattering (Widlowski *et al.*, 2015). The results of the RAMI-IV experiment showed variation in the simulated spectra between the different 3D RTM models tested (Widlowski *et al.*, 2013).

Additional aims of the simulations were to study the influence of woody materials and understory vegetation on the forest plots reflectance. It was found that the woody materials had no contribution to the plots' reflectance and NDWI in forest scene 1, most likely because the woody materials in the upper canopy were missing as a result of occlusion, while the woody materials had some influence on the reflectance and NDWI in forest scene 2. This agreed with the results of DART simulations conducted in Malenovský *et al.* (2008), and FLIGHT RT simulations conducted in Verrelst *et al.* (2010), with both reporting that the woody materials had a low effect on the forest plot reflectance, and the latter showing that the effects increased in old, open forest canopies. The understory had some effects on forest plot 1 reflectance, as the plot had some canopy gaps, in addition to the missing leaves in the canopy top layers that allowed more irradiance to reach the understory. On the other hand, the understory had minimal effects on forest plot 2 reflectance, as the plot had no gaps and also did not suffer from occlusion. This agreed to with what has been previously reported in the literature that tree density and canopy gap distribution determined the contribution of understory to forest plot reflectance (Guyot *et al.*, 1989; Spanner *et al.*, 1990; Miller *et al.*, 1997; Zarco-Tejada *et al.*, 2001; Rautiainen and Lukeš, 2015; Landry *et al.*, 2018).

8.3 Suggestions for future research directions

Towards using TLS to quantify other vegetation water status metrics:

This study showed that canopy EWT can be retrieved successfully in 3D using dual-wavelength TLS data. The 3D EWT estimates can then be used to retrieve other key vegetation water status metrics. As shown in Chapter 7, tree 3D models can be generated from TLS point clouds and used to estimate canopy LAI. Previous studies in the literature also showed that canopy LAI can be successfully estimated from TLS data (Moorthy *et al.*, 2008; Antonarakis *et al.*, 2010;

Zheng *et al.*, 2013; Vincent *et al.*, 2015; Meng *et al.*, 2019). Combining the 3D EWT estimates with LAI measurements can lead to estimating canopy water content (kg m^{-2}), as CWC is the product of EWT and LAI. The CWC estimated from TLS is expected to better-represent the whole canopy than that retrieved from optical RS data, as it is based on 3D EWT estimates. Tree 3D models generated from TLS point clouds can also be used to estimate the total leaf surface area in each canopy layer. Coupling the EWT vertical profiles with the leaf surface area estimates can lead to quantifying the water content in each canopy layer (kg), which allows the characterization of whole-tree leaf water status and total water content (kg).

Furthermore, this research focused only on studying the relationship between NDI of laser wavelengths and leaf moisture content. Expanding this to include wood moisture content can lead to the use of TLS to estimate both leaf and wood water content, if a relationship between NDI and wood moisture content can be established. This can lead to estimating the total vegetation water content (kg m^{-2}) from TLS data. VWC is a different water status metric to CWC, as the former can be used in retrieving soil moisture content under vegetation from active and passive microwave remote sensing (Njoku and Entekhabi, 1996; Yilmaz *et al.*, 2008), while the latter is a vegetation stress indicator and a parameter of interest in studying the water cycle and its role in the global climate change (Clevers *et al.*, 2010; Mendiguren *et al.*, 2015). CWC represents the total moisture content in canopy per unit ground surface area, while VWC represents the total moisture content in leaves, branches and stems per unit ground surface area. However, it is expected that this method may be able to only detect moisture in the surface and outer layer of stems and branches, and not to quantify total moisture in wood components. In vegetation with small stems filled with watery sap, such as the willow plots scanned in this study, this method may be able to better-quantify the wood moisture content.

EWT vertical profiles can also represent the vertical heterogeneity in LMA (g cm^{-2}), as EWT was found to be highly correlated to LMA in this study and also in Junttila *et al.* (2019). The EWT – LMA relationship can be used to generate 3D LMA point clouds from the 3D EWT estimates, but the accuracy of the estimation may be of concern as the errors will accumulate. Although LMA is not a water status metric, it is an important trait in plant growth rate (Gutschick and Wiegel, 1988; Poorter *et al.*, 2009). Another metric that is correlated to EWT and LMA is FMC (%), which can be estimated as EWT divided by LMA. Coupling the 3D EWT estimates retrieved from TLS with LMA measurements retrieved from field spectroscopy, destructive sampling, or hyperspectral imagery, can lead to estimating FMC in 3D. Studying FMC distribution in 3D may lead to a better characterization of forest fire ignition and

propagation, as FMC in each canopy layer can be quantified. The results obtained in this research showed that NDI can be used to estimate FMC directly, but also highlighted that the NDI – FMC relationship was species-specific and highly influenced by the variation in LMA, and testing this approach in a real forest environment is still needed. Figure 8-4 summarizes the different metrics that can be retrieved from the 3D EWT point clouds.

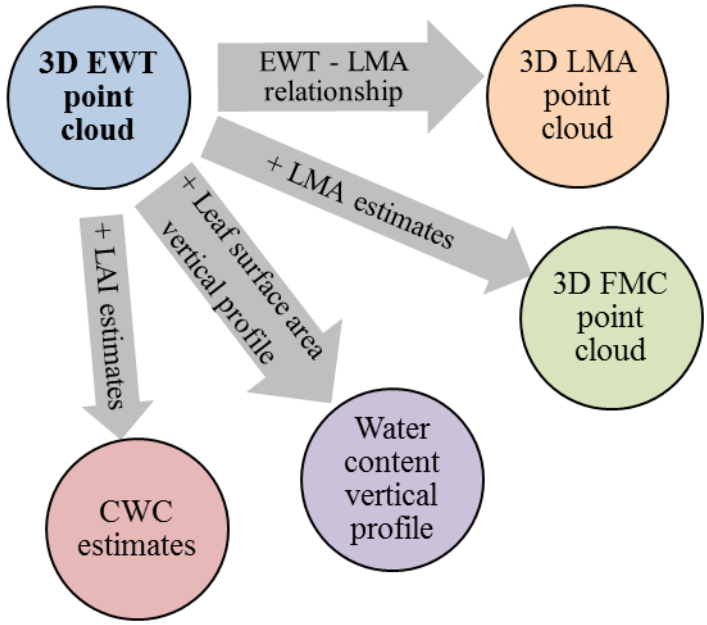

Figure 8-4. Retrieving other vegetation water status metrics and LMA from the 3D EWT point cloud.

Towards improving the accuracy of EWT estimation from optical RS data:

In this study, although the TLS data were collected at the plot level, EWT was studied at leaf and canopy levels only, and the understory was excluded during the point cloud processing to reduce computational time. Estimating EWT at the plot level can allow a direct comparison with EWT estimates retrieved from spaceborne and airborne optical RS data. By generating 3D EWT estimates at the plot level in forest plots that correspond to specific pixels in the satellite imagery, TLS can provide ground truth data to validate the satellite estimation of EWT. Furthermore, the 3D EWT estimates allow the study of the EWT distribution separately in each component of the plot: in the understory, in the whole canopy excluding the woody materials, and in each canopy layer, and thus can be used to study how EWT of these different components contributes to the EWT estimated from optical RS data per pixel. The radiative transfer modelling conducted in this study showed that the upper canopy was the main component that

dominated the forest plot reflectance and the change in NDWI, but a direct comparison between TLS estimated EWT and satellite estimated EWT is still needed. With this achieved, TLS can then serve as a tool to calibrate the satellite estimated EWT by excluding the understory and woody materials' influence on the estimation, aiming at a more accurate estimation of canopy EWT from spaceborne and airborne imagery.

Towards improving spaceborne sensors early-detection of forest stress and wildfire risk:

The results obtained from the DART simulations conducted in this study revealed that the canopy top layers (top four meters) dominated the forest plot reflectance in the two plots examined. This suggested that spaceborne sensors can monitor the water status of canopy top layers only, and that the water status metrics estimated from optical RS data may not necessarily represent the whole canopy. For instance, the results of the simulations suggested that using Sentinel-2 imagery to estimate EWT in the two forest plots simulated would result in an overestimation of EWT, because the majority of the received satellite signal came from the canopy top, which has higher EWT than the canopy bottom according to the EWT vertical profiles generated from TLS. However, the EWT vertical profiles can be used to expand the satellite estimation of EWT to include lower canopy layers as well as upper canopy layers. Figure 8-5 demonstrates the use of TLS to expand the satellite estimation of EWT in the forest plot scanned in the Wytham dataset. Although EWT vertical profiles cannot be generated in forest plots corresponding to every pixel in the satellite imagery, generating EWT vertical profiles in multiple plots in the same forest may be sufficient to represent the EWT vertical heterogeneity in the forest. However, the plots must represent the different species in the forest.

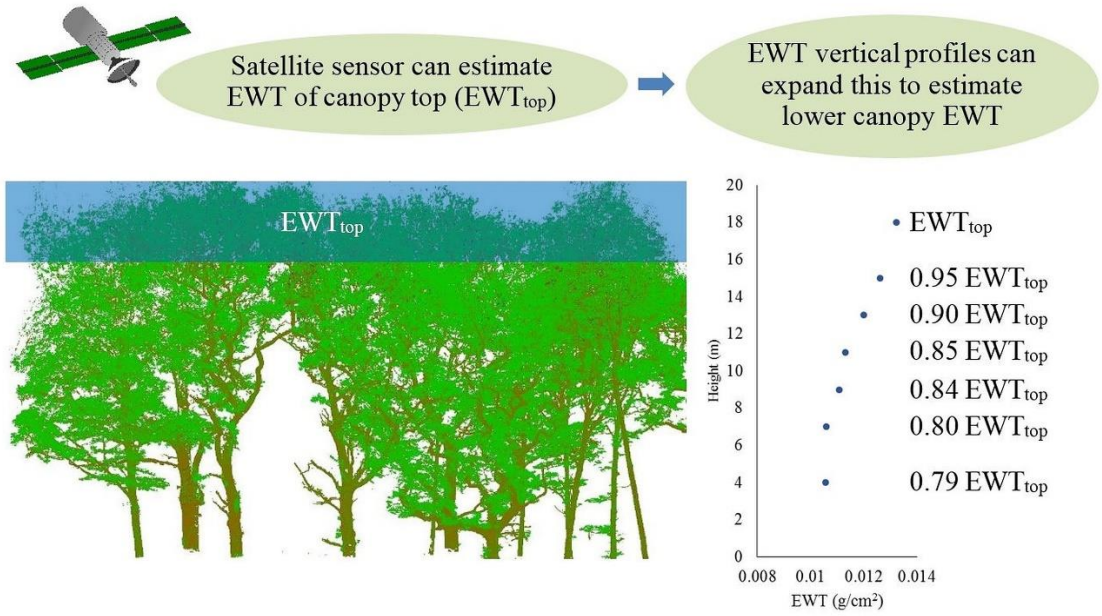

Figure 8-5. The use of EWT vertical profiles generated from TLS to determine EWT reduction coefficients that can be used to retrieve EWT of lower canopy layers from EWT of canopy top layers, estimated from optical RS data. Additional layers can then be added to the 2D EWT distribution map generated from the satellite imagery, with each layer representing EWT in a lower canopy layer.

During drought conditions, trees were found to lose water content unequally from different canopy layers, as shown in the EWT vertical profiles generated in the indoors dry-down experiment and in the Exhibition Park datasets. Although the temporal changes in EWT vertical profiles still need to be examined in forest canopies, it is expected that during drought conditions trees may attempt to maintain healthy canopy top layers and will most likely lose more moisture from canopy bottom layers. This is because in a forest, canopy top leaves are typically sun leaves (Chazdon and Fetcher, 1984), and trees tend to dedicate more nutrients and water to sun leaves to optimize photosynthesis (Hirose and Werger, 1987; Hikosaka, 2004). In the case of forest canopies losing more moisture from lower canopy layers than from upper canopy layers during a drought, a satellite sensor may not be able to detect the water stress that started in the canopy bottom. Using TLS to study the drying patterns of forest canopies and how the trees react to drought conditions and redistribute the resources to different canopy layers can help addressing this limitation. EWT vertical profiles generated during drought conditions can quantify how much moisture was lost from the different canopy parts, then used to expand the satellite estimation of EWT to account for the water stress in lower canopy layers, if any (Figure 8-5). The threshold used in early-detection of wildfire risk using a satellite sensor

can then be adjusted to include the lower EWT in canopy bottom layers, which may improve the decision making during heatwaves and droughts.

Towards the use of dual-wavelength TLS in vegetation health monitoring

This study showed that dual-wavelength TLS can provide 3D EWT estimates at the canopy level in mixed-species vegetation sites (forest and urban park tree plots) using general, site-specific, species-independent EWT estimation models. It was also possible to develop a site- and species-independent general model that was successfully applied in the forest and urban park tree plots and achieved EWT estimation accuracy close to that achieved using the site-specific models. This was mainly because the leaf structure coefficient (N) of the species involved in this study ranged between 1.5 and 2, according to the PROSPECT simulations, and the general EWT model was calibrated using leaf samples that covered this range. This suggested that the general EWT model derived in this study can be used to estimate canopy EWT at the plot and landscape levels in mixed-species deciduous woodlands. Species classification and species-specific models will not be needed, as long as the species present in the site have N values ranging between 1.5 and 2. The leaf samples collected in this study from 11 deciduous species were all found to be in this range of N values, further indicating that the developed model can be considered a general EWT model for deciduous species. The model can be further improved by adding more species to the calibration data, and also by adding more leaf samples in the low EWT region (less than 0.009 g cm^{-2}). However, it was not possible to use the general EWT model to estimate EWT for holly trees, which had thick leaves with waxy, glossy surfaces (N > 2 according to PROSPECT simulations). Thus, in mixed-species sites, the presence of trees from species that have significantly thicker leaves than those used in calibrating the model (N > 2) can complicate the use of this method at the landscape level. Such trees will require their own EWT estimation model and must be identified and segmented in the point cloud. Leaf sampling will also be needed to build the species-specific models.

One solution for this issue is to use the NDI values to auto-detect trees in the point cloud, if any, that have N > 2, as such trees will have significantly higher NDI values than the other species, making them appear as statistical outliers. For instance, NDI values of all trees scanned in this study, both in the forest and urban park tree plots, ranged between 0.17 and 0.42, with mean NDI of 0.26 and standard deviation of 0.044. Using the mean and standard deviation, holly trees can be auto-detected in the point cloud by using a threshold of the mean + one standard deviation (the threshold = 0.3, NDI of holly = 0.42, highest NDI in all other

trees = 0.29). Afterwards, the general EWT model can be applied to all trees in the point cloud, while the species-specific model can be applied to the auto-detected holly trees. To further automate the process, general EWT estimation models derived from PROSPECT simulations can be used instead of those derived from destructive sampling. An EWT estimation model corresponding to N of 1.7, derived from PROSPECT simulations, can be used as a general model for the species that have N values between 1.5 and 2. Furthermore, it was observed that forest canopies had thicker leaves than tree canopies in the urban park tree plot, even if they were from the same species. For instance, beech leaf samples collected from the forest plot were thicker than those collected from the beech tree in the urban park tree plot (Figure 8-1). Thus, the use of general EWT models based on habitat type can further improve the accuracy of the EWT estimation. The PROSPECT simulations suggested that an EWT model corresponding to N of 1.5 can represent deciduous broadleaf canopies in urban tree plots, and a general model corresponding to N of 1.8 can be suitable for deciduous broadleaf trees in woodlands. A general EWT model corresponding to N of 2.3 can be used for species with thick leaves (N > 2), such as holly, as the highest value of N for non-senescent, dicot leaves is 2.5 (Jacquemoud and Baret, 1990). Table 8-1 shows the suggested general EWT models derived from the PROSPECT simulations. Figure 8-6 shows the processing steps to generate the 3D EWT point clouds.

Table 8-1. General EWT estimation models based on the PROSPECT simulations.

Habitat	Species	N	EWT estimation model
Urban tree plot	Beech Swedish Whitebeam Ash Snake-bark maple Lime Grey Alder Common Alder Poplar	1.5	EWT (g cm^{-2}) = 0.0690 × NDI – 0.0077
Deciduous woodland	Sycamore Oak Beech Ash	1.8	EWT (g cm^{-2}) = 0.0733 × NDI – 0.0076
Urban tree plot	Holly	2.3	EWT (g cm^{-2}) = 0.0794 × NDI – 0.0074
General model	Deciduous	1.7	EWT (g cm^{-2}) = 0.0720 × NDI – 0.0076
General model	Species with thick leaves (N > 2)	2.3	EWT (g cm^{-2}) = 0.0794 × NDI – 0.0074

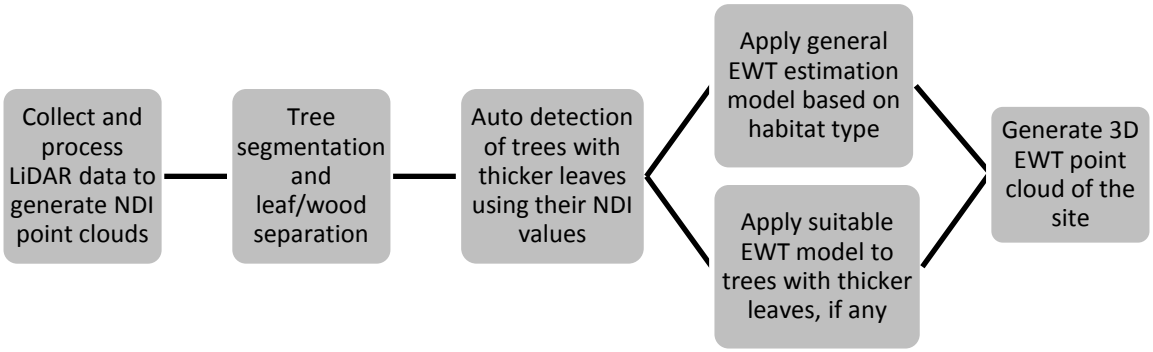

Figure 8-6. A flowchart of the LiDAR data processing pipeline to generate 3D EWT point clouds in mixed-species sites using the general EWT estimation models derived from PROSPECT simulations.

The aforementioned approach and the general EWT estimation models described in Table 8-1 still need to be tested by reprocessing the point clouds collected in this study and comparing the accuracy achieved using the site-specific models, derived from destructive sampling, and that achieved using the general EWT models derived from the PROSPECT simulations. Furthermore, general EWT models still need to be developed for coniferous species, and transferring the models suggested in Table 8-1 to other types of forests (boreal forests and tropical rainforests) also needs to be examined.

The use of general EWT models, being independent of species and transferable to different sites, can make dual-wavelength TLS a useful tool for operational landscape-scale EWT estimation in mixed-species vegetation areas, with no need for a prior knowledge of the species present in the site. Time series of the change in EWT can be produced at much higher temporal resolution than spaceborne sensors. For instance, during drought conditions, the daily change in EWT can be monitored, with the potential to even detect the changes in EWT throughout the day. As the EWT estimates are provided in 3D, the change in EWT vertical profiles can be observed, and trees reaction to drought conditions, regarding how they redistribute water and resources, can be studied at very high spatial and temporal resolutions. However, one challenge associated with the use of TLS to estimate EWT at the landscape level is the scan time required to cover large areas of vegetation. For instance, applying this method to generate 3D EWT estimates in a one-hectare forest plot, using 20 m × 20 m scan grid and 3 mm point spacing, would require at least 25 hours of scanning (5 days of scanning, 5 hours per day). This would reduce the temporal resolution of the time series of the change in EWT produced for such large

areas, which may also be further reduced because of the wind effects, as scans cannot be conducted in windy conditions. The scanning time can be reduced by increasing the point spacing (reducing the scan resolution) or increasing the scan grid size. However, at the landscape level, TLS can only be suitable for detecting the weekly or monthly changes in EWT, depending on the size of the area to be scanned. Scanning only a set of plots that represent the different species in the site can be more useful, as these plots can be scanned daily and the rapid changes in EWT can be monitored. Another factor that needs to be taken in consideration while applying this approach at the plot and landscape levels is the effect of the variation of the canopy LAI in heterogeneous sites. Although the use of a vegetation index can be sufficient to reduce the effects of incidence angle, leaf internal structure, and leaf BRDF, canopy LAI can influence the accuracy of the EWT estimation using vegetation indices. Thus, at the plot and landscape levels, LAI measurements are needed, and canopy EWT should be quantified as the product of EWT and LAI.

Towards the use of dual-wavelength airborne LiDAR in vegetation health monitoring

Recently, the Optech Titan (Teledyne Optech) multispectral airborne LiDAR sensor was launched, being the first multispectral LiDAR system commercially available. The system collects data in three channels, employing 1550 nm SWIR, 1064 nm NIR, and 532 nm visible wavelengths. Channels 1 and 2 have similar beam divergence (0.35 mrad), and also have similar wavelengths to those utilized in the DWEL and SALCA dual-wavelength TLS systems, which have been previously linked to EWT. Thus, the system has the potential to provide 3D EWT estimates at the landscape level, if the point clouds from the two different channels could be accurately aligned. Similar to TLS, the use of airborne LiDAR in EWT estimation at the landscape level in mixed-species woodlands can be complicated by the presence of species with significantly thicker leaves than the other species in the site, preventing the use of general EWT estimation model derived from destructive sampling. Unlike TLS, airborne LiDAR data collection does not require accessing the forest, making it more feasible for woodlands with limited or no accessibility. However, this also limits the amount of information obtainable about the species present in the woodland, making identifying the trees with thicker leaves more challenging. In this case, the EWT estimation models presented in Table 8-1, and the processing steps shown in Figure 8-6, can be used, without the need for accessing the woodland to collect leaf samples to build EWT estimation models, or to identify species with significantly thicker leaves. However, further investigation is still needed for senescent leaves, as it was found in this study that the level of senescence affected the EWT estimation model and prevented the

develop of site- and species-independent EWT estimation model. It was found that a general EWT model with N of 2.5 can represent the senescent trees in the urban park tree plot. However, the model did not represent the NDI – EWT relationship for the willow plots, and site-specific models were mandatory in this case.

Overall, this study showed the potential of using commercially-available TLS instruments to provide important insights into the EWT distribution within canopy, by mapping the EWT at canopy level in 3D. The proposed approach can serve as a powerful tool to study the variation of EWT within the canopy and between different species, can provide high spatial and temporal EWT estimations, is independent of the cloud coverage and solar illumination, and has the potential to estimate EWT predawn. This approach can also be used in detecting temporal changes in EWT, showing how the vertical profiles of EWT change during drought conditions, and how trees redistribute water and resources to cope with the water deficiency. Being the first study to successfully map canopy EWT in 3D in forest and urban park tree plots, and to provide detailed vertical profiles of canopy EWT, the method proposed in this study can help fill the gap in the literature regarding quantifying and studying the vertical heterogeneity in canopy biochemistry. This study showed that canopy EWT varied vertically. It was always higher in the canopy top (sun leaves) than in the canopy bottom (shade leaves) in forest canopies, while this was not the case in the urban part tree plot, where different species and different trees within each species had different EWT vertical profiles. It was found that the EWT vertical profiles seemed to be affected by the illumination conditions and the location of sun and shade leaves layers in the canopy. EWT and LMA were found to be highly correlated, which affected the EWT distribution within the canopy, as leaves with higher LMA, typically thicker, held more moisture than thinner leaves. Other key findings were that trees did not lose moisture equally from all the canopy layers while being water-stressed, and that they seemed to attempt to maintain EWT in sun leaf layers unchanged, while losing more moisture from shade leaf layers. This study also introduced a method to integrate the vertical heterogeneity in canopy biochemistry into 3D radiative transfer modelling by utilizing the EWT vertical profiles retrieved from TLS into the DART 3D RTM. The simulations showed that the upper canopy layers dominated the forest plot reflectance and that the spaceborne sensor was not able to detect severe water stress in the bottom canopy layers. This suggested that spaceborne optical sensors can monitor the change in EWT in the canopy top layers only, which should be taken into consideration while monitoring forest health during drought conditions. This can improve the decision making regarding preventing and fighting forest wildfires.

The method proposed in this study can be improved by coupling TLS data with *in situ* multispectral or hyperspectral data in order to quantify the LMA distribution within the canopy and establish relationships between the EWT and LMA distribution. Furthermore, chlorophyll content can be estimated using the multispectral or hyperspectral data, and the relationship between EWT and chlorophyll content vertical profiles can be studied, especially during drought conditions. The tree 3D models generated in this study, and used in the radiative transfer modelling, can be improved by coupling the TLS data with airborne LiDAR data to reduce the effects of occlusion. The tree 3D models were used to estimate canopy LAI, and *in situ* measurements of LAI using hemispherical imagery or litter traps are needed to evaluate this LAI estimation method. Also, the radiative transfer modelling conducted in this study, despite the results being close to those obtained from actual satellite data, can be improved by collecting leaf spectra of the understory vegetation in the forest plots and model the understory as turbid medium. The results are also expected to improve, especially in the NIR reflectance region, if TLS and airborne LiDAR data are used to reconstruct the forest plot, as the canopy LAI will be more realistic. Finally, this study utilized single-wavelength, commercial TLS instruments as no commercial multispectral TLS systems have yet become available. Although it showed that combining data from two commercially-available TLS systems can be an alternative to commercial multispectral TLS systems, the TLS instruments used in this study were pulsed systems. Commercial, full-waveform multispectral TLS systems, if developed, have the potential to provide more information about the canopy structure and biochemistry, especially inside the canopy. Next steps include combining the EWT vertical profiles with the canopy LAI in order to quantify the water content (g) in each canopy layer and characterise the whole-tree leaf water status and total water content, and applying the method predawn to examine its potential in measuring the predawn canopy EWT.

8.4 Conclusions

This research showed the potential of commercial dual-wavelength TLS as a powerful tool to monitor vegetation water status by estimating canopy EWT in three dimensions. Key findings of this study were: (1) EWT exhibited vertical heterogeneity within canopy, which varied between species, sites, and individual trees, (2) trees were found to lose moisture content unequally from different canopy layers during drought conditions, (3) forest plot reflectance was dominated by canopy top layers, and severe water stress that started in lower canopy was not detected by the satellite sensor until it affected the top four metres of canopy. The presented method can help improve understanding of 3D biochemistry and resource allocation in trees,

and provide new insights into how trees react to heatwaves and droughts. The method can also provide EWT vertical profiles and allow the study of their temporal changes, and such measurements cannot be obtained using optical RS spaceborne and airborne sensors. EWT estimates retrieved from TLS can fill the gaps in the time series of EWT temporal changes produced from optical RS data. The proposed method also has the potential to be used to calibrate and validate the optical RS estimates of EWT, and to provide EWT estimates predawn.

References

Aber, J.D. (1979) 'Foliage-height profiles and succession in northern hardwood forests', *Ecology*, 60(1), pp. 18-23.

Åkerblom, M., Raumonen, P., Casella, E., Disney, M.I., Danson, F.M., Gaulton, R., Schofield, L.A. and Kaasalainen, M. (2018) 'Non-intersecting leaf insertion algorithm for tree structure models', *Interface Focus*, 8(2), p. 20170045.

Al-Moustafa, T., Armitage, R.P. and Danson, F.M. (2012) 'Mapping fuel moisture content in upland vegetation using airborne hyperspectral imagery', *Remote sensing of Environment*, 127, pp. 74-83.

Ali, A.M., Darvishzadeh, R., Skidmore, A.K. and Duren, I.v. (2016) 'Effects of canopy structural variables on retrieval of leaf dry matter content and specific leaf area from remotely sensed data', *Journal of Selected Topics in Applied Earth Observations and Remote Sensing*, 9, pp. 898–909.

Allen, C.D., Breshears, D.D. and McDowell, N.G. (2015) 'On underestimation of global vulnerability to tree mortality and forest die-off from hotter drought in the Anthropocene', *Ecosphere*, 6(8), pp. 1-55.

Allen, W.A., Gausman, H.W., Richardson, A.J. and Thomas, J.R. (1969) 'Interaction of isotropic light with a compact plant leaf', *Josa*, 59(10), pp. 1376-1379.

Alonso, M., Camarasa Belmonte, A.M., Chuvieco Salinero, E., Cocero Matesanz, D., Kyun, I.A., Martín, M.P. and Salas Rey, F.J. (1996) 'Estimating temporal dynamics of fuel moisture content of Mediterranean species from NOAA-AVHRR data', *EARSeL Advances in Remote Sensing, 1996, vol. 4, num. 4, p. 9-24*.

Améglio, T., Archer, P., Cohen, M., Valancogne, C., Daudet, F.-a., Dayau, S. and Cruiziat, P. (1999) 'Significance and limits in the use of predawn leaf water potential for tree irrigation', *Plant and Soil*, 207(2), pp. 155-167.

Anderson, K. and Gaston, K.J. (2013) 'Lightweight unmanned aerial vehicles will revolutionize spatial ecology', *Frontiers in Ecology and the Environment*, 11(3), pp. 138-146.

Antonarakis, A.S., Richards, K.S., Brasington, J. and Muller, E. (2010) 'Determining leaf area index and leafy tree roughness using terrestrial laser scanning', *Water Resources Research*, 46(6).

Anttila, K., Hakala, T., Kaasalainen, S., Kaartinen, H., Nevalainen, O., Krooks, A., Kukko, A. and Jaakkola, A. (2016) 'Calibrating laser scanner data from snow surfaces: Correction of intensity effects', *Cold Regions Science and Technology*, 121, pp. 52-59.

Aponte, C., de Groot, W.J. and Wotton, B.M. (2016) 'Forest fires and climate change: causes, consequences and management options', *International Journal of Wildland Fire*, 25(8), pp. i-ii.

Arellano, P., Tansey, K., Balzter, H. and Boyd, D.S. (2017) 'Field spectroscopy and radiative transfer modelling to assess impacts of petroleum pollution on biophysical and biochemical parameters of the Amazon rainforest', *Environmental Earth Sciences*, 76(5), p. 217.

Asner, G.P., Scurlock, J.M. and A. Hicke, J. (2003) 'Global synthesis of leaf area index observations: implications for ecological and remote sensing studies', *Global Ecology and Biogeography*, 12(3), pp. 191-205.

Atzberger, C. (2004) 'Object-based retrieval of biophysical canopy variables using artificial neural nets and radiative transfer models', *Remote sensing of environment*, 93(1-2), pp. 53-67.

Balduzzi, M.A.F., Van der Zande, D., Stuckens, J., Verstraeten, W.W. and Coppin, P. (2010) 'The Properties of terrestrial laser system intensity for measuring leaf geometries: a case study with conference pear trees (Pyrus Communis)', *Sensors*, 11(2), pp. 1657-1681.

Ballesteros, R., Ortega, J.F., Hernández, D. and Moreno, M.Á. (2015) 'Characterization of vitis vinifera L. canopy using unmanned aerial vehicle-based remote sensing and photogrammetry techniques', *American Journal of Enology and Viticulture*, 66(2), pp. 120-129.

Bannari, A., Morin, D., Bonn, F. and Huete, A. (1995) 'A review of vegetation indices', *Remote sensing reviews*, 13(1-2), pp. 95-120.

Banskota, A., Wynne, R., Thomas, V., Serbin, S., Kayastha, N., Gastellu-Etchegorry, J. and Townsend, P. (2013) 'Investigating the utility of wavelet transforms for inverting a 3-D radiative transfer model using hyperspectral data to retrieve forest LAI', *Remote Sensing*, 5(6), pp. 2639-2659.

Barbier, N., Couteron, P., Gastelly-Etchegorry, J.-P. and Proisy, C. (2012) 'Linking canopy images to forest structural parameters: potential of a modeling framework', *Annals of forest science*, 69(2), pp. 305-311.

Barbier, N., Couteron, P., Proisy, C., Malhi, Y. and Gastellu-Etchegorry, J.P. (2010) 'The variation of apparent crown size and canopy heterogeneity across lowland Amazonian forests', *Global Ecology and Biogeography*, 19(1), pp. 72-84.

Baret, F., Clevers, J. and Steven, M. (1995) 'The robustness of canopy gap fraction estimates from red and near-infrared reflectances: A comparison of approaches', *Remote Sensing of Environment*, 54(2), pp. 141-151.

Baret, F. and Guyot, G. (1991) 'Potentials and limits of vegetation indices for LAI and APAR assessment', *Remote sensing of environment*, 35(2-3), pp. 161-173.

Baret, F., Hagolle, O., Geiger, B., Bicheron, P., Miras, B. and Huc, M. (2007) 'LAI, FAPAR and f-Cover CYCLOPES Global Products Derived from Vegetation. Part 1: Principles of the algorithm', *Remote Sensing of Environment*, 110, p. 275−286.

Baret, F., Jacquemoud, S., Guyot, G. and Leprieur, C. (1992) 'Modelled Analysis of the Biophysical Nature of Spectral Shifts and Comparison with Information Content of Broad Bands', *Remote Sensing of Environment*, 41, p. 133−142.

Bartlett, M.K., Klein, T., Jansen, S., Choat, B. and Sack, L. (2016) 'The correlations and sequence of plant stomatal, hydraulic, and wilting responses to drought', *Proceedings of the National Academy of Sciences*, 113(46), pp. 13098-13103.

Beghi, R., Giovenzana, V., Brancadoro, L. and Guidetti, R. (2017) 'Rapid evaluation of grape phytosanitary status directly at the check point station entering the winery by using visible/near infrared spectroscopy', *Journal of Food Engineering*, 204, pp. 46-54.

Béland, M., Baldocchi, D.D., Widlowski, J.L., Fournier, R.A. and Verstraete, M.M. (2014) 'On seeing the wood from the leaves and the role of voxel size in determining leaf area distribution of forests with terrestrial LiDAR', *Agricultural and Forest Meteorology*, 184 pp. 82–97.

Béland, M., Widlowski, J.-L., Fournier, R.A., Côté, J.-F. and Verstraete, M.M. (2011) 'Estimating leaf area distribution in savanna trees from terrestrial LiDAR measurements', *Agricultural and Forest Meteorology*, 151(9), pp. 1252-1266.

Berni, J.A., Zarco-Tejada, P.J., Suárez, L. and Fereres, E. (2009) 'Thermal and narrowband multispectral remote sensing for vegetation monitoring from an unmanned aerial vehicle', *IEEE Transactions on Geoscience and Remote Sensing*, 47(3), pp. 722-738.

Blaskow, R. and Schneider, D. (2014) 'Analysis and correction of the dependency between laser scanner intensity values and range', *The International Archives of Photogrammetry, Remote Sensing and Spatial Information Sciences*, 40(5), pp. 107-112.

Bolkas, D. (2019) 'Terrestrial laser scanner intensity correction for the incidence angle effect on surfaces with different colours and sheens', *International Journal of Remote Sensing*, 40(18), pp. 7169-7189.

Bonan, G.B. (2008) 'Forests and climate change: forcings, feedbacks, and the climate benefits of forests', *science*, 320(5882), pp. 1444-1449.

Brodu, N. and Lague, D. (2012) '3D terrestrial lidar data classification of complex natural scenes using a multi-scale dimensionality criterion: Applications in geomorphology', *ISPRS Journal of Photogrammetry and Remote Sensing*, 68, pp. 121-134.

Buchanan-Wollaston, V. (1997) 'The molecular biology of leaf senescence', *Journal of experimental botany*, 48(2), pp. 181-199.

Burgan, R.E. (1996) 'Use of remotely sensed data for fire danger estimation', *EARSeL. Advances in remote sensing*, pp. 1-8.

Burt, A., Disney, M. and Calders, K. (2018) 'Extracting individual trees from lidar point clouds using treeseg', *Methods in Ecology and Evolution*.

Butt, N., Campbell, G., Malhi, Y., Morecroft, M., Fenn, K. and Thomas, M. (2009) 'Initial results from establishment of a long-term broadleaf monitoring plot at Wytham Woods, Oxford, UK', *University Oxford, Oxford, UK, Rep*.

Calders, K., Burt, A., Origo, N., Disney, M., Nightingale, J., Raumonen, P. and Lewis, P. (2016) *Geoscience and Remote Sensing Symposium (IGARSS), 2016 IEEE International*. IEEE.

Calders, K., Disney, M.I., Armston, J., Burt, A., Brede, B., Origo, N., Muir, J. and Nightingale, J. (2017) 'Evaluation of the range accuracy and the radiometric calibration of multiple terrestrial laser scanning instruments for data interoperability', *IEEE Transactions on Geoscience and Remote Sensing*, 55(5), pp. 2716-2724.

Calders, K., Newnham, G., Burt, A., Murphy, S., Raumonen, P., Herold, M., Culvenor, D., Avitabile, V., Disney, M. and Armston, J. (2015) 'Nondestructive estimates of above-ground biomass using terrestrial laser scanning', *Methods in Ecology and Evolution*, 6(2), pp. 198-208.

Calders, K., Origo, N., Burt, A., Disney, M., Nightingale, J., Raumonen, P., Åkerblom, M., Malhi, Y. and Lewis, P. (2018) 'Realistic forest stand reconstruction from terrestrial LiDAR for radiative transfer modelling', *Remote Sensing*, 10(6), p. 933.

Carter, G.A. (1993) 'Responses of leaf spectral reflectance to plant stress', *American Journal of Botany*, 80(3), pp. 239-243.

Ceccato, P., Flasse, S., Tarantola, S., Jacquemoud, S. and Grégoire, J.-M. (2001) 'Detecting vegetation leaf water content using reflectance in the optical domain', *Remote sensing of environment*, 77(1), pp. 22-33.

Ceccato, P., Gobron, N., Flasse, S., Pinty, B. and Tarantola, S. (2002) 'Designing a Spectral Index to Estimate Vegetation Water Content from Remote Sensing Data: Part 1—Theoretical Approach', *Remote Sensing of Environment*, 82, pp. 188–197.

Chakraborty, A. and Sehgal, V. (2010) 'Assessment of agricultural drought using MODIS derived normalized difference water index', *Journal of Agricultural Physics*, 10, pp. 28-36.

Champagne, C.M., Staenz, K., Bannari, A., McNairn, H. and Deguise, J.-C. (2003) 'Validation of a hyperspectral curve-fitting model for the estimation of plant water content of agricultural canopies', *Remote Sensing of Environment*, 87(2-3), pp. 148-160.

Chavana-Bryant, C., Malhi, Y., Wu, J., Asner, G.P., Anastasiou, A., Enquist, B.J., Caravasi, C., Eric, G., Doughty, C.E. and Saleska, S.R. (2016) 'Leaf aging of Amazonian canopy trees as revealed by spectral and physiochemical measurements', *New Phytologist*, 214(3), pp. 1049-1063.

Chaves, M.M., Maroco, J.P. and Pereira, J.S. (2003) 'Understanding plant responses to drought—from genes to the whole plant', *Functional plant biology*, 30(3), pp. 239-264.

Chazdon, R.L. and Fetcher, N. (1984) 'Photosynthetic light environments in a lowland tropical rain forest in Costa Rica', *The Journal of Ecology*, pp. 553-564.

Chen, D., Huang, J. and Jackson, T.J. (2005) 'Vegetation water content estimation for corn and soybeans using spectral indices derived from MODIS near-and short-wave infrared bands', *Remote Sensing of Environment*, 98(2-3), pp. 225-236.

Chen, K.C. and Wang, C.K. (2016) 'Evaluation of Forest Canopy and Understory Gap Fraction Derived from Terrestrial Laser Scanning', *ISPRS-International Archives of the Photogrammetry, Remote Sensing and Spatial Information Sciences*, pp. 589-591.

Chen, Y., Räikkönen, E., Kaasalainen, S., Suomalainen, J., Hakala, T., Hyyppä, J. and Chen, R. (2010) 'Two-channel hyperspectral LiDAR with a supercontinuum laser source', *Sensors*, 10(7), pp. 7057-7066.

Cheng, Y.-B., Ustin, S.L., Riaño, D. and Vanderbilt, V.C. (2008a) 'Water content estimation from hyperspectral images and MODIS indexes in Southeastern Arizona', *Remote Sensing of Environment*, 112(2), pp. 363-374.

Cheng, Y.B., Ustin, S.L., Riano, D. and Vanderbilt, V.C. (2008b) 'Water Content Estimation from Hyperspectral Images and MODIS Indexes in South-eastern Arizona', *Remote Sensing of Environment*, 112(2), pp. 363–374.

Chone, X., Van Leeuwen, C., Dubourdieu, D. and Gaudillère, J.P. (2001) 'Stem water potential is a sensitive indicator of grapevine water status', *Annals of botany*, 87(4), pp. 477-483.

Chuvieco, E., Cocero, D., Aguado, I., Palacios, A. and Prado, E. (2004a) 'Improving burning efficiency estimates through satellite assessment of fuel moisture content', *Journal of Geophysical Research: Atmospheres*, 109(D14).

Chuvieco, E., Cocero, D., Riano, D., Martin, P., Martınez-Vega, J., de la Riva, J. and Perez, F. (2004b) 'Combining NDVI and surface temperature for the estimation of live fuel moisture content in forest fire danger rating', *Remote Sensing of Environment*, 92(3), pp. 322-331.

Chuvieco, E., Deshayes, M., Stach, N., Cocero, D. and Riaño, D. (1999) 'Short-term fire risk: foliage moisture content estimation from satellite data', in *Remote Sensing of Large Wildfires*. Springer, pp. 17-38.

Chuvieco, E., Wagtendok, J., Riaño, D., Yebra, M. and Ustin, S. (2009) *Estimation of fuel conditions for fire danger assessment*. Berlin Heidelberg: Springer.

Ciganda, V., Gitelson, A. and Schepers, J. (2008) 'Vertical profile and temporal variation of chlorophyll in maize canopy: quantitative crop vigor indicator by means of reflectance-based techniques', *Agronomy Journal*, 100, pp. 1409–1417.

Clevers, J.G.P.W., Kooistra, L. and Schaepman, M.E. (2010) 'Estimating Canopy Water Content Using Hyperspectral Remote Sensing Data', *International Journal of Applied Earth Observation and Geoinformation*, 12, pp. 119–125.

Coble, A.P., VanderWall, B., Mau, A. and Cavaleri, M.A. (2016) 'How vertical patterns in leaf traits shift seasonally and the implications for modeling canopy photosynthesis in a temperate deciduous forest', *Tree Physiology*, 36(9), pp. 1077-1091.

Colombo, R., Meroni, M., Marchesi, A., Busetto, L., Rossini, M., Giardino, C. and Panigada, C. (2008) 'Estimation of Leaf and Canopy Water Content in Poplar Plantations by Means of Hyperspectral Indices and Inverse Modelling', *Remote Sensing of Environment*, 112(4), pp. 1820–1834.

Combal, B., Baret, F., Weiss, M., Trubuil, A., Mace, D., Pragnere, A., Myneni, R., Knyazikhin, Y. and Wang, L. (2003) 'Retrieval of canopy biophysical variables from bidirectional

reflectance: Using prior information to solve the ill-posed inverse problem', *Remote sensing of environment*, 84(1), pp. 1-15.

Côté, J.-F., Widlowski, J.-L., Fournier, R.A. and Verstraete, M.M. (2009) 'The structural and radiative consistency of three-dimensional tree reconstructions from terrestrial lidar', *Remote Sensing of Environment*, 113(5), pp. 1067-1081.

Cote, J.F., Widlowski, J.L., Fournier, R.A. and M., V.M. (2009) 'The structural and radiative consistency of three-dimensional tree reconstructions from terrestrial lidar', *Remote Sensing of Environment*, 113(5), pp. 1067–1081.

Danson, F.M. and Bowyer, P. (2004) 'Estimating live fuel moisture content from remotely sensed reflectance', *Remote Sensing of Environment*, 92(3), pp. 309-321.

Danson, F.M., Gaulton, R., Armitage, R.P., Disney, M., Gunawan, O., Lewis, P., Pearson, G. and Ramirez, A.F. (2014) 'Developing a dual-wavelength full-waveform terrestrial laser scanner to characterize forest canopy structure', *Agricultural and Forest Meteorology*, 198, pp. 7-14.

Danson, F.M., Hetherington, D., Morsdorf, F., Koetz, B. and Allgower, B. (2007) 'Forest canopy gap fraction from terrestrial laser scanning', *IEEE Geoscience and Remote Sensing Letters*, 4(1), pp. 157-160.

Danson, F.M., Sasse, F. and Schofield, L.A. (2018) 'Spectral and spatial information from a novel dual-wavelength full-waveform terrestrial laser scanner for forest ecology', *Interface focus*, 8(2), p. 20170049.

Danson, F.M., Steven, M.D., Malthus, T.J. and Clark, J.A. (1992) 'High-spectral resolution data for determining leaf water content', *International Journal of Remote Sensing*, 13, pp. 461–470.

Darvishzadeh, R., Skidmore, A., Schlerf, M. and Atzberger, C. (2008) 'Inversion of a radiative transfer model for estimating vegetation LAI and chlorophyll in a heterogeneous grassland', *Remote Sensing of Environment*, 112(5), pp. 2592-2604.

Dash, J.P., Watt, M.S., Pearse, G.D., Heaphy, M. and Dungey, H.S. (2017) 'Assessing very high resolution UAV imagery for monitoring forest health during a simulated disease outbreak', *ISPRS Journal of Photogrammetry and Remote Sensing*, 131, pp. 1-14.

Datt, B. (1999) 'Remote sensing of water content in Eucalyptus leaves', *Australian Journal of botany*, 47(6), pp. 909-923.

Dawson, T.P., Curran, P.J. and Plummer, S.E. (1998) 'LIBERTY—Modeling the effects of leaf biochemical concentration on reflectance spectra', *Remote Sensing of Environment*, 65(1), pp. 50-60.

de Castro Oliveira, J., Féret, J.-B., Ponzoni, F.J., Nouvellon, Y., Gastellu-Etchegorry, J.-P., Campoe, O.C., Stape, J.L., Rodriguez, L.C.E. and Le Maire, G. (2017) 'Simulating the canopy reflectance of different eucalypt genotypes with the DART 3-D model', *IEEE Journal of Selected Topics in Applied Earth Observations and Remote Sensing*, 10(11), pp. 4844-4852.

De Jong, S.M., Addink, E.A. and Doelman, J.C. (2014) 'Detecting Leaf Water Content in Mediterranean Trees Using High Resolution Spectrometry', *International Journal of Applied Earth Observation and Geoinformation*, 27, pp. 128-136.

Demarez, V. and Gastellu-Etchegorry, J.P. (2000) 'A Modelling Approach for Studying Forest Chlorophyll Content', *Remote Sensing of Environment*, 71, pp. 226-238.

Dennison, P., Roberts, D.A., Peterson, S.H. and Rechel, J. (2005) 'Use of normalized difference water index for monitoring live fuel moisture', *International journal of remote sensing*, 26(5), pp. 1035-1042.

Disney, M. (2019) 'Terrestrial Li DAR: a three-dimensional revolution in how we look at trees', *New Phytologist*, 222(4), pp. 1736-1741.

Douglas, E.S., Martel, J., Li, Z., Howe, G., Hewawasam, K., Marshall, R.A., Schaaf, C.L., Cook, T.A., Newnham, G.J. and Strahler, A. (2015) 'Finding leaves in the forest: the dual-wavelength Echidna lidar', *IEEE Geoscience and Remote Sensing Letters*, 12(4), pp. 776-780.

Downer, J. (2006) 'Diagnosing your oak tree: Part 1" Diseases"', *Landescapes Notes. University of California*, 19(4), p. 12.

Du, L., Gong, W., Shi, S., Yang, J., Sun, J., Zhu, B. and Song, S. (2016) 'Estimation of rice leaf nitrogen contents based on hyperspectral LIDAR', *International Journal of Applied Earth Observation and Geoinformation*, 44, pp. 136-143.

Du, L., Gong, W. and Yang, J. (2018) 'Application of spectral indices and reflectance spectrum on leaf nitrogen content analysis derived from hyperspectral LiDAR data', *Optics & Laser Technology*, 107, pp. 372-379.

Durrieu, S., Cherchali, S., Costeraste, J., Mondin, L., Debise, H., Chazette, P., Dauzat, J., Gastellu-Etchegorry, J.-P., Baghdadi, N. and Pélissier, R. (2013) *2013 IEEE International Geoscience and Remote Sensing Symposium-IGARSS*. IEEE.

Eastman, J., Sangermano, F., Machado, E., Rogan, J. and Anyamba, A. (2013) 'Global trends in seasonality of normalized difference vegetation index (NDVI), 1982–2011', *Remote Sensing*, 5(10), pp. 4799-4818.

Ehrler, W., Idso, S., Jackson, R.D. and Reginato, R. (1978) 'Wheat Canopy Temperature: Relation to Plant Water Potential 1', *Agronomy Journal*, 70(2), pp. 251-256.

Eitel, J.U.H., Magney, T.S., Vierling, L.A., Brown, T.T. and Huggins, D.R. (2014a) 'LiDAR based biomass and crop nitrogen estimates for rapid, non-destructive assessment of wheat nitrogen status', *Field Crops Research*, 159, pp. 21-32.

Eitel, J.U.H., Magney, T.S., Vierling, L.A. and Dittmar, G. (2014b) 'Assessment of crop foliar nitrogen using a novel dual-wavelength laser system and implications for conducting laser-based plant physiology', *ISPRS Journal of Photogrammetry and Remote Sensing*, 97, pp. 229-240.

Eitel, J.U.H., Vierling, L.A. and Long, D.S. (2010) 'Simultaneous measurements of plant structure and chlorophyll content in broadleaf saplings with a terrestrial laser scanner', *Remote Sensing of Environment*, 114(10), pp. 2229-2237.

Eitel, J.U.H., Vierling, L.A., Long, D.S. and Hunt, E.R. (2011) 'Early season remote sensing of wheat nitrogen status using a green scanning laser', *Agricultural and Forest Meteorology*, 151(10), pp. 1338-1345.

Ellsworth, D. and Reich, P. (1993) 'Canopy structure and vertical patterns of photosynthesis and related leaf traits in a deciduous forest', *Oecologia*, 96(2), pp. 169-178.

Elsherif, A., Gaulton, R. and Mills, J. (2018) 'Estimation of vegetation water content at leaf and canopy level using dual-wavelength commercial terrestrial laser scanners', *Interface Focus*, 8(2), pp. 59-69.

Elsherif, A., Gaulton, R. and Mills, J. (2019a) 'Four Dimensional Mapping of Vegetation Moisture Content Using Dual-Wavelength Terrestrial Laser Scanning', *Remote Sensing*, 11, p. 2311.

Elsherif, A., Gaulton, R. and Mills, J. (2019b) 'Measuring leaf equivalent water thickness of short-rotation coppice willow canopy using terrestrial laser scanning', *IEEE International Geoscience and Remote Sensing Symposium (IGARSS), Yokohama, Japan, 28 July - 2 August*.

Elsherif, A., Gaulton, R. and Mills, J.P. (2019c) 'THE POTENTIAL OF DUAL-WAVELENGTH TERRESTRIAL LASER SCANNING IN 3D CANOPY FUEL MOISTURE CONTENT MAPPING', *Int. Arch. Photogramm. Remote Sens. Spatial Inf. Sci.*, XLII-2/W13, pp. 975-979.

Elsherif, A., Gaulton, R., Shenkin, A., Malhi, Y. and Mills, J. (2019d) 'Three dimensional mapping of forest canopy equivalent water thickness using dual-wavelength terrestrial laser scanning', *Agricultural and Forest Meteorology*, 276, p. 107627.

Eriksson, H.M., Eklundh, L., Kuusk, A. and Nilson, T. (2006) 'Impact of understory vegetation on forest canopy reflectance and remotely sensed LAI estimates', *Remote Sensing of Environment*, 103(4), pp. 408-418.

Eysn, L., Pfeifer, N., Ressl, C., Hollaus, M., Grafl, A. and Morsdorf, F. (2013) 'A practical approach for extracting tree models in forest environments based on equirectangular projections of terrestrial laser scans', *Remote Sensing*, 5(11), pp. 5424-5448.

Fang, W., Huang, X., Zhang, F. and Li, D. (2015) 'Intensity correction of terrestrial laser scanning data by estimating laser transmission function', *IEEE Transactions on Geoscience and Remote Sensing*, 53, no. 2, pp. 942–951.

Farquhar, G.D. and Sharkey, T.D. (1982) 'Stomatal conductance and photosynthesis', *Annual review of plant physiology*, 33(1), pp. 317-345.

Faurtyot, T. and Baret, F. (1997) 'Vegetation water and dry matter contents estimated from top-of-the-atmosphere reflectance data: a simulation study', *Remote Sensing of Environment*, 61(1), pp. 34-45.

Fensholt, R. and Sandholt, I. (2003) 'Derivation of a shortwave infrared water stress index from MODIS near-and shortwave infrared data in a semiarid environment', *Remote Sensing of Environment*, 87(1), pp. 111-121.

Feret, J.-B., François, C., Asner, G.P., Gitelson, A.A., Martin, R.E., Bidel, L.P.R., Ustin, S.L., Le Maire, G. and Jacquemoud, S. (2008) 'PROSPECT-4 and 5: Advances in the leaf optical properties model separating photosynthetic pigments', *Remote sensing of environment*, 112(6), pp. 3030-3043.

Féret, J.-B., le Maire, G., Jay, S., Berveiller, D., Bendoula, R., Hmimina, G., Cheraiet, A., Oliveira, J., Ponzoni, F. and Solanki, T. (2018) 'Estimating leaf mass per area and equivalent water thickness based on leaf optical properties: Potential and limitations of physical modeling and machine learning', *Remote Sensing of Environment*.

Ferreira, M.P., Féret, J.-B., Grau, E., Gastellu-Etchegorry, J.-P., Shimabukuro, Y.E. and de Souza Filho, C.R. (2018) 'Retrieving structural and chemical properties of individual tree crowns in a highly diverse tropical forest with 3D radiative transfer modeling and imaging spectroscopy', *Remote sensing of environment*, 211, pp. 276-291.

Ferretti, M. (1997) 'Forest health assessment and monitoring–issues for consideration', *Environmental monitoring and assessment*, 48(1), pp. 45-72.

Foley, W.J., McIlwee, A., Lawler, I., Aragones, L., Woolnough, A.P. and Berding, N. (1998) 'Ecological applications of near infrared reflectance spectroscopy–a tool for rapid, cost-effective prediction of the composition of plant and animal tissues and aspects of animal performance', *Oecologia*, 116(3), pp. 293-305.

Fourty, T. and Baret, F. (1998) 'On spectral estimates of fresh leaf biochemistry', *International Journal of Remote Sensing*, 19(7), pp. 1283-1297.

Gao, B.C. (1996) 'NDWI – A Normalised Difference Water Index for Remote Sensing of Vegetation Liquid Water from Space', *Remote Sensing of Environment*, 58, pp. 257 – 266.

Gara, T.W., Darvishzadeh, R., Skidmore, A.K. and Wang, T. (2018) 'Impact of vertical canopy position on leaf spectral properties and traits across multiple species', *Remote sensing*, 10(2), p. 346.

García-Herrera, R., Díaz, J., Trigo, R.M., Luterbacher, J. and Fischer, E.M. (2010) 'A review of the European summer heat wave of 2003', *Critical Reviews in Environmental Science and Technology*, 40(4), pp. 267-306.

Gascon, F., Gastellu-Etchegorry, J.-P., Lefevre-Fonollosa, M.-J. and Dufrene, E. (2004) 'Retrieval of forest biophysical variables by inverting a 3-D radiative transfer model and using high and very high resolution imagery', *International Journal of Remote Sensing*, 25(24), pp. 5601-5616.

Gascon, F., Gastellu-Etchegorry, J.-P. and Lefèvre, M.-J. (2001) 'Radiative transfer model for simulating high-resolution satellite images', *IEEE Transactions on Geoscience and Remote Sensing*, 39(9), pp. 1922-1926.

Gastellu-Etchegorry, J.-P., Demarez, V., Pinel, V. and Zagolski, F. (1996) 'Modeling radiative transfer in heterogeneous 3-D vegetation canopies', *Remote sensing of environment*, 58(2), pp. 131-156.

Gastellu-Etchegorry, J.-P., Yin, T., Lauret, N., Cajgfinger, T., Gregoire, T., Grau, E., Feret, J.-B., Lopes, M., Guilleux, J. and Dedieu, G. (2015) 'Discrete Anisotropic Radiative Transfer (DART 5) for modeling airborne and satellite spectroradiometer and LIDAR acquisitions of natural and urban landscapes', *Remote Sensing*, 7(2), pp. 1667-1701.

Gastellu-Etchegorry, J., Guillevic, P., Zagolski, F., Demarez, V., Trichon, V., Deering, D. and Leroy, M. (1999) 'Modeling BRF and radiation regime of boreal and tropical forests: I. BRF', *Remote Sensing of Environment*, 68(3), pp. 281-316.

Gastellu-Etchegorry, J., Martin, E. and Gascon, F. (2004) 'DART: a 3D model for simulating satellite images and studying surface radiation budget', *International journal of remote sensing*, 25(1), pp. 73-96.

Gaulton, R., Danson, F.M., Ramirez, F.A. and Gunawan, O. (2013) 'The potential of dual-wavelength laser scanning for estimating vegetation moisture content', *Remote Sensing of Environment*, 132, pp. 32-39.

Gaulton, R., Taylor, J. and Watkins, N. (2015) 'Unmanned Aerial Vehicles for Pre-Harvest Biomass Estimation in Willow (Salix spp.) Coppice Plantations', *ISPRS Geospatial Week*.

Gausman, H.W. (1977) 'Reflectance of leaf components', *Remote sensing of Environment*, 6(1), pp. 1-9.

Goel, N.S. and Thompson, R.L. (2000) 'A snapshot of canopy reflectance models and a universal model for the radiation regime', *Remote Sensing Reviews*, 18(2-4), pp. 197-225.

Grau, E. and Gastellu-Etchegorry, J.-P. (2013) 'Radiative transfer modeling in the Earth–Atmosphere system with DART model', *Remote Sensing of Environment*, 139, pp. 149-170.

Greaves, H.E., Vierling, L.A., Eitel, J.U.H., Boelman, N.T., Magney, T.S., Prager, C.M. and Griffin, K.L. (2015) 'Estimating aboveground biomass and leaf area of low-stature Arctic shrubs with terrestrial LiDAR', *Remote Sensing of Environment*, 164, pp. 26-35.

Große-Stoltenberg, A., Hellmann, C., Werner, C., Oldeland, J. and Thiele, J. (2016) 'Evaluation of continuous VNIR-SWIR spectra versus narrowband hyperspectral indices to discriminate the invasive Acacia longifolia within a Mediterranean dune ecosystem', *Remote Sensing*, 8(4), p. 334.

Guillevic, P. and Gastellu-Etchegorry, J. (1999) 'Modeling BRF and radiation regime of boreal and tropical forest: II. PAR regime', *Remote Sensing of Environment*, 68(3), pp. 317-340.

Gutschick, V.P. and Wiegel, F.W. (1988) 'Optimizing the canopy photosynthetic rate by patterns of investment in specific leaf mass', *The American Naturalist*, 132(1), pp. 67-86.

Guyot, G., Guyon, D. and Riom, J. (1989) 'Factors affecting the spectral response of forest canopies: a review', *Geocarto International*, 4(3), pp. 3-18.

Hackenberg, J., Spiecker, H., Calders, K., Disney, M. and Raumonen, P. (2015) 'SimpleTree—an efficient open source tool to build tree models from TLS clouds', *Forests*, 6(11), pp. 4245-4294.

Hakala, T., Nevalainen, O., Kaasalainen, S. and Mäkipää, R. (2015) 'Technical Note: Multispectral lidar time series of pine canopy chlorophyll content', *Biogeosciences*, 12(5), pp. 1629-1634.

Hakala, T., Suomalainen, J., Kaasalainen, S. and Chen, Y. (2012) 'Full waveform hyperspectral LiDAR for terrestrial laser scanning', *Optics express*, 20(7), pp. 7119-7127.

Hancock, S., Gaulton, R. and Danson, F.M. (2017) 'Angular reflectance of leaves with a dual-wavelength terrestrial lidar and its implications for leaf-bark separation and leaf moisture estimation', *IEEE Transactions on Geoscience and Remote Sensing*, 55(6), pp. 3084 - 3090.

Hancock, S., Lewis, P., Foster, M., Disney, M. and Muller, J.-P. (2012) 'Measuring forests with dual wavelength lidar: A simulation study over topography', *Agricultural and Forest Meteorology*, 161, pp. 123-133.

Hardisky, M., Klemas, V. and Smart, M. (1983) 'The influence of soil salinity, growth form, and leaf moisture on the spectral radiance of', *Spartina alterniflora*, 49, pp. 77-83.

He, L., Zhang, H.-Y., Zhang, Y.-S., Song, X., Feng, W., Kang, G.-Z., Wang, C.-Y. and Guo, T.-C. (2016) 'Estimating canopy leaf nitrogen concentration in winter wheat based on multi-angular hyperspectral remote sensing', *European Journal of Agronomy*, 73, pp. 170-185.

Henning, J.G. and Radtke, P.J. (2006) 'Ground-based laser imaging for assessing three-dimensional forest canopy structure', *Photogrammetric Engineering & Remote Sensing*, 72(12), pp. 1349-1358.

Hernández-Clemente, R., Navarro-Cerrillo, R.M. and Zarco-Tejada, P.J. (2012) 'Carotenoid content estimation in a heterogeneous conifer forest using narrow-band indices and PROSPECT+ DART simulations', *Remote Sensing of Environment*, 127, pp. 298-315.

Herrera, C.M. and Bazaga, P. (2013) 'Epigenetic correlates of plant phenotypic plasticity: DNA methylation differs between prickly and nonprickly leaves in heterophyllous Ilex aquifolium (Aquifoliaceae) trees', *Botanical Journal of the Linnean Society*, 171(3), pp. 441-452.

Hikosaka, K. (2004) 'Leaf canopy as a dynamic system: ecophysiology and optimality in leaf turnover', *Annals of botany*, 95(3), pp. 521-533.

Hilker, T., van Leeuwen, M., Coops, N.C., Wulder, M.A., Newnham, G.J., Jupp, D.L. and Culvenor, D.S. (2010) 'Comparing canopy metrics derived from terrestrial and airborne laser scanning in a Douglas-fir dominated forest stand', *Trees*, 24(5), pp. 819-832.

Hirose, T. and Werger, M. (1987) 'Maximizing daily canopy photosynthesis with respect to the leaf nitrogen allocation pattern in the canopy', *Oecologia*, 72(4), pp. 520-526.

Höfle, B. (2014) 'Radiometric correction of terrestrial LiDAR point cloud data for individual maize plant detection', *IEEE Geoscience and Remote Sensing Letters*, 11 (1), pp. 94–98.

Höfle, B. and Pfeifer, N. (2007) 'Correction of laser scanning intensity data: Data and model-driven approaches', *ISPRS Journal of Photogrammetry and Remote Sensing*, 62(6), pp. 415-433.

Honkavaara, E., Saari, H., Kaivosoja, J., Pölönen, I., Hakala, T., Litkey, P., Mäkynen, J. and Pesonen, L. (2013) 'Processing and assessment of spectrometric, stereoscopic imagery collected using a lightweight UAV spectral camera for precision agriculture', *Remote Sensing*, 5(10), pp. 5006-5039.

Horst, R.K. and Horst, R.K. (2013) 'Anthracnose', *Westcott's Plant Disease Handbook*, pp. 59-67.

Hosgood, B., Jacquemoud, S., Andreoli, G., Verdebout, J., Pedrini, G. and Schmuck, G. (1995) 'Leaf optical properties experiment 93 (LOPEX93)', *Report EUR*, 16095.

Huemmrich, K. (2001) 'The GeoSail model: a simple addition to the SAIL model to describe discontinuous canopy reflectance', *Remote Sensing of Environment*, 75(3), pp. 423-431.

Hunt, E.R., Friedman, J., Cosh, M., Li, L., Gaiser, P. and Twarog, E. (2017) *2017 6th International Conference on Agro-Geoinformatics*. IEEE.

Hunt, J.E. and Rock, B. (1989) 'Detection of Changes in Leaf Water Content Using Near- And Middle-Infrared Reflectance', *Remote Sensing of Environment*, 30, pp. 43-54.

Hunt Jr, E.R., Daughtry, C.S.T. and Li, L. (2016) 'Feasibility of estimating leaf water content using spectral indices from WorldView-3's near-infrared and shortwave infrared bands', *International Journal of Remote Sensing*, 37(2), pp. 388-402.

Hunt Jr, E.R., Rock, B.N. and Nobel, P.S. (1987) 'Measurement of leaf relative water content by infrared reflectance', *Remote sensing of environment*, 22(3), pp. 429-435.

Idso, S., Reginato, R., Jackson, R. and Pinter, j.P. (1981) 'Measuring yield-reducing plant water potential depressions in wheat by infrared thermometry', *Irrigation Science*, 2(4), pp. 205-212.

Illera, P., Fernandez, A. and Delgado, J. (1996) 'Temporal evolution of the NDVI as an indicator of forest fire danger', *International Journal of remote sensing*, 17(6), pp. 1093-1105.

Jackson, T. (2004) 'Vegetation Water Content Mapping Using Landsat Data Derived Normalized Difference Water Index for Corn and Soybeans', *Remote Sensing of Environment*, 92, pp. 475-482.

Jacquemoud, S. and Baret, F. (1990) 'PROSPECT—A Model of Leaf Optical-Properties Spectra', *Remote Sensing of Environment*, 34, pp. 75–91.

Jacquemoud, S., Baret, F., Andrieu, B., Danson, F. and Jaggard, K. (1995) 'Extraction of vegetation biophysical parameters by inversion of the PROSPECT+ SAIL models on sugar beet canopy reflectance data. Application to TM and AVIRIS sensors', *Remote sensing of environment*, 52(3), pp. 163-172.

Jacquemoud, S., Verhoef, W., Baret, F., Bacour, C., Zarco-Tejada, P.J., Asner, G.P., François, C. and Ustin, S.L. (2009) 'PROSPECT+ SAIL models: A review of use for vegetation characterization', *Remote sensing of environment*, 113, pp. S56-S66.

Jarvis, P. (1976) 'The interpretation of the variations in leaf water potential and stomatal conductance found in canopies in the field', *Philosophical Transactions of the Royal Society of London. B, Biological Sciences*, 273(927), pp. 593-610.

Jarvis, P.G. and McNaughton, K. (1986) 'Stomatal control of transpiration: scaling up from leaf to region', in *Advances in ecological research*. United Kingdom: Elsevier, pp. 1-49.

Jasinski, M.F. and Eagleson, P.S. (1989) 'The structure of red-infrared scattergrams of semivegetated landscapes', *IEEE Transactions on Geoscience and Remote Sensing*, 27(4), pp. 441-451.

Jelalian, A.V. (1992) *Laser radar systems*. Artech House.

Jonckheere, I., Fleck, S., Nackaerts, K., Muys, B., Coppin, P., Weiss, M. and Baret, F. (2004) 'Review of methods for in situ leaf area index determination: Part I. Theories, sensors and hemispherical photography', *Agricultural and forest meteorology*, 121(1-2), pp. 19-35.

Jones, H. and Tardieu, F. (1998) 'Modelling water relations of horticultural crops: a review', *Scientia Horticulturae*, 74(1-2), pp. 21-46.

Jones, H.G. and Vaughan, R.A. (2010) *Remote sensing of vegetation: principles, techniques, and applications*. Oxford university press.

Junttila, S., Holopainen, M., Vastaranta, M., Lyytikäinen-Saarenmaa, P., Kaartinen, H., Hyyppä, J. and Hyyppä, H. (2019) 'The potential of dual-wavelength terrestrial lidar in early detection of Ips typographus (L.) infestation–Leaf water content as a proxy', *Remote Sensing of Environment*, 231, p. 111264.

Junttila, S., Sugano, J., Vastaranta, M., Linnakoski, R., Kaartinen, H., Kukko, A., Holopainen, M., Hyyppä, H. and Hyyppä, J. (2018) 'Can Leaf Water Content Be Estimated Using Multispectral Terrestrial Laser Scanning? A Case Study With Norway Spruce Seedlings', *Frontiers in plant science*, 9, p. 299.

Junttila, S., Vastaranta, M., Liang, X., Kaartinen, H., Kukko, A., Kaasalainen, S., Holopainen, M., Hyyppä, H. and Hyyppä, J. (2016) 'Measuring Leaf Water Content with Dual-Wavelength Intensity Data from Terrestrial Laser Scanners', *Remote Sensing*, 9(1), p. 8.

Jurdao, S., Yebra, M., Guerschman, J.P. and Chuvieco, E. (2013) 'Regional Estimation of Woodland Moisture Content by Inverting Radiative Transfer Models', *Remote Sensing of Environment*, 132, pp. 59–70.

Jutzi, B. and Gross, H. (2009) 'Normalization of LiDAR intensity data based on range and surface incidence angle', *ISPRS International Archives of the Photogrammetry, Remote Sensing and Spatial Information Sciences*, 38, pp. 213–218.

Kaasalainen, S., Åkerblom, M., Nevalainen, O., Hakala, T. and Kaasalainen, M. (2018) 'Uncertainty in multispectral lidar signals caused by incidence angle effects', *Interface focus*, 8(2), p. 20170033.

Kaasalainen, S., Jaakkola, A., Kaasalainen, M., Krooks, A. and Kukko, A. (2011) 'Analysis of incidence angle and distance effects on terrestrial laser scanner intensity: Search for correction methods', *Remote Sensing*, 3(10), pp. 2207-2221.

Kaasalainen, S., Krooks, A., Kukko, A. and Kaartinen, H. (2009) 'Radiometric calibration of terrestrial laser scanners with external reference targets', *Remote Sensing*, 1(3), pp. 144-158.

Kaasalainen, S., Krooks, A., Liski, J., Raumonen, P., Kaartinen, H., Kaasalainen, M., Puttonen, E., Anttila, K. and Mäkipää, R. (2014) 'Change detection of tree biomass with terrestrial laser scanning and quantitative structure modelling', *Remote Sensing*, 6(5), pp. 3906-3922.

Kaasalainen, S., Nevalainen, O., Hakala, T. and Anttila, K. (2016) 'Incidence Angle Dependency of Leaf Vegetation Indices from Hyperspectral Lidar Measurements', *Photogrammetrie-Fernerkundung-Geoinformation*, 2016(2), pp. 75-84.

Kashani, A., Olsen, M., Parrish, C. and Wilson, N. (2015) 'A review of LiDAR radiometric processing: From ad hoc intensity correction to rigorous radiometric calibration', *Sensors*, 15(11), pp. 28099-28128.

Kazhdan, M. and Hoppe, H. (2013) 'Screened poisson surface reconstruction', *ACM Transactions on Graphics (ToG)*, 32(3), p. 29.

Keating, B.A. and Wafula, B.M. (1992) 'Modelling the Fully Expanded Area of Maize Leaves', *Field Crops Research*, 29, pp. 163–176.

Kiehl, J.T. and Trenberth, K.E. (1997) 'Earth's annual global mean energy budget', *Bulletin of the American Meteorological Society*, 78(2), pp. 197-208.

Knipling, E.B. (1970) 'Physical and physiological basis for the reflectance of visible and near-infrared radiation from vegetation', *Remote sensing of environment*, 1(3), pp. 155-159.

Koetz, B., Morsdorf, F., van der Linden, S., Curt, T. and Allgöwer, B. (2008) 'Multi-source land cover classification for forest fire management based on imaging spectrometry and LiDAR data', *Forest Ecology and Management*, 256, pp. 263–271.

Kötz, B., Schaepman, M., Morsdorf, F., Bowyer, P., Itten, K. and Allgöwer, B. (2004) 'Radiative transfer modeling within a heterogeneous canopy for estimation of forest fire fuel properties', *Remote Sensing of Environment*, 92(3), pp. 332-344.

Kozlowski, T.T. and Pallardy, S.G. (1996) *Physiology of woody plants*. Elsevier.

Krooks, A., Kaasalainen, M., Hakala, T. and Nevalainen, O. (2013) 'Correction of Intensity Incidence Angle Effect in Terrestrial Laser Scanning', *ISPRS Annals of the Photogrammetry, Remote Sensing and Spatial Information Sciences*, II-5/W2(2), pp. 145-150.

Kuusk, A. (2001) 'A two-layer canopy reflectance model', *Journal of Quantitative Spectroscopy and Radiative Transfer*, 71(1), pp. 1-9.

Landry, S., St-Laurent, M.-H., Nelson, P.R., Pelletier, G. and Villard, M.-A. (2018) 'Canopy Cover Estimation from Landsat Images: Understory Impact onTop-of-canopy Reflectance in a Northern Hardwood Forest', *Canadian Journal of Remote Sensing*, pp. 1-12.

Laurin, G.V., Ding, J., Disney, M., Bartholomeus, H., Herold, M., Papale, D. and Valentini, R. (2019) 'Tree height in tropical forest as measured by different ground, proximal, and remote sensing instruments, and impacts on above ground biomass estimates', *International Journal of Applied Earth Observation and Geoinformation*, 82, p. 101899.

Lawlor, D.W. and Cornic, G. (2002) 'Photosynthetic carbon assimilation and associated metabolism in relation to water deficits in higher plants', *Plant, cell & environment*, 25(2), pp. 275-294.

Leinonen, I., Grant, O., Tagliavia, C., Chaves, M. and Jones, H. (2006) 'Estimating stomatal conductance with thermal imagery', *Plant, Cell & Environment*, 29(8), pp. 1508-1518.

Lewis, S.L., Edwards, D.P. and Galbraith, D. (2015) 'Increasing human dominance of tropical forests', *Science*, 349(6250), pp. 827-832.

Li, P. and Wang, Q. (2011) 'Retrieval of leaf biochemical parameters using PROSPECT inversion: A new approach for alleviating ill-posed problems', *IEEE Transactions on Geoscience and Remote Sensing*, 49(7), pp. 2499-2506.

Li, W., Niu, Z., Sun, G., Gao, S. and Wu, M. (2016) 'Deriving backscatter reflective factors from 32-channel full-waveform LiDAR data for the estimation of leaf biochemical contents', *Optics Express*, 24(5), pp. 4771-4785.

Li, W., Sun, G., Niu, Z., Gao, S. and Qiao, H. (2014) 'Estimation of leaf biochemical content using a novel hyperspectral full-waveform LiDAR system', *Remote Sensing Letters*, 5(8), pp. 693-702.

Li, Z., Schaefer, M., Strahler, A., Schaaf, C. and Jupp, D. (2018) 'On the utilization of novel spectral laser scanning for three-dimensional classification of vegetation elements', *Interface focus*, 8(2), p. 20170039.

Lichtenthaler, H.K., Buschmann, C., Döll, M., Fietz, H.J., Bach, T., Kozel, U., Meier, D. and Rahmsdorf, U. (1981) 'Photosynthetic activity, chloroplast ultrastructure, and leaf characteristics of high-light and low-light plants and of sun and shade leaves', *Photosynthesis research*, 2(2), pp. 115-141.

Lillesaeter, O. (1982) 'Spectral reflectance of partly transmitting leaves: laboratory measurements and mathematical modeling', *Remote Sensing of Environment*, 12(3), pp. 247-254.

Liu, L.-y., Huang, W.-j., Pu, R.-l. and Wang, J.-h. (2014) 'Detection of internal leaf structure deterioration using a new spectral ratio index in the near-infrared shoulder region', *Journal of Integrative Agriculture*, 13(4), pp. 760-769.

Liu, L., Zhang, S. and Zhang, B. (2016) 'Evaluation of hyperspectral indices for retrieval of canopy equivalent water thickness and gravimetric water content', *International Journal of Remote Sensing*, 37(14), pp. 3384-3399.

Liu, S., Peng, Y., Wei, D., Le, Y. and Li, L. (2015) 'Remote Estimation of Leaf and Canopy Water Content in Winter Wheat with Different Vertical Distribution of Water-Related Properties', *Remote Sensing*, 7, pp. 4626-4650.

Lovell, J.L., Jupp, D.L.B., Newnham, G.J. and Culvenor, D.S. (2011) 'Measuring tree stem diameters using intensity profiles from ground-based scanning lidar from a fixed viewpoint.', *ISPRS Journal of Photogrammetry and Remote Sensing*, 66, pp. 46–55.

Ma, L. and Upadhyaya, M. (2018) 'Effects of leaf position on reflectance, transmittance and absorption of red and far-red light in tomato, Chenopodium album and Amaranthus retroflexus leaves', *Weed research*, 58(1), pp. 17-24.

Ma, L., Zheng, G., Eitel, J.U.H., Magney, T.S. and Moskal, L.M. (2016) 'Determining woody-to-total area ratio using terrestrial laser scanning (TLS)', *Agricultural and Forest Meteorology*, 228, pp. 217-228.

Magney, T.S., Eusden, S.A., Eitel, J.U.H., Logan, B.A., Jiang, J. and Vierling, L.A. (2014) 'Assessing leaf photoprotective mechanisms using terrestrial LiDAR: towards mapping canopy photosynthetic performance in three dimensions', *New Phytologist*, 201(1), pp. 344-356.

Maki, M., Ishiahra, M. and Tamura, M. (2004) 'Estimation of leaf water status to monitor the risk of forest fires by using remotely sensed data', *Remote Sensing of Environment*, 90(4), pp. 441-450.

Malenovský, Z., Homolová, L., Zurita-Milla, R., Lukeš, P., Kaplan, V., Hanuš, J., Gastellu-Etchegorry, J.-P. and Schaepman, M.E. (2013) 'Retrieval of spruce leaf chlorophyll content from airborne image data using continuum removal and radiative transfer', *Remote Sensing of Environment*, 131, pp. 85-102.

Malenovský, Z., Martin, E., Homolová, L., Gastellu-Etchegorry, J.-P., Zurita-Milla, R., Schaepman, M.E., Pokorný, R., Clevers, J.G. and Cudlín, P. (2008) 'Influence of woody elements of a Norway spruce canopy on nadir reflectance simulated by the DART model at very high spatial resolution', *Remote Sensing of Environment*, 112(1), pp. 1-18.

McCutchan, H. and Shackel, K. (1992) 'Stem-water potential as a sensitive indicator of water stress in prune trees (Prunus domestica L. cv. French)', *Journal of the American Society for Horticultural Science*, 117(4), pp. 607-611.

McDowell, N., Pockman, W.T., Allen, C.D., Breshears, D.D., Cobb, N., Kolb, T., Plaut, J., Sperry, J., West, A. and Williams, D.G. (2008) 'Mechanisms of plant survival and mortality during drought: why do some plants survive while others succumb to drought?', *New phytologist*, 178(4), pp. 719-739.

McDowell, N.G., Fisher, R.A., Xu, C., Domec, J., Hölttä, T., Mackay, D.S., Sperry, J.S., Boutz, A., Dickman, L. and Gehres, N. (2013) 'Evaluating theories of drought-induced vegetation mortality using a multimodel–experiment framework', *New Phytologist*, 200(2), pp. 304-321.

McMahon, S.M., Bebber, D.P., Butt, N., Crockatt, M., Kirby, K., Parker, G.G., Riutta, T. and Slade, E.M. (2015) 'Ground based LiDAR demonstrates the legacy of management history to canopy structure and composition across a fragmented temperate woodland', *Forest Ecology and Management*, 335, pp. 255-260.

Meentemeyer, R.K., Anacker, B.L., Mark, W. and Rizzo, D.M. (2008) 'Early detection of emerging forest disease using dispersal estimation and ecological niche modeling', *Ecological Applications*, 18(2), pp. 377-390.

Mendiguren, G., Pilar Martín, M., Nieto, H., Pacheco-Labrador, J. and Jurdao, S. (2015) 'Seasonal variation in grass water content estimated from proximal sensing and MODIS time series in a Mediterranean Fluxnet site', *Biogeosciences*, 12(18), pp. 5523-5535.

Meng, Y., Meng, F., Wu, J. and Lin, W. (2019) 'Comparison of four methods for estimating leaf area index based on terrestrial three-dimensional laser scanning', *Journal of Sustainable Forestry*, 38(3), pp. 244-261.

Millar, C.I. and Stephenson, N.L. (2015) 'Temperate forest health in an era of emerging megadisturbance', *Science*, 349(6250), pp. 823-826.

Miller, J.R., White, H.P., Chen, J.M., Peddle, D.R., McDermid, G., Fournier, R.A., Shepherd, P., Rubinstein, I., Freemantle, J. and Soffer, R. (1997) 'Seasonal change in understory reflectance of boreal forests and influence on canopy vegetation indices', *Journal of Geophysical Research: Atmospheres*, 102(D24), pp. 29475-29482.

Mirzaie, M., Darvishzadeh, R., Shakiba, A., Matkan, A.A., Atzberger, C. and Skidmore, A. (2014) 'Comparative Analysis of Different Uni- and Multi-variate Methods for Estimation of Vegetation Water Content Using Hyper-spectral Measurements', *International Journal of Applied Earth Observation and Geoinformation*, 26, pp. 1–11.

Mitchell, D., Kornhuber, K., Huntingford, C. and Uhe, P. (2019) 'The day the 2003 European heatwave record was broken', *The Lancet Planetary Health*, 3(7), pp. e290-e292.

Moghaddam, M. and Saatchi, S.S. (1999) 'Monitoring tree moisture using an estimation algorithm applied to SAR data from BOREAS', *IEEE Transactions on Geoscience and Remote Sensing*, 37(2), pp. 901-916.

Mooney, H., Ehleringer, J. and Björkman, O. (1977) 'The energy balance of leaves of the evergreen desert shrub Atriplex hymenelytra.', *Oecologia*, 29, pp. 301–310.

Moorthy, I., Miller, J.R., Hu, B., Chen, J. and Li, Q. (2008) 'Retrieving crown leaf area index from an individual tree using ground-based lidar data', *Canadian Journal of Remote Sensing*, 34(3), pp. 320-332.

Moran, E., Lauder, J., Musser, C., Stathos, A. and Shu, M. (2017) 'The genetics of drought tolerance in conifers', *New Phytologist*, 216(4), pp. 1034-1048.

Morecroft, M.D., Stokes, V.J., Taylor, M.E. and Morison, J.I.L. (2008) 'Effects of climate and management history on the distribution and growth of sycamore (Acer pseudoplatanus L.) in a southern British woodland in comparison to native competitors', *Forestry*, 81(1), pp. 59-74.

Morecroft, M.D., Taylor, M.E., Ellwood, S.A. and Quinn, S.A. (2001) 'Impacts of deer herbivory on ground vegetation at Wytham Woods, central England', *Forestry*, 74(3), pp. 251-257.

Moskal, L.M. and Zheng, G. (2011) 'Retrieving forest inventory variables with terrestrial laser scanning (TLS) in urban heterogeneous forest', *Remote Sensing*, 4(1), pp. 1-20.

Nelson Jr, R.M. (2001) 'Water relations of forest fuels', in *Forest fires*. Elsevier, pp. 79-149.

Neto, A.J.S., de Carvalho Lopes, D., da Silva, T.G.F., Ferreira, S.O. and Grossi, J.A.S. (2016) 'Estimation of leaf water content in sunflower under drought conditions by means of spectral reflectance', *Engineering in Agriculture, Environment and Food*.

Nevalainen, O., Hakala, T., Suomalainen, J., Mäkipää, R., Peltoniemi, M., Krooks, A. and Kaasalainen, S. (2014) 'Fast and nondestructive method for leaf level chlorophyll estimation using hyperspectral LiDAR', *Agricultural and Forest Meteorology*, 198, pp. 250-258.

Newnham, G.J., Armston, J.D., Calders, K., Disney, M.I., Lovell, J.L., Schaaf, C.B., Strahler, A.H. and Danson, F.M. (2015) 'Terrestrial laser scanning for plot-scale forest measurement', *Current Forestry Reports*, 1(4), pp. 239-251.

Nilsson, H. (1991) 'Hand-held radiometry and IR-thermography of plant diseases in field plot experiments', *International Journal of Remote Sensing*, 12(3), pp. 545-557.

Njoku, E.G. and Entekhabi, D. (1996) 'Passive microwave remote sensing of soil moisture', *Journal of hydrology*, 184(1-2), pp. 101-129.

North, P.R.J. (1996) 'Three-dimensional forest light interaction model using a Monte Carlo method', *IEEE Transactions on geoscience and remote sensing*, 34(4), pp. 946-956.

Olofsson, K., Holmgren, J. and Olsson, H. (2014) 'Tree stem and height measurements using terrestrial laser scanning and the ransac algorithm', *Remote Sensing*, 6(5), pp. 4323-4344.

Orémusová, E., Makovická Osvaldová, L. and Osvald, A. (2012) 'Gross calorific value of leaves, bark, and branches of selected deciduous trees'.

Paltridge, G. and Barber, J. (1988) 'Monitoring grassland dryness and fire potential in Australia with NOAA/AVHRR data', *Remote Sensing of Environment*, 25(3), pp. 381-394.

Pan, Y., Birdsey, R.A., Fang, J., Houghton, R., Kauppi, P.E., Kurz, W.A., Phillips, O.L., Shvidenko, A., Lewis, S.L. and Canadell, J.G. (2011) 'A large and persistent carbon sink in the world's forests', *Science*, p. 1201609.

Parker, G.G., Lefsky, M.A. and Harding, D.J. (2001) 'Light transmittance in forest canopies determined using airborne laser altimetry and in-canopy quantum measurements', *Remote Sensing of Environment*, 76(3), pp. 298-309.

Penasa, L., Franceschi, M., Preto, N., Teza, G. and Polito, V. (2014) 'Integration of intensity textures and local geometry descriptors from Terrestrial Laser Scanning to map chert in outcrops', *ISPRS Journal of Photogrammetry and Remote Sensing*, 93, pp. 88–97.

Peñuelas, J., Filella, I., Biel, C., Serrano, L. and Save, R. (1993) 'The reflectance at the 950–970 nm region as an indicator of plant water status', *International journal of remote sensing*, 14(10), pp. 1887-1905.

Peñuelas, J., Gamon, J., Fredeen, A., Merino, J. and Field, C. (1994) 'Reflectance indices associated with physiological changes in nitrogen-and water-limited sunflower leaves', *Remote sensing of Environment*, 48(2), pp. 135-146.

Peñuelas, J., Savé, R., Marfà, O. and Serrano, L. (1992) 'Remotely measured canopy temperature of greenhouse strawberries as indicator of water status and yield under mild and very mild water stress conditions', *Agricultural and Forest Meteorology*, 58(1-2), pp. 63-77.

Pettorelli, N., Vik, J.O., Mysterud, A., Gaillard, J.-M., Tucker, C.J. and Stenseth, N.C. (2005) 'Using the satellite-derived NDVI to assess ecological responses to environmental change', *Trends in ecology & evolution*, 20(9), pp. 503-510.

Pfeifer, N., Gorte, B. and Winterhalder, D. (2004) *Proceedings of 20th ISPRS Congress*. ISPRS Istanbul.

Pfeifer, N., Höfle, B., Briese, C., Rutzinger, M. and Haring, A. (2008) 'Analysis of the backscattered energy in terrestrial laser scanning data', *Int. Arch. Photogramm. Remote Sens. Spat. Inf. Sci*, 37, pp. 1045-1052.

Pinty, B., Gobron, N., Widlowski, J.L., Gerstl, S.A., Verstraete, M.M., Antunes, M., Bacour, C., Gascon, F., Gastellu, J.P. and Goel, N. (2001) 'Radiation transfer model intercomparison (RAMI) exercise', *Journal of Geophysical Research: Atmospheres*, 106(D11), pp. 11937-11956.

Pinty, B., Widlowski, J.L., Taberner, M., Gobron, N., Verstraete, M., Disney, M., Gascon, F., Gastellu, J.P., Jiang, L. and Kuusk, A. (2004) 'Radiation Transfer Model Intercomparison (RAMI) exercise: Results from the second phase', *Journal of Geophysical Research: Atmospheres*, 109(D6).

Pitkänen, T.P., Raumonen, P. and Kangas, A. (2019) 'Measuring stem diameters with TLS in boreal forests by complementary fitting procedure', *ISPRS journal of photogrammetry and remote sensing*, 147, pp. 294-306.

Pokorny, J.D. (2015) 'How to recognize common diseases of oaks in the Midwest', *NA-FR; 01-15*.

Poorter, H., Niinemets, Ü., Poorter, L., Wright, I.J. and Villar, R. (2009) 'Causes and consequences of variation in leaf mass per area (LMA): a meta-analysis', *New Phytologist*, 182(3), pp. 565-588.

Proisy, C., Barbier, N., Guéroult, M., Pélissier, R., Gastellu-Etchegorry, J.-P., Grau, E. and Couteron, P. (2012) 'Biomass prediction in tropical forests: the canopy grain approach', in *Remote Sensing of Biomass-Principles and Applications*. IntechOpen.

Pu, R., Gong, P., Biging, G.S. and Larrieu, M.R. (2003) 'Extraction of Red Edge Optical Parameters from Hyperion Data for Estimation of Forest Leaf Area Index', *IEEE Transactions on Geoscience and Remote Sensing*, 41(4), pp. 916–921.

Qi, S.H., Zhang, Y.P., Niu, Z., Wang, C.Y. and Zheng, L. (2005) 'Application of Water Deficit Index in Drought Monitoring in China with Remote Sensing', *Acta Pedologica Sinica*, 42(3), pp. 367-372.

Quan, X., He, B., Yebra, M., Yin, C., Liao, Z. and Li, X. (2017) 'Retrieval of forest fuel moisture content using a coupled radiative transfer model', *Environmental Modelling & Software*, 95, pp. 290-302.

Ramirez, F.A., Armitage, R.P. and Danson, F.M. (2013) 'Testing the application of terrestrial laser scanning to measure forest canopy gap fraction', *Remote Sensing*, 5 (6), pp. 3037–3056.

Raumonen, P., Casella, E., Calders, K., Murphy, S., Åkerblom, M. and Kaasalainen, M. (2015) 'Massive-scale tree modelling from TLS data', *ISPRS Annals of the Photogrammetry, Remote Sensing and Spatial Information Sciences*, 2(3), pp. 189-196.

Rautiainen, M. and Lukeš, P. (2015) 'Spectral contribution of understory to forest reflectance in a boreal site: an analysis of EO-1 Hyperion data', *Remote Sensing of Environment*, 171, pp. 98-104.

Riaño, D., Vaughan, P., Chuvieco, E., Zarco-Tejada, P.J. and Ustin, S.L. (2005) 'Estimation of fuel moisture content by inversion of radiative transfer models to simulate equivalent water thickness and dry matter content: Analysis at leaf and canopy level', *IEEE Transactions on Geoscience and Remote Sensing*, 43(4), pp. 819-826.

Rodríguez-Pérez, J.R., Riaño, D., Carlisle, E., Ustin, S. and Smart, D.R. (2007) 'Evaluation of hyperspectral reflectance indexes to detect grapevine water status in vineyards', *American Journal of Enology and Viticulture*, 58(3), pp. 302-317.

Rosema, A., Verhoef, W., Noorbergen, H. and Borgesius, J. (1992) 'A new forest light interaction model in support of forest monitoring', *Remote Sensing of Environment*, 42(1), pp. 23-41.

Ross, J. (1981) 'The radiation regime and architecture of plant stands', *Dr. W. Junk Publ.: The Hague, The Netherlands*.

Ross, J. (2012) *The radiation regime and architecture of plant stands*. Springer Science & Business Media.

Rouse Jr, J.W., Haas, R., Schell, J. and Deering, D. (1974) 'Monitoring vegetation systems in the Great Plains with ERTS'.

Schär, C., Vidale, P.L., Lüthi, D., Frei, C., Häberli, C., Liniger, M.A. and Appenzeller, C. (2004) 'The role of increasing temperature variability in European summer heatwaves', *Nature*, 427(6972), p. 332.

Schneider, C.A., Rasband, W.S. and Eliceiri, K.W. (2012) 'NIH Image to ImageJ: 25 years of image analysis', *Nature methods*, 9(7), pp. 671-675.

Scholander, P.F., Bradstreet, E.D., Hemmingsen, E. and Hammel, H. (1965) 'Sap pressure in vascular plants: negative hydrostatic pressure can be measured in plants', *Science*, 148(3668), pp. 339-346.

Seinfeld, J.H. and Pandis, S.N. (2016) *Atmospheric chemistry and physics: from air pollution to climate change*. John Wiley & Sons.

Sepulcre-Cantó, G., Zarco-Tejada, P.J., Jiménez-Muñoz, J., Sobrino, J., De Miguel, E. and Villalobos, F.J. (2006) 'Detection of water stress in an olive orchard with thermal remote sensing imagery', *Agricultural and Forest Meteorology*, 136(1-2), pp. 31-44.

Sepulcre-Canto, G., Zarco-Tejada, P.J., Sobrino, J., Berni, J.A., Jimenez-Munoz, J. and Gastellu-Etchegorry, J.-P. (2009) 'Discriminating irrigated and rainfed olive orchards with thermal ASTER imagery and DART 3D simulation', *Agricultural and Forest Meteorology*, 149(6-7), pp. 962-975.

Serrano, L., Ustin, S.L., Roberts, D.A., Gamon, J.A. and Penuelas, J. (2000) 'Deriving water content of chaparral vegetation from AVIRIS data.', *Remote Sensing of Environment*, 74, pp. 570-581.

Sevanto, S., McDowell, N.G., Dickman, L.T., Pangle, R. and Pockman, W.T. (2014) 'How do trees die? A test of the hydraulic failure and carbon starvation hypotheses', *Plant, cell & environment*, 37(1), pp. 153-161.

Sims, D.A. and Gamon, J.A. (2003) 'Estimation of vegetation water content and photosynthetic tissue area from spectral reflectance: a comparison of indices based on liquid water and chlorophyll absorption features', *Remote sensing of environment*, 84(4), pp. 526-537.

Smith, R.J. (2009) 'Use and misuse of the reduced major axis for line-fitting', *American Journal of Physical Anthropology: The Official Publication of the American Association of Physical Anthropologists*, 140(3), pp. 476-486.

Spanner, M.A., Pierce, L.L., Peterson, D.L. and Running, S.W. (1990) 'Remote sensing of temperate coniferous forest leaf area index The influence of canopy closure, understory vegetation and background reflectance', *TitleREMOTE SENSING*, 11(1), pp. 95-111.

Srinivasan, S., Popescu, S.C., Eriksson, M., Sheridan, R.D. and Ku, N.-W. (2014) 'Multi-temporal terrestrial laser scanning for modeling tree biomass change', *Forest Ecology and Management*, 318, pp. 304-317.

Stott, P.A., Stone, D.A. and Allen, M.R. (2004) 'Human contribution to the European heatwave of 2003', *Nature*, 432(7017), p. 610.

Sun, G., Niu, Z., Gao, S., Huang, W., Wang, L., Li, W. and Feng, M. (2014) *SPIE Asia Pacific Remote Sensing*. International Society for Optics and Photonics.

Sun, J., Shi, S., Yang, J., Chen, B., Gong, W., Du, L., Mao, F. and Song, S. (2018) 'Estimating leaf chlorophyll status using hyperspectral lidar measurements by PROSPECT model inversion', *Remote Sensing of Environment*, 212, pp. 1-7.

Sun, J., Shi, S., Yang, J., Gong, W., Qiu, F., Wang, L., Du, L. and Chen, B. (2019) 'Wavelength selection of the multispectral lidar system for estimating leaf chlorophyll and water contents through the PROSPECT model', *Agricultural and Forest Meteorology*, 266, pp. 43-52.

Takeda, T., Oguma, H., Sano, T., Yone, Y. and Fujinuma, Y. (2008) 'Estimating the plant area density of a Japanese larch (Larix kaempferi Sarg) plantation using a ground-based laser scanner', *Agricultural and Forest Meteorology*, 148, pp. 428–438.

Tan, K., Chen, J., Qian, W., Zhang, W., Shen, F. and Cheng, X. (2019) 'Intensity Data Correction for Long-Range Terrestrial Laser Scanners: A Case Study of Target Differentiation in an Intertidal Zone', *Remote Sensing*, 11(3), p. 331.

Tan, K. and Cheng, X. (2016) 'Surface reflectance retrieval from the intensity data of a terrestrial laser scanner', *JOSA A*, 33(4), pp. 771-778.

Tan, K., Cheng, X., Ding, X. and Zhang, Q. (2016) 'Intensity data correction for the distance effect in terrestrial laser scanners', *IEEE Journal of Selected Topics in Applied Earth Observations and Remote Sensing*, 9(1), pp. 304-312.

Tan, K., Zhang, W., Shen, F. and Cheng, X. (2018) 'Investigation of tls intensity data and distance measurement errors from target specular reflections', *Remote Sensing*, 10(7), p. 1077.

Tang, H., Dubayah, R., Swatantran, A., Hofton, M., Sheldon, S., Clark, D.B. and Blair, B. (2012) 'Retrieval of vertical LAI profiles over tropical rain forests using waveform lidar at La Selva, Costa Rica', *Remote Sensing of Environment*, 124, pp. 242–250.

Terashima, I., Hanba, Y.T., Tazoe, Y., Vyas, P. and Yano, S. (2005) 'Irradiance and phenotype: comparative eco-development of sun and shade leaves in relation to photosynthetic CO2 diffusion', *Journal of Experimental Botany*, 57(2), pp. 343-354.

Thenkabail, P.S., Teluguntla, P., Gumma, M.K. and Dheeravath, V. (2015) 'Hyperspectral remote sensing for terrestrial applications', *Environmental Monitoring and Assessment*, pp. 201-233.

Tian, J., Dai, T., Li, H., Liao, C., Teng, W., Hu, Q., Ma, W. and Xu, Y. (2019) 'A Novel Tree Height Extraction Approach for Individual Trees by Combining TLS and UAV Image-Based Point Cloud Integration', *Forests*, 10(7), p. 537.

Trombetti, M., Riaño, D., Rubio, M.A., Cheng, Y.B. and Ustin, S.L. (2008) 'Multi-temporal Vegetation Canopy Water Content Retrieval and Interpretation Using Artificial Neural Networks for the Continental USA', *Remote Sensing of Environment*, 112, pp. 203–215.

Trumbore, S., Brando, P. and Hartmann, H. (2015) 'Forest health and global change', *Science*, 349(6250), pp. 814-818.

Tucker, C.J. (1979) 'Red and Photographic Infrared Linear Combinations for Monitoring Vegetation', *Remote Sensing of Environment*, 8, pp. 127–150.

Tucker, C.J. (1980) 'Remote sensing of leaf water content in the near infrared', *Remote sensing of Environment*, 10(1), pp. 23-32.

Ustin, S.L., Roberts, D.A., Pinzon, J., Jacquemoud, S., Gardner, M., Scheer, G., Castaneda, C.M. and Palacios-Orueta, A. (1998) 'Estimating canopy water content of chaparral shrubs using optical methods', *Remote Sensing of Environment*, 65(3), pp. 280-291.

Valentinuz, O.R. and Tollenaar, M. (2004) 'Vertical Profile of Leaf Senescence During the Grain-filling Period in Older and Newer Maize Hybrids', *Crop Science*, 44, pp. 827–834.

Van Niel, T., McVicar, T., Fang, H. and Liang, S. (2003) 'Calculating environmental moisture for per-field discrimination of rice crops', *International Journal of Remote Sensing*, 24(4), pp. 885-890.

Verhoef, W. (1984) 'Light Scattering by Leaf Layers with Application to Canopy Reflectance Modelling: the SAIL Model', *Remote Sensing of Environment*, 16, pp. 125–141.

Verrelst, J., Schaepman, M.E., Malenovský, Z. and Clevers, J.G. (2010) 'Effects of woody elements on simulated canopy reflectance: Implications for forest chlorophyll content retrieval', *Remote Sensing of Environment*, 114(3), pp. 647-656.

Viegas, D., Viegas, M. and Ferreira, A. (1992) 'Moisture content of fine forest fuels and fire occurrence in central Portugal', *International Journal of Wildland Fire*, 2(2), pp. 69-86.

Vila, H., Hugalde, I. and Di Filippo, M. (2011) 'Estimation of leaf water potential by thermographic and spectral measurements in grapevine', *RIA: Revista de Investigaciones Agropecuarias*.

Vincent, G., Antin, C., Dauzat, J., Grau, E. and Durrieu, S. (2015) 'Mapping plant area index of tropical forest by Lidar: calibrating ALS with TLS', *Proceedings of silviLaser*, 2015, pp. 146-148.

Vogel, M.M., Zscheischler, J., Wartenburger, R., Dee, D. and Seneviratne, S.I. (2019) 'Concurrent 2018 Hot Extremes Across Northern Hemisphere Due to Human-Induced Climate Change', *Earth's Future*, 7(7), pp. 692-703.

Wang, Q. and Li, P. (2013) 'Canopy vertical heterogeneity plays a critical role in reflectance simulation', *Agricultural and Forest Meteorology*, 169, pp. 111–121.

Wang, Z., Chen, Y., Li, C., Tian, M., Zhou, M., He, W., Wu, H., Zhang, H., Tang, L. and Wang, Y. (2018) *IGARSS 2018-2018 IEEE International Geoscience and Remote Sensing Symposium*. IEEE.

Wangab, X., Zhaoa, C., Guob, N., Lib, Y., Jiana, S. and Yua, K. (2015) 'Determining the Canopy Water Stress for Spring Wheat Using Canopy Hyperspectral Reflectance Data in Loess Plateau Semiarid Regions', *Spectroscopy Letters: An International Journal for Rapid Communication*, 48, pp. 492-498.

Wanner, W., Strahler, A., Hu, B., Lewis, P., Muller, J.P., Li, X., Schaaf, C. and Barnsley, M. (1997) 'Global retrieval of bidirectional reflectance and albedo over land from EOS MODIS and MISR data: Theory and algorithm', *Journal of Geophysical Research: Atmospheres*, 102(D14), pp. 17143-17161.

Waterman, P.G., Choo, G.M., Vedder, A.L. and Watts, D. (1983) 'Digestibility, digestion-inhibitors and nutrients of herbaceous foliage and green stems from an African montane flora and comparison with other tropical flora', *Oecologia*, 60(2), pp. 244-249.

Weerasinghe, L.K., Creek, D., Crous, K.Y., Xiang, S., Liddell, M.J., Turnbull, M.H. and Atkin, O.K. (2014) 'Canopy position affects the relationships between leaf respiration and associated traits in a tropical rainforest in Far North Queensland', *Tree physiology*, 34(6), pp. 564-584.

Wei, G., Shalei, S., Bo, Z., Shuo, S., Faquan, L. and Xuewu, C. (2012) 'Multi-wavelength canopy LiDAR for remote sensing of vegetation: Design and system performance', *ISPRS journal of photogrammetry and remote sensing*, 69, pp. 1-9.

Weiss, M., Baret, F., Myneni, R., Pragnère, A. and Knyazikhin, Y. (2000) 'Investigation of a model inversion technique to estimate canopy biophysical variables from spectral and directional reflectance data'.

White, K., Pontius, J. and Schaberg, P. (2014) 'Remote sensing of spring phenology in northeastern forests: A comparison of methods, field metrics and sources of uncertainty', *Remote Sensing of Environment*, 148, pp. 97-107.

Widlowski, J.-L., Mio, C., Disney, M., Adams, J., Andredakis, I., Atzberger, C., Brennan, J., Busetto, L., Chelle, M. and Ceccherini, G. (2015) 'The fourth phase of the radiative transfer model intercomparison (RAMI) exercise: Actual canopy scenarios and conformity testing', *Remote Sensing of Environment*, 169, pp. 418-437.

Widlowski, J.-L., Robustelli, M., Disney, M., Gastellu-Etchegorry, J.-P., Lavergne, T., Lewis, P., North, P., Pinty, B., Thompson, R. and Verstraete, M. (2008) 'The RAMI On-line Model Checker (ROMC): A web-based benchmarking facility for canopy reflectance models', *Remote Sensing of Environment*, 112(3), pp. 1144-1150.

Widlowski, J.L., Pinty, B., Lopatka, M., Atzberger, C., Buzica, D., Chelle, M., Disney, M., Gastellu-Etchegorry, J.P., Gerboles, M. and Gobron, N. (2013) 'The fourth radiation transfer model intercomparison (RAMI-IV): Proficiency testing of canopy reflectance models with ISO-13528', *Journal of Geophysical Research: Atmospheres*, 118(13), pp. 6869-6890.

Widlowski, J.L., Taberner, M., Pinty, B., Bruniquel-Pinel, V., Disney, M., Fernandes, R., Gastellu-Etchegorry, J.P., Gobron, N., Kuusk, A. and Lavergne, T. (2007) 'Third Radiation Transfer Model Intercomparison (RAMI) exercise: Documenting progress in canopy reflectance models', *Journal of Geophysical Research: Atmospheres*, 112(D9).

Williams, L.E. and Araujo, F.J. (2002) 'Correlations among predawn leaf, midday leaf, and midday stem water potential and their correlations with other measures of soil and plant water status in Vitis vinifera', *Journal of the American Society for Horticultural Science*, 127(3), pp. 448-454.

Wright, I.J., Reich, P.B., Westoby, M., Ackerly, D.D., Baruch, Z., Bongers, F., Cavender-Bares, J., Chapin, T., Cornelissen, J.H. and Diemer, M. (2004) 'The worldwide leaf economics spectrum', *Nature*, 428(6985), p. 821.

Xu, T., Xu, L., Li, X. and Yao, J. (2018) 'Detection of water leakage in underground tunnels using corrected intensity data and 3d point cloud of terrestrial laser scanning', *IEEE Access*, 6, pp. 32471-32480.

Xue, J. and Su, B. (2017) 'Significant remote sensing vegetation indices: a review of developments and applications', *Journal of Sensors*, 2017.

Yáñez-Rausell, L., Malenovský, Z., Rautiainen, M., Clevers, J.G., Lukeš, P., Hanuš, J. and Schaepman, M.E. (2015) 'Estimation of spruce needle-leaf chlorophyll content based on DART and PARAS canopy reflectance models', *IEEE Journal of Selected Topics in Applied Earth Observations and Remote Sensing*, 8(4), pp. 1534-1544.

Yao, R.T., Scarpa, R., Turner, J.A., Barnard, T.D., Rose, J.M., Palma, J.H.N. and Harrison, D.R. (2014) 'Valuing biodiversity enhancement in New Zealand's planted forests: Socioeconomic and spatial determinants of willingness-to-pay', *Ecological Economics*, 98, pp. 90-101.

Yebra, M. and Chuvieco, E. (2009) 'Linking ecological information and radiative transfer models to estimate fuel moisture content in the Mediterranean region of Spain: Solving the ill-posed inverse problem', *Remote Sensing of Environment*, 113(11), pp. 2403-2411.

Yebra, M., Chuvieco, E. and Riaño, D. (2008) 'Estimation of Live Fuel Moisture Content from MODIS Images for Fire Risk Assessment', *Agricultural and Forest Meteorology*, 148, p. 523−536.

Yebra, M., Dennison, P.E., Chuvieco, E., Riano, D., Zylstra, P., Hunt Jr, E.R., Danson, F.M., Qi, Y. and Jurdao, S. (2013) 'A global review of remote sensing of live fuel moisture content for fire danger assessment: Moving towards operational products', *Remote Sensing of Environment*, 136, pp. 455-468.

Yi, Q., Wang, F., Bao, A. and Jiapaer, G. (2014) 'Leaf and Canopy Water Content Estimation in Cotton Using Hyperspectral Indices and Radiative Transfer Models', *International Journal of Applied Earth Observation and Geoinformation*, 33, pp. 67–75.

Yilmaz, M.T., Hunt Jr, E.R. and Jackson, T.J. (2008) 'Remote sensing of vegetation water content from equivalent water thickness using satellite imagery', *Remote Sensing of Environment*, 112(5), pp. 2514-2522.

Yu, X., Liang, X., Hyyppä, J., Kankare, V., Vastaranta, M. and Holopainen, M. (2013) 'Stem biomass estimation based on stem reconstruction from terrestrial laser scanning point clouds', *Remote sensing letters*, 4(4), pp. 344-353.

Yuan, L., Huang, Y., Loraamm, R.W., Nie, C., Wang, J. and Zhang, J. (2014) 'Spectral analysis of winter wheat leaves for detection and differentiation of diseases and insects', *Field Crops Research*, 156, pp. 199-207.

Zarco-Tejada, P.J., Miller, J.R., Noland, T.L., Mohammed, G.H. and Sampson, P.H. (2001) 'Scaling-up and model inversion methods with narrowband optical indices for chlorophyll content estimation in closed forest canopies with hyperspectral data', *IEEE Transactions on Geoscience and Remote Sensing*, 39(7), pp. 1491-1507.

Zarco-Tejada, P.J., Rueda, C.A. and Ustin, S.L. (2003) 'Water Content Estimation in Vegetation with MODIS Reflectance Data and Model Inversion Methods', *Remote Sensing of Environment*, 85, pp. 109–124.

Zhang, F. and Zhou, G. (2015) 'Estimation of Canopy Water Content by Means of Hyperspectral Indices Based on Drought Stress Gradient Experiments of Maize in the North Plain China', *Remote Sensing*, 7, pp. 15203-15223.

Zhang, J.-C., Pu, R.-L., Wang, J.-H., Huang, W.-J., Yuan, L. and Luo, J.-H. (2012) 'Detecting powdery mildew of winter wheat using leaf level hyperspectral measurements', *Computers and Electronics in Agriculture*, 85, pp. 13-23.

Zhang, Z., Tang, B.-H. and Li, Z.-L. (2019) 'Retrieval of leaf water content from remotely sensed data using a vegetation index model constructed with shortwave infrared reflectances', *International Journal of Remote Sensing*, 40(5-6), pp. 2313-2323.

Zhao, S., Wang, Q., Yao, Y., Du, S., Zhang, C., Li, J. and Zhao, J. (2016) 'Estimating and Validating Wheat Leaf Water Content with Three MODIS Spectral Indexes: A Case Study in Ningxia Plain, China', *Journal of Agricultural Science and Technology*, 18(2), pp. 387-398.

Zheng, G., Ma, L., He, W., Eitel, J.U.H., Moskal, L.M. and Zhang, Z. (2016) 'Assessing the contribution of woody materials to forest angular gap fraction and effective leaf area index using terrestrial laser scanning data', *IEEE Transactions on Geoscience and Remote Sensing*, 54(3), pp. 1475-1487.

Zheng, G., Moskal, L.M. and Kim, S.-H. (2013) 'Retrieval of Effective Leaf Area Index in Heterogeneous Forests With Terrestrial Laser Scanning', *IEEE Trans. Geoscience and Remote Sensing*, 51(2), pp. 777-786.

Zhu, X., Skidmore, A.K., Darvishzadeh, R., Niemann, K.O., Liu, J., Shi, Y. and Wang, T. (2018) 'Foliar and woody materials discriminated using terrestrial LiDAR in a mixed natural forest', *International journal of applied earth observation and geoinformation*, 64, pp. 43-50.

Zhu, X., Skidmore, A.K., Darvishzadeh, R. and Wang, T. (2019) 'Estimation of forest leaf water content through inversion of a radiative transfer model from LiDAR and hyperspectral data', *International Journal of Applied Earth Observation and Geoinformation*, 74, pp. 120-129.

Zhu, X., Wang, T., Darvishzadeh, R., Skidmore, A.K. and Niemann, K.O. (2015) '3D leaf water content mapping using terrestrial laser scanner backscatter intensity with radiometric correction', *ISPRS Journal of Photogrammetry and Remote Sensing*, 110, pp. 14-23.

Zhu, X., Wang, T., Skidmore, A.K., Darvishzadeh, R., Niemann, K.O. and Liu, J. (2017) 'Canopy leaf water content estimated using terrestrial LiDAR', *Agricultural and Forest Meteorology*, 232, pp. 152-162.

Zivcak, M., Brestic, M., Balatova, Z., Drevenakova, P., Olsovska, K., Kalaji, H.M., Yang, X. and Allakhverdiev, S.I. (2013) 'Photosynthetic electron transport and specific photoprotective responses in wheat leaves under drought stress', *Photosynthesis research*, 117(1-3), pp. 529-546.